Past to Future and Land to Sea: Constraining Global Glacier Models by Observations and exploring Ice-Ocean Interactions

A dissertation presented for the degree of
Doktor der Naturwissenschaften

by
Jan-Hendrik Malles

submitted to:
Institute of Geography
Faculty 8
University of Bremen

First Reviewer:	Prof. Dr. Ben Marzeion Institute of Geography University of Bremen
Second Reviewer:	Prof. Dr. Fiamma Straneo Scripps Institution of Oceanography University of California San Diego

Colloquium: 26th of June 2023

Abstract

Glacier mass loss is an iconic process induced by anthropogenic climate change. It threatens human livelihood at coasts affected by the rising sea level and in glacierized hydrological basins where the glacial runoff is essential for water availability. Moreover, as glacier mass loss adds large amounts of freshwater to the oceans, it might alter ocean circulation in a way that affects marine ecosystems and the climate system. Only recently, satellite-data processing revealed mass changes on an individual glacier level (outside the large ice sheets), but only for the last two decades. Glacier mass change observations become increasingly sparse going back in time. Therefore, the glaciers' past contribution to global mean sea level rise can only be reconstructed using numerical models. Since glacier mass change will continue during this century, it is vital to understand how this will affect global mean sea level, ocean circulation, and regional hydrology. Again, this is only possible using numerical models. Hence, it is essential to improve these models by incorporating previously neglected processes of glacier mass change into them, mainly in the form of parametrizations, and by constraining them using observations. Moreover, it is crucial to understand the uncertainties of results produced by numerical models, as they can never fully represent the natural world, which also hinges on the amount and quality of observational data. This work will tackle aspects of three issues in numerically modeling glacier mass changes: past glacier mass change reconstructions' uncertainties, future mass change projections' uncertainties, specifically regarding marine-terminating glaciers, and ice-ocean interactions in the northern hemisphere outside the Greenland ice sheet. All three issues are relevant in addressing the question of how glaciers respond to changes in their mass balance due to climatic changes and what consequences such changes have for the Earth system and, ultimately, human livelihood. It is found that the further outside the glaciological and meteorological observations' spatial and temporal domain a numerical model is applied, the more uncertain reconstructed glacier mass changes become. Similarly, one primary source of uncertainty in future glacier mass change projections is the difference in climate models' outputs of near-surface temperatures and precipitation. More accurately describing marine-terminating glacier dynamics and considering volume changes below sea level reduces estimates of future glacier contribution to global mean sea level rise systematically. However, significant uncertainties due to uncertainty about appropriate values for parameters involved in modeling (marine-terminating) glaciers' dynamics are detected. Concerning ice-ocean interactions, it was found that including the freshwater input from glacier mass loss in the northern hemisphere (outside the Greenland ice sheet) in an ocean general circulation model significantly impacts the simulated high-latitude ocean circulation. Finally, a first estimate of the ice mass glaciers lose due to melting directly into the ocean was produced.

Zusammenfassung

Der Massenverlust der Gletscher ist ein ikonischer Prozess, der durch den anthropogenen Klimawandel verursacht wird. Er bedroht die Lebensgrundlage der Menschen an den Küsten, die vom Anstieg des Meeresspiegels betroffen sind, und in vergletscherten Wassereinzugsgebieten, wo der Gletscherabfluss für die Wasserverfügbarkeit von entscheidender Bedeutung ist. Da durch den Massenverlust der Gletscher große Mengen an Süßwasser in den Ozean gelangen, könnte dies die Ozeanzirkulation in einer Weise verändern, die sich auf marine Ökosysteme und das Klimasystem auswirkt. Erst in jüngster Zeit hat die Verarbeitung von Satellitendaten Massenänderungen auf der Ebene einzelner Gletscher (außerhalb der großen Eisschilde) aufgezeigt, allerdings nur für die letzten zwei Jahrzehnte. Die Beobachtungen von Gletschermassenveränderungen werden immer spärlicher, je weiter man in die Vergangenheit zurückgeht. Daher kann der frühere Beitrag der Gletscher zum mittleren globalen Meeresspiegelanstieg nur mit Hilfe numerischer Modelle rekonstruiert werden. Da sich die Gletschermassenänderung in diesem Jahrhundert fortsetzen wird, ist es wichtig zu verstehen, wie sich dies auf den mittleren globalen Meeresspiegel, die Ozeanzirkulation und die regionale Hydrologie auswirken wird. Auch dies ist nur mit Hilfe numerischer Modelle möglich. Daher müssen diese Modelle stetig verbessert werden, indem bisher vernachlässigte Prozesse der Gletschermassenänderung einbezogen werden, häufig durch Parametrisierungen, und indem sie durch Beobachtungen angepasst werden. Darüber hinaus ist es von Bedeutung, die Unsicherheiten der Ergebnisse numerischer Modelle zu verstehen, da diese die natürliche Welt nie vollständig abbilden können, was auch von der Menge und Qualität der Beobachtungsdaten abhängt. Diese Arbeit wird sich mit drei Aspekten der numerischen Modellierung von Gletschermassenänderungen befassen: den Unsicherheiten bei der Rekonstruktion vergangener Gletschermassenänderungen, den Unsicherheiten bei der Vorhersage zukünftiger Massenänderungen, insbesondere in Bezug auf marin-terminierende Gletscher, und den Wechselwirkungen zwischen Eis und Ozean in der nördlichen Hemisphäre außerhalb des grönländischen Eisschildes. Alle drei Themen sind relevant für die Frage, wie Gletscher auf Veränderungen in ihrer Massenbilanz aufgrund von Klimaveränderungen reagieren und welche Folgen solche Veränderungen für das Erdsystem und letztlich für die Lebensgrundlage des Menschen haben. Es zeigte sich, dass die rekonstruierten Gletschermassenänderungen umso unsicherer werden, je weiter außerhalb des räumlichen und zeitlichen Bereichs der glaziologischen und meteorologischen Beobachtungen ein numerisches Modell angewendet wird. Eine der Hauptursachen für Unsicherheiten bezüglich künftiger Gletschermassenänderungen sind die unterschiedlichen Ergebnisse der Klimamodelle für oberflächennahe Temperaturen und Niederschläge. Eine genauere Beschreibung der Dynamik marin-terminierender Gletscher und die Berücksichtigung von Volumenänderungen unterhalb des Meeresspiegels verringern die Schätzungen des künftigen Beitrags der Gletscher zum globalen mittleren Meeresspiegelanstieg systematisch. Es wurden jedoch erhebliche Unsicherheiten festgestellt, die auf die Ungewissheit über geeignete Werte für die Parameter zurückzuführen sind, die bei der Modellierung der Dynamik von (marin-terminierenden) Gletschern eine Rolle spielen. In Bezug auf die Wechselwirkungen zwischen Eis und Ozean wurde festgestellt, dass die Einbeziehung des Süßwassereintrags aus dem Massenverlust der Gletscher auf der Nordhalbkugel (außerhalb des grönländischen Eisschildes) in ein Ozeanzirkulationsmodell die simulierte Ozeanzirkulation in den hohen Breiten signifikant beeinflusst. Schließlich wurde eine erste Schätzung der Eismasse vorgenommen, die die Gletscher durch ihr submarines Schmelzen verlieren.

Acknowledgments

First and foremost, I want to thank my loving companion Nadja Gallus for always supporting me in stressful times. I would also like to thank Ben Marzeion for his thoughtful supervision and for always being approachable. Fabien Maussion, as the maintainer of the Open Global Glacier Model, was also instrumental in my work's progress. Further, thanks go to Michal Kucera, one of the graduate school program ArcTrain's initiators. I was fortunate to participate in this program, as it provided unique possibilities for international exchange and professional formation. Therefore, I want to thank everyone involved in ArcTrain for making it a vivid scientific community, especially Paul Myers, for facilitating my research stay in Edmonton. Finally, I would like to thank my friend Jöran Schlömer for always being forthcoming when asked for advice on issues concerning mathematics or physics.

Thesis Outline

After a short introduction of the main concepts and methods that will be applied in this work, the objectives of this thesis will be defined. These objectives will subsequently be addresses in three main chapters. Two of these chapters have been published as articles in peer-reviewed scientific journals, and the third chapter is currently in review for such a journal:

- Malles, J.-H. and Marzeion, B., 2021: *Twentieth century global glacier mass change: an ensemble-based model reconstruction*, The Cryosphere, 15, 3135–3157, doi:10.5194/tc-15-3135-2021
- Malles, J.-H., Maussion, F., Ultee, L., Kochtitzky, W., Copland, L., and Marzeion, B., 2023: *Exploring the impact of a frontal ablation parameterization on projected 21st-century mass change for Northern Hemisphere glaciers*, Journal of Glaciology, 1–16, doi: 10.1017/jog.2023.19
- Malles, J.-H., Marzeion, B., and Myers, P. G., 2023: *Freshwater input from glacier melt outside Greenland alters modeled northern high-latitude ocean circulation*, in review for Journal of Geophysical Research: Oceans

In the last two chapters, the whole thesis and its outcomes regarding the stated objectives will be discussed, the outcomes summarized, and avenues for future research pointed out.

Table of Contents

Chapter 1: Introduction

Presently, humans are emitting vast quantities of so-called greenhouse gases into Earth's atmosphere by the combustion of fossil fuels, land cover changes, land use, livestock breeding and manure, and ancillary industrial processes. This conduct has already altered Earth's atmosphere's chemical composition due to a drastic increase in the three major greenhouse gases' concentrations (carbon dioxide, methane, and nitrous oxide), which are now higher than during any time of the human species' existence (Gulev et al., 2021). Since the name *greenhouse* gas originates from the fact that these gases absorb portions of the Earth's outgoing longwave radiation and partly re-emit it, the main consequence of increasing greenhouse gas concentrations is an increased longwave radiation (i.e., radiative forcing) from the atmosphere back towards Earth's surface (Gulev et al., 2021). This increasing radiative forcing increases the amount of heat stored in the Earth system leading to a warming climate, but has the potential to evoke complex processes in the dynamical Earth system that can increase or decrease the radiative forcing (positive and negative *feedbacks*). The release of stored carbon reservoirs (fossil fuels) are a perturbation of the natural carbon cycle. Massive perturbations of Earth's carbon cycle can lead to the crossing of tipping points or thresholds in the dynamical system, leading to changes that are either self-sustained or too fast for life to adapt to, thereby moving the Earth system from one steady state to another with potentially catastrophic implications for life on the planet (Steffen et al., 2018; Rothman, 2017, 2019; McKay et al., 2022).

Consequently, anthropogenic climate change can be comprehended as an experiment on the planetary scale with imponderable consequences. In contrast to the common conception of a scientific experiment, humans did not contrive the release of greenhouse gases in advance with a hypothesis in mind. However, they gradually became aware of the implications when the experiment was already well underway, and scientists started piecing together the puzzle of the increasing greenhouse gas concentrations' impact on the Earth system. It became apparent that the large majority of the accumulating heat is stored in the oceans and that of the different subsystems the atmosphere actually stores the smallest amount of the additional heat until today (von Schuckmann et al., 2020). This is partly because increasing atmospheric temperatures cause ice masses to warm up and ultimately melt, draining heat from the atmosphere in the process. To a smaller extent, this is also true for the ocean, as some of Earth's ice bodies are losing mass by being in contact with ocean water at temperatures above the freezing point. Changes in Earth's ice coverage had intrigued scientists already before the issue of glacier melt due to anthropogenic climate change arose, mainly in the context of *glacial cycles*. Today, glacier melt due to anthropogenic climate change is of importance to humanity because the demise of Earth's ice bodies and the concomitant release of large amounts of freshwater raises global mean sea level and changes the hydrology in glacierized basins, impacting human livelihood in affected areas (Hock et al., 2019a; Oppenheimer et al., 2019). Glaciers are sometimes also referred to as a canary in the coal mine, for their melting is an iconic signal of anthropogenic climate change recognizable for people not involved in climate science. From 1900 to 2018, glaciers outside Greenland and Antarctica have contributed roughly 55 %, or around 0.7 mm a^{-1}, to total ice melt-related sea level rise (Frederikse et al., 2020). Moreover, the freshwater input to the oceans changes its near-surface density and surface height. Thus, it can change ocean circulation with potential consequences for the planet's livelihood, as the ocean plays a vital role in global heat distribution and carbon cycle (Bigg et al., 2003).

This work will focus on the broader topic of how ice masses outside the large ice sheets in Greenland and Antarctica are responding to changes in the atmosphere as well as in the ocean. As observational data on the state of the Earth system are temporally and spatially sparse, one often resorts to the use of numerical computer models when trying to infer knowledge about changes in the system outside the observations' temporal and spatial domain. Such mathematical representations are inherently limited because some physical processes of the natural world might either not be correctly understood and implemented in the models or occur on too small spatial or temporal scales to be resolved without exceeding available computational resources. Numerical models aimed at simulating real-world processes also depend on observational data of modeled variables, as the models' validity can not be examined without them. This work will address issues of numerically modeling glaciers' past and future evolution, how observations of Earth's glaciers can be used for this, and the current limitations of such endeavors. The following will introduce some basic concepts of current knowledge about how Earth's glaciers' mass evolves in response to a warming planet. Furthermore, it will be introduced how this knowledge is applied in numerical models to better understand past and future glacier evolution on decadal to centennial timescales. Moreover, one chapter of this thesis investigates the northern high-latitude ocean circulations' response to increased freshwater input due to glacier melt. After stating objectives for enhancing the knowledge on numerically modeling glacier evolution and ice-ocean interactions, three chapters, each addressing one of these objectives, will follow. Subsequently, a discussion will be presented regarding the stated objectives and issues to be addressed in future work on the topics touched upon. This work will then conclude by briefly summarizing the primary outcomes.

1.1 Inventory of Earth's glaciers

The first question that must be addressed when investigating global glacier changes: How many glaciers are there, and where are they situated? Generally, glaciers can emerge in locations where more snow falls than melts over several years. This allows the snow to accumulate and subsequently be transformed into ice by gravitational compaction. Since ice and snow have distinct spectral characteristics, getting a hold of the planets' glaciers' distribution is possible using satellite-derived surface reflectance or imagery data (Paul et al., 2013). In order to facilitate the investigation of Earth's glaciers, efforts were put into creating an inventory that collects knowledge about the location and outlines of glaciers as well as their hypsometric properties. The product of this effort is the Randolph Glacier Inventory (RGI), which was first released in 2012 and continues to be updated. The current version 6 of the RGI counts over 200,000 glaciers not connected to the Greenland and Antarctic ice sheets, covering an area of over 700,000 km^2 (Pfeffer et al., 2014; RGI Consortium, 2017). This inventory data is an essential input to large-scale numerical glacier evolution models, as it makes it possible to anchor the temporal evolution of glaciers to the state recorded in the inventory.

1.2 Glacier mass balance

For glaciers to grow, they need a positive mass balance, and the mass of glaciers is water in its solid form. Hence, glaciers are found where climatic and topographic conditions allow(ed) for an accumulation of snow over an extended period. The opposite of accumulation is ablation; the mass removal from a glacier, in the case of a typical mountain glacier, primarily due to surface melt by transfer of atmospheric and solar heat energy into the ice. This means that locations where accumulation is higher than ablation over several years can host the formation/growth of glaciers and that the mass balance of glaciers is mostly driven by atmospheric climate (Cuffey and Paterson, 2010, pp. 91 - 100). The accumulated snow compacts to ice over time by gravity. When enough ice has accumulated at a location, gravity forces the ice body to move along the topography like a highly viscous fluid. At some point, the glacier will flow into an area with atmospheric conditions that no longer allow for a net accumulation, and ablation over that part of the glacier will dominate. The glacier then has an accumulation area, where the mass balance is positive, and an ablation area, where the mass balance is negative; hence, there is a mass balance gradient along the glacier. A glacier that has a net mass balance over its entire area of zero is denoted to be in equilibrium (or steady state). Some glaciers never reach such an equilibrium state and maintain a net-positive (surface) mass balance before encountering the ocean, thus experiencing frontal ablation; mass removal caused by iceberg calving, and submarine melt. Hence, throughout this work, the mass balance of land-terminating glaciers will be referred to as solely the surface mass balance, whereas the mass balance of a marine-terminating glacier also has a frontal ablation component. In a strict sense, surface mass balance is not the most accurate term since internal processes (refreezing) can influence the mass balance (see Fig. 1.1). The more accurate term is climatic mass balance. However, the term surface mass balance will still be used for coherence throughout the work since internal mass balance processes will not be explicitly treated. For a glacier to attain a state of equilibrium, it would have to experience a certain period of stable climate conditions and thus stable net mass balance. That is because a glacier generally takes several years to adjust to changes in the mass balance due to its (slow) flow (Nye, 1963). How the description of glacier flow can be simplified for application in large-scale numerical models will be addressed in Section 1.4.3. Regarding marine-terminating glaciers, this issue is complicated by the fact that the frontal ablation and dynamics are influenced by the submerged bed topography, which can lead to self-sustained retreat in response to an initial perturbation (Schoof, 2007).

It stands to reason that most glaciers are not in equilibrium today due to anthropogenic climate change since the accumulation of heat in Earth's atmosphere (and ocean) causes increased ablation of most glaciers. While a warmer atmosphere can also hold more moisture and thus a potential increase in solid precipitation might partly compensate for increased ablation, less liquid precipitation actually reaches Earth's surface in most regions (Tamang et al., 2020; Mankin and Diffenbaugh, 2015).

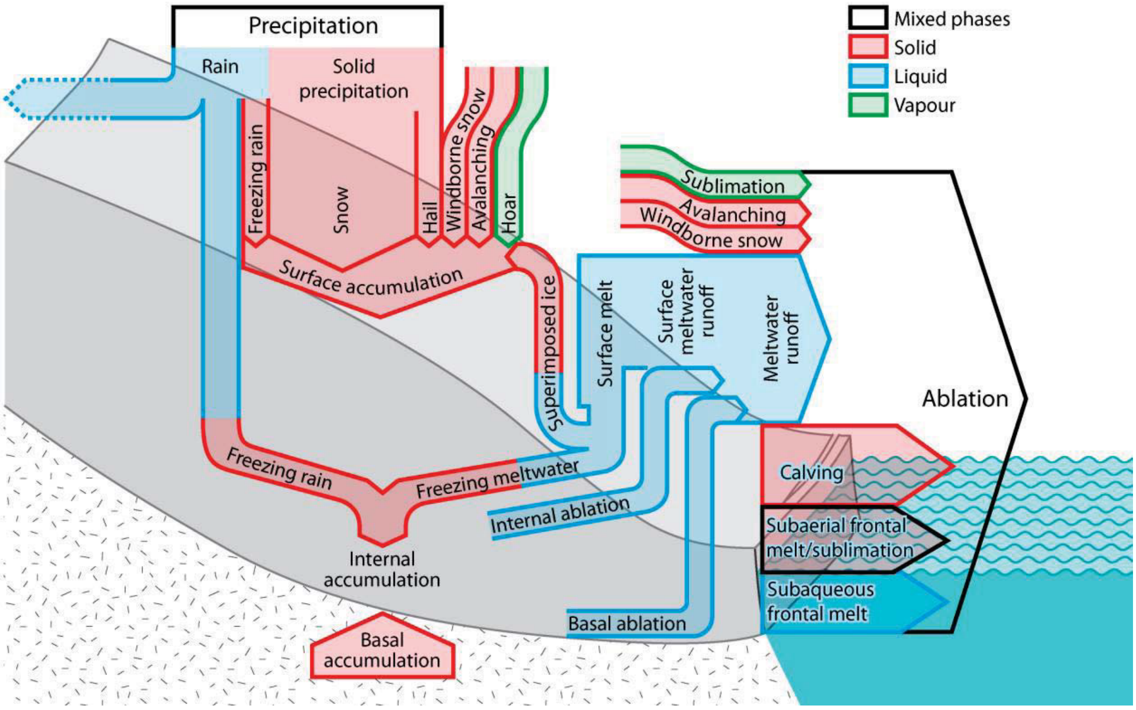

Figure 1.1: Components of the mass balance of a glacier. The arrows have arbitrary widths and do not indicate physical pathways of mass transfer. Taken from Cogley et al. (2011).

Marine-terminating Glaciers

Since this work focuses on ice-ocean interactions, the phenomenon of glaciers flowing into the ocean shall be introduced in more detail. As stated above, a glacier needs an area-wide positive surface mass balance for this to occur, causing it to grow until it meets the ocean. This encounter of water in all its three phases substantially alters a glacier's characteristics. Due to the lower density of ice compared to water, a glacier in contact with the ocean will experience an upward buoyancy force at its parts that are grounded below sea level. This force reduces friction between the ground and the glacier's base, causing that part of the glacier to flow faster as sliding overtakes deformation as the primary mode of movement (Meier and Post, 1987). Moreover, the ocean transfers heat into the glacier, causing submarine melt. The combination of mechanical processes and submarine melt induces the shedding of large chunks of ice at marine-terminating glaciers' fronts, a process commonly termed iceberg calving. Calving is related to submarine melt due to the undercutting the latter process causes. The undercut ice volume is destabilized as the net hydrostatic force at the front increases, which increases the likelihood of mechanical failure (Slater et al., 2021a). Consequently, marine-terminating glaciers are not solely subject to atmospheric climate but also to processes invoked by their contact with the ocean and the resulting mechanical processes at their termini. Nearly one-third of Earth's glacierized area (outside the ice sheets) is recorded as marine-terminating in the RGI. Understanding their dynamical response is hence important when assessing global-scale glacier mass evolution. The frontal mass budget of such glaciers shall be briefly introduced here. Generally, mass at the fronts of marine-terminating glaciers is removed by iceberg calving and submarine melt, while dynamical ice flux from upstream supplies the front with mass. This mass flux delivering ice to the terminus, denoted as (solid ice) discharge, is usually defined as the product of ice velocity, thickness, and width at the terminus/grounding line or a similar cross-section some distance upstream of it. The part of the glacier downstream of this cross-section hence defines the front. The frontal mass balance (FMB) at a point in time can thus be stated as:

$$FMB = D - M_{sm} - C \tag{1.1}$$

where D is discharge , M_{sm} submarine melt, and C iceberg calving (all in m^3 s^{-1}). In case the discharge is calculated for a cross-section upstream of the terminus, the surface mass balance of the glacier's part downstream of this cross-section should be taken into account as well. Hence, if the frontal mass budget is positive, the glacier is advancing while it is retreating, if the frontal mass balance is negative. A marine-terminating glacier with a glacier-wide net negative surface mass balance can only be in retreat, and it could even be in retreat with a glacier-wide net positive surface mass balance if the frontal mass budget is more negative. For it to be in equilibrium, frontal ablation (iceberg calving plus submarine melt) has to be balanced by discharge. This can only occur if the marine-terminating glacier has a sufficiently positive glacier-wide net surface mass balance. Note that surface mass balance acts vertically on the glacier, while ice velocity (discharge) and frontal ablation act horizontally.

1.3 Observations of glacier mass changes

Glaciers are mostly situated in remote locations that are difficult to reach, especially with scientific equipment. Hence, there are only 480 glaciers on which direct (in-situ/glaciological) annual surface mass balance observations were conducted, a tiny fraction of the number of glaciers worldwide. Moreover, these in-situ observations are spatially biased towards more accessible regions and temporally biased towards more recent years. In total, close to 7400 in-situ mass balance observations from 1900 to 2019 are recorded by the World Glacier Monitoring Service (Zemp et al., 2021). Recent advances in processing satellite data for glaciological purposes have brought about a global coverage of glacier mass changes. Though these satellite-derived data often lack accurate information about the mass balances' interannual variability, in contrast to repeated glaciological measurements, they constitute a major advance in the knowledge about global glacier changes and thus the ability to constrain large-scale numerical glacier evolution models (Hugonnet et al., 2021; Millan et al., 2022).

While mass change observations are crucial to understanding glaciers' temporal evolution, other variables also offer valuable insights into glaciers' state and behavior. The most prominent in this regard are area, thickness, and (surface) velocity since they are necessary to describe the dynamical state of a glacier. As stated above, numerical models of glaciers often anchor their area estimates to those recorded in the RGI, using the RGI area as the initial state or constraining the model to reproduce the area recorded for a particular year for the respective glacier (Marzeion et al., 2012; Huss and Hock, 2015). For knowing the total volume of a glacier, it is essential to know its thickness as well, but measuring glacier thickness is a laborious endeavor since it cannot be measured from space for individual glaciers as area or velocity. Therefore, there are only roughly 3000 glaciers outside the ice sheets for which direct thickness observations are available (Welty et al., 2020). This has led to indirect (inverse) approaches to estimating global glacier volume, sometimes using surface velocity measurements (Huss and Farinotti, 2012; Millan et al., 2022). Estimates of surface velocity can be derived from satellite data but cannot differentiate between the two main mechanisms of ice movement: mechanical deformation and sliding. Observations of glacier velocity and thickness are also crucial in estimating frontal processes of marine-terminating glaciers, as together they provide information about solid ice discharge, which, together with the volume change (and surface mass balance) in the frontal area, constitutes frontal ablation (see Eq. 1.1).

1.4 Numerical glacier evolution models

Several steps are involved in setting up a numerical model that can be used to model glacier evolution under certain topographic and climate conditions. Here, a brief overview of the main issues shall be given. For a more detailed review, the reader is referred to Zekollari et al. (2022).

1.4.1 Topographic and atmospheric data

Next to information about the location and outline of glaciers, it is also essential to know the topography of the glacier itself in order to model its evolution. This information about surface topography is routinely taken from digital elevation models (DEM), which might have different coverage and accuracy depending on the region one aims to examine (Maussion et al., 2019). As explained above, it is crucial to have information about the atmospheric conditions during the period that shall be modeled. For such data outside the temporal and spatial domain of measured weather station data, one usually relies on reanalysis (for the past) or climate models (for the future). A typical issue with this so-called atmospheric forcing data is that it usually is provided with coarser spatial resolution than an individual glacier's size, making it necessary to interpolate the data onto glacier locations. Additionally, these locations mostly lie within complex topography, complicating estimating atmospheric conditions. Particularly precipitation data from atmospheric models routinely used in large-scale glacier evolution modeling might be flawed in mountainous regions (Giesen and Oerlemans, 2012b), but temperatures must also be adjusted for the atmospheric lapse rate based on the glaciers' surface topography.

1.4.2 Mass balance models

The surface mass balance is the main driver of (land-terminating) glacier evolution. Several processes configure a glacier's mass balance: partitioning between liquid and solid precipitation, heat energy balance, refreezing of meltwater, and snow redistribution (see Fig. 1.1; Cuffey and Paterson, 2010, pp. 96 - 100). In order to prevent including too many processes in a model and thus too many parameters that can not be constrained by observations or making the model too computationally costly for modeling many glaciers simultaneously, models often rely on simplifying assumptions and parameterizations. While there are several approaches to the issue of modeling the surface mass balance of glaciers, here only the one that will be applied throughout this work shall be explained in more detail. It is a temperature index model, parameterizing ablation caused by snow and ice melt solely based on an empirical relationship between snow or ice melt and air temperature. Such a relationship is based on the assumption that most of the melt-inducing atmospheric heat energy is supplied to a glacier by surface energy balance components well correlated with (near-surface) air temperature (Ohmura, 2001). In the two glacier evolution models used throughout this work, the specific (surface area-average) surface mass balance (SMB) at a distance x from the glacier head along the glacier's main flow direction takes the following form:

$$SMB(x,t) = P_s(x,t) - f_m max(T_a(x,t) - T_{min}, 0) \tag{1.2}$$

where P_s is solid precipitation (in m s^{-1}), f_m an empirical melt factor (in m K^{-1} s^{-1}), T_a the near-surface air temperature at the glacier location (in °C), and T_{min} a threshold temperature above which ice and snow melt is assumed to occur (in °C). This parameterization implies that all the processes relevant for snow and ice melt are subsumed in the melt factor and the assumption that near-surface air temperature is the primary atmospheric variable driving these processes. Since most atmospheric data does not directly provide values of solid precipitation, its share in total precipitation reaching the glacier surface must also be parameterized. This is usually done by applying a threshold temperature above which all precipitation is assumed to be liquid. While such approaches have proven valuable for their simplicity yet good performance in terms of reproducing observations (Hock, 2003), they lack an explicit representation of the energy balance and more intricate processes such as refreezing. This hinders their ability to most accurately represent the surface mass balance of glaciers.

Modeling the frontal mass balance of marine-terminating glaciers is complicated by the fact that iceberg calving is a complex (stochastic) process evoked by the interplay of mechanical processes and submarine melt. Individual iceberg calving events are thus intricate to predict. However, when numerically modeling glacier evolution over a longer period, one might assert that it is sufficient to get the temporal average of the frontal mass balance close to observed values. What makes this problematic is that iceberg calving is related to the subglacial topography of the parts of a glacier that contain volume below the sea level. This is because the buoyancy forcing of the ocean water in conjunction with a non-uniform slope of the frontal subglacial topography (over-deepening) can prompt acceleration and self-sustenance of an initiated retreat. However, subglacial topography and bathymetry close to marine-terminating glaciers are often not well-constrained.

The mechanical process of iceberg detachment can be simulated by relating it to the stresses acting on the ice at the terminus area (Schlemm and Levermann, 2019), and submarine melt by relating it to the ocean's temperature and salinity (i.e., thermal forcing) in the proximity of the glacier front (De Andrés et al., 2018). Submarine melt is also influenced by subglacial discharge, as it changes the water circulation close to the glacier front and thereby the amount of ocean water entrained towards the glacier front. In this work, a simplified parameterization of frontal ablation will be applied, which merely scales total frontal ablation linearly to the water depth at the glacier front. However, Chapter 4 will expand this by an explicit parameterization of submarine melt.

1.4.3 Ice dynamics

A glacier's geometric adjustment to changes in the mass balance is regulated by ice dynamics, mainly because of two feedbacks between elevation and surface mass balance. The terminus-elevation feedback is negative because as the glacier retreats/advances to higher/lower elevations, the mean air temperature at the glacier's terminus decreases/increases. On the other hand, the surface-elevation feedback is positive, as a lower/higher glacier surface elevation increases/decreases the mean air temperature across the glacier's surface. Both feedbacks are related to the atmospheric temperature lapse rate, and their relative influence depends on the mass balance gradient, ice dynamics, and topography. Hence, to be able to take the geometric response of glaciers to changes in their mass balance (gradient) into account in a numerical model, it is necessary to find an appropriate description of ice dynamics. The most common approaches range from volume-area power-law scaling, over power-law scaling of ice velocity along the main flow direction with ice thickness and surface slope (shallow ice approximation; see next paragraph), to sophisticated applications of the Navier-Stokes equations. In this work, only the two former approaches will be employed since numerically solving the Navier-Stokes equations requires considerable computational resources, rendering this approach unfeasible for modeling many glaciers over several decades. However, machine-learning approaches can be used to emulate the Navier-Stokes equations' solution, drastically reducing the computational power needed (Jouvet et al., 2022). Volume-area scaling is a method founded on dimensional analysis (Buckingham-Pi theorem), from which a power law that scales a glacier's volume to its area can be derived:

$$V = cA^{\gamma} \tag{1.3}$$

where c is the empirical scaling factor (in $\mathrm{m}^{3-2\gamma}$), and γ the scaling exponent derived from the theory. A similar area-length scaling can also be derived (Bahr et al., 2015).

Such scalings allow for circumventing an explicit computation of ice dynamics. However, when using them to calculate a geometric change from a volume change (given from the (surface) mass balance), the delayed geometric response of a glacier to a perturbation in its mass balance has to be taken into account in the form of a temporal relaxation.

The other simplifying approach to simulating ice dynamics is the shallow ice approximation. It is based on the observation that ice behaves like a slow fluid. More precisely, ice behaves like a nonlinearly-viscous (non-Newtonian) fluid, which means that larger shear strain rates imply smaller viscosity (Greve and Blatter, 2009, pp. 52 - 56). Therefore, ice viscosity is not constant, and this complication led to deducing an empirical power law from laboratory experiments (Glen, 1955). This law allows to relate the viscosity to the applied (shear) stress, and thereby, the ice velocity can be related to the basal shear stress, as follows. Usually, the Navier-Stokes equations are employed to describe the viscous flow of fluids. Under the assumption that a typical glacier is shallow, meaning the length and width are much larger than the thickness, the combination of empirical flow law and Navier-Stokes equations can be substantially simplified to (Greve and Blatter, 2009, p. 72 - 85):

$$u(x,t) = \frac{2A}{n+2}(\rho g \alpha(x,t))^n \; h(x,t)^{n+1} + u_b(x,t) \tag{1.4}$$

where u is the average vertical ice velocity through a cross-section along the main flow direction x (in m s^{-1}), A the ice temperature-dependent scaling (or ice creep) parameter (in s^{-1} Pa^{-3}), n the scaling exponent, α the glacier's surface slope (dimensionless), ρ the ice density (in kg m^{-3}), g the gravitational acceleration (in m s^{-2}), $h(x)$ the glacier's thickness (in m), and u_b the basal velocity (in m s^{-1}; Cuffey and Paterson, 2010, pp. 309 - 310). Note that $\rho g \alpha h$ is the basal shear (or driving) stress. The basal velocity is the part of the ice flow that is not caused by stress-related deformation but by sliding. Getting hold of glacier sliding is intricate, mainly because it is difficult to observe it directly. The fraction of total velocity caused by sliding depends on basal pressure (related to subglacial hydrology) and the material the glaciers are moving over (Zoet and Iverson, 2020). Hence, modeling ice flow is complicated by finding an appropriate description of sliding velocity. Marine-terminating glaciers, in particular, move increasingly by sliding towards their termini as basal pressure decreases due to the uplift of ice by ocean water caused by the lower density of ice.

With the formulation of ice velocity and surface mass balance, the thickness change along the glacier can be computed as follows:

$$\frac{dh(x,t)}{dt} = SMB(x,t) - \frac{du(x,t)}{dx}h(x,t) \tag{1.5}$$

For application in a numerical model, Eq. 1.5 can be spatially and temporally discretized and solved along the glacier's main flow direction (centerline or flowline), neglecting mass balance and velocity variations in other spatial directions than x. How centerlines can be derived from glacier outlines and digital elevation models (DEM) is described in Kienholz et al. (2014).

Throughout this work, two different numerical glacier models will be employed. One allows for a comparably simple reconstruction of past glacier states, as it does not rely on explicitly computing ice dynamics but on the empirical geometric scaling laws introduced above (Marzeion et al., 2012). The other model applies the shallow ice approximations' explicit, yet simplified, description of ice dynamics (Maussion et al., 2019), which is conducive to more accurately modeling marine-terminating glaciers' dynamics, if adapted for large terminal cliffs. Since roughly one-quarter of the glacierized area outside the ice sheets is marine-terminating, accurately representing their dynamics is beneficial for the model's ability to capture large-scale glacier mass changes. For this aim, it is also necessary to represent Eq. 1.1 in the model. This issue will be treated in more detail in Chapter 3.

1.4.4 Ice thickness and initialization

Once one has decided how to numerically model the glacier mass balance and ice dynamics, the issue of initializing the glacier geometry remains. As indicated above, while there is an inventory of Earth's glaciers' location, outlines, and hypsometry, thickness observations are lacking for most glaciers. Even if there are thickness estimates for a glacier, the year they were recorded for might not coincide with the year the area was recorded for in the RGI. Thus, when one wants to initialize a glacier evolution simulation from the data recorded in the RGI, a decision on how to initialize the ice thickness has to be made. The two main approaches for this, next to volume-area scaling, are inverse methods: either i) the ice flux of the glacier that compensates its mass balance gradient in a (hypothetical) steady state is computed (Farinotti et al., 2009; Huss and Farinotti, 2012), or ii) surface velocity estimates, often derived from satellite data, are used (Millan et al., 2022). Both approaches then derive an ice thickness consistent with the ice flux/velocity and surface topography, mostly by utilizing the shallow ice approximation (Eq. 1.4). While the first approach has the shortcoming of implicitly assuming a glacier's steady state (glacier-wide net zero surface mass balance and no thickness change) with the atmospheric forcing and area one chooses for initialization, the second circumvents this problem directly using observed surface velocity. Still, both rely on estimating a value for A in Eq. 1.4 and a parameterization of sliding velocity.

When trying to reconstruct a glacier's state before the year its area was recorded for, one faces the problem that ice dynamics cannot be calculated backward (*arrow of time* problem). In that case, iterative methods can be used to identify potential glacier states in the year the model is initialized for. The basic idea is to iteratively run the model forward from different glacier states one deems viable as a starting point and select the initial state that results in the closest reproduction of the observed state (Marzeion et al., 2012; Eis et al., 2019, 2021).

1.4.5 Calibration

As the sections above indicate, numerically modeling large-scale glacier evolution involves several parameters and approximations for simulating mass changes and the resulting geometric adjustment to such changes. Since parameters are used to adjust the approximations to reflect the reality best, data on the process to be approximated is needed. Observational data is generally desirable since it should represent the physical reality most accurately. Nevertheless, when observational data is lacking, data from higher-resolution numerical models or numerical models closer to first principles might be used, as such models are generally considered better representations of the natural world.

Different calibration strategies can be deployed depending on the temporal and spatial resolution of the data used for calibration. Exemplary, the calibration of the melt factor (f_m) in Eq. 1.2 shall be briefly schematized here. First, atmospheric data of (solid) precipitation and near-surface atmospheric temperature is needed, for which observational records are lacking on most glaciers. As a consequence, one often resorts to the use of meteorological reanalysis data, which often underestimates the amount of precipitation the glaciers receive, though, leading to the introduction of another parameter to account for this. Even if one had perfect knowledge of the meteorological conditions over a period, knowledge about the (surface) mass balance over the same period is also needed to derive f_m from Eq. 1.2. Before the advent of coherent individual-glacier scale data products from satellite observations, it was necessary to deal with significant spatial data gaps, for instance, by interpolation approaches (Marzeion et al., 2012) or using regional averages (Huss and Hock, 2015). While the spatial coverage of mass balance observations has dramatically improved with satellite data processing for glaciological purposes, the temporal resolution of observational mass balance remains an issue. While in-situ measurements can provide reasonably accurate annual measurements, obtaining such measurements is laborious, and their (spatial) coverage can thus never match that of satellite data. On the other hand, the problem with satellite data is that their accuracy can be relatively low on an annual timescale. Hence, using at least pentadal averages is preferable (Hugonnet et al., 2021).

This then evokes the issue of reproducing temporal variability of a process since this might reflect how well a model is able to reproduce the response to changes in, e.g., atmospheric conditions. This issue also points to the larger question of calibration: How does one ensure that a numerical model reproduces observations as accurately as possible and gives accurate results outside the temporal and spatial domain of the calibration data? Addressing this becomes more complicated with the number of parameters since involving more parameters requires observational data of the parameterized processes, and processes might be interrelated. Therefore, calibration is a complex issue of its own and hence not discussed in more detail at this point, although it will come up throughout this work in the three main Chapters 2 - 4.

1.5 Large-scale ocean circulation

To make the contents of Chapter 4 clearer, a basic description of the (northern hemisphere) ocean's circulation and its main features in the northern hemisphere Atlantic will follow. On the large scale, one can think of ocean circulation as having two main components (neglecting tides): a circulation consisting of quasi-horizontal near-surface currents and gyres, and a deeper, meridional overturning circulation. First, the quasi-horizontal component is introduced, which is caused by the near-surface winds' mechanical force exerting stress on the ocean surface. Due to the Coriolis force acting on the water that is moved by the wind stress, the movement is deflected to the right (in the northern hemisphere) of the initial wind forcing's direction (*Ekman transport*). Thus, water is piling up (converging) in the transition zone between primarily easterly winds in the subtropics and westerly winds in the mid-latitudes. This creates a hydrostatic pressure gradient force that moves the water along the gradient while also under the influence of the Coriolis force. If the pressure gradient and Coriolis forces are in balance, the flow is called *geostrophic*. The result is the subtropical gyre's clockwise (or anticyclonic) rotation. Further north, the subpolar gyre is situated between the primarily westerly winds in the mid-latitudes and easterly winds in the Arctic. The wind stress field in this region causes the water to diverge, thus creating an anticlockwise (cyclonic) rotation. (Vallis, 2012, pps. 45 - 62, 77 - 82).

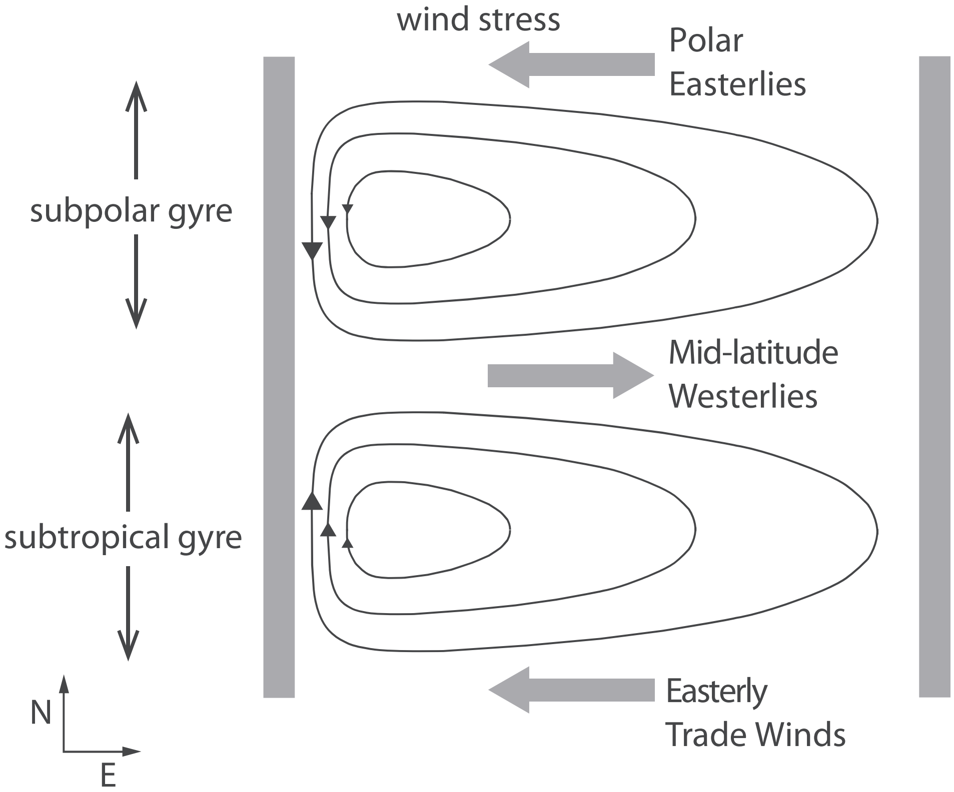

Figure 1.2: An idealized gyre circulation in a rectangular ocean basin in the northern hemisphere, showing the subtropical gyre (lower, typically extending from about 15 °N to 45 °N), the subpolar gyre (upper), and the intense western boundary currents on the left. Taken from Vallis (2012), p. 78.

However, these two main gyres of the Atlantic ocean are not symmetric, as there is a much stronger flow at their western boundaries (see Fig. 1.2). This western intensification phenomenon can be explained by considering conservation of mass and angular momentum (i.e., *vorticity*). There are two types of vorticity: *planetary* vorticity induced by Earth's rotation, and *relative* vorticity induced by movement relative to Earth's rotation, for instance, due to the wind or pressure gradient force. The total or potential (relative plus planetary) vorticity is usually treated as a conservative quantity. Planetary vorticity increases towards the poles alongside the Coriolis force, while relative vorticity (in the northern hemisphere) is negative in clockwise and positive in anticlockwise rotation. In the interior large-scale ocean circulation, velocity gradients are typically small. Thus relative vorticity can mostly be assumed to be negligibly small compared to planetary velocity in the interior regions (Cushman-Roisin and Beckers, 2011, p. 662), but it becomes important in explaining the western boundary currents.

As indicated above, the gyres are caused by water's convergence (subtropical) and divergence (subpolar). In the case of the subtropical gyre, convergence not only causes the water to be forced out of the higher sea surface area by the pressure gradient but also a downward vertical velocity. Similarly, an upward vertical velocity is induced in a divergence zone (e.g., subpolar gyre). This can be derived by inserting the Ekman transport into the mass conserving transport (or continuity) equation and is called *Ekman pumping* (Cushman-Roisin and Beckers, 2011, pp. 251 - 254). As the wind forcing's effect decreases with depth, so does the absolute vertical velocity in the near-surface layer. Thus, when there is a downward/upward pumping, the water is squeezed/stretched, and this decreases/increases its vorticity. The two gyres discussed here occur in the large-scale interior ocean; hence, as stated above, potential vorticity can be neglected, and planetary vorticity decreases/increases. In order to conserve its potential vorticity, the water must move equator-/poleward (*Sverdrup transport*), and due to the conservation of mass, this meridional flow has to be balanced. In the case of the subtropical gyre, which causes a south-/equatorward Sverdrup transport, the flow needs to be balanced by a north-/poleward flow. The conservation of potential vorticity requires that this flow can only occur at the western boundary, as the increasing planetary vorticity of the north-/poleward flow balancing the Sverdrup transport must be balanced by decreasing relative vorticity. A current at the western boundary accomplishes this. Moreover, based on the scale considerations of vorticity mentioned above, there has to be a steep velocity gradient towards the western boundary to meaningfully increase the relative vorticity. The resulting fast and narrow current is the Gulf Stream (Cushman-Roisin and Beckers, 2011, pp. 660 - 673). Following the same arguments, one finds that the subpolar gyre also has a western boundary current, which is called Labrador Current.

The density-driven meridional overturning circulation is the second main component of ocean circulation. Generally, denser water can be found at higher latitudes since the ocean loses more heat to the atmosphere at higher latitudes and gains more solar heat at lower latitudes. The resulting density gradient between the equator and the (north) pole makes it possible for the colder, denser water in the north to sink convectively in plumes and move southward (Stommel, 1958; Vallis, 2012, pp. 76 - 77, pp. 89 - 96). For this deep convection to occur, water at the surface has to be exposed to a cold and dry atmosphere, which causes thermal contraction and evaporation. This makes the surface water denser than typical seawater, causing it to sink in the water column. By again considering mass conservation, it becomes clear that the sinking water has to be replaced; thereby, the meridional overturning circulation is induced (Cushman-Roisin and Beckers, 2011, p. 677 - 681). The Gulf Stream and its extension (North Atlantic Current) also play a role in this. They move warmer and more saline water than higher latitude ocean water northward and can thus influence the density in regions where deep convection typically occurs (Manabe and Stouffer, 1988). Similarly, the Labrador Current brings comparably cold and fresh water southward. The two prominent locations in the northern hemisphere, where the density near the surface becomes sufficiently high for deep convection, are the Labrador Sea and the Greenland-Norwegian Sea (Cushman-Roisin and Beckers (2011, p. 658); Vallis (2012, p.39)).

The ocean's circulation is much more complex than what can be laid out in this work. However, the paragraphs above indicate how increasing freshwater input due to glacier mass loss can influence it: by i) increasing the sea surface height gradient where it enters the ocean, thereby altering (near-surface) geostrophic flow patterns, and by ii) decreasing the surface layer density, which can affect near-surface vertical mixing processes (Cushman-Roisin and Beckers, 2011, p. 425 - 429) and potentially even the large-scale density-driven meridional overturning circulation.

1.6 Numerical ocean circulation models

Since the third main chapter of this work will deal with an approach to coupling a glacier model to an ocean model, the basic idea of a numerical ocean model shall be introduced here. Ocean general circulation models describe the dynamical and thermodynamical processes in the ocean (Le Sommer et al., 2018). The model used in this work is the Nucleus for European Modelling of the Ocean (NEMO, version 3.6). Its core engine solves the primitive equations of the ocean (thermo-)dynamics on a three-dimensional Arakawa C-type grid. Primitive equations comprise the Navier-Stokes equations and a nonlinear equation of state that couples the temperature and salinity fields to the fluid velocity (Madec et al., 2016). The equation of state describes density variations in the ocean caused by temperature, salinity, and pressure variations, but density variations are not retained in the continuity equation. Thereby conservation of mass technically becomes conservation of volume (*Boussinesq approximation*; Cushman-Roisin and Beckers, 2011, p. 425 - 429). Furthermore, the ocean is assumed to be in hydrostatic equilibrium and incompressible. In reality, static instabilities (i.e., water masses with higher over such with lower potential densities) can occur, and convective processes act to restore the water columns' static stability (e.g., deep convection). Since these processes cannot occur in the model due to the hydrostatic equilibrium assumption, they must be parameterized. NEMO can be coupled to sea-ice and biogeochemistry models, while it is usually not coupled to an atmospheric model. Atmospheric forcing is thus usually provided to NEMO by external atmospheric data. The interaction of marine-terminating glaciers and the ocean is investigated in this work by one-way coupling a glacier model that explicitly includes ice dynamics to NEMO. This is done by incorporating a submarine melt parameterization in the glacier model, applying the ocean models' output, and using modeled glacier mass loss estimates as an additional freshwater forcing of the ocean model.

1.7 Thesis objectives

In order to examine large-scale glacier mass changes and their impact on global mean sea level as well as ocean circulation, it is essential to improve our knowledge about glacier mass changes outside the observational domain. Since only the application of numerical models can achieve this, understanding the limitations and potential improvements of the models is mandatory. The ways in which this issue will be tackled in this work are by i) quantifying the uncertainty introduced to numerical glacier models by atmospheric forcing data, ii) investigating how the introduction of new physical processes to a numerical glacier model influences the results, and iii) coupling a numerical glacier model to a numerical ocean circulation model. More precisely, this work aims to accomplish the following objectives:

1. Quantify the uncertainty in numerical global glacier mass change reconstructions for the 20th century.
2. Incorporate more accurate descriptions of marine-terminating glaciers in a numerical glacier evolution model and characterize the resulting changes in future glacier mass change projections.
3. Generate a first estimate of northern hemisphere ice-ocean interactions outside the Greenland Ice Sheet by coupling a glacier evolution to an ocean circulation model.
    (a) Produce a first estimate of marine-terminating glaciers' submarine melt outside the ice sheets.
    (b) Explore the impact of increased freshwater input due to glacier melt on an ocean circulation model.

Generally, this thesis aims to identify shortcomings of the applied numerical global-scale glacier models to delineate potential future improvements. It also aims to highlight uncertainties in the model results generated by a lack of knowledge about adequate values for parameters involved in the glacier evolution models.

Chapter 2

Context

Glaciers have contributed substantially to past global mean sea level rise, and estimating this contribution is relevant for closing the sea level (rise) budget compared to observations (Frederikse et al., 2020). When trying to quantify glaciers' past mass changes, numerical models have to be used, for the number of observations decreases strongly going back in time. Since initializing more complex models that could simulate actual ice dynamics for a period earlier than the year a glacier was recorded for in the RGI, is intricate and computationally expensive, using simpler models with volume-area scaling approaches is adequate. However, even for simpler models quantifying the uncertainty is not straightforward since the common assumption of uncorrelated and thus partially canceling model errors for individual glaciers leads to relatively small model error estimates on the global scale. Another primary source of uncertainty are the data used for computing the surface mass balance, as it is the main variable driving glacier mass change. Particularly in the context of reconstructions, the uncertainty in atmospheric data becomes relevant, since meteorological data, especially at glacier locations, also becomes sparse when going back in time. Hence, to better estimate uncertainties in reconstructions, it is advisable to quantify the uncertainty of modeled past glacier mass changes caused by differences in atmospheric forcing data sets. One approach for this is to exercise the same calibration method using different atmospheric data sets available for the past, then run the reconstruction model and investigate the differences in the results. In this chapter, such an ensemble approach is applied.

Twentieth century global glacier mass change: an ensemble-based model reconstruction

Jan-Hendrik Malles[1,2] and Ben Marzeion[1,2]

[1]Climate Lab, Institute of Geography, University of Bremen, Bremen, Germany
[2]MARUM – Center for Marine Environmental Sciences, University of Bremen, Bremen, Germany

Abstract

Negative glacier mass balances in most of Earth's glacierized regions contribute roughly one-quarter to currently observed rates of sea-level rise and have likely contributed an even larger fraction during the 20th century. The distant past and future of glaciers' mass balances, and hence their contribution to sea-level rise, can only be estimated using numerical models. Since, independent of complexity, models always rely on some form of parameterizations and a choice of boundary conditions, a need for optimization arises. In this work, a model for computing monthly mass balances of glaciers on the global scale was forced with nine different data sets of near-surface air temperature and precipitation anomalies, as well as with their mean and median, leading to a total of 11 different forcing data sets. The goal is to better constrain the glaciers' 20th century sea-level budget contribution and its uncertainty. Therefore, five global parameters of the model's mass balance equations were varied systematically, within physically plausible ranges, for each forcing data set. We then identified optimal parameter combinations by cross-validating the model results against in situ annual specific mass balance observations, using three criteria: model bias, temporal correlation, and the ratio between the observed and modeled temporal standard deviation of specific mass balances. These criteria were chosen in order not to trade lower error estimates by means of the root mean squared error (RMSE) for an unrealistic interannual variability. We find that the disagreement between the different optimized model setups (i.e., ensemble members) is often larger than the uncertainties obtained via the leave-one-glacier-out cross-validation, particularly in times and places where few or no validation data are available, such as the first half of the 20th century. We show that the reason for this is that in regions where mass balance observations are abundant, the meteorological data are also better constrained, such that the cross-validation procedure only partly captures the uncertainty of the glacier model. For this reason, ensemble spread is introduced as an additional estimate of reconstruction uncertainty, increasing the total uncertainty compared to the model uncertainty merely obtained by the cross-validation. Our ensemble mean estimate indicates a sea-level contribution by global glaciers (outside of the ice sheets; including the Greenland periphery but excluding the Antarctic periphery) for 1901–2018 of $69.2 \pm 24.3\,\mathrm{mm}$ sea-level equivalent (SLE), or $0.59 \pm 0.21\,\mathrm{mm\,SLE\,yr^{-1}}$. While our estimates lie within the uncertainty range of most of the previously published global estimates, they agree less with those derived from GRACE data, which only cover the years 2002–2018.

2.1 Introduction

Glacier mass loss across most of the world constitutes a major part of the contemporary and projected 21st century sea-level rise (e.g., Slangen et al., 2017; Oppenheimer et al., 2019). Moreover, glaciers are important freshwater reservoirs for some regions of the world, and the vanishing of glaciers is thus likely to induce seasonal water scarcity in regions depending on those reservoirs (Cruz et al., 2007; Huss and Hock, 2018; Wijngaard et al., 2018; Kaser et al., 2010; Small and Nicholls, 2003).

Changes in a glacier's mass are often referred to in terms of *surface mass balance*: the difference between snow/ice accumulation and snow/ice loss (ablation) – mostly due to melting – over the glacier's surface. Dividing this value by the glacier's surface area yields the *specific mass balance*, which is an important variable in attempts to quantify glacier mass changes. Specific mass balances are a function of meteorological conditions at glacier locations and glacier-specific characteristics. The future evolution of the global glacier mass is usually estimated using numerical models (Hock et al., 2019b; Marzeion et al., 2020). This is the case for the last century or even more distant past as well (e.g., Goosse et al., 2018; Parkes and Goosse, 2020), since satellites able to observe the Earth's surface only became available well into the second half of the 20th century. Glaciers also lack comprehensive in situ mass balance measurements, at least before 1950, since they are mostly situated in remote locations (see Figs. 2.6 and 2.7 in WGMS, 2020). It is therefore important to assess and improve glacier mass balance models used to reconstruct or project glacier mass evolution. An ensemble-based, long-term reconstruction can add to our understanding of the uncertainties in glacier modeling, which might in turn enhance our ability to make more robust projections of glacier mass change (Hock et al., 2019b; Marzeion et al., 2020). Marzeion et al. (2020) have shown that ca. 25 % of global mass change uncertainty in 21st century projections of a glacier model ensemble can be attributed to differences in the output of climate models. About 50 % of the uncertainty in 2020, declining to ca. 25 % in 2100, was attributed to differences between individual glacier models. In this work we show that differences in meteorological reanalysis data add considerably to the uncertainty of an individual glacier model's reconstruction as well. The modeling approaches to establishing global estimates for the glaciers' mass balances mostly make use of temperature-index melt models to represent the energy available for melting solid precipitation (i.e., snow) and ice (e.g., Huss and Hock, 2015; Radić and Hock, 2011; Hirabayashi et al., 2013). As a glacier's mass balance is interrelated with the glacier's geometric and hypsometric properties, some kind of length-area-volume scaling relation is often incorporated to account for changes in these properties in the models (Bahr et al., 2015) in order to avoid the computational cost of modeling physical processes involved in glacier dynamics. This is especially relevant for an approach like ours, for which we need to run the model many times. The model used in the work presented here additionally includes a response time scale to account for the glacier geometries' response lagging climatic forcing but lacks an explicit representation of ice dynamic processes such as deformation, sliding, or calving/frontal ablation (Marzeion et al., 2012).

Although there are approaches based on solving the energy balance at the ice surface, these models usually either lack ice dynamics or geometric scaling (Shannon et al., 2019), can only be applied to a small number of glaciers and depend on upscaling to obtain global numbers (Giesen and Oerlemans, 2013), or do not perform significantly better than a similar model without energy balance implementation (Huss and Hock, 2015). Another difficulty for models resolving the energy balance is the introduction of additional parameters that have to be constrained, which in turn adds complexity to the model optimization. This indicates that implementing ice dynamics and the energy balance simultaneously is a difficult task and therefore not yet done routinely but might still have the potential to enhance the accuracy of glacier modeling. That is because such models would have the ability to represent the physical mechanisms influencing a glacier in a more detailed, and thus possibly more realistic, fashion.

As mentioned above, for computational limitations, models solving the full equations of motion and thermodynamics individually for each glacier are generally not applied at the global scale. However, the Open Global Glacier Model (OGGM, Maussion et al., 2019) has been applied to compute ice velocity and thickness for each glacier based on a flow line approach but is not yet able to routinely reconstruct glacier changes for such long time periods as in this work. The initialization of OGGM for times prior to recorded glacier areas was also just recently explored (Eis et al., 2019, 2021).

None of the models resolving the energy balance or explicitly calculating ice dynamics have been applied to globally reconstruct the glacier mass change on a century timescale. This implies that a comprehensive analysis determining which modeling approach might be most appropriate is not yet possible; at least not for all global glaciers and the whole 20th century. The need for a robust model evaluation, which can also be used to better understand the glacier model contribution to projection uncertainty (Marzeion et al., 2020), is apparent.

Uncertainties of numerical models are mainly caused by (i) uncertain boundary and initial conditions, (ii) approximations of the model's equations, and (iii) lack of knowledge about parameters involved in the model setup (Hourdin et al., 2017). Therefore, optimization of parameters and/or input data is a standard procedure in glacier modeling (Huss and Hock, 2015; Radić and Hock, 2011; Marzeion et al., 2012). Often, a single metric is chosen to be minimized (e.g., the model's RMSE with respect to observed in situ mass balances). Rye et al. (2012) suggested multi-objective optimization for a (regional) glacier model, striving for Pareto optimality (Marler and Arora, 2004), to constrain parameters more robustly.

Models of (parts of) the Earth system are typically evaluated using observations and/or proxy data, usually with the objective to minimize the model's deviation from observations, e.g., by minimizing the RMSE (Gleckler et al., 2008; Taylor, 2001). Although in the case of glaciers direct in situ specific mass balance measurements are sparse and very heterogeneously distributed in space and time, they are essential in assessing the uncertainty, i.e., validation, of mass balance models. Nevertheless, other evaluation methods exist; for example using a combination of satellite gravimetry, altimetry, and glaciological measurement data (Huss and Hock, 2015). Such combined calibration data usually are not available for individual glaciers and/or do not have the temporal resolution required to assess the model's ability to capture interannual variability, making them impractical for our calibration and validation approach.

To avoid a confusion of the terms optimization, calibration, and validation, we briefly state our notions of these. Validation means calculating metrics that relate model outputs to observed values in a certain variable and that quantify the estimated model uncertainty. Optimization refers to choosing the best global parameter set with respect to the aims one sets regarding the validation. With calibration, we mean the deduction of glacier-specific model parameters from observational data.

In this work, we apply a multi-objective optimization, concerning the five global parameters most relevant in the applied model, for each of nine meteorological forcing data sets (see Table 2.1), their mean, and their median. The term global parameter here refers to parameters that are used in the model formulation (see Sect. 2.2.2) and not varied for each glacier but applied globally. Since the model is able to hindcast glacier evolution, the aim of this work is to (i) optimize the global model parameters in order to obtain model setups that reproduce in situ mass balance observations as closely as possible and (ii) to more robustly estimate model uncertainty, taking into account ensemble spread at times and in regions where observations are sparse. We use the model of Marzeion et al. (2012) but introduce changes to the mass balance calibration routine (see Sect. 2.2.2). Additionally, we incorporate newer boundary and initial conditions as well as reference data, against which the model is validated. We show that the ensemble approach to the reconstruction produces more robust estimates of model uncertainty than taking into account results from a leave-one-glacier-out cross-validation (see Sect. 2.2.2 and green box in Fig. 2.1) alone.

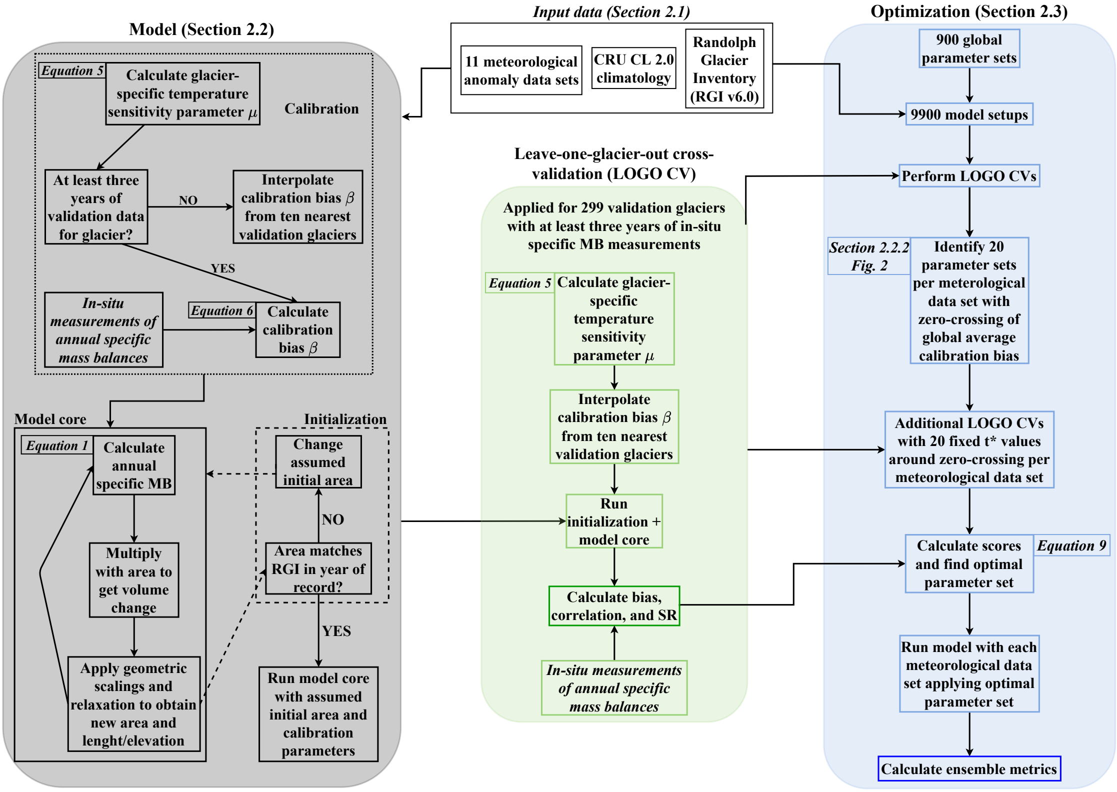

Figure 2.1: Flowchart depicting the modeling and optimization chain.

2.2 Data and methods

In this section we introduce the data and the modeling as well as the optimization chain we applied in this work. In order to make the whole section more accessible to the reader, we point to the flowchart (Fig. 2.1), which illustrates how the individual steps described in the text are connected.

2.2.1 Data

Meteorological data

We conducted the search for an optimal parameter set for the version 4.03 of the CRU TS data (corresponding to an update of Marzeion et al., 2012) and additionally eight reanalysis data sets, as well as the mean and the median of all the data sets (see Table 2.1). The 5 of the 11 data sets not extending back to 1901 (see Table 2.1) were filled with CRU TS 4.03 data, exclusively for the purpose of initialization of glacier areas; the results are only shown (and evaluated) during time periods for which we have forcing data from the respective data set.

Anomalies of temperature and precipitation were calculated with respect to the 1961 to 1990 reference period used in CRU CL 2.0. For those data sets not covering the period 1961 to 1991, these anomalies were obtained by calculating the difference between the 1961 to 1990 and the 1981–2010 periods in the CRU TS 4.03 data set and subsequently subtracting this value from the respective data set's 1981–2010 mean.

Table 2.1: Resolution and time range of the meteorological data sets used as boundary conditions.

Label used in text and figures	Resolution (°)	Time range	Publication
20CRV3	2×2	1871–2014	Slivinski et al. (2019)
CFSR	0.5×0.5	1979–2010	Saha et al. (2010)
CRU CL 2.0	$10' \times 10'$	1961–1991 (climatology)	New et al. (1999)
CRU TS 4.03	0.5×0.5	1901–2018	Harris and Jones (2020), Harris et al. (2014)
CERA20C	0.28×0.28	1900–2010	Laloyaux et al. (2018)
ERA5	0.5×0.5	1979–2018	Hersbach et al. (2020)
ERA20C	1.13×1.13	1900–2010	Poli et al. (2016)
ERA-Interim	$\sim 0.7 \times 0.7$	1979–2018	Dee et al. (2011)
JRA55	1.25×1.25	1958–2018	Kobayashi et al. (2015)
MERRA2	0.63×0.63	1980–2018	Gelaro et al. (2017)

Glacier data

The glacier model requires information about location, area, terminus, and maximum elevation of each glacier at some point in time within the modeled time interval (1901–2018), which were taken from the most recent version of the Randolph Glacier Inventory (RGI v6.0, RGI, 2017). The RGI relies mostly on Landsat and other satellite imagery. Distinction of individual glaciers within glacier complexes was realized mostly by semi-automatic algorithms for detecting watershed divides. It includes Greenland's peripheral glacier with a high connectivity level "CL2 (strongly connected)" (RGI, 2017), which we exclude from the model results we present. Note that we neglect missing or disappeared glaciers that are not recorded in the RGI. This might lead to an underestimation of global mass changes, especially in the early 20th century (Parkes and Marzeion, 2018). The majority of recorded glacier areas date back to the years between 2000 and 2010, while there are a few early records between 1970 and 1980. The exact distribution is given in Fig. 2 of RGI (2017).

To be able to cross-validate the modeled annual specific mass balances, we use in situ (glaciological) observations of glacier-wide annual specific glacier mass balances collected by the World Glacier Monitoring Service (WGMS, 2018). For the sake of simplicity and because observational errors of in situ specific mass balance measurements are not always known, we ignore any uncertainties of these observations (Cogley, 2009) and treat them as the "true" annual specific mass balance of a glacier in the recorded year. As stated in the introduction, our validation approach is based on a decomposition of the RMSE into the three statistical measures: temporal correlation, interannual variability ratio, and bias. Due to the lack of a comprehensive data set for geodetic measurements comparable to that of the WGMS for in situ measurements, i.e., with the temporal and spatial resolution necessary for the calculation of the first two aforementioned metrics, it is unfortunately not yet possible to use those in the validation framework we established. Since the calculation of correlations and interannual variabilities requires a time series of data, we only take into account glaciers for which at least 3 years of in situ mass balance were recorded. Those are 299 glaciers with a total of 5977 annual specific mass balance measurements. Before 1950, only 110 annual records of 14 glaciers are contained in this data set. Of those 14 glaciers, 12 are situated in Central Europe and Scandinavia and one in Alaska and Iceland each (WGMS, 2020).

2.2.2 The global glacier mass balance model

Basic equations and parameters

In this section, those features of the mass balance model that are relevant to the optimization procedure are described (see grey box in Fig. 2.1). A more thorough description is given in Marzeion et al. (2012). The annual specific mass balance $B(t)$ of each glacier is computed as

$$B(t) = \left[\sum_{i=1}^{12} \left[P_i^{solid}(t) - \mu^* \cdot max\left(T_i^{terminus}(t) - T_{melt}, 0\right)\right]\right] - \beta^* \tag{2.1}$$

where B is the annual modeled mass balance for an individual glacier in year t, P_i^{solid} is the amount of solid precipitation in month i, μ^* is a glacier-specific temperature sensitivity parameter, T_i^{terminus} is the mean temperature in month i at the glacier's terminus elevation, T_{melt} is a global threshold temperature for snow and ice melt at the glacier surface, and β^* is a calibration bias correction parameter. Terminus elevation temperature is calculated as

$$T_i^{terminus}(t) = T_i^{CRUclim} + \gamma_{temp} \cdot (z_{terminus}(t) - z_{CRUclim}) + T_i^{anom}(t) \tag{2.2}$$

where T_i^{CRUclim} is the climatological temperature in month i taken from the grid point of the CRU CL 2.0 data set (New et al., 2002) closest to the respective glacier, γ_{temp} is an empirically derived temperature lapse rate, z_{terminus} is the elevation of the glacier's terminus, z_{CRUclim} is the elevation of the grid point in the CRU CL 2.0 data set, and $T_i^{\text{anom}}(t)$ is the monthly temperature anomaly deduced from the forcing data set. Values for μ^* and β^* can theoretically be obtained by assuming an equilibrium state of the glacier in present-day geometry during a 31-year period centered around year t^* when annual specific mass balance measurements are available for that glacier. In contrast to the initial publication of the model, we objectify the selection of t^*: while Marzeion et al. (2012) argue that t^* is a function of the regional climatological history, it also depends on the glacier's response time scale, as discussed in Roe et al. (2021), for which there is no reason to assume spatial coherence. This means that we now do not spatially interpolate t^* as in Marzeion et al. (2012) but introduce it as an additional global parameter. In the next section we elaborate further on this point.

The inference of the glacier-specific parameters (μ^* and β^*; see Sect. 2.2.2) is assessed in a leave-one-glacier-out cross-validation procedure to determine the out-of-sample uncertainty, which should theoretically be done every time the model setup (i.e., parameter set and/or forcing data) is changed. Leave-one-glacier-out cross-validation means we run the model once for each validation glacier, which are those with at least three recorded annual specific mass balances, treating the respective glacier as if we did not have in situ mass balance measurements available (see green box in Fig. 2.1). In other words, $\beta(t^*)$ is spatially interpolated in an inverse-distance-weighted manner from the 10 closest glaciers for the computation of annual specific mass balances of that glacier. The modeled annual specific mass balances of the individual validation glaciers obtained like this are then compared against the in situ measurements in the optimization procedure (see Sect. 2.2.3 and blue box in Fig. 2.1). Hence, we obtain an estimate of the model's uncertainty attached to the calibration procedure (see Sect. 2.2.2). While values for μ^* can be computed for each individual glacier based on t^*, those for β^* are spatially interpolated from the 10 closest validation glaciers, using inverse-distance weighting. This will certainly work better in regions with high measurement densities and thus be a major part of our estimates' inaccuracy due to the previously mentioned heterogeneous distribution of in situ mass balance measurements. Also, it is sensitive to errors or biases in the in situ observations we use.

One global parameter (T_{melt}) was introduced in Eq. (2.1), but three additional ones are associated with the calculation of the monthly solid precipitation $P_i^{\mathrm{solid}}(t)$:

$$P_i^{solid}(t) = (a \cdot P_i^{CRUclim} + P_i^{anom}(t)) \cdot (1 + \gamma_{precip} \cdot (z_{mean} - z_{CRUclim})) \cdot f_i^{solid}(t) \quad (2.3)$$

where a is a precipitation correction factor, P_i^{CRUclim} is the monthly climatological precipitation sum taken from the grid point of the CRU CL 2.0 data set closest to the respective glacier in month i, $P_i^{\mathrm{anom}}(t)$ is the monthly total precipitation anomaly deduced from the forcing data set, γ_{precip} is a global precipitation lapse rate, z_{mean} is the mean elevation of the glacier, and $f_i^{\mathrm{solid}}(t)$ is the fraction of solid precipitation:

$$f_i^{\mathrm{solid}}(t) = \left\{ \begin{array}{l} 1 \ \text{ if } \ T_i^{\mathrm{terminus}}(t) \leq T_{\mathrm{prec\ solid}} \\ 0 \ \text{ if } \ T_i^{z_{\mathrm{max}}} \geq T_{\mathrm{prec\ solid}}, \\ \quad \text{with } T_i^{z_{\mathrm{max}}}(t) = T_i^{\mathrm{terminus}}(t) \\ \quad + \gamma_{\mathrm{temp}} \cdot (z_{\mathrm{max}} - z_{\mathrm{terminus}}(t))\,, \\ 1 + \frac{T_{\mathrm{prec\ solid}} - T_i^{\mathrm{terminus}}(t)}{\gamma_{\mathrm{temp}} \cdot (z_{\mathrm{max}} - z_{\mathrm{terminus}}(t))} \ \text{ otherwise} \end{array} \right\}, \quad (2.4)$$

where $T_{\mathrm{prec\ solid}}$ is a global threshold temperature for solid precipitation, and z_{max} is the maximum glacier elevation. The amount of solid precipitation a glacier receives is hence estimated by applying an empirical negative temperature lapse rate and a parameterized positive precipitation lapse rate. The assumption of increasing precipitation with elevation might not hold for some glaciers that are located on the downwind side of a mountain or for ones with very high maximum elevations, but this should be accounted for by treating it as a global parameter subject to optimization.

The four global parameters (T_{melt}, a, γ_{precip}, and $T_{\mathrm{prec\ solid}}$) introduced in Eqs. (2.1)–(2.4) are at the core of the model's mass balance computations and hence subject to the optimization presented here. Marzeion et al. (2012) used the CRU TS 3.0 data set to obtain $T_i^{\mathrm{anom}}(t)$ and $P_i^{\mathrm{anom}}(t)$. Here, we include additional meteorological data sets as well as their mean and median values in the optimization (see Sect. 2.2.1).

The monthly mass balances are subsequently translated into volume, area, and length changes by geometric scaling and relaxation (see grey box in Fig. 2.1). The geometric scalings by means of a power law, reviewed in Bahr et al. (2015), are currently the only option for estimating geometric changes from mass changes without having to resolve actual physical processes as in a flow line or higher-order model. From the theory discussed in Bahr et al. (2015) it follows that the exponent in these power law scalings is a constant and the scale factor is a random variable. In the model, we applied the constant exponents for mountain/valley glaciers and ice caps given from that theory and scale factors empirically derived in Bahr (1997) and Bahr et al. (1997). Since there are uncertainties attached to the scale factor, we estimate a 40 % error in the volume-area scaling and a 100 % error in the volume-length scaling for the model's error propagation, as in Marzeion et al. (2012). Theoretically, the scale factors could be treated as global parameters as well, but it is not clear whether an optimization of those would benefit the overall (global) model accuracy, while it would increase the efforts in computation and evaluation. Concerning the relaxation, a response time scale of the volume-length change is estimated by assuming that smaller glaciers and those with higher mass turnover will react faster to volume changes (details in Marzeion et al., 2012).

Initial values for the area of each individual glacier at the start of the model run (e.g., beginning of the 20th century) are found using an iterative approach that minimizes the difference in area between modeled glacier and the RGI record in the year of the respective observation (see grey box in Fig. 2.1). If this iterative procedure is not successful, the glacier is not included in the reconstruction. For these glaciers, a simple upscaling is applied in the computation of regional and global results. The optimized CRU TS 4.03 model setup was able to initialize glaciers accounting for 98 % of the glacier area recorded in the RGI. This value is roughly the same for the optimized model setups that performed well according to our validation procedure, although it is slightly lower for those forced with the mean/median of the meteorological data ensemble (see Table 2.2). A failure of the initialization for an individual glacier might occur when, for example, the calibration (see Sect. 2.2.2 and grey box in Fig. 2.1) results in a very high temperature sensitivity for that glacier. The iterative search of an initial area might then not be able to capture the very large starting area necessary for the implicated strong mass change. The largest fractions of area not successfully modeled with the optimized CRU TS 4.03 model setup are located in the Greenland periphery (ca. 9 %) and Russian Arctic (ca. 5 %).

Note that since the CRU CL 2.0 data set used to obtain P_i^{CRUclim} and T_i^{CRUclim} does not cover Antarctica, we do not consider glaciers in the periphery of Antarctica and Subantarctic glaciers here (labeled region 19 in RGI, 2017).

Mass balance calibration

As explained above, we treat the parameter t^* as a global one, as opposed to a glacier-specific estimation in Marzeion et al. (2012). In order to illustrate the reasoning, we need to discuss the mass balance calibration for an individual glacier in the model in more detail (see grey box in Fig. 2.1). The calibration is based on the idea of inferring a glacier's temperature sensitivity μ^* by finding a climatological time period in the forcing data set (centered around t^*) which would result in a zero specific annual mass balance of the glacier in present-day geometry. Thus, for each center year $\tilde{t}$ of a 31-year period, we can calculate $\mu(\tilde{t})$ by requiring

$$B(\tilde{t}) = \sum_{i=1}^{12} \left[P_{i,clim}^{solid}(\tilde{t}) - \mu(\tilde{t}) \cdot max\Big(T_{i,clim}^{terminus}(\tilde{t}) - T_{melt}, 0 \Big) \right] = 0 \tag{2.5}$$

where $P_{i,\mathrm{clim}}^{\mathrm{solid}}(\tilde{t})$ and $T_{i,\mathrm{clim}}^{\mathrm{terminus}}(\tilde{t})$ are climatological averages of $P_i^{\mathrm{solid}}(\tilde{t})$ and $T_i^{\mathrm{terminus}}(\tilde{t})$. Note that the calculation is based on a smaller number of years when $\tilde{t} < 1916$ or $\tilde{t} > 2003$. For each of the 299 glaciers that have at least 3 years of in situ mass balance observations, we calculate the modeled annual specific mass balance (based on Eq. 2.1) for each $\tilde{t}$. Then, the associated calibration bias of an individual validation glacier is calculated as

$$\overline{B_{\mathrm{M}}} - \overline{B_{\mathrm{O}}} = \beta(\tilde{t}), \tag{2.6}$$

where $\overline{B_{\mathrm{M}}}$ is the mean modeled specific annual mass balance of the validation glacier, with μ^* equal to $\mu(\tilde{t})$ in Eq. (2.1), for the years of available mass balance measurements, and $\overline{B_{\mathrm{O}}}$ is the mean observed mass balance. Hence, a negative (positive) $\beta(\tilde{t})$ means that the glacier with its present-day geometry would have presumably gained (lost) mass during the climate period around $\tilde{t}$, applying the inferred $\mu(\tilde{t})$. Accordingly, the glacier would be too (in)sensitive to changes in the forcing, and the application of $\beta(\tilde{t})$ is required to balance this in Eq. (2.1). The general problem here is to infer t^* for glaciers without available annual in situ mass balance measurements. Marzeion et al. (2012) chose t^* to be that $\tilde{t}$, for which $|\beta(\tilde{t})|$ was minimal; μ^* was then calculated from Eq. (2.5) applied to t^*, and β^* taken as $\beta(t^*)$. For glaciers without in situ observations of mass balances, t^* and β^* were interpolated from the 10 closest glaciers with observations, using an inverse-distance weighting. Using this method, Marzeion et al. (2012) were able to identify a suitable parameter set in the leave-one-glacier-out cross-validation procedure that did not show a large bias against in situ measurements, applying CRU TS 3.0 as atmospheric boundary conditions, a previous version of the RGI, and other mass balance validation data. However, this is not generally the case for the data sets applied here, and there is a conceptual shortcoming in the spatial interpolation of t^*, which we will illustrate for one exemplary model setup.

Figure 2.2a shows the global average of $\beta(\tilde{t})$, weighted by the length of each glacier's in situ mass balance measurement time series (henceforth, all mentioned averages over different validation glaciers imply such a weighting), using CRU TS 4.03 as boundary condition, applying the optimal parameter set (see Sect. 2.2.3).

Figure 2.2b shows that the distribution of t^* estimated directly is bi-modal, with frequent values either at the beginning or at the end of the considered period, but the spatial interpolation leads to a more even distribution. This in turn means that, generally speaking, the spatial interpolation moves t^* towards the middle of the considered time period, thereby increasing the value of β^* for glaciers with an early t^* and decreasing it for those with a late t^*. Figure 2.2b also shows that there are more validation glaciers with t^* at the beginning of the 20th century than at the end of the 20th century or the beginning of the 21st century.

Furthermore, those glaciers with a directly estimated individual t^* at the beginning of the 20th century tend to have a positive β^*, implying that even with present-day geometry, those glaciers would have lost mass under climatic conditions of the early 20th century applying $\mu(t^*)$. The zero crossing of the global average $\beta(\tilde{t})$ is thus found at a period when positively and negatively biased glaciers cancel each other out. Since moving the median of t^* towards the middle of the of the modeled period generally goes along with an increase in the globally averaged calibration bias $\overline{\beta(t^*)}$, using the spatial interpolation of t^* tends to lead to a positively biased model setup, which then becomes apparent in the leave-one-glacier-out cross-validation. That is because there are more validation glaciers with an early than late individual t^*, as stated above.

In order to avoid this effect and taking into account that neighboring glaciers will have different response times, such that even if they experience a very similar evolution of climate anomalies we cannot expect a close spatial coherence of t^*, we do not spatially interpolate t^* as was done by Marzeion et al. (2012) but treat it as a fifth global parameter instead. Note that μ^* is still a glacier-specific parameter following Eq. (2.5) and that $\beta(t^*)$ is still interpolated from the 10 closest glaciers in an inverse-distance-weighted manner. Although retaining the interpolation of $\beta(t^*)$ seems to contradict the argument about regional climatology made above, it is the only way to handle the calibration bias for glaciers without validation data, and we expect biases caused by this approach on the scale of an individual glacier to cancel out globally. Ultimately, the leave-one-glacier-out cross-validation will reveal any potential new model errors introduced through this change.

At this point we recapitulate the reasoning behind our changes to the calibration procedure compared to previous studies that applied the same model, since it is an important point of this work: in contrast to Marzeion et al. (2012), we do not rely on the assumption of a steady state for every single glacier using present-day geometry and climate conditions during a glacier-specific period around t^* but rather on a global mean steady state of glaciers in their present-day geometry with climate conditions during a (globally equal) period around t^*. This means that while some glaciers with present-day geometry would gain mass when exposed to the climate around the global t^*, others would lose mass. Figure 2.2a shows the mean bias of glaciers for which glacier-specific values of t^* can directly be obtained based on in situ observations – once for glaciers with t^* before 1920 and once with t^* after 1998. It can be seen that the (global) calibration bias ($\beta(\tilde{t})$) is a function of the center year of the climatology ($\tilde{t}$) we assume glaciers (with present-day geometry) to be in equilibrium with globally. For a glacier with an early individual t^*, the calibration bias will be increasingly positive as we depart from the climatology of its t^* to warmer climate periods (i.e., later $\tilde{t}$). This is because μ will be underestimated using a warmer climate for calibration (see Eq. 2.5). If there are glaciers with early and late individual t^* in close proximity of each other, the $\beta(\tilde{t})$ we interpolate to a glacier with early individual t^* will often be too low, while it will be too high on glaciers with a late individual t^*. Because there are more glaciers with an early individual t^* (before 1920) than a late t^* (after 1998; see Fig. 2.2b), moving the globally applied t^* to a warmer climate period then results in an overall positive bias in the global cross-validation result. Interpolating t^* has a similar effect. Overall, the cross-validation shows that this method is able to yield unbiased model setups (see Sect. 2.3.1), disregarding possible biases in the validation data.

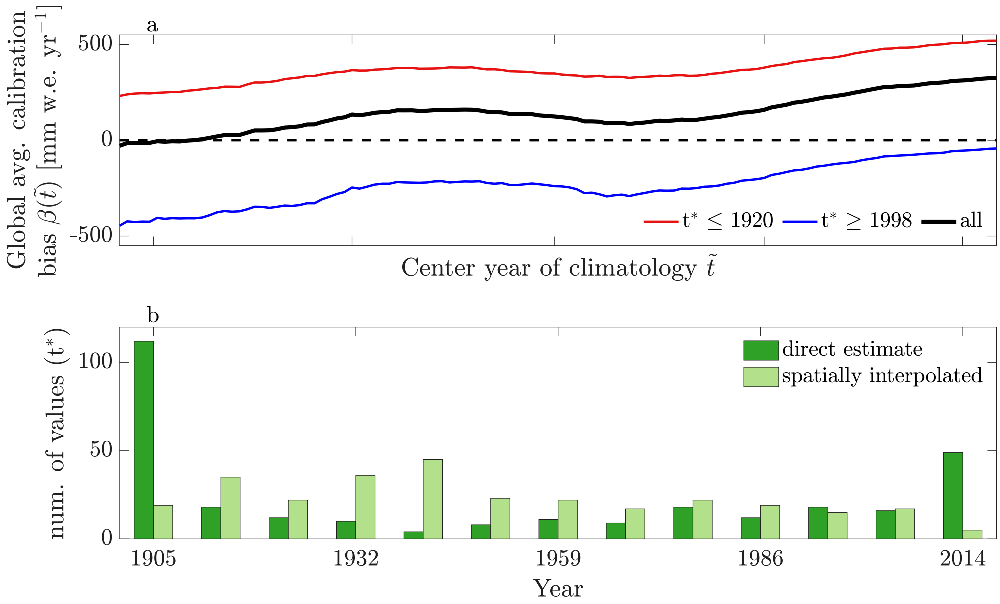

Figure 2.2: **(a)** Average calibration bias β as a function of the center year of a climatological window around $\tilde{t}$ for validation glaciers showing the lowest calibration bias around the center years $t^* \leq 1920$ (red, $n = 132$) and ≥ 1998 (blue, $n = 72$) as well as the weighted average of all validation glaciers (black, $n = 298$). **(b)** Distributions of t^* directly estimated from Eqs. (2.5) and (2.6) (green) and spatially interpolated as in Marzeion et al. (2012, light green). Values in both panels are derived from the cross-validation procedure (see Sect. 2.2.2 and 2.2.3) with the optimized CRU TS 4.03 model setup.

2.2.3 Parameter optimization strategy

For the identification of an optimal parameter set, we applied a brute-force approach (see blue box in Fig. 2.1). This means that we varied each parameter other than t^* (see above) using the following ranges, which are similar to those used in Marzeion et al. (2012):

- threshold temperature for snow/ice melt (T_{melt}) (°C): $\{-2, -1, 0, 1, 2\}$;
- threshold temperature for solid phase precipitation ($T_{\mathrm{prec.\ solid}}$) (°C): $\{-1, 0, 1, 2, 3, 4\}$;
- precipitation lapse rate (γ_{precip}) ($\%\,(100\,\mathrm{m})^{-1}$): $\{0, 1, 2, 3, 4, 5\}$;
- precipitation correction factor (a): $\{1, 1.5, 2, 2.5, 3\}$.

We did so for each meteorological data set and performed a leave-one-glacier-out cross-validation for each of the 900 parameter combinations possible within these ranges. This resulted in 9900 validation runs (900 times 11 forcing data sets), which we used to identify parameter sets that yield a zero crossing of the global average $\beta(\tilde{t})$ in a first step. For all forcing data sets except 20CRV3, those zero crossings were found with $\tilde{t} < 1920$ (applying 20CRV3, some were found in 1962 and 1976). We then performed additional cross-validations with the 20 best-performing parameter sets yielding a zero crossing of the global average $\beta(\tilde{t})$ to fine-tune t^*, applying the range 1901 to 1920, except for 20CRV3 where we applied the ranges 1909–1918, 1960–1964, and 1974–1978. Hence, we performed 400 (4400) additional cross-validation runs per data set (in total).

From those cross-validations, three characteristic statistical measures of model performance were computed: model bias (i.e., mean model error) with respect to observations, the temporal correlation with observations, and the ratio of standard deviations of interannual variability between modeled and observed mass balances. We do not include the mean squared error (MSE) as a performance measure, since it is simply a (weighted) combination of the three performance measures:

$$\mathrm{MSE} = \sigma_{\mathrm{M}}^2 + \sigma_{\mathrm{O}}^2 - 2\sigma_{\mathrm{M}}\sigma_{\mathrm{O}}R + \left(\overline{M} - \overline{O}\right)^2 , \tag{2.7}$$

where σ_{M} is the standard deviation of modeled mass balances, σ_{O} is the standard deviation of observed mass balances, R is the Pearson correlation coefficient, $\overline{M}$ is the mean of modeled mass balances, and $\overline{O}$ is the mean of observed mass balances (thus, the last term corresponds to the squared bias).

From Eq. (2.7) it can be inferred that a minimum MSE occurs for a model setup in which the standard deviation ratio equals the correlation coefficient. Hence, in a model setup that is not perfectly (positively) correlated with the observations (i.e., $0 < R < 1$), a more realistic standard deviation ratio (e.g., $1 \geq \frac{\sigma_{\mathrm{M}}}{\sigma_{\mathrm{O}}} > R$) will result in a higher MSE. However, a correlation coefficient equal to 1 is generally not achievable in models such as the one used in this work. Consequently, minimizing the MSE will lead to preference of parameter sets that underestimate variance. This is problematic, since a correct representation of variance is indicative of correct model sensitivity to changes in the forcing. For example, it is possible to imagine to apply a model setup that yields a low bias and good correlation but largely underestimates the interannual variation of mass balances. It is therefore beneficial to not only minimize the MSE but rather to minimize the three statistical coefficients it comprises individually, in order to not trade a realistic model sensitivity for a smaller MSE.

All three performance measures were calculated for each validated glacier and then averaged over all these glaciers, weighted by the number of available mass balance observations per glacier. This was done for every cross-validation run in order to be able to identify the overall best-performing model setups.

Standard deviation ratios were brought to represent the deviation from an optimum value (i.e., one) by

$$\mathrm{SR} = \frac{\sigma_\mathrm{M}}{\sigma_\mathrm{O}} - 1. \tag{2.8}$$

To determine for each meteorological data set a model parameter set that, on average, shows the highest skill to represent the behavior of observed glaciers, we normalize the performance measures introduced above such that the individual scores s range from 0 for the worst to 1 for the best validation result by the following equations:

$$\begin{aligned}
s_{i,\mathrm{bias}} &= \frac{\max(|\mathrm{bias}|) - |\mathrm{bias}_i|}{\max(|\mathrm{bias}|) - \min(|\mathrm{bias}|)},\\
s_{i,\mathrm{SR}} &= \frac{\max(|\mathrm{SR}|) - |\mathrm{SR}_i|}{\max(|\mathrm{SR}|) - \min(|\mathrm{SR}|)},\\
s_{i,R} &= \frac{R_i - \min(R)}{\max(R) - \min(R)},
\end{aligned} \tag{2.9}$$

where i is the individual model setup the score is calculated for. These scores were then added up to identify the optimal model setup as the one with the maximum overall score. If a model setup obtained the single best result for all three performance measures individually, it would thus yield a score of three. Note that the three (or potentially other) performance measures might be weighted differently, based on the objective of the model application. However, as shown below, we do not find substantial trade-offs between the three performance measures, such that any potential weighting would have a very limited influence on the results.

2.3 Results

2.3.1 Cross-validation and uncertainty assessment

Performance measures

Table 2.2 shows the values obtained for performance measures and optimal global parameters. We differentiate between the mean and median of the forcing data input used as individual boundary conditions (mean/median input) and the mean and median of the ensemble output values (mean/median output). For more than half of the optimized model setups, the global mean bias of the optimal parameter set is smaller than 10 mm w.e. yr^{-1}, and the correlation is larger than 0.6, while the amplitude of the interannual variability is estimated correctly within a small range (ca. 5 %). RMSEs lie roughly between 700 and 800 mm w.e. yr^{-1} for most optimized model setups. Only 20CRV3 shows a significantly higher RMSE, caused by some large outliers. Note that the number of glaciers that cannot be initialized also depends on the meteorological data set used as boundary condition. CERA20C, e.g., not only performs the worst (obtaining an overall score of 1.38 using the optimal parameter set) but leads to only 274 of 299 validation glaciers being initialized in the cross-validation and 180 481 of the 211 838 glaciers in the global reconstruction run, representing 84 % of today's global glacier area outside Antarctica. In contrast, the best-performing model setup that covers the whole model period (CRU TS 4.03) is able to initialize 298 validation glaciers and 200 443 glaciers in the global reconstruction run, representing ca. 98 % of the global glacier area. Following our scoring system, we find that the statistically best performing single data set covering the whole model period is CRU TS 4.03, and the overall best-performing data set, but only covering 1979–2018, is ERA5. Our best estimate for the whole model period is the mean model output.

Independent of the time period considered, the mean output of the ensemble shows the best performance, exceeding not only the best individual ensemble member, but also the result obtained by the mean and median input. The statistically best performing individual ensemble members vary with the time periods that are covered by the meteorological data sets. For example, during the period 1958–2018, JRA55 leads to the best performance; from 1979 onward, it is ERA5. Table 2.2 also shows that the performance measures attain better values if the averages are weighted by the length of the observation time series than with the non-weighted average, illustrating the need for long-term observations for reliable model validation.

In order to assess the consistency of cross-validation results among the ensemble members, two-sample Kolmogorov–Smirnov tests for the similarity of distributions were conducted for all 55 possible unique pairs of the 11 optimized model setups. This was done for modeled annual specific mass balance and model deviation distributions. Model deviation here refers to the differences between each modeled and observed annual specific mass balance value in the cross-validation procedure; its average thus corresponds to the average of the bias weighted by the number of available mass balance observations per validation glacier. The confidence level we require for rejecting the similarity of distributions is at

95 %. Regarding the distributions of modeled mass balances, only 10 (18 %) of the tested pairs are not significantly different – all involving the six best-scored model setups (see Table 2.2). Model deviation distribution pairs do not significantly differ in 27 (49 %) cases, of which only 1 (2 %) involved 20CRV3, CERA20C, or ERA20C. We conducted Welch's t test for the similarity of means in the same manner. Here, only the three lowest-scored model setups' means of modeled mass balances are significantly distinguishable from other ensemble members. Concerning the mean model deviation, only that of CERA20C significantly differs from the others. Hence, the similarity tests indicate that the results of model setups with higher scores (see Table 2.2) tend to be more consistent among each other and to differ from lower-scored ones statistically. Model deviation distributions significantly different from those of other ensemble members are to a large degree produced by low-scored model setups, while the mean is only significantly different for CERA20C. The significantly high bias and low score of CERA20C indicate particular issues with this forcing data set and lead us to exclude it from the following ensemble calculations. In the subsequent section we will explore where these issues stem from. In doing so, we try to explain why the temporal and spatial constraints of the validation data hinder us to make assertions over which individual model setup is the most reliable one over the whole temporal and spatial model domain.

Table 2.2: Values of the performance measures for each tested data set, applying the best-scored parameter set. Values behind coefficients in brackets display non-weighted averages (see text). For the mean and median model output, the score with/without CERA20C is displayed. The total number of cross-validated glaciers used for the respective data set is n. A_M is the percentage of glacier area (as recorded in the RGI) covered by the glaciers the model was able to initialize. The last five columns contain the selected global parameters (see Eqs. 2.1–2.5).

	Bias (mm w.e. yr^{-1})	R	SR	RMSE (mm w.e. yr^{-1})	score	n	A_M (%)	t^*	$T_\mathrm{m.}$ (°C)	$T_\mathrm{p.\,s.}$ (°C)	$\gamma_\mathrm{p.}$ (% (100 m)$^{-1}$)	a
20CRV3	14.1 (57.4)	0.61 (0.56)	−0.02 (−0.13)	978.0 (816.9)	2.30	295	86.6	1978	2	2	1	2.5
CERA20C	79.0 (30.9)	0.56 (0.52)	0.07 (0.13)	747.1 (715.3)	1.38	274	83.9	1902	2	0	4	3
CFSR	0.0 (−15.1)	0.60 (0.56)	0.13 (0.03)	804.2 (740.9)	2.13	276	93.4	1917	1	4	3	2
CRU TS 4.03	0.6 (11.5)	0.63 (0.59)	0.01 (−0.05)	739.6 (695.9)	2.62	298	97.8	1917	0	4	4	3
ERA−Interim	1.7 (14.7)	0.64 (0.61)	0.02 (−0.02)	715.1 (674.0)	2.70	297	97.6	1907	0	4	3	3
ERA5	0.0 (10.4)	0.67 (0.64)	0.02 (−0.04)	714.0 (680.5)	2.96	299	97.8	1919	0	4	5	2.5
ERA20C	4.6 (−38.9)	0.58 (0.54)	0.05 (0.03)	791.0 (735.8)	2.04	281	97.2	1902	0	4	1	3
JRA55	−2.0 (18.7)	0.64 (0.60)	0.00 (−0.03)	701.1 (670.5)	2.66	298	98.6	1915	−1	4	5	3
MERRA2	0.2 (14.8)	0.64 (0.60)	0.01 (−0.04)	719.7 (685.4)	2.72	299	97.5	1908	0	4	1	3
Mean in.	9.1 (−13.6)	0.66 (0.63)	0.13 (0.07)	767.5 (714.5)	2.59	299	93.3	1901	1	4	3	3
Median in.	16.3 (−5.5)	0.66 (0.62)	0.02 (−0.03)	725.9 (679.7)	2.75	299	93.8	1901	1	4	1	3
Mean out.	3.9 (23.7)	0.68 (0.65)	−0.06 (−0.14)	704.1 (651.7)	2.84/2.90	–	–	–	–	–	–	–
Median out.	18.3 (26.3)	0.67 (0.64)	−0.06 (−0.13)	680.1 (640.2)	2.67/2.77	–	–	–	–	–	–	–

Spread of the ensemble inconsistent with model uncertainty from cross-validation

The leave-one-glacier-out cross-validation procedure applied here is designed to estimate the uncertainty of model results for glaciers that have no in situ mass balance observations and for times where there are no in situ observations. Therefore, in principle, the results of the individual ensemble members should agree within their corresponding uncertainty estimates. However, there is a strong spatial bias in in situ mass balance observations towards certain RGI regions – mostly locations where also the past state of the atmosphere is well constrained, since both atmospheric and glaciological observations are denser in easily accessible regions. The majority of glaciers, though, are situated in remote locations where observations of the state of the atmosphere were very sparse, particularly in the first half of the 20th century. Thus, the cross-validation is biased towards times and places where the state of the atmosphere, i.e., the boundary conditions of the glacier model, can be assumed to be exceptionally well constrained.

Figure 2.3 shows that 66 % of the validation data originate from only four RGI regions: Western Canada and US, Scandinavia, Central Europe, and Central Asia. Panel (b) shows the fraction of mean annual ensemble variance of global mass change rates in the modeled period attributable to each RGI region. Most of the ensemble spread is due to disagreement in sparsely observed regions that contain much glacier ice. Of the mean annual global ensemble spread, nearly 60 % can be attributed to the disagreement in estimates for the regions of Alaska, Arctic Canada (North), and the Greenland periphery. The value for the Greenland periphery increases from 21 % to 36 % if we included CERA20C in the calculation. This indicates that peripheral glaciers in Greenland are responsible for a considerable amount of the ensemble spread as well as for most of the large divergence of CERA20C from the other ensemble members. The only region that shows a large spread among ensemble members but does not contain as much glacier ice as the previously mentioned ones is the Southern Andes.

In Fig. 2.4a, the issue of temporally biased validation data (all are from the second half of the 20th century or the beginning of the 21st) can be recognized. Mean mass loss rates calculated with forcing data sets that have complete data coverage over the whole model period for the four previously mentioned well-observed regions are shown. Comparing results for the four best-observed regions to global results (Fig. 2.4b), it can be seen that the disagreement on the global scale is larger than in the well-observed regions and that the global reconstruction forced by CERA20C is far off the three other ensemble members, while it is not so in the well-observed regions. This behavior can be explained by the much more pronounced warming of glacier locations at the global scale in CERA20C until ca. 1960 (Fig. 2.4d): during the calibration, lower temperatures at t^* will lead to higher temperature sensitivities (see Eq. 2.5). Similarly, the greater increase in temperature will result in higher mass loss rates.

Concerning these issues with CERA20C, it is striking that in spite of its large positive specific mass balance bias in the cross-validation, global mass change estimates obtained with it are much larger than those of the other ensemble members. This underlines the fact that even though the cross-validation is crucial in the optimization process, we cannot entirely rely on it for assessing global and long-term reconstruction performance of individual model setups. Therefore, because, as stated in the previous section, the best-performing data sets do produce statistically quite similar results for the validation glaciers, we will only use estimates based on the ensemble – i.e., not individual members – in the following. We exclude the results of model runs forced with the mean and median input from our ensemble calculations in order not to bias them towards the central value and also because they contain the problematic values of the CERA20C data. If a full ensemble approach as done in this study is not feasible (e.g., due to computational constraints) we still recommend to use a mean/median input data set as the meteorological forcing for reconstructions outside the spatial and temporal domain of validation data, since a single best-performing data set cannot be identified conclusively.

In both the well-observed regions (Fig. 2.4a) and the global scale (Fig. 2.4b), the different model setups disagree more strongly in the first half of the 20th century, reflecting that uncertainty in the atmospheric conditions during that time is also greater. All in all, we find that the ensemble spread tends to be larger than uncertainty estimates obtained via the cross-validation and that this is caused by the majority of glacier observations coming from places and times where the uncertainty of the state of the atmosphere is smaller than what can typically be expected in glacierized regions. Furthermore, we assume that the individual glaciers' error estimates are uncorrelated with each other and random, i.e., independent, as we do not have direct model error estimates for every glacier and can thus not account for correlations of individual glaciers' errors. However, the ensemble approach allows us to explore if, and to which degree, the cross-validation underestimates the true uncertainty of the reconstruction.

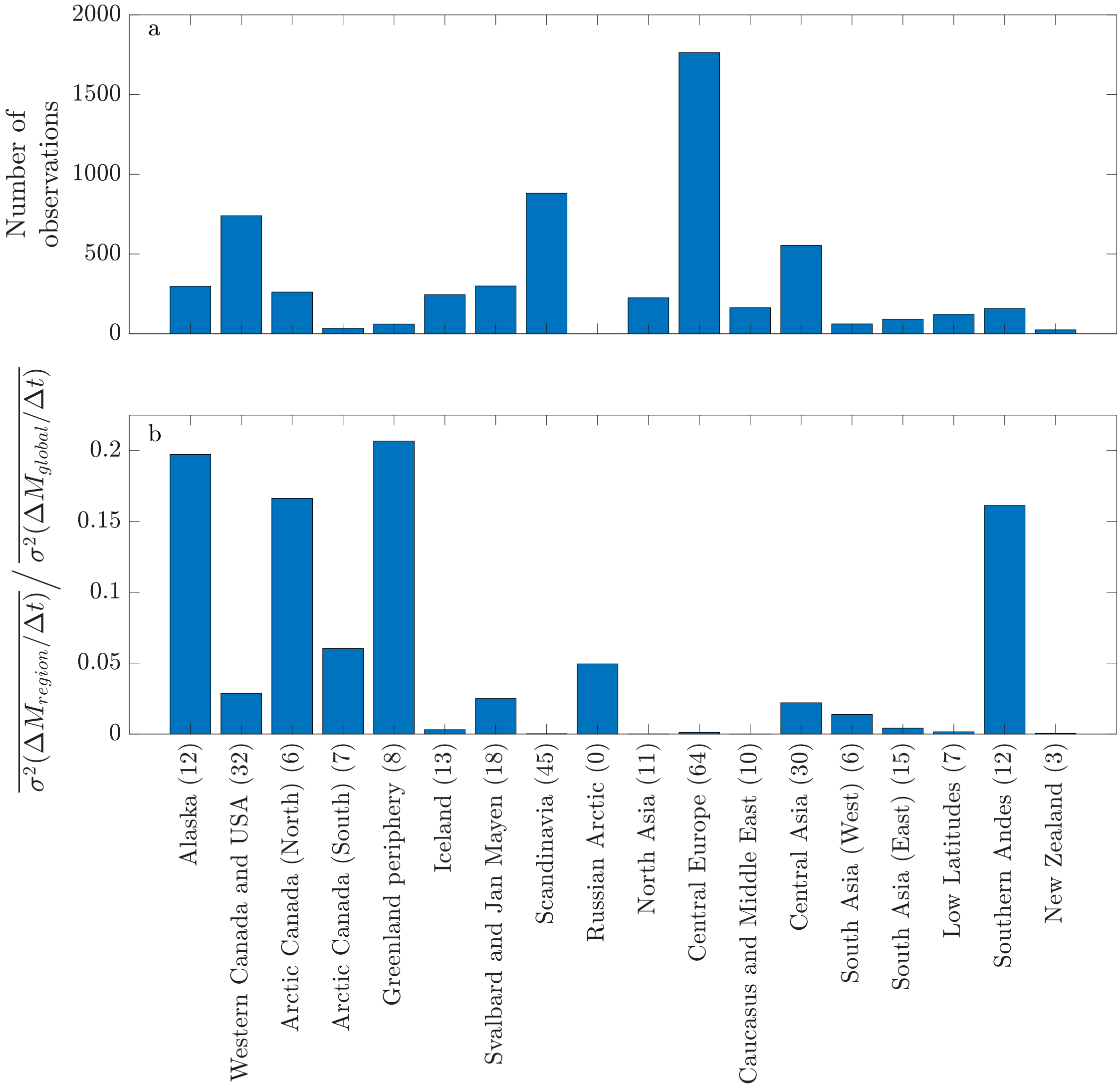

Figure 2.3: **(a)** Number of specific annual mass balance observations available for calibration and validation in each RGI region. **(b)** Fraction of ensemble variance of global mean mass change rate ($\Delta M/\Delta t$) in the modeled period (1901–2018) attributable to each RGI region. In brackets is the number of glaciers used for calibration and validation in each region.

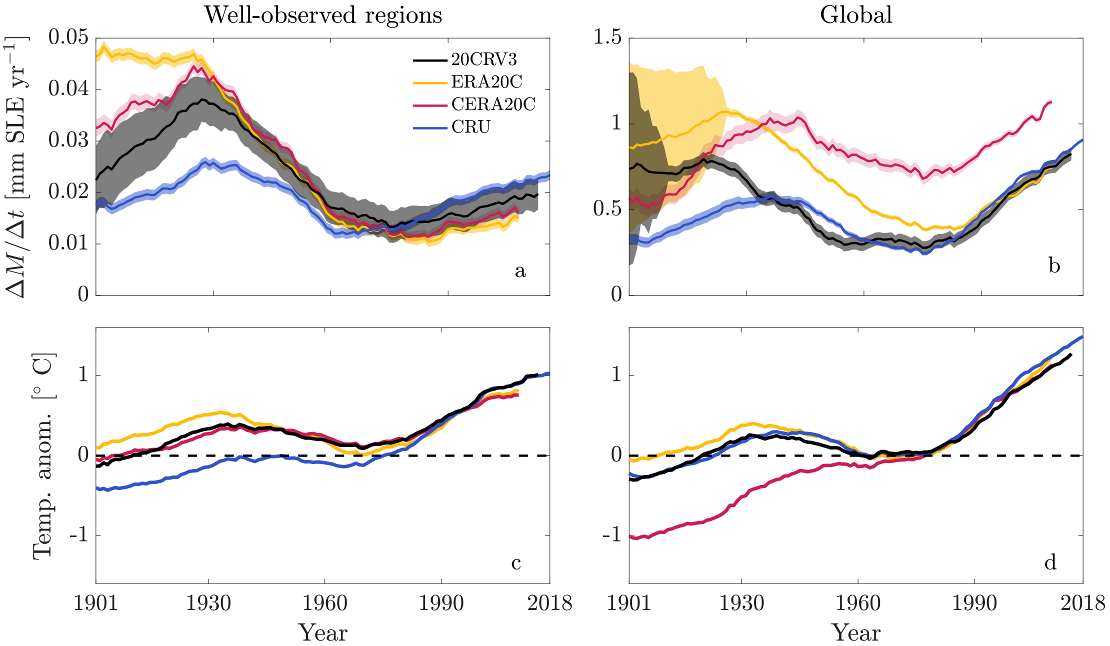

Figure 2.4: Mass loss rate estimates for meteorological forcing data sets with whole 20th century coverage: **(a)** averaged over well-observed regions (Western Canada and US, Scandinavia, Central Europe, and Central Asia) and **(b)** globally. Average temperature anomalies at glacier tongue locations in **(c)** well-observed regions and **(d)** globally, weighted by glacier area. In all graphs, 31-year moving averages are shown for clarity.

Combining model and ensemble uncertainty

To account for both the model error, as calculated in the cross-validation procedure, and the ensemble spread, the total uncertainty of the ensemble average is calculated as follows. First, we calculate the model error of the ensemble average solely determined by the means of the RMSEs obtained from the leave-one-glacier out cross-validation:

$$\epsilon_{\text{model}}(t) = \frac{\sqrt{\sum_{i}^{n} \epsilon_i(t)^2}}{n}, \tag{2.10}$$

where $\epsilon_i(t)$ is the model uncertainty computed in the cross-validation procedure for an individual ensemble member i for year t. Then we add the ensemble spread as a further uncertainty measure to the model error of the ensemble average:

$$\epsilon_{\text{ensemble}}(t) = \sqrt{\epsilon_{\text{model}}(t)^2 + \sigma(t)^2}, \tag{2.11}$$

where $\sigma(t)$ is the ensemble standard deviation in year t. Here, we treat the individual model setups' errors, obtained from the cross-validation procedure, to be independent from each other and the model error of the ensemble average to be independent from the ensemble spread. This might lead to an underestimation of total uncertainty, since there might be correlations of the individual sources of uncertainty for which we cannot account.

Because we model more than 200 000 glaciers and assume their errors to be independent as well, thereby assuming that their errors partly cancel each other out, the true uncertainty is probably higher than our estimate. However, we do account for interannual covariances of the ensemble when estimating the uncertainty of mean values over periods longer than 1 year.

Figure 2.5 shows the temporal evolution of total uncertainty ($\epsilon_{\text{ensemble}}$) as well as the aggregated model uncertainty (ϵ_{model}) and ensemble spread (σ_{ensemble}) of the ensemble mean mass change rate estimate. The total uncertainty of the ensemble mean estimate is high in earlier years, with a sharp decrease after the first 20 years. This is due to the decrease in the high model error of the ensemble average, especially during the first decade of the 20th century, which is produced by very high mass losses of a few glaciers in some model setups during that period. The ensemble spread is also greater during the first half of the 20th century compared to later years, which can be attributed to less agreement between meteorological data sets in earlier years. Note that the further back in time we go, the fewer meteorological data sets are available, since not all reanalysis products provide data for the whole period.

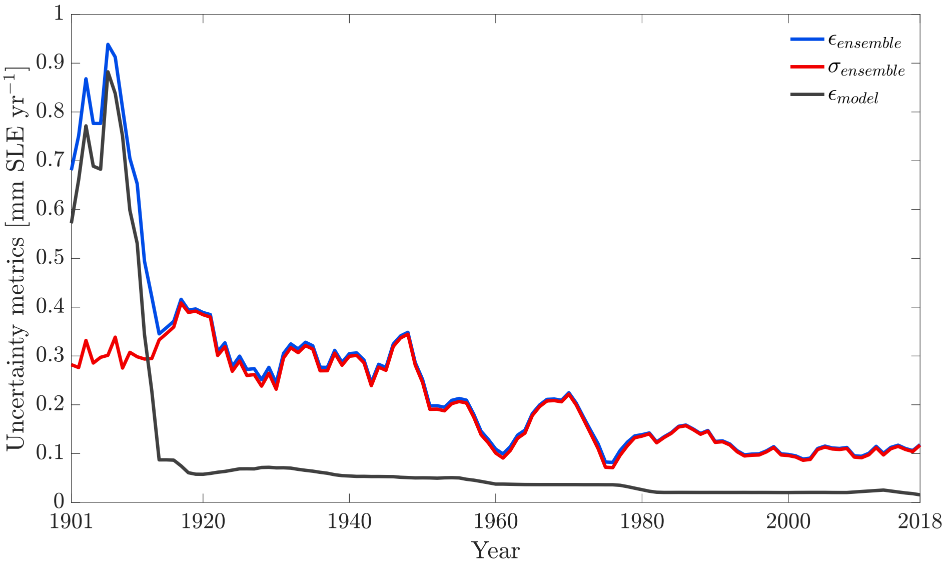

Figure 2.5: Five-year moving average of the temporal evolution of model uncertainty metrics for annual global mass change rates. $\epsilon_{\text{ensemble}}$ is the total uncertainty, i.e., combined model uncertainty (ϵ_{model}) and ensemble spread (σ_{ensemble}; see Eq. 2.11).

2.3.2 Global glacier mass change

In the following we present our modeled estimates of global glacier mass change. Note that we express those in units of sea-level contribution. This means positive values indicate a contribution to sea-level rise and thus a mass loss of the glaciers.

Figure 2.6 shows the temporally accumulated mass change estimates, relative to 1980 (the year from which onward all meteorological data sets have data coverage), and their uncertainties. Figure 2.6a shows the estimates for each individual ensemble member as well as their model uncertainties $\epsilon_{\mathrm{model}}$. Especially in the first half of the 20th century, ensemble members diverge, with CRU TS 4.03 showing the lowest and ERA20C, next to CERA20C, the highest mass loss during that period. The ensemble average mass change estimate over the whole model period is $69.2 \pm 24.3\,\mathrm{mm\,SLE}$, which translates to an average mass change rate of $0.59 \pm 0.21\,\mathrm{mm\,SLE\,yr^{-1}}$ and a mass loss of roughly 18 % relative to 1901.

Table 2.3 displays the regional and global mass loss rates for different reference periods. Mass change rate estimates for more recent periods are increasing across most regions, reaching $0.90 \pm 0.12\,\mathrm{mm\,SLE\,yr^{-1}}$ accumulated globally in the most recent period (2006–2018). The only time and region for which an increase in glacier mass is estimated are the Southern Andes during 1901–1990, although with a relatively high uncertainty due to ensemble spread (see Fig. 2.3).

To explore the period of decelerated mass loss between roughly 1940 and 1980 visible in Fig. 2.7, the periods 1901 to 1940 and 1941 to 1980 are shown in Table 2.3. For most regions, the mass change rate estimates are substantially smaller in the latter period; only New Zealand exhibits a significantly larger mass loss. Regarding the global estimate, most of the mass loss deceleration took place in the Greenland periphery and the North American continent (i.e., RGI regions 1 to 5). Thus, after increasing mass loss rates until around 1930 (see Fig. 2.7), glaciers started to lose less mass until around 1980, possibly caused by atmospheric cooling induced by increasing aerosol concentrations (Ohmura, 2006; Ohmura et al., 2007; Wild, 2012). From then on, the glaciers' contribution to sea-level rise accelerated again until the end of the modeled period (2018). Figure 2.8 shows the drivers of this behavior: the global ensemble mean temperature (lower panel) and precipitation anomalies as well as total amount of solid precipitation (upper panel; see Eqs. 2.3 and 2.4; all weighted by glacier area). From ca. 1980 on, heat available for ice and snowmelt, i.e., the temperature anomaly, increased monotonously. While precipitation at the glacier locations tended to increase over time, the amount of solid precipitation at glacier locations decreased from roughly 1980 on – implying that not only ablation increased, but also accumulation decreased. In contrast to that, the increase in total precipitation between ca. 1930 to 1950 was accompanied by a similar increase in solid precipitation, indicating that the warm anomaly at the same period was too weak to reduce accumulation as much. In order to get an impression of the relative importance of precipitation and temperature anomalies, we ran the model with the optimized median input model setup – once holding total precipitation constant at the climatology around t^* and once holding temperature constant in the same way (Fig. 2.A.1). Initialization and calibration were done with the full forcing in order to enable meaningful comparisons with the regular model run. Holding the temperature constant resulted in a 65 % lower mass loss, while the constant lower precipitation increased mass loss by only 5 %. This indicates that the temperature increase plays a much larger role for glacier mass change than increased precipitation. This is expected, because increased temperatures do, as mentioned above, not only increase the melt of a glacier's ice mass, but also decrease the amount of solid precipitation it receives. The finding that precipitation changes play a minor role in glacier mass change is consistent with the literature (Van de Wal and Wild, 2001; Leclercq et al., 2011). Moreover, the interannual variability is larger with varying temperatures compared to only varying precipitation (see Fig. 2.A.1).

Our results also indicate that the glaciers' retreat to higher altitudes acted as a negative feedback on mass loss in more recent times. This is based on the observation that although the global average temperature anomalies at glacier locations were considerably higher after 2000 than around 1930, and the amount of solid precipitation was lower, the global glacier sea-level contribution rates are not higher according to our model results (see Figs. 2.7 and 2.8). However, this result might have been influenced by the applied scaling and relaxation laws (see Sect. 2.2.2), as they control the geometric response to mass changes in our model. Comparing our results of glacier geometry to a publication that estimated contemporary global glacier volumes (Farinotti et al., 2019), on the basis of modeling results as well, we find that our global volume estimate differs less than 1 % from their result. Another feedback that certainly plays a role here, but cannot be resolved by our model, is the positive mass-balance–surface-elevation feedback: as a glacier's surface elevation decreases due to mass loss, it experiences higher temperatures, because of the atmospheric temperature lapse rate. This in turn enhances the initial mass loss (Harrison et al., 2001). Since our model is calibrated and validated with data from more recent years, it could be argued that mass change was actually lower in earlier years due to higher surface elevations of glaciers (Huss et al., 2012).

Concerning uncertainty estimates, Table 2.3 shows that most of the uncertainty stems from the regions of Alaska, Arctic Canada (North), and the Greenland periphery in more recent periods (e.g., 1993–2018). In the earliest period (1901–1940), the Russian Arctic region exhibits a high uncertainty as well, indicating that the large model error in the early 20th century (see Fig. 2.5) is produced there alongside regions 1 to 5.

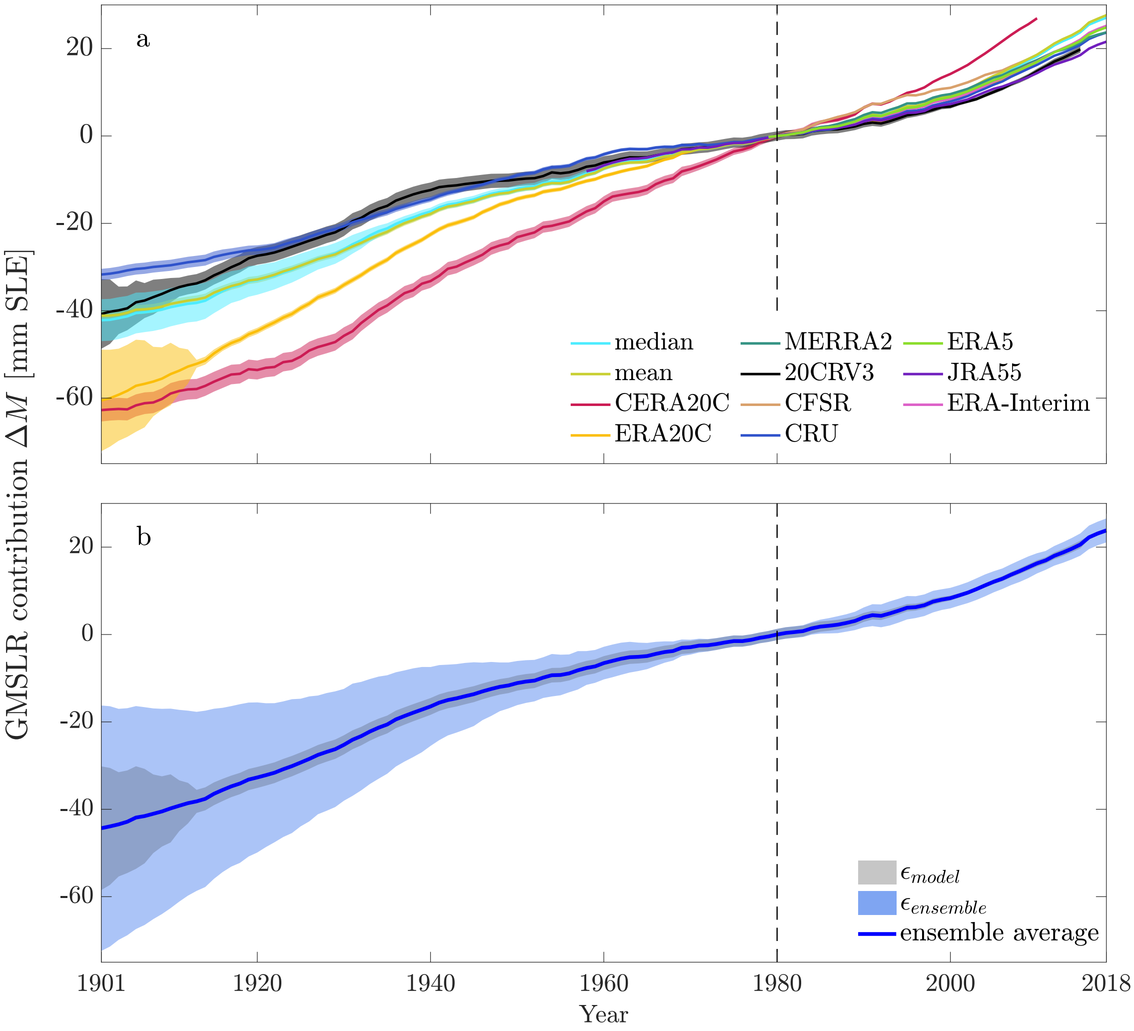

Figure 2.6: **(a)** Estimates of temporally accumulated global mean sea-level rise (GMSLR) contribution relative to 1980 for all forcing data sets. Shaded areas are model uncertainties calculated for individual model setups. **(b)** Ensemble mean output estimate. Shaded areas are the mean model uncertainty (grey, ϵ_{model}; see Eq. 2.10) and total ensemble uncertainty (blue, $\epsilon_{\text{ensemble}}$; see Eq. 2.11), which are shown at the 90 % confidence level. Results of the CERA20C forcing are excluded from the ensemble mean (see Sect. 2.3.1).

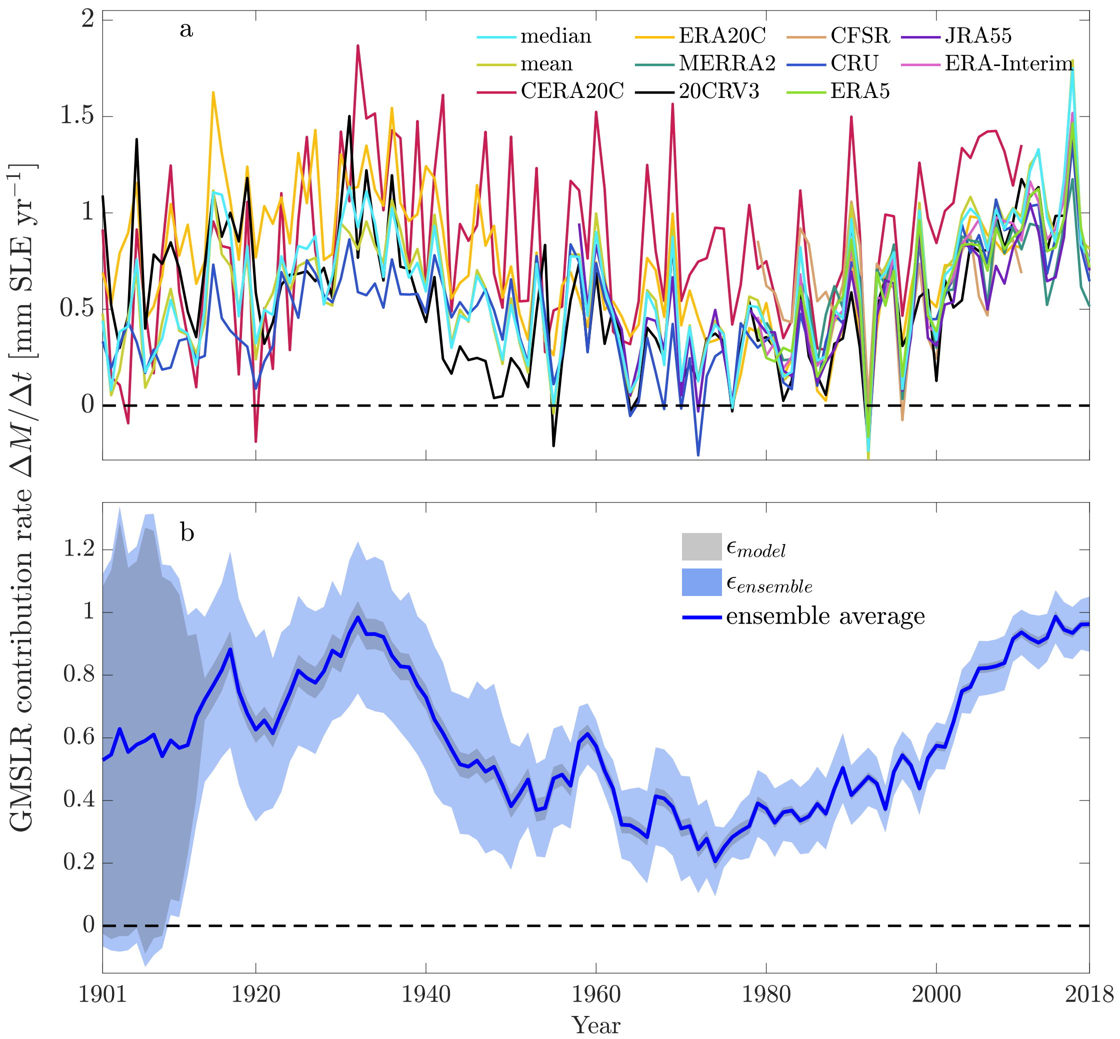

Figure 2.7: **(a)** Annual glacier mass change rates expressed in GMSLR contribution rate for all forcing data sets. **(b)** Mean of ensemble output mass change rates. A 5-year moving average is shown for clarity. Shaded areas are the mean model uncertainty (grey, $\epsilon_{\mathrm{model}}$; see Eq. 2.10) and total ensemble uncertainty (blue, $\epsilon_{\mathrm{ensemble}}$; see Eq. 2.11), which are shown at the 90 % confidence level. Results of the CERA20C forcing are excluded from the ensemble mean (see Sect. 2.3.1). Note the different vertical scales of the panels.

Table 2.3: Ensemble mean regional mass change rate estimates (in $\mathrm{mm\,SLE\,yr^{-1}}$) for 18 primary RGI regions over different time periods. Results of the CERA20C forcing are excluded from the ensemble mean (see Sect. 2.3.1). Values in brackets for the Southern Andes exclude 20CRV3 results (see Sect. 2.4).

	1901–1940	1941–1980	1901–1990	1971–2018	1993–2018	2006–2018
1 Alaska	0.08 ± 0.17	0.05 ± 0.03	0.06 ± 0.07	0.09 ± 0.03	0.13 ± 0.04	0.14 ± 0.04
2 Western Canada and US	0.07 ± 0.10	0.02 ± 0.01	0.04 ± 0.05	0.0017 ± 0.006	0.020 ± 0.006	0.023 ± 0.003
3 Arctic Canada (North)	0.10 ± 0.10	0.06 ± 0.04	0.08 ± 0.05	0.09 ± 0.02	0.13 ± 0.02	0.18 ± 0.03
4 Arctic Canada (South)	0.08 ± 0.10	0.03 ± 0.03	0.06 ± 0.04	0.036 ± 0.008	0.05 ± 0.01	0.07 ± 0.02
5 Greenland periphery	0.17 ± 0.13	0.05 ± 0.06	0.10 ± 0.08	0.07 ± 0.04	0.12 ± 0.05	0.15 ± 0.08
6 Iceland	0.01 ± 0.01	0.012 ± 0.006	0.010 ± 0.008	0.012 ± 0.002	0.020 ± 0.002	0.023 ± 0.004
7 Svalbard	0.05 ± 0.02	0.03 ± 0.01	0.04 ± 0.01	0.06 ± 0.01	0.08 ± 0.01	0.09 ± 0.02
8 Scandinavia	0.003 ± 0.002	0.0026 ± 0.0009	0.003 ± 0.001	0.0024 ± 0.0007	0.0044 ± 0.0009	0.0057 ± 0.0007
9 Russian Arctic	0.06 ± 0.10	0.05 ± 0.01	0.05 ± 0.05	0.06 ± 0.01	0.07 ± 0.01	0.09 ± 0.02
10 North Asia	0.002 ± 0.002	0.0004 ± 0.0003	0.002 ± 0.001	0.0016 ± 0.0004	0.0025 ± 0.0005	0.030 ± 0.004
11 Central Europe	0.001 ± 0.002	0.001 ± 0.002	0.002 ± 0.001	0.004 ± 0.002	0.006 ± 0.002	0.006 ± 0.001
12 Caucasus and Middle East	0.002 ± 0.002	0.0001 ± 0.0004	0.001 ± 0.001	0.0008 ± 0.0003	0.0016 ± 0.0006	0.0021 ± 0.0005
13 Central Asia	0.06 ± 0.04	0.05 ± 0.01	0.05 ± 0.02	0.049 ± 0.006	0.052 ± 0.005	0.057 ± 0.007
14 South Asia (West)	0.04 ± 0.02	0.04 ± 0.01	0.04 ± 0.01	0.034 ± 0.005	0.034 ± 0.006	0.04 ± 0.01
15 South Asia (East)	0.02 ± 0.02	0.02 ± 0.01	0.02 ± 0.01	0.015 ± 0.005	0.017 ± 0.003	0.018 ± 0.005
16 Low Latitudes	0.01 ± 0.01	0.006 ± 0.007	0.007 ± 0.008	0.003 ± 0.003	0.004 ± 0.002	0.004 ± 0.002
17 Southern Andes	−0.03 ± 0.10 (0.007 ± 0.002)	−0.01 ± 0.07 (−0.002 ± 0.002)	−0.01 ± 0.08 (0.004 ± 0.001)	0.01 ± 0.04 (0.009 ± 0.001)	0.01 ± 0.03 (0.016 ± 0.002)	0.01 ± 0.02 (0.022 ± 0.003)
18 New Zealand	0.002 ± 0.004	0.003 ± 0.004	0.003 ± 0.003	0.0016 ± 0.0005	0.0013 ± 0.0004	0.016 ± 0.0008
Global (without peripheral Antarctic and Subantarctic)	0.73 ± 0.46	0.42 ± 0.21	0.56 ± 0.27	0.56 ± 0.06	0.75 ± 0.07	0.90 ± 0.12

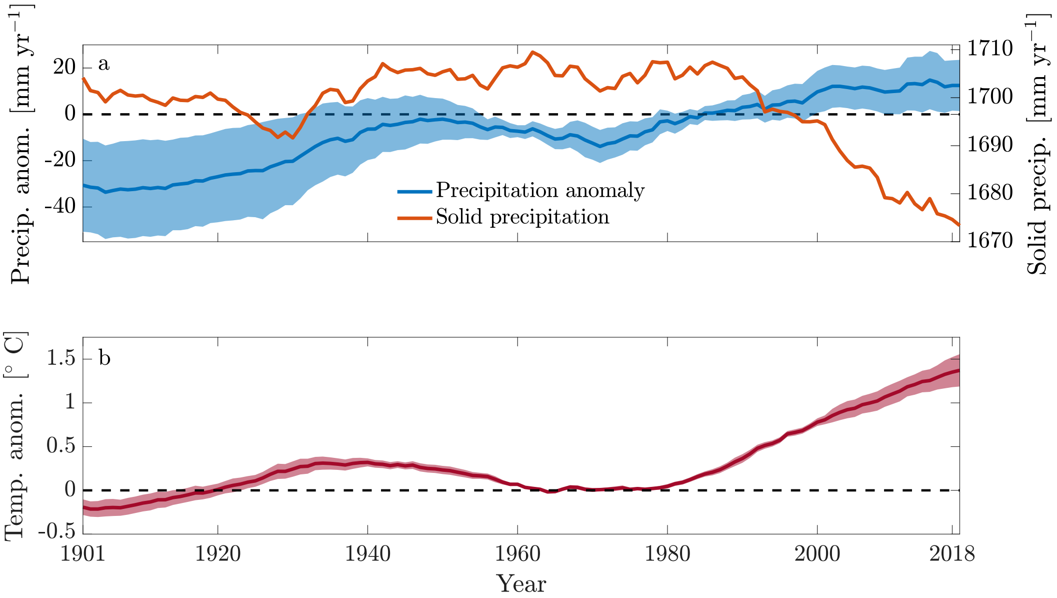

Figure 2.8: **(a)** Global mean annual precipitation anomaly relative to 1961–1990 and amount of solid precipitation. **(b)** Global mean annual temperature anomaly relative to 1961–1990. The shadings show $\pm 1\sigma$, i.e., standard deviation among meteorological forcing data sets. Values in both panels are 31-year moving averages of the ensemble mean at glacier tongue locations and weighted by glacier area, except for the graph of solid precipitation, which is based on the mean forcing input data. Since scales of computed solid precipitation might vary between ensemble members depending on model parameters (see Eqs. 2.3 and 2.4), the computation of an average, especially with a temporally varying number of ensemble members, is less meaningful. Values of the CERA20C forcing are excluded from the ensemble mean (see Sect. 2.3.1).

2.4 Discussion

Table 2.4 shows our global results compared to previously published estimates for mass change rates over certain periods. We mostly find good agreement within the respective uncertainty ranges. For the periods 2003–2009, 2002–2016, and 1992–2016 there is a significant disagreement between literature values and our model results. The disagreeing values for 2002–2016 from Wouters et al. (2019) were solely derived from gravimetry (GRACE) data. Estimates for 2003–2009 from Gardner et al. (2013) and for 1992–2016 from Bamber et al. (2018b) involve GRACE data as well. Interestingly, we find that when we compare the five pentads Bamber et al. (2018b) studied during 1992–2016 individually to our estimates, those for the first three pentads (when the GRACE mission had not yet started) agree within uncertainty ranges. Another work based on GRACE data (Jacob et al., 2012) estimated a mass loss of glaciers outside of Antarctica and Greenland for the period 2003–2010 of 0.41 ± 0.08, while our estimate for that period lies at 0.66 ± 0.08 and that of Gardner et al. (2013, for 2003–2009) at 0.59 ± 0.07. Part of these disagreements might be explained by the storage of meltwater for example in glacial lakes (Shugar et al., 2020), which because of the close proximity to the glaciers cannot be separated from the ice mass in gravimetry data. GRACE will therefore observe lower mass change values than in situ or geodetic observations. Since these lower values might be closer to the glaciers' actual contribution to sea-level rise, the issue points to the larger problem of distinguishing between glacier mass change and the corresponding sea-level change, which are not exactly equal. However, Shugar et al. (2020) also point out that glacial lake storage accounts for only about 1 % of glacier melt volume (excluding Greenland and Antarctica), which indicates that this process is of limited relevance. Other hydrological processes like groundwater flow or human activities (e.g., building of reservoirs) might still induce discrepancies between gravimetric and in situ/geodetic measurements. Another potential source of underestimating glacier mass loss by using gravimetry data in regions with many marine-terminating glaciers is the presence of discharged icebergs close to the glaciers that GRACE is presumably not able to separate from the actual glacier mass.

Gardner et al. (2013) point to discrepancies between satellite-derived and in situ estimates of glacier mass changes, suggesting a negative bias in in situ observations for regions where the density of those measurements is low. They hence only relied on in situ observations in regions where those have a high density. Zemp et al. (2019) addressed this issue as well by combining glaciological and geodetic measurements. Although our model is calibrated solely using in situ observations, its estimates are still close to Zemp et al. (2019), in which the uncertainty for some periods is admittedly large (Table 2.4). Comparing our results to Zemp et al. (2019) in periods where we included the Greenland periphery (2003–2009 and 1961–2010), we see a slightly lower agreement. Our estimates' uncertainty range also overlaps more with the one of Gardner et al. (2013) for 2003–2009 if we exclude that region. This indicates that our mass change estimates for the Greenland periphery might be too large in these time periods. We also included estimates from WGMS (2015) in Table 2.4, which are merely arithmetic averages of the available in situ (glaciological) and geodetic mass balance measurements to show that our estimates, although solely calibrated and validated with in situ measurements, are lower than those and closer to more thorough analyses of mass change data. Our estimates lying close to those of Marzeion et al. (2012) or Marzeion et al. (2015) cannot be explained merely by the fact that the same model was used. One reason for this is that we used newer and more validation data and a newer RGI version. Another one is the change in calibration strategy that we applied in this work (see Sect. 2.2.2). Furthermore, driven with other meteorological data, the Marzeion et al. (2015) mass loss estimates for 2003 to 2009 lie lower than ours when using the same model but a different calibration procedure, while those of Marzeion et al. (2012) lie higher (see Table 2.4). This underlines the influence of boundary and initial conditions on modeling results.

Finally, the global glacier sea-level rise contribution estimates of Frederikse et al. (2020), excluding the Greenland and Antarctic periphery, agree well with ours for the more recent time intervals they specify (1957–2018 and 1993–2018), while our estimates lie at the very low end of the confidence interval given for the whole time interval they studied (1900–2018). This is presumably due to the modeling approach that their estimates in early years rely on, which includes estimations of disappeared and missing glaciers that are not included in the RGI. The increase in global glacier mass loss estimations this causes declines throughout the 20th century by roughly 66 % (Parkes and Marzeion, 2018).

Regarding regional values, Table 2.3 shows that roughly two-thirds of our global mass loss estimate during 2006–2018 occurred in the Greenland periphery and the North American continent. A large amount of the global uncertainty originates from these regions as well. Comparing our regional mass change estimates for recent years to those in the literature (Ciracì et al., 2020; Wouters et al., 2019; Zemp et al., 2019), the most obvious discrepancy can be found in estimates for the Southern Andes, where our ensemble mean is substantially smaller and even positive in earlier periods shown in Table 2.3 (e.g., 1901–1940), caused mainly by the model setup forced with 20CRV3 reanalysis data. The opposite is true for the regions Arctic Canada (North) and Svalbard, where our estimate is larger than those previously published. This might be caused by the relatively large portion of area draining into marine-terminating glaciers in those regions, since glacier–ocean interactions are not included in the model we applied, and the calibration applying solely atmospheric forcing might thus be problematic. Moreover, our regional estimates for the Greenland periphery and Alaska in the most recent period (2006–2016) are close to each other, while Alaska lost significantly more mass according to Zemp et al. (2019) or Ciracì et al. (2020) during that time. This could be indicative of our mass loss estimates for Alaska being too small or those for the Greenland periphery being too high. Two regions for which our estimates are significantly larger than in the previously published literature are Central Asia and South Asia (West). This might be caused by a negative bias of the in situ measurements used for calibration and validation in this region.

Another region of interest is the Russian Arctic, for which no in situ measurements of annual specific mass balances were available in the data we used for calibration and validation. That is either because the sparse amount of measurements for that region was not covering at least 3 years for the individual observed glaciers or we did not find a link of the glaciers to the RGI. Also, more than half of the glacierized area in the Russian Arctic region drains into marine-terminating glaciers. For this region we estimate an average mass change rate of $0.08 \pm 0.02\,\mathrm{mm\,SLE\,yr^{-1}}$ during 2002–2016, while Wouters et al. (2019) estimate 0.03 ± 0.01 and Zemp et al. (2019) $0.07 \pm 0.03\,\mathrm{mm\,SLE\,yr^{-1}}$. Regarding the whole period that Zemp et al. (2019) provide estimates for in that region (1951–2016), the average they find is $0.05 \pm 0.02\,\mathrm{mm\,SLE\,yr^{-1}}$. Our average estimate for that period and region lies at $0.06 \pm 0.01\,\mathrm{mm\,SLE\,yr^{-1}}$. This shows that our model results do not, as is the case globally, agree well with GRACE-derived data in that region, but they still do with one other previously published estimate although we did not have calibration/validation data at hand in this region.

Thus, while we find an overall good agreement of our global mass change estimates with previously published ones, besides most of those derived with GRACE data, there are still significant differences in certain regional estimates. These require further research into the causes and hence point to potential model shortcomings as, for example, area initialization, geometric scalings, neglecting frontal ablation, debris cover, and radiation, as well as into the calibration and validation procedure applied. Incorporating frontal ablation processes of marine-terminating glaciers in the model and calibration procedure as well as distinguishing between mass loss above and below sea level would be crucial model developments for enhancing the reliability of modeled global glacier sea-level rise contribution estimates. Generally speaking, the influence of ice–ocean interaction on global glacier mass loss remains elusive, although one study that conducted global glacier mass change projections, applying a simple frontal ablation parameterization, estimated a total of ca. 10 % global glacier mass loss caused by frontal ablation (Huss and Hock, 2015).

Although the largest potential of reducing the global uncertainty relevant to sea-level rise estimates is in strongly glaciated but little observed regions (e.g., Greenland periphery), reducing it in less glaciated regions (e.g., Southern Andes) could still be valuable concerning hydrological changes and hence water availability. Future studies on mass loss reconstructions could benefit from addressing the abovementioned processes that are neglected thus far and from expanding the validation framework applied here in such a way that it would be able to include geodetic mass balance estimates as well as the uncertainties attached to in situ/geodetic reference data. This is because in situ measurements of annual specific mass balances are not only sparse and heterogeneously distributed but reportedly negatively biased in some regions (Gardner et al., 2013). Since geodetic measurements provide glacier mass change data for much larger areas than in situ glaciological measurements, they add considerably to our understanding of glacier mass change. Unfortunately, they are not yet standardized and readily available as the in situ data are, making it unpractical to use them in the validation framework we applied.

Concerning the high uncertainty of mass change estimates during the early 20th century, it would be beneficial to have a suite of models that are able to hindcast glacier changes over that period, similar to intercomparison efforts for projections (Marzeion et al., 2020). More reanalysis products covering that time interval and also the Antarctic periphery would certainly help to constrain global estimates and their uncertainty more, although this might be of limited value due to the lack of historical validation data. In order to not only rely on reanalysis data, it would also be possible to run the model with data of climate models' historical experiments. A comparison with results obtained by applying reanalysis data could bring valuable insights into how, why, and where reanalysis and climate model forcings of the mass balance model differ. Finally, the application of a robust initialization method (e.g., Eis et al., 2019, 2021) could help to understand if and how inaccuracies of the initialization method propagate through the modeled period.

Table 2.4: Different estimates for mean annual glacier mass change rates (in mm SLE yr^{-1}) over time periods given in the respective literature. Uncertainties at the 90 % level for all values except for Wouters et al. (2019) and Zemp et al. (2019), which are at the 95 % level. Estimates exclude the Greenland and Antarctic periphery; columns marked with [a] include Greenland periphery. Cells highlighted in bold font are published estimates disagreeing significantly with ours as discussed in Sect. 2.4. Results of the CERA20C forcing are excluded from the ensemble mean (see Sect. 2.3.1).

	1961–2016	1992–2016	2003–2010	2002–2016	2002–2018	2006–2016	1902–2010[a]	1961–2010[a]	2003–2009[a]	Data type
Ensemble mean	0.45 ± 0.06	0.60 ± 0.06	0.66 ± 0.08	0.72 ± 0.07	0.72 ± 0.07	0.76 ± 0.08	0.57 ± 0.22	0.46 ± 0.08	0.83 ± 0.10	Modeling
Ciracì et al. (2020)	–	–	–	–	0.78 ± 0.08	–	–	–	–	GRACE
Zemp et al. (2019)	0.4 ± 0.3	0.6 ± 0.1	0.6 ± 0.3	0.7 ± 0.2	–	0.7 ± 0.2	–	0.4 ± 0.1	0.8 ± 0.3	Glaciological & geodetic
Bamber et al. (2018b)	–	**0.48 ± 0.05**	–	–	–	–	–	–	–	Synthesis
Wouters et al. (2019)	–	–	–	**0.55 ± 0.09**	–		-	–	–	GRACE
WGMS (2015)	–	–	–	–	–	–	–	0.57	1.12	Glaciological
WGMS (2015)	–	–	–	–	–	–	–	0.85	1.05	Geodetic
Marzeion et al. (2012)	–	–	–	–	–	–	–	–	0.96 ± 0.12	Modeling
Marzeion et al. (2015)	–	–	–	–	–	–	0.62 ± 0.05	0.49 ± 0.05	0.78 ± 0.15	Modeling
Cogley (2009)[b]	–	–	–	–	–	–	–	0.54 ± 0.05	0.75 ± 0.07	Glaciological & geodetic
Leclercq et al. (2011)[b]	–	–	–	–	–	–	0.78 ± 0.19	0.58 ± 0.15	0.87 ± 0.64	Length observations
Gardner et al. (2013)	–	–	0.59 ± 0.07	–	–	–	–	–	0.70 ± 0.07	Synthesis
Jacob et al. (2012)	–	–	**0.41 ± 0.08**	–	–	–	–	–	–	GRACE

[a] Estimates include the Greenland periphery. [b] Updated in Marzeion et al. (2017).

2.5 Conclusions

A multi-objective optimization of a global glacier mass balance reconstruction model, forced with an ensemble of meteorological data sets, was presented. We demonstrated that it is possible to find statistically well performing sets of model parameters for each forcing data set but that we cannot robustly identify which model setup is the most reliable when applied outside of the temporal and spatial domain of available in situ mass balance validation data. However, one data set (CERA20C) can be identified as performing worse than the others. Disagreement between ensemble members is to a large degree attributable to differences in the forcing data in times and at locations where few validation and calibration data are available. The differences in the forcing data result in diverging glacier mass change estimates, especially in the first half of the 20th century, and thus are a major part of our ensemble estimates' uncertainty. Although our estimates lie within the uncertainty range of most of the previously published global estimates, they agree less with those derived from gravimetry (GRACE) data and show significant differences to the literature in individual regions. Our reconstruction ensemble average suggests that around the 1930s mass loss rates from glaciers were comparable to those of today. This finding is possibly weakened by the lack of an explicit mass-balance–surface-elevation feedback in the model we applied, and it might be that mass change rates during the 1930s were actually smaller than in recent years. According to our results, the increase in mass loss until the 1930s was followed by a phase of mass loss deceleration until roughly 1980. The glaciers' contribution to sea-level rise has been accelerating again since then, despite an indication of the their retreat to more favorable climatic conditions, i.e., higher altitudes. Our results also indicate that this acceleration was partly driven by decreasing amounts of solid precipitation at glacier locations from ca. 1980 onward. This implies that the enhanced atmospheric warming not only increased ablation rates but probably lowered the amount of snow the glaciers received, notwithstanding a slight increase in total precipitation.

2.A Appendix

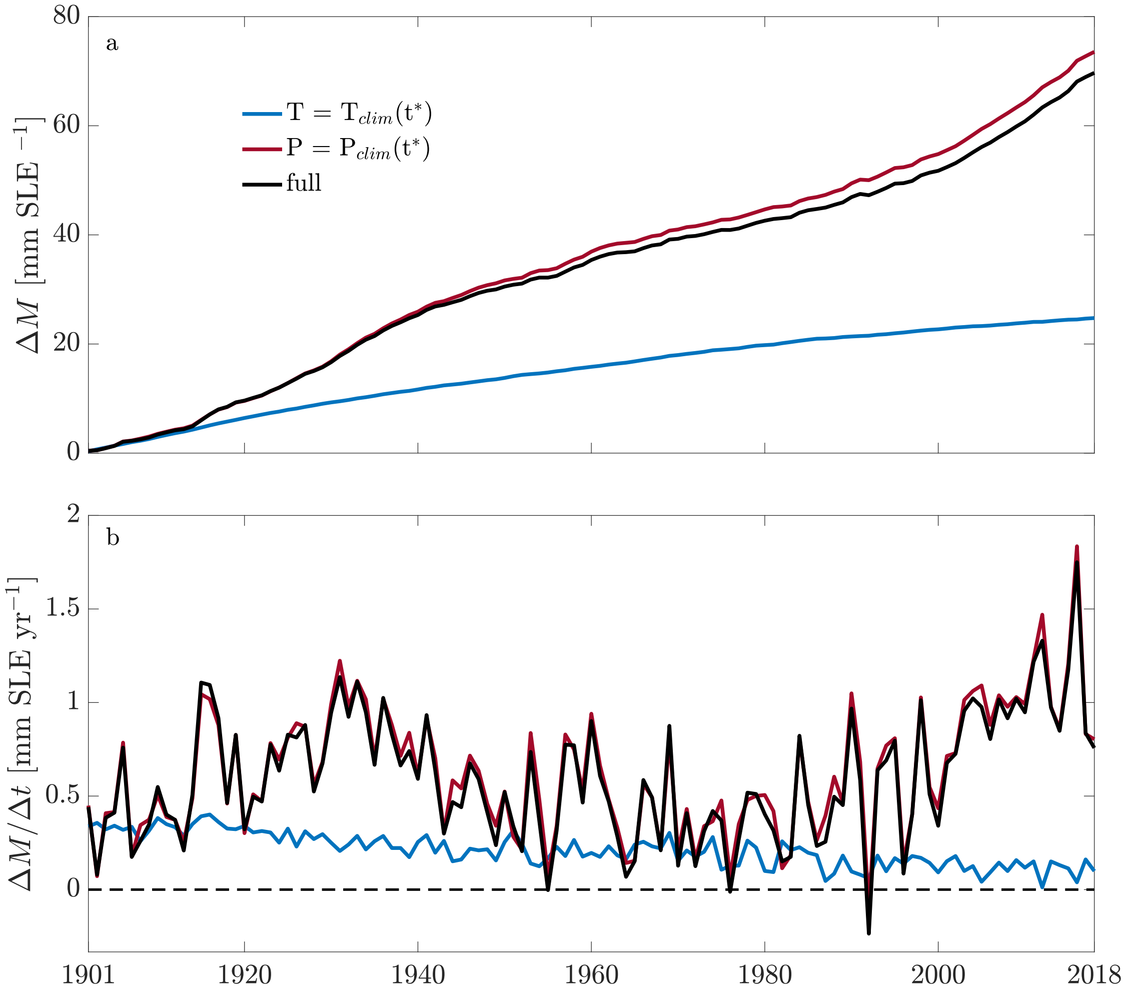

Figure 2.A.1: Estimated influence of temperature and precipitation anomalies on global glacier mass change. Blue lines are modeled glacier mass change with temperature held constant at the climatology around t^*. Red lines are modeled glacier mass change with total precipitation held constant at the climatology around t^*. Black lines represent the model run with full forcing. Note that in the case of this forcing data set we found optimal model performance with $t^* = 1901$, which implies the climatology only includes 16 years. **(a)** Estimates of GMSLR contribution relative to 1901. **(b)** Estimated annual GMSLR contribution.

Data availability

The reconstructed, optimized time series of area, mass, and mass change for the RGI regions, except Antarctic and Subantarctic, are available at PANGAEA: `doi:10.1594/PANGAEA.931657`. Global results on a 0.5° grid, excluding the aforementioned region, can be obtained by contacting the corresponding author.

Author contributions

JHM contributed to designing the research, conducted the simulations and statistical evaluation, and wrote the manuscript. BM designed the research and contributed to the manuscript.

Chapter 3

Context

As indicated in the previous chapter, neglecting frontal ablation and volume changes below sea level in the model calibration as well as in the glacier evolution model might lead to inaccuracies in model results, especially when trying to quantify glacier contributions to global mean sea level rise. Since the initialization of glacier evolution models that employ an explicit representation of ice dynamics, particularly for marine-terminating glaciers, cannot be routinely done yet for the time before the glaciers were recorded for in the RGI, it suggests itself to first tackle the issue of modeling marine-terminating glaciers in a forward-run dynamical glacier evolution model. While there has been some previous work on adapting the ice thickness inversion procedure in the Open Global Glacier Model (OGGM) for marine-terminating glaciers, the effect of including marine frontal processes in the model's calibration and dynamical evolution component has not been tested yet. This chapter describes an approach to tackling this issue by implementing more detailed descriptions of marine frontal processes in the model and using glacier-specific mass balance and frontal ablation estimates from satellite-derived data products for calibration. Model runs including this physically more plausible representation of marine-terminating glaciers are compared to such runs in which marine-terminating glaciers are treated equally to land-terminating ones throughout the modeling chain.

Exploring the impact of a frontal ablation parameterization on projected 21st-century mass change for Northern Hemisphere glaciers

Jan-Hendrik Malles[1,2], Fabien Maussion[3], Lizz Ultee[4], William Kochtitzky[5,6], Luke Copland[5], and Ben Marzeion[1,2]

[1]Institute of Geography, University of Bremen, Bremen, Germany
[2]MARUM - Center for Marine Environmental Sciences, University of Bremen, Bremen, Germany
[3]Department of Atmospheric and Cryospheric Sciences, University of Innsbruck, Innsbruck, Austria
[4]Department of Geology, Middlebury College, Middlebury, USA
[5]Department of Geography, Environment and Geomatics, University of Ottawa, Ottawa, Canada
[6]School of Marine and Environmental Programs, University of New England, Biddeford, USA

Abstract

Marine-terminating glaciers cover more than one-fourth of the total glacierized area in the Northern Hemisphere outside the Greenland Ice Sheet. It is therefore crucial to ensure an adequate representation of these glaciers when projecting large-scale glacier mass changes. We investigate how the introduction of marine frontal processes in the modeling chain influences the results of mass change projections, compared to projections neglecting such processes. We find that including frontal processes reduces the projected glacier mass loss, since incorporating frontal ablation in the model's mass balance calibration results in a decrease in marine-terminating glaciers' sensitivity to atmospheric temperatures. We also find that retrograde bed slopes lead to increased frontal ablation as the atmosphere warms, while frontal ablation decreases if bed slopes are prograde. These opposing effects have the potential to partly cancel each other when considering large glacier ensembles. Although we do not account for potential future changes in oceanic climate yet, any effect of these would be moderated by around half of today's marine-terminating glaciers becoming land-terminating in the course of the 21st century. While we find a significant influence of ice flow parameters on our results, boundary conditions remain the largest source of uncertainty in our projections.

3.1 Introduction

Earth's glaciers are rapidly losing mass, causing global mean sea level rise (GMSLR) and changing the hydrology of regions where they are part of the landscape (Zemp et al., 2019; Huss and Hock, 2018; Hugonnet et al., 2021). In regions where glaciers are located close to the ocean, their direct export of freshwater can substantially change the ocean's surface water properties and thus its local and regional circulation as well as ecology (Castro de la Guardia et al., 2015; Meire et al., 2017). Some glaciers are in direct contact with the ocean, often producing icebergs. These marine-terminating glaciers are special insofar as they do not only undergo mass changes due to atmospheric climate perturbations, but also by ice-ocean interaction processes taking place at the their front, such as iceberg calving and submarine melt (Straneo et al., 2013). The contact of marine-terminating glaciers' terminal boundary with ocean water also makes them subject to different ice flow dynamics compared to land-terminating ones. Overall, marine-terminating glaciers comprise more than one-fourth of the glaciated area in the northern hemisphere outside the Greenland Ice Sheet (RGI Consortium, 2017). Hence, they contain such a large amount of ice that their mass loss has the potential to intensify freshwater input to the oceans, thereby increasing GMSLR as well as triggering changes in circulation and ecological patterns. In order to understand and project regional and global glacier mass changes as well as their wider implications, it is therefore necessary to investigate processes occurring at marine-terminating fronts and to incorporate them in numerical models.

One example illustrating the need to include marine frontal processes comprehensively in a numerical glacier model is that neglecting frontal ablation in the surface mass balance model's calibration will result in overestimating marine-terminating glaciers' sensitivity to atmospheric temperatures. That is because geodetic observations, for instance, do not usually distinguish between surface and frontal ablation. Thus, if such data are used in the surface mass balance model's calibration and frontal ablation is not taken into account, it is implicitly assumed that all of the ablation takes places on the surface. Although the inclusion of frontal ablation in the dynamical model compensates part of the decrease in mass removal due to the lowering of sensitivities to atmospheric temperatures, the question arises whether there is a net effect of actually partitioning these two types of ablation.

Accounting for frontal processes does not only affect model projections, but model estimates of initial ice thicknesses as well (Recinos et al., 2019, 2021). Since ice volume cannot be measured at large scales, models constrained by observations are often used (Farinotti et al., 2009). Among these approaches, those relying on mass-conservation typically do not account for frontal ablation in the mass budget (i.e., not allowing for an ice flux through the glacier's terminal boundary), which results in a systematic underestimation of volumes of marine-terminating glaciers and their thicknesses at the front (Recinos et al., 2019).

So far only one effort to estimate the impact of frontal ablation on global glacier mass change projections has been undertaken, though not focusing on frontal dynamics (Huss and Hock, 2015). However, that work neglected some processes that might be important for modeling marine-terminating glaciers' volume evolution. Most prominent in this regard is ice dynamics, and particularly sliding, since marine-terminating glaciers' fronts can be sensitive to dynamic thinning at the front (McFadden et al., 2011). Additionally, Huss and Hock (2015) pooled frontal ablation and surface mass balance in their approach to estimate surface elevation changes, although the mass removal by frontal ablation acts horizontally at the glacier front, as opposed to vertical changes by surface melt.

Here, we use a numerical model capable of simulating ice dynamics in a simplified flowline fashion (Maussion et al., 2019). This approach allows the model to be run on a large number of glaciers using reasonable computing resources. We configure the model in such a way that it is able to capture important features of marine-terminating glaciers' behavior. For this purpose, we incorporated a frontal ablation parameterization (Oerlemans and Nick, 2005), water-depth dependent basal sliding, and the hydrostatic stress balance at the front into both the ice thickness inversion as well as the dynamical core. We then calibrate the model on a glacier-per-glacier basis for all glaciers in the Randolph Glacier Inventory (RGI; Pfeffer et al., 2014), disaggregating the total glacier mass budget into surface mass balance and frontal ablation, where applicable, using independent datasets for each. Thereby we are able to constrain the involved parameters for both mass budget parts separately.

Accounting for frontal processes in the modeling chain allows us to investigate the differences to model runs ignoring it. This is to get an impression of such processes' relevance for glacier mass change projections and to identify further development prospects for large-scale glacier models. We do so by running the modeling chain once without special treatment of marine-terminating glaciers, as was the standard setup of the model used previous to this work, and once including the aforementioned aspects of marine-terminating glaciers' dynamics. Furthermore, we examine the uncertainty in such findings caused by the variation of particular unknown parameters.

3.2 Numerical model

3.2.1 The Open Global Glacier Model

The Open Global Glacier Model (OGGM) is a flowline model capable of modeling large numbers of glaciers at once (Maussion et al., 2019). Due to the fact that it relies on certain (simplifying) assumptions, this model has a reasonable computational cost. Here, we give a brief overview of the model's functionality.

The RGI (RGI Consortium, 2017; Pfeffer et al., 2014) is the basis of OGGM, similar to several other global glacier models (Marzeion et al., 2020). In its recent version (RGI V6), the coordinates and outlines of ca. 210 000 glaciers worldwide, which are not connected to the ice sheets, are recorded. The glacier outlines are projected onto a local gridded map for each glacier. Topographical data, based on an appropriate digital elevation model (DEM), is automatically retrieved depending on the glacier's location and interpolated onto the local grid. The grid's spatial resolution is scaled to the square root of the glacier area, with a maximum of 200 m and a minimum of 10 m. Here, we use single, binned elevation-band flowlines, based on the approach described by Werder et al. (2020). Dynamical simulations start at the date a glacier was recorded in the RGI. The initial geometry consists of the surface area given by the RGI, and the result of the ice thickness inversion, which will be described in Section 3.2.4. Simulations before the RGI date are only possible with fixed geometries, since it is generally not possible to find glacier states before the RGI date without large computational effort (Eis et al., 2019, 2021).

The gridded meteorological data set (monthly temperature and precipitation) is interpolated to the glacier location in a nearest-neighbour manner. For this work the Climatic Research Unit Time-Series dataset version 4.03 (CRU TS 4.03; Harris et al., 2020) is used. The temperature is subsequently corrected using a globally fixed linear lapse rate (6.50 °C/km). For precipitation we do not apply a lapse rate, but a global correction factor (see below). A glacier's monthly surface mass balance for grid point i at elevation z_i is then calculated at each of the flowline's grid points as:

$$m_i(z) = f_p P_i^{solid}(z) - \mu \; max(T_i^m(z), 0) \tag{3.1}$$

where f_p is a dimensionless precipitation factor (Giesen and Oerlemans, 2012a), $P_i^{solid}(z)$ the solid precipitation (in millimeter water equivalent (mm w.e.)) that is calculated assuming threshold temperatures for solid and liquid precipitation, μ the surface temperature sensitivity (in mm w.e. K^{-1}), and $T_i^m(z)$ the temperature above the threshold for ice melt at the glacier surface (in K). In Section 3.3.2 we will further elaborate on the calibration of μ and other involved parameters. Former versions of OGGM relied on an interpolation approach for the surface mass balance calibration, since observational data was sparse and not available on every single glacier, but we are now able to calibrate on a glacier-per-glacier basis (see Section 3.3). In the following sections we will describe the formulation of ice dynamics and ice thickness inversion in greater detail, since these two aspects of the model were subject to the most changes from Maussion et al. (2019) in this work.

3.2.2 Modulation of the shallow ice approximation for terminal cliffs

In OGGM, the thickness-averaged deformation velocity u_d of a glacier, utilizing the shallow ice approximation (SIA), is computed as follows:

$$u_d = \frac{2A}{n+2} h \tau^n \tag{3.2}$$

where A is the temperature-dependent ice creep parameter (here we use the default value of 2.4 x 10^{-24} s^{-1} Pa^{-3}), n the exponent of Glen's flow law (here we use $n = 3$), h the ice thickness (in meters), and τ the basal shear stress (in Pascal), which can be approximated as follows:

$$\tau = \rho g h \alpha \tag{3.3}$$

where ρ is the ice density (here we use 900 kg m^{-3}), g the gravitational acceleration (9.81 ms^{-2}), and α the surface slope computed numerically along the flowline on a staggered grid:

$$\alpha = \frac{z_i - z_{i+1}}{\Delta x} \tag{3.4}$$

where z_i is the surface elevation of that grid cell (in meters), and Δx the size of the grid that is defined on the glacier (in meters).

Equation 3.4 indicates that α can become arbitrarily large at a glacier's terminus, if there is a discontinuity of the ice thickness. This situation occurs in the presence of a terminal cliff. For a glacier whose thickness decreases smoothly to zero towards the terminus, velocity at the terminus is mostly very small, since the ice thickness (h) and the surface slope (α) are small. Hence, the SIA, conveyed here in Equations 3.2 and 3.3, holds well and a change in Δx will essentially not affect the dynamics at the glacier front. However, for a marine-terminating glacier with a terminal cliff, the grid size dependency can be noticeable, since a halving of Δx will result in an eight-fold increase in velocity (see Equations 3.2 - 3.4), with ice thickness at the terminus not being negligibly small. In that case, the higher stress would be distributed over a smaller volume of the glacier as well, as it only acts on the last grid cell in the SIA formulation we applied. To tackle these issues of large changes in the stress balance when modeling glaciers with a terminal cliff, we introduce the hydrostatic pressure balance at the terminal boundary of a marine-terminating glacier as an additional force F_H governing frontal dynamics, similar to the approach of Howat et al. (2005). This additional force (per unit width) can be calculated as:

$$F_H = \frac{1}{2} g(\rho_i h_f^2 - \rho_o d_f^2) \tag{3.5}$$

where h_f is the thickness of the glacier front, ρ_i the density of ice (as above), ρ_o the density of ocean water (here we use 1028 kg m^{-3}), and d_f the water depth at the glacier front (in meters). The additional force is then distributed over a distance (L_F) inland. In order to emulate that this force acts more strongly at the boundary than further upstream, we apply the following weight w_{i_L} for grid cells within L_F:

$$w_{i_L} = \frac{2i_L}{n_L + 1} \tag{3.6}$$

where i_L is a grid cell within the n_L grid cells contained in L_F, and for the first grid cell inland $i_L = n_L$. Then the stress that is thereby added to the driving stress τ (see Equation 3.3) at grid cell i_L is:

$$\tau_H = w_{i_L} \frac{F_H}{L_F} \tag{3.7}$$

Hence, the mean additional stress is:

$$\overline{\tau_H} = \frac{F_H}{L_F} \tag{3.8}$$

and it is ensured that:

$$\sum_{i_L=1}^{n_L} w_{i_L} \frac{F_H}{L_F} \Delta x = F_H \tag{3.9}$$

This formulation allows for application of the SIA on marine-terminating glaciers with a terminal cliff, but a surface slope is still needed for computing the average velocity through the boundary of the last grid cell (see Equations 3.2 and 3.3). We approximate it simply as the mean slope over L_F from the front inland. Our approach introduces L_F as a new parameter, similar to a stress coupling length (Enderlin et al., 2016a), which is hard to constrain for individual glaciers. Although theoretically there is a dependence on a glacier's ice thickness at the front, we set it to 8 km for all glaciers here. The motivation for this choice is that this value should be higher than the roughly 4 to 6 ice thicknesses found by Enderlin et al. (2016a), ensuring numerical stability in all cases. If a glacier's length (L) is smaller than 8 km, $L_F = L$. Note that it would be possible in our approach to also include sea-ice or ice mélange backpressure in Equation 3.5 (Robel, 2017), but we chose to neglect this here for simplicity. Note also that Equation 3.6 implies a linearly decreasing additional stress upstream of the glacier front. It would be possible to change this to some kind of non-linear weighting function, if such was found to better represent the physics of the process, which we do not examine closer here. Furthermore, it should be noted that we used a different approach to incorporating the hydrostatic stress imbalance than previous works (e.g., Nick et al., 2009; Enderlin et al., 2013b). In our case the hydrostatic stress imbalance is integrated over the glacier-water boundary to get the additional driving force, which is then distributed over a distance upstream and added to the driving stress of the shallow ice approximation. In the cases of aforementioned previous works, the authors integrated the momentum-conservation equations to find a velocity gradient. Those works used the Nye-Glen rheology to directly calculate the gradients in longitudinal stress needed for their approach from the hydrostatic pressure difference at the calving face.

3.2.3 Sliding parameterization

At a marine-terminating glaciers' front, the ice velocity induced by sliding is a relevant part of the dynamics (Benn et al., 2007a). Previously, the sliding velocity in OGGM was calculated as:

$$u_s = \frac{f_s \tau^n}{h} \tag{3.10}$$

where f_s is a sliding parameter (default value 10^{-20} m^2 s^{-1} Pa^{-3}), based on Oerlemans (1997). This parameterization follows the assumption that sliding is related to basal pressure, which itself is related to the ice thickness h. Basal pressure at the front of marine-terminating glaciers is not only related to the ice thickness though, but to the water depth of the glacier's bed as well. Therefore, we now calculate the sliding velocity as:

$$u_s = \frac{f_s \tau^n}{h^*} \tag{3.11}$$

where h^* is the height above buoyancy:

$$h^* = h - \frac{\rho_o}{\rho_i} d \tag{3.12}$$

Hence, sliding for all grid cells with a bed elevation above the water level will be the same as in Equation 3.10. For grid cells close to the front, the sliding velocity can sometimes become too large when using the value for f_s proposed by Oerlemans (1997) (5.7 x 10^{-20} m^2 s^{-1} Pa^{-3}) in Equation 3.11, resulting in numerical instabilities. Therefore, we use that value as an upper bound in the attempt to quantify parameter sensitivity in appendix 3.B, and apply a value of 10^{-20} m^2 s^{-1} Pa^{-3} here. Although this formulation might be an improvement for marine-terminating glaciers, the appropriate sliding parameterization for ice flow is generally still not ascertained (Benn et al., 2007a; Zoet and Iverson, 2020; Stearns and Van der Veen, 2018).

3.2.4 Ice thickness inversion

For consistency, the changes to OGGM explained in the previous sections do not only need to be incorporated into the dynamical model core, but into the ice thickness inversion as well. That means we now numerically solve for the ice thickness by the following polynomial:

$$q = \frac{2A}{n+2}(f_\tau \tau)^n h^2 + f_s (f_\tau \tau)^n r_h \tag{3.13}$$

where q is the ice mass flux per unit width (in m^2 a^{-1}), f_τ an amplification factor related to the additional driving stress caused by the hydrostatic stress balance at the front (see Section 3.2.2, Equation 3.7):

$$f_\tau = \frac{\tau_H}{\tau} + 1 \tag{3.14}$$

and r_h the inverse of the relative height above buoyancy:

$$r_h = \frac{h}{h^*} \tag{3.15}$$

For grid cells that are more than L_F (see Section 3.2.2) upstream of the front and that do not have a bed elevation below the water level, this equals the ice thickness inversion approach usually applied in OGGM, because f_τ and r_h equal one.

A further peculiarity of marine-terminating glaciers that needs to be taken into account here is the occurrence of frontal ablation. We parameterize the latter following Oerlemans and Nick (2005):

$$Q_f = k d_f h_f w_f \tag{3.16}$$

where Q_f is the frontal ablation flux (m^3 a^{-1}), k the water-depth sensitivity parameter (a^{-1}; hereafter named frontal ablation parameter), and d_f, h_f, and w_f are the water depth, ice thickness, and width at the glacier front (all in meters). As introduced to OGGM by Recinos et al. (2019), the mass budget closure requires Q_f to be balanced by ice discharge, which is the dynamical ice flux through the terminal boundary of the inverted glacier. That, in turn, implies a larger ice thickness at the glacier's terminus compared to an inversion neglecting frontal ablation, assuming the same ice flow parameters (see Equation 3.13). Although simple and thus readily applicable, this frontal ablation parameterization is limited insofar as it does not explicitly capture physical processes, but lumps them into one parameter (k). The two main processes relevant in that regard are brittle fracturing and submarine melt, which is related to ocean/water temperatures and subglacial discharge. Note that our framework is also not capable of capturing sediment dynamics and hence the time evolution of proglacial submarine moraines that might influence frontal dynamics/ablation (see, e.g., Brinkerhoff et al., 2017; Oerlemans and Nick, 2006).

One further change compared to previous studies on the ice thickness inversion of marine-terminating glaciers is that we neither assume the water level to necessarily be at 0 m a.s.l., nor prescribe the freeboard to be within a range of 10 to 50 m (Recinos et al., 2019, 2021). This change is motivated by several factors: i) the DEMs used can be erroneous, ii) the RGI outlines can be erroneous and the incorrect geometry (i.e., width) at the front derived from these outlines for the elevation-band flowlines can deteriorate the result of the ice thickness inversion, iii) the assumed values for the flow parameters (A, f_s) in Equation 3.13 and the frontal ablation parameter (k in Equation 3.16) are uncertain and thus the water level may have to be shifted in order to satisfy Equation 3.16 and find a solution for Equation 3.13, and iv) a maximum freeboard of 50 m would mean that ice thicknesses at the front could not exceed roughly 400 m without going into flotation. However, dealing with floating tongues would involve shelf dynamics, which we cannot model using the SIA without special treatment and a refined grid at the front (Vieli and Payne, 2005). Therefore, we inhibit glacier states that feature a floating tongue. Thus, we do not directly seek for a water depth at the front, which ensures that the ice flux given by the frontal ablation parameterization equals that of the apparent mass balance and ice dynamics, but for a value of r_h (Equation 3.15) as explained below. By doing so, we can make sure that the ice thickness inversion never results in a floating tongue, and with a value for the freeboard this can be translated into the frontal ice thickness:

$$h_f = \frac{\frac{\rho_o}{\rho_i} r_h (z_f - z_w)}{r_h(\frac{\rho_o}{\rho_i} - 1) + 1} \tag{3.17}$$

where z_f is the surface elevation of the last grid cell according to the DEM used, and z_w the water level (all in meters). If the initial guess for the freeboard (i.e., z_w = 0 meters above sea level) results in an error of the numerical solver, we shift the water level until the algorithm successfully finds a value for r_h and thereby for h_f. Tuning of the initial freeboard estimate means that we could calculate different water levels for the same glacier for different values of the flow parameters (A, f_s), and the frontal ablation parameter (k). Here it should be noted that a shift of the water level does not imply a shift of the surface elevations recorded in the DEM. It is merely a numerical attempt to allow for the compensation of inconsistencies, which may arise from model approximations and errors/uncertainties in the observational data. Thereby we are able to ensure a consistent solution of the ice thickness inversion for every glacier with any given set of parameters. For the majority of glaciers shifting the water level is not necessary and if it is, the shift is often relatively small (less than 100 m in 90 % of the cases).

3.2.5 Frontal ablation in the dynamical model

We apply the same frontal ablation parameterization in the dynamical model as in the ice thickness inversion procedure (see above section). Since frontal ablation does not act vertically, as surface melt does, one has to decide how to remove the volume calculated with Equation 3.16 from the gridded glacier in a time stepping scheme. For that, we use two reservoirs: one is the temporally accumulated frontal ablation flux (Q_f) and the other one is the temporally accumulated ice flux through the terminus cross-section (Q_t). Note that here, unlike in Equation 3.16, $Q_f \neq Q_t$, for in the dynamical model we do not assume a steady state situation. Then, in every time step we remove the accumulated Q_f from the accumulated Q_t. If the remaining Q_f is still large enough, entire grid cells can be removed from the front. Vice versa, if $Q_f < Q_t$ over a certain time interval, the accumulation of Q_t can lead to an advance of the glacier. Furthermore, if the thickness of one or more grid cell(s) falls below flotation in a certain time step, the part of this volume which is contained in grid cells beyond the one adjacent to the last grid cell above flotation is removed and added to the frontal ablation output variable. That is in order to prevent shelf dynamics (see above). Because most marine-terminating glaciers outside of the ice sheets do not have a floating tongue anymore (Copland and Mueller, 2017), we do not anticipate that neglecting shelf dynamics will have significant influence on our results. For future model developments it might be considered to incorporate stress-related criteria, linked to the findings of Bassis and Walker (2011), to confine the height above buoyancy in the ice thickness inversion and dynamical model.

3.3 Data and calibration

3.3.1 Data

Mass change above sea level

We use the mass changes estimates for each glacier in the RGI over the years 2010 - 2020 provided by Hugonnet et al. (2021). Since reanalysis data of meteorological conditions are available over the same time period, it is possible to calibrate surface mass balance models for each glacier individually. The data of Hugonnet et al. (2021) is based on computing differences in the surface elevations of glaciers, derived from digital elevation models (DEMs), between different points in time. However, it does not include any mass changes occurring below sea level, since the satellite data it is based upon can only detect changes above the water line. This is problematic for estimating total mass changes and when calibrating models of marine-terminating glaciers, because part of the mass budget would be disregarded, if it is not corrected for.

Frontal ablation and mass change below water-level

We use the satellite-derived data from Kochtitzky et al. (2022) for estimating mass changes below sea level and to obtain frontal ablation estimates. Doing so is necessary to prevent an erroneous calibration of the surface mass balance model described above (Section 3.2.1), which will be further elaborated on in Section 3.3.2. The necessity of using mass changes below sea level in addition to frontal ablation estimates arises from the fact that frontal ablation estimates include the mass change below sea level, while the Hugonnet et al. (2021) data is not able to capture it, which would lead to inconsistencies.

The dataset given by Kochtitzky et al. (2022) is largely derived from satellite observations of velocity, glacier area, and observed and modeled ice thickness. It does not include estimates for the southern hemisphere and lake-terminating glaciers. We thus solely focus on marine-terminating glaciers (outside the Greenland Ice Sheet) in the northern hemisphere. Moreover, we exclude the Flade Isblink Ice Cap from our work here, because it possesses problematic outlines in the RGI and a floating tongue, which we are currently not able to model with OGGM (Möller et al., 2022; Recinos et al., 2021). As it also contains a lot of ice, we rather neglect it here than largely distort our (regional) results by modeling it erroneously. We acknowledge that there are some smaller glaciers with a floating tongue in far northern Canada and Greenland, but their impact on our results should be minor, as their ice volume is small (Copland and Mueller, 2017) and many floating tongues have collapsed in the last few decades (Kochtitzky and Copland, 2022; White and Copland, 2019).

Atmospheric forcing data

The temperature and precipitation data needed as boundary conditions for the surface mass balance model are taken from the CRU TS 4.03 dataset for historical runs (from the RGI record date of a glacier until 2020) and from different general circulation models (GCMs) from the CMIP6 archive for projections (Eyring et al., 2016). In order to avoid potential step changes in the atmospheric forcing when switching from the reanalysis data to GCM output data, OGGM features a function that adjusts the GCM data based on its bias to a climate period in the historical data (here we used 1981 to 2018). A list of used GCMs, and for which scenarios they provide data, is given in Table 3.A.1. The CRU TS dataset has a spatial resolution of 0.5°, and the range of the GCM ensemble's spatial resolution is 0.75° to 2.0°. As calibrating the surface mass balance parameterization is done for the years 2010 - 2020 (see Section 3.3.2), the CRU data is used for that purpose as well.

3.3.2 Calibration

Calibration of surface mass balance

The arrival of abundant satellite-derived data for glaciers worldwide offers the new possibility to calibrate glacier-specific parameters without the need to interpolate for glaciers with no observational data, or use regionally aggregated values (as, e.g., in Huss and Hock (2015), Radić et al. (2014), or Marzeion et al. (2012)). Since we have observational values as well as meteorological data from reanalysis now for each individual glacier, the sensitivity to atmospheric temperatures in the temperature index surface mass balance model of OGGM (see Equation 3.1) can be approximated as follows:

$$\mu = (f_p P_{solid} - \frac{\Delta M_{awl} + C + f_{bwl}\Delta M_f}{A_{RGI}})\frac{1}{T_m} \tag{3.18}$$

where:

- ΔM_{awl} is the observed annual mass balance above sea level of a glacier (mm^3 a^{-1}) as given by Hugonnet et al. (2021),
- C is the observed annual frontal ablation rate of a glacier as given by Kochtitzky et al. (2022) (mm^3 a^{-1})
- ΔM_f is the observed annual rate of mass change due to area changes in the terminus region of a glacier (mm^3 a^{-1}; hereafter named retreat volume) as given by Kochtitzky et al. (2022)
- f_{bwl} is the assumed fraction of ΔM_f occurring below the waterline
- A_{RGI} is the glacier surface area of a glacier as given by the RGI (mm^2)
- T_m is the annually accumulated temperature above the threshold for ice melt at the glacier surface (K a^{-1})

The second term in the brackets consequently represents the observed specific surface mass balance, and $f_{bwl}\Delta M_f$ the mass balance below sea level (ΔM_{bwl}). Note that our convention assigns positive frontal ablation to the case of mass removal, and we neglect the case of a positive frontal mass budget in the calibration as well as in the dynamical model.

As indicated in Section 3.2.1, the value of μ in Equation 3.18 depends on the global parameter values chosen for f_p (2.5), the threshold temperatures for liquid/solid precipitation (2/0 °C), and the threshold temperature for ice melt (-1 °C). Here, we adopted parameter values that were previously derived from a leave-one-glacier-out cross-validation procedure with annual in-situ mass balance measurements (Maussion et al., 2019). Because the data of Hugonnet et al. (2021) has large uncertainties associated with it for annual values of individual glaciers, it makes most sense to use an average over longer time intervals, although it is not possible to constrain interannual variability in that way. Here we use the time period 2010 to 2020. The motivation for this is the assumption that most of the recording dates in the RGI lie before that interval and thus potential spin-up effects caused by assumptions in the ice thickness inversion procedure are attenuated (see Section 3.5.3). We also ignore the fact here that the uncertainty for longer time intervals given by Hugonnet et al. (2021) can nevertheless be quite large for individual glaciers, since we focus on large spatial scales and thus assume that uncertainties of individual glaciers will, at least partially, cancel each other out.

We use estimates of mass changes due to changes in the terminus area as well as of mean frontal ablation rates (ΔM_f, and C in Equation 3.18), given by Kochtitzky et al. (2022) for the time interval 2010 to 2020, for each marine-terminating glacier in the northern hemisphere outside the Greenland Ice Sheet (see Section 3.3.1). Hence, we can adjust the Hugonnet et al. (2021) data by assuming that 75 % of the mass change in the terminus area happens below sea level and adding it to the mass balance ($f_{bwl} = 0.75$ in Equation 3.18). Although the assumption of 75 % is arbitrary, this part of the total northern hemisphere's glacier mass budget is only roughly one-fifth of the total frontal ablation (see Table 3.1), and thus a change from 75 % to, for instance, 87.5 % (flotation), will presumably not make a large difference. We investigate the implications of that assumption further in appendix 3.B.

Calibration of frontal ablation parameterization

In order to disaggregate the total mass change of marine-terminating glaciers, we do not only calibrate the surface mass balance, but the frontal ablation parameter (k in Equation 3.16) as well. For this, we take satellite-derived estimates of the average frontal ablation rates over the years 2010 to 2020 (see Section 3.3.1). We use an iterative procedure which seeks for a value of k that produces a frontal ablation estimate over this time interval within the uncertainty bounds of the frontal ablation data used. During that procedure, we use the same value for k in the ice thickness inversion and a subsequent (historical) dynamical run, which is forced with CRU TS 4.03 meteorological reanalysis data.

3.3.3 Setup of model runs

Here we briefly describe how we set up the different types of projections compared in the Results. For the projections including frontal processes of marine-terminating glaciers, we first calibrate the glaciers' sensitivity to atmospheric temperatures (μ in Equations 3.1 and 3.18) and then the frontal ablation parameter (k in Equation 3.16) as explained in the previous section. Following that we apply the ice thickness inversion procedure and run the model for a historical period starting at the individual glacier's RGI recording date and ending in 2020 with CRU TS 4.03 data as atmospheric boundary conditions. From there we switch to the individual members of the GCM ensemble given in Table 3.A.1 as the source of atmospheric boundary conditions and run the model for each member until 2100. The projections we compare these to are conducted in a similar manner, but exclude C and $f_{bwl}\Delta M_f$ in Equation 3.18 in the μ calibration. Furthermore, in these runs we neither include frontal ablation in the ice thickness inversion nor in the forward runs. This means that in those projections marine-terminating glaciers are treated as if they were land-terminating, and thus like in previously published OGGM projections. For results labeled *northern hemisphere*, the model is run for the RGI regions 1 to 15.

3.4 Results

3.4.1 Calibration / Ice thickness inversion

Inspecting the observational estimates of the frontal mass budget used for the calibration given in Table 3.1, it is visible that most of the frontal ablation occured in Svalbard and the Russian Arctic. Although roughly 66 % of the estimated frontal ablation between 2010 and 2020 occurred there, Svalbard and the Russian Arctic account for only 39 % of the marine-terminating glacier area considered here and for 38 % of the number of marine-terminating glaciers in the northern hemisphere (n in Table 3.1). In contrast, Arctic Canada North covers around 35 % of the marine-terminating glacier area, but accounts for only 16 % of the number of marine-terminating glaciers and for only 8 % of the annual frontal ablation. Roughly 20 % of the northern hemisphere's frontal ablation was observed in Alaska, but that region only accounts for 3 % of the marine-terminating glaciers and covers only 7 % of the marine-terminating glacier area. In contrast to Alaska, the Greenland periphery shows a high count of marine-terminating glaciers, and percentage of the region's volume contained in these (36 % and 37 %), while only accommodating 6 % of the northern hemisphere's frontal ablation. Despite marine-terminating glaciers containing 8 %, and 14 % of the ice volume in Arctic Canada South, and Iceland, respectively, the total amount of frontal ablation in these two regions is so small that we neglect them in the further analysis. Table 3.1 additionally shows that in most regions, between 23 and 33 % of all marine-terminating glaciers contribute 90 % of the regions' total frontal ablation. Only in Alaska is this number notably lower at 15 %. For the whole northern hemisphere this value is also less then 20 %, illustrating that most of the findings that will be discussed in the following sections are caused by a rather small number of glaciers.

Table 3.2 displays the results of the frontal ablation parameterization's calibration and the ice thickness inversion. The highest percentage of estimated regional ice volume stored in marine-terminating glaciers is found in Svalbard and the Russian Arctic, also where most of the northern hemisphere frontal ablation was observed. In most regions the area-weighted average of the frontal ablation parameter (k) lies between 0.15 and 0.63; the only region (besides Iceland) that markedly falls out of this range is Alaska. This might point to the high turnover of Alaskan glaciers, since in Svalbard and the Russian Arctic we found much smaller values for k, but the reduction of the temperature sensitivity is quite similar; another hint at this is the rather high frontal ablation but low retreat volume per glacier given in Table 3.1. In some individual regions (e.g., Greenland periphery) and the whole northern hemisphere, the area-weighted standard deviation of k is larger than the average, which indicates rather heavy-tailed distributions, since k cannot be negative. The same can be seen for the reduction of glaciers' melt sensitivities to atmospheric temperatures ($\Delta\mu_{mt}$).

Furthermore, Tables 3.1 and 3.2 show that the regions with the largest observed frontal ablation rates also exhibit the largest (i) increases in computed volume and (ii) reductions in sensitivities to atmospheric temperatures when the inversion and calibration account for frontal ablation. These changes are attenuated by the frontal volume lost during retreat. As we assume that 75 % of ΔM_f happens below sea level for marine-terminating glaciers and is hence not captured by the data of Hugonnet et al. (2021), we add a corresponding amount to the total mass budget (Section 3.3.2 as in Equation 3.18). Therefore, if the difference between the absolute value of retreat volume and total frontal ablation (per glacier) is low, the reduction of the surface temperature sensitivity will be rather low. Accordingly, a higher reduction in sensitivity to atmospheric temperatures will allow for more additional ice flux (due to less surface melt) and thus result in more ice volume in the ice thickness inversion.

Our calibration routine succeeds for most of the glaciers (n = 1322 out of 1367). Table 3.2 also shows that in most regions the bias and root mean squared error (RMSE) are low. The bias is smaller than 5 % and the RMSE below 1 % in most regions. An unsuccessful calibration can be either caused by model errors on a glacier (n = 3), or an irreducible difference between the modeled and the observed frontal ablation being higher than the estimated uncertainty of the calibration dataset. The latter case can be caused by erroneous RGI outlines and/or DEMs yielding erroneous frontal geometries. Otherwise, erroneous calibration data, or the application of inadequate parameter values (e.g., for the precipitation scaling factor or flow parameters) could inhibit a realistic modeling of the affected glaciers, leading to a failing calibration. Seeing that on the hemispheric scale the bias is 2 % and the RMSE is close to that of the calibration dataset provides some confidence in the reliability of the results.

Table 3.1: Mass budget components of marine-terminating glaciers as annual mean values over the years 2010 - 2020 estimated for different RGI regions and the northern hemisphere given by Kochtitzky et al. (2022) (see Section 3.3.1). ΔM_f is the mass change due to area changes at the glaciers' fronts (retreat volume), C the estimated annual frontal ablation used for model calibration, A_{mt} the marine-terminating glacier area in the region given by the RGI, and n the number of marine-terminating glaciers in that region. The number of glaciers with the largest observed frontal ablation rates, together contributing 90 % of the regions' total frontal ablation, are given in brackets after n.

Region	ΔM_f (Gt a^{-1})	C (Gt a^{-1})	A_{mt} (10^3 km^2)	n
01 Alaska	-0.89 ± 0.04	10.68 ± 0.02	10.2	40 (6)
03 Arctic Canada North	-2.03 ± 0.07	4.28 ± 0.02	49.2	225 (52)
04 Arctic Canada South	-0.06 ± 0.01	0.088 ± 0.002	3.1	86 (24)
05 Greenland periphery	-1.30 ± 0.05	2.880 ± 0.006	21.6	492 (128)
06 Iceland	-0.03 ± 0.03	0.03 ± 0.04	1.1	1 (1)
07 Svalbard	-2.40 ± 0.19	16.81 ± 0.04	21.8	163 (43)
09 Russian Arctic	-4.86 ± 0.18	16.92 ± 0.03	32.4	360 (120)
Northern hemisphere	-11.6 ± 0.22	51.68 ± 0.02	139.4	1367 (239)

Table 3.2: Results of the frontal ablation parameterization's calibration and ice thickness inversion for different RGI regions and the northern hemisphere. A_{mt} is the percentage of regional area covered by marine-terminating glaciers according to the RGI, V_{mt} the estimated percentage of volume contained in marine-terminating glaciers, ΔV_{mt} the change in volume of marine-terminating glaciers due to including frontal ablation in the ice thickness inversion, $\Delta\mu_{mt}$ the average and 1-σ standard deviation (weighted by surface area) of the change in the glaciers' melt sensitivities to atmospheric temperatures due to including frontal ablation and retreat volume in the surface mass balance calibration, k the average and 1-σ standard deviation (weighted by surface area) of the frontal ablation parameter, bias the mean difference to the observational estimates of annual frontal ablation, and RMSE the root mean squared error of the modeled frontal ablation with respect to the calibration dataset. Note that values were computed using the *default* parameter values in Table 3.B.1 and exclude the Flade Isblink ice cap.

Region	A_{mt} (%)	V_{mt} (%)	ΔV_{mt} (%)	$\Delta\mu_{mt}$ (%)	k (a^{-1})	Bias (Gt a^{-1})	RMSE (Gt a^{-1})
01 Alaska	11.8	15.6	15.1	-38 ± 29	3.02 ± 2.44	0.24	0.04
03 Arctic Canada North	46.8	58.8	2.2	-8 ± 18	0.15 ± 0.14	0.03	0.01
04 Arctic Canada South	7.6	8.0	0.7	-1 ± 1	0.43 ± 0.64	0.00	0.09
05 Greenland periphery	26.4	36.8	3.8	-8 ± 13	0.63 ± 1.09	-0.14	0.003
06 Iceland	9.7	13.5	0.0	-0.1 ± 0	0.01 ± 0.00	0.30	0.3
07 Svalbard	64.1	77.9	16.0	-32 ± 29	0.39 ± 0.36	-0.99	0.04
09 Russian Arctic	62.9	67.8	16.9	-38 ± 27	0.29 ± 0.26	-0.52	0.02
Northern hemisphere	26.3	41.0	8.6	-21 ± 27	0.50 ± 1.08	-1.09	0.02

3.4.2 Projected frontal ablation

Figure 3.1 displays the projected frontal ablation accumulated over the 21st century (using the conversion of 1 mm sea level equivalent (SLE) $\approx$ 362.5 gigatonnes (Gt)). It also shows these values excluding the amount of volume lost below the water level that has to be replaced by freshwater in order to cause GMSLR, which indicates the regionally aggregated stability of front positions. Moreover, it can be seen that the slope of the projected accumulated frontal ablation for the northern hemisphere decreases over the course of the 21st century, which means that the annual rate of frontal ablation decreases. It is noteworthy that the projected amount of frontal ablation is almost independent of the applied climate scenario/atmospheric forcing. We interpret that this is due to two different effects of the atmospheric climate on frontal ablation that cancel each other out to a certain degree in the northern hemisphere. Those are shown for two example glaciers in Fig. 3.2. The left-hand panels a) and c) show the exemplary behavior of a glacier which experiences less frontal ablation in higher emission scenarios, more typical for the Greenland periphery and Alaska. Such a behavior is determined by a mostly continuous prograde slope of the bed topography, which means that with increased surface melt the glacier will experience less frontal ablation. That is because its thinner front is situated in shallower water in the same years and our frontal ablation parameterization explicitly depends on these two variables (h_f and d_f in Equation 3.16). The glacier shown on the right, panels b) and d), represents a behavior more typical to the region Arctic Canada North, meaning more frontal ablation in a higher emission scenario (see Fig. 3.1). This behavior is characterized by glaciers being close to flotation and a retrograde bed slope. Higher surface melt thus triggers a rapid retreat when such glaciers are forced beyond a bathymetric pinning point.

Although we find these two counteractive effects of atmospheric warming on projected frontal ablation, the total projected amount is slightly larger in the higher emission scenarios for the whole northern hemisphere. This is probably due to the flotation criterion we implemented being triggered more often in higher emission scenarios owing to enhanced surface thinning. It is likely that there is a positive feedback of surface melt and thinning at marine-terminating glacier fronts, as the melt-induced surface thinning decreases the height above buoyancy and thereby increases the sliding velocity (see Equations 3.11 and 3.12). If this increases the total frontal velocity in the absence of increased mass transport to the terminus, it will inevitably lead to further thinning and retreat.

Concerning regional frontal ablation estimates, it is interesting that there is little projected mass change below the water level in Alaska. This indicates that front positions of glaciers contributing the largest amounts of frontal ablation in this region are mostly stable in our simulations, while the total number of marine-terminating glaciers is decreasing significantly (see Fig. 3.3). Consistent with what we described above, Arctic Canada North is the only region for which we project slightly higher frontal ablation rates towards the end of the century than in 2020 (increasing slope in Fig. 3.1). Furthermore, we find rapidly increasing frontal ablation rates for this region already in the last few years of the calibration period (2010 to 2020; not shown in Fig. 3.1). This leads to the cumulative total frontal ablation estimates being roughly twice what we found for Alaska by 2100, where frontal ablation rates decrease throughout the first half of the 21st century. Additionally, we project more accumulated frontal ablation by 2100 in the higher than in the lower emission scenarios for this region. Cook et al. (2019) found that marine-terminating glacier retreat patterns in the Canadian Arctic Archipelago showed no significant correlation with subsurface ocean temperature changes until 2015. Assuming the oceanic influence in that region remains small in the future and acknowledging that we cannot model the effect of oceanic melt in our current modeling framework, an explanation would be that a significant number of marine-terminating glaciers there are close to flotation today (and have undulating/retrograde bed slopes). Such a geometric configuration makes them prone to rapid retreat and thereby enhanced frontal ablation when experiencing stronger surface melt/thinning. Our simulations result in more frontal ablation throughout the 21st century under the higher emission scenarios in Svalbard and the Russian Arctic as well. On the other hand, we project less accumulated frontal ablation by 2100 in the higher than in the lower emission scenarios for Alaska and the Greenland periphery.

The number of glaciers in each region containing volume below the water level in a certain year of our simulations is displayed in Fig. 3.3. It shows that this number depends on the atmospheric forcing applied, with higher emission scenarios leading to less marine-terminating glaciers in general. The most drastic decrease is simulated for the Greenland periphery, consistent with the relatively large retreat volume given in Table 3.1. The least (relative) decrease is simulated for Svalbard. Interestingly, the GCM ensemble's standard deviation and the spread between emission scenarios differ among the regions shown in Fig. 3.3, indicating differences in the sensitivity of marine-terminating glaciers' dynamic response to atmospheric forcing.

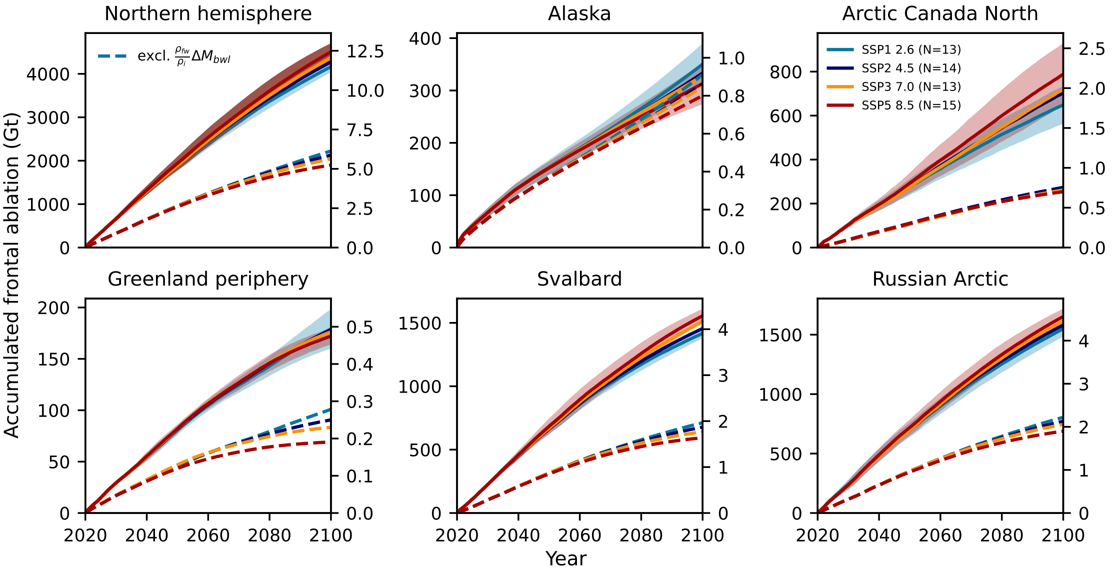

Figure 3.1: Projected accumulated frontal ablation for the northern hemisphere and different RGI regions for the remainder of the 21st century. Dashed lines exclude the amount of volume loss below the water level that has to be replaced by freshwater and thus does not contribute to GMSLR (ρ_{fw} is the density of freshwater: 1000 kg m^{-3}). N is the number of GCMs used for the respective emission scenario. The 1-σ standard deviation of the GCM ensemble for scenarios SSP1 2.6 and SSP5 8.5 is displayed as shading. The right y-axes display gigatonnes (Gt) converted to mm SLE. Note the different scales for each region.

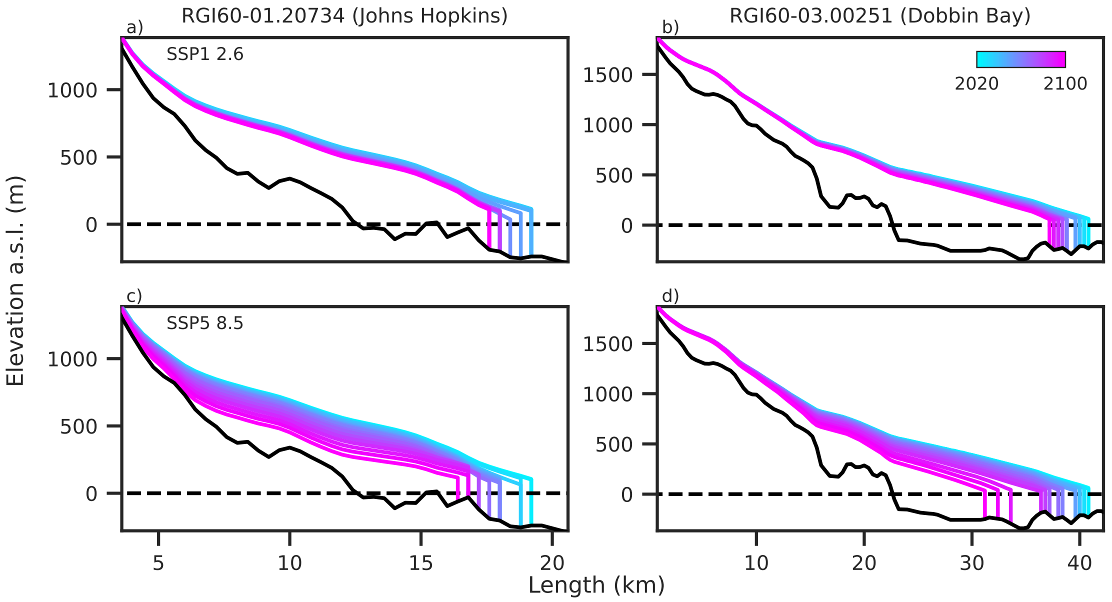

Figure 3.2: Lateral view of two example glaciers' states at different points in time (5-year increments from 2020 to 2100), simulated using the BCC-CSM2-MR climate model data for atmospheric boundary conditions. The upper panels (a and b) show the glacier states in simulations forced with the emission scenario SSP1 2.6, and the lower panels those in simulations forced with SSP5 8.5. Note the different scales for both glaciers.

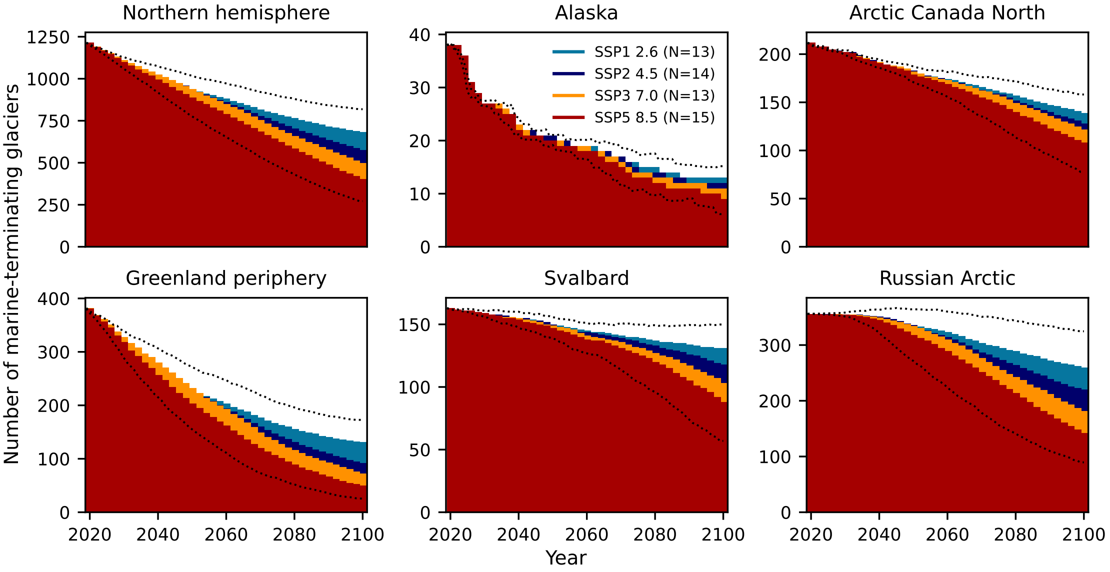

Figure 3.3: Number of glaciers with volume below the water level for the northern hemisphere and different RGI regions. The uncertainty in the GCM ensemble is displayed as dotted black lines. The upper line is the positive 1-σ standard deviation for the scenario SSP1 2.6, and the lower line the negative 1-σ for SSP5 8.5. Note the different scales for each region.

3.4.3 Northern hemisphere and regional mass change

The main aim of this work is to compare projections of glacier mass change including marine frontal processes with projections disregarding these. When comparing such results concerning GMSLR, three effects will play a role: i) the surface temperature sensitivity of marine-terminating glaciers is reduced and therefore their response to temperature changes is dampened, ii) frontal ablation takes place and compensates a certain amount of the dampened surface ablation, and iii) retreating marine-terminating glaciers lose volume below the water level, which does not contribute to GMSLR because it already displaced ocean water. Hence, the amount of volume loss below the water level has to first be translated to freshwater volume and then be subtracted from total glacier mass loss when calculating GMSLR contributions. Figure 3.4 shows the total projected accumulated glacier contribution to GMSLR, including marine frontal processes and accounting for volume changes below water level. The values are relatively similar to what has been previously presented by Marzeion et al. (2020) for the regions displayed. Table 3.3 shows the estimated cumulative GMSLR contribution at the end of the century given by our two types of projections as well as by the OGGM projections published with Marzeion et al. (2020). It is visible that for most of the regions considered here the glacier-by-glacier surface mass balance calibration does not significantly alter the estimates. Only for Svalbard larger differences are recognisable. For the entire northern hemisphere our estimates are consistently lower than the ones previously derived from OGGM, but it is out of the scope of this work to investigate whether this comes from the different calibration method or differences in the applied atmospheric forcing ensemble.

Figures. 3.1 and 3.4 indicate that frontal ablation is a large part of the projected total mass budget for glaciers in Svalbard and the Russian Arctic, while it is a small part in the Greenland periphery and Alaska (see Fig. 3.1). Overall, our results imply that atmospheric forcing will play an increasingly dominant role throughout the 21st century for the northern hemisphere's glaciers (outside the Greenland Ice Sheet) in higher emission scenarios, as the rate of frontal ablation decreases while that of the total mass loss increases in most cases. This is also suspected to be the case for the Greenland Ice Sheet (Goelzer et al., 2020).

Figure 3.5 shows the accumulated difference in northern hemisphere glaciers' GMSLR contribution, relative to 2020, between the two different types of projections. It is visible that less glacier mass loss above the water level is projected for the northern hemisphere when taking frontal ablation into account. This is due to the lowering of the sensitivity to atmospheric temperatures, which is not compensated by the amount of projected volume above the water level removed by frontal ablation. Understandably, such a reduction has less of an absolute effect in lower emission scenarios, since atmospheric temperatures increase less in those during the 21st century. The absolute difference in reduction of glacier mass loss contribution to GMSLR between the lowest and highest emission scenario considered here is ∼5 mm SLE (Fig. 3.5). Of this amount, roughly 2 mm SLE can be attributed to differences in mass loss below the water level; in the lower emission scenarios, glaciers retreat less and thus less mass below the waterline is lost. In the highest emission scenario a total of roughly 7 mm SLE are lost below the water level. Evidently, the absolute difference in projected glacier contribution to GMSLR between different emission scenarios is smaller when applying our marine-terminating glacier framework than in projections neglecting marine frontal processes.

The only region shown in Fig. 3.5 for which the opposite is true is the Greenland periphery, where the temperature sensitivity is only reduced by an (area-weighted) average of 8 %. Regarding that region, it is also intriguing that our projections result in up to 0.5 mm SLE more mass loss above sea level when including marine frontal processes in the model, but accumulated frontal ablation that can actually contribute to GMSLR is only around 0.2 mm SLE (see Fig. 3.1). This suggests that other dynamical effects play a role here. Another outstanding feature of Fig. 3.5 is the difference in projected contribution to GMSLR applying the highest emission scenario (SSP5 8.5) in the region Arctic Canada North. In that situation the difference flattens out markedly during the last third of the 21st century, which could be caused by an increase in frontal ablation due to more glaciers rapidly retreating in this region and scenario (see section above), and/or by the disappearance of glaciers for which the decreases in sensitivity to atmospheric temperature were rather large.

Regarding percentages, the contribution of glacier mass loss in the northern hemisphere to GMSLR by the end of the 21st century is reduced by around 9 % for the different emission scenarios (see Table 3.4). If we only consider northern hemispheric marine-terminating glaciers, the reduction is around 30 %. Concerning individual regions, it can be seen in Table 3.4 that the reduction of mass loss above sea level reaches up to 30 % in Svalbard and the Russian Arctic. The marine-terminating glaciers of Alaska lose around 60 % less mass above sea level in our simulations. The other extreme is the Greenland periphery, where we estimate that marine-terminating glaciers contribute up to 8 % more to GMSLR when accounting for frontal ablation.

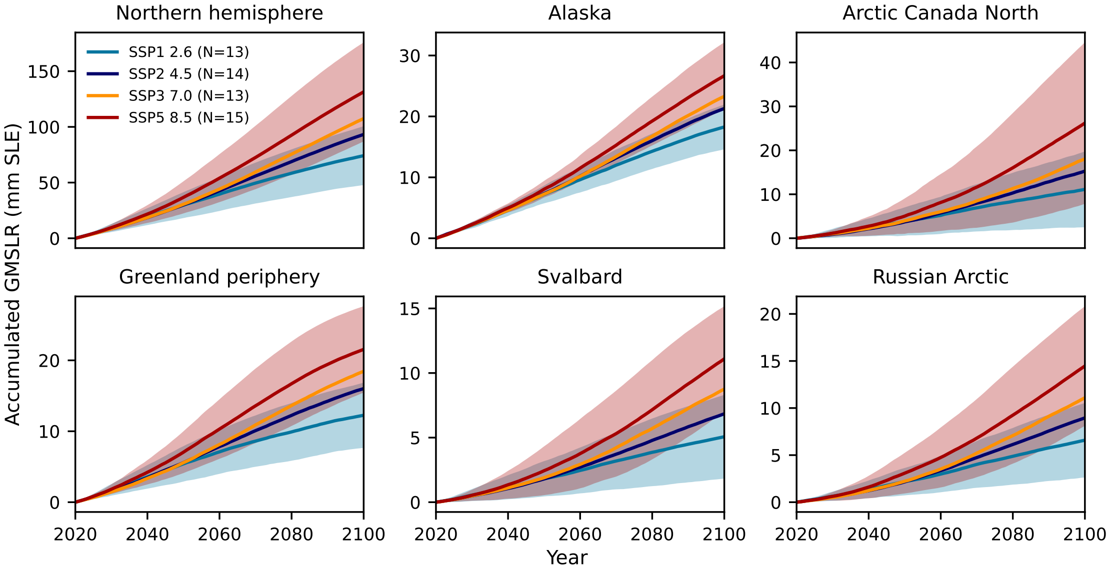

Figure 3.4: Projected accumulated glacier contribution to GMSLR for the northern hemisphere and different RGI regions taking frontal ablation and mass changes below water level into account. N is the number of GCMs used for the respective emission scenario. The 1-σ standard deviation of the GCM ensemble is displayed as shading for the different scenarios. Note the different scales for each region.

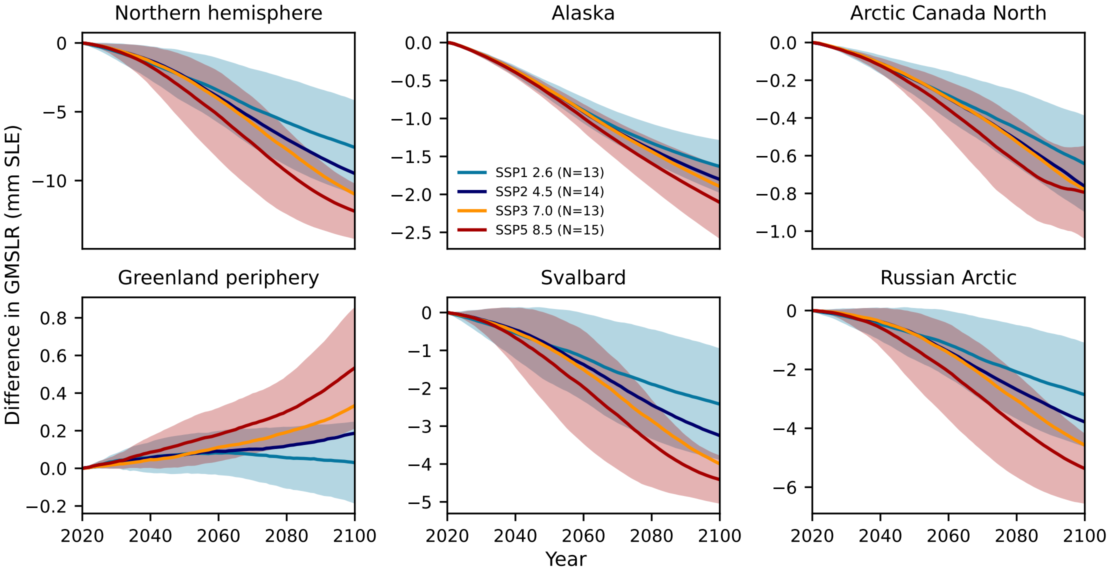

Figure 3.5: Difference in GMSLR contribution between projections including marine frontal processes and those neglecting these processes for the northern hemisphere and different RGI regions. N is the number of GCMs used for the respective emission scenario. The 1-σ standard deviation of the GCM ensemble is displayed as shading. Note the different scales for each region.

Table 3.3: Northern hemisphere glaciers' contribution to GMSLR by 2100 estimated by projections including frontal processes and by those not doing so as well as by OGGM projections published with Marzeion et al. (2020), for different RGI regions and all glaciers in the northern hemisphere. Columns represent different emission scenarios. Note that the scenarios given here correspond to RCP2.6, RCP4.5, and RCP8.5 used with a different GCM ensemble in Marzeion et al. (2020).

Region		SSP1 2.6	SSP2 4.5	SSP5 8.5
01 Alaska	with frontal ablation	18 ± 4	21 ± 4	27 ± 5
	without frontal ablation	20 ± 4	23 ± 5	29 ± 6
	OGGM in Marzeion et al. (2020)	19 ± 4	22 ± 3	28 ± 5
03 Arctic Canada North	with frontal ablation	11 ± 9	15 ± 12	26 ± 18
	without frontal ablation	12 ± 9	16 ± 12	27 ± 18
	OGGM in Marzeion et al. (2020)	13 ± 6	16 ± 5	26 ± 8
05 Greenland periphery	with frontal ablation	12 ± 5	16 ± 5	22 ± 6
	without frontal ablation	12 ± 5	16 ± 5	21 ± 6
	OGGM in Marzeion et al. (2020)	12 ± 4	14 ± 4	20 ± 4
07 Svalbard	with frontal ablation	5 ± 3	7 ± 4	11 ± 4
	without frontal ablation	7 ± 5	10 ± 5	16 ± 4
	OGGM in Marzeion et al. (2020)	14 ± 4	17 ± 5	21 ± 3
09 Russian Arctic	with frontal ablation	7 ± 4	9 ± 6	14 ± 6
	without frontal ablation	9 ± 6	13 ± 7	20 ± 7
	OGGM in Marzeion et al. (2020)	9 ± 5	13 ± 6	19 ± 6
Northern hemisphere	with frontal ablation	74 ± 26	93 ± 33	131 ± 44
	without frontal ablation	82 ± 29	103 ± 36	144 ± 46
	OGGM in Marzeion et al. (2020)	91 ± 31	110 ± 32	150 ± 33

Table 3.4: Percent difference in glaciers' contribution to GMSLR by 2100 between projections including frontal processes in the modeling chain and those not doing so, for different RGI regions and all glaciers in the northern hemisphere. Lower rows for each region display the values only regarding marine-terminating glaciers. Columns represent different emission scenarios.

Region		SSP1 2.6	SSP2 4.5	SSP3 7.0	SSP5 8.5
01 Alaska	all	-8 ± 0	-8 ± 0	-8 ± 0	-7 ± 0
	only MT	-65 ± 6	-59 ± 6	-56 ± 4	-53 ± 3
03 Arctic Canada North	all	-6 ± 2	-5 ± 2	-4 ± 2	-3 ± 3
	only MT	-13 ± 5	-11 ± 6	-9 ± 6	-6 ± 7
05 Greenland periphery	all	0 ± 1	1 ± 1	2 ± 1	2 ± 1
	only MT	0 ± 4	3 ± 4	6 ± 3	8 ± 3
07 Svalbard	all	-32 ± 4	-32 ± 4	-31 ± 6	-28 ± 6
	only MT	-41 ± 5	-41 ± 5	-40 ± 7	-37 ± 8
09 Russian Arctic	all	-30 ± 4	-30 ± 4	-29 ± 4	-27 ± 5
	only MT	-42 ± 6	-43 ± 5	-42 ± 5	-40 ± 5
Northern hemisphere	all	-9 ± 2	-9 ± 2	-10 ± 2	-9 ± 1
	only MT	-31 ± 4	-31 ± 5	-30 ± 6	-27 ± 7

3.5 Discussion

3.5.1 Calibration / Ice thickness inversion

Although a comparison with previously estimated values for k is not straightforward, because these studies either used one value for a whole region (Recinos et al., 2019) or a different calibration strategy (Recinos et al., 2021), it appears that our calibrated values are consistently higher. Additionally, the mentioned studies calibrated k only using the ice thickness inversion routine and not a dynamical model, further impeding a meaningful comparison. Concerning our ice thickness inversion, the volume increases due to including frontal ablation we found for the regions Alaska and Greenland periphery are close to previously published ones (see Table 3.2). Recinos et al. (2019) found a 16 % increase in ice volume for Alaska, and our estimate for the Greenland periphery lies between results from the two calibration methods (1.2 and 9.5 %) applied by Recinos et al. (2021). The larger volume increase in Alaska is related to the larger reduction in the temperature sensitivity ($\Delta\mu_{mt}$ in Table 3.2), which itself is related to the difference between retreat volume and total frontal ablation (ΔM_f and C in Table 3.1). This difference indicates how destabilized frontal positions in a region are, as it indicates whether the ice volume flux arriving at the glacier fronts can balance frontal ablation. An even larger difference (per glacier) than in the Greenland periphery was observed in Arctic Canada North, suggesting that dynamic effects are at play there, since it was found by Cook et al. (2019) that glacier mass changes in that region were mostly forced by changes in atmospheric conditions up until recently. It could therefore indicate that, as described above, the retreat (and a potential increase in frontal ablation) is caused by the influence of surface thinning and bathymetry on frontal dynamics and is mainly driven by an imbalance in the surface mass budget.

The interrelation of surface mass balance and frontal dynamics furthermore points to the larger problem of how to partition marine-terminating glaciers' mass changes between surface and frontal mass budget, because such glaciers could be in disequilibrium and retreat even with a positive surface mass balance. Such an assessment of surface versus dynamic (or frontal) disequilibrium is complicated by the fact that it is a transient problem and both mass budget parts are dependent on geometric changes and hence on topography/bathymetry. Similar problems apply to the ice thickness inversion procedure we used, which generates the initial ice thicknesses at the RGI date. It has the caveat that it is a transient problem as well for glaciers not in a steady state (Rabatel et al., 2018). For simplicity, we assume steady state at the RGI date (Maussion et al., 2019), which is inaccurate, given that most glaciers had a glacier-wide negative mass balance, and were thus not in a steady state, around their RGI recording date. This problem is difficult to solve, especially in the presence of frontal ablation, but may be tackled with inverse methods relying on velocity observations as in Millan et al. (2022). The equilibrium assumption might result in too much ice volume at the beginning of our simulations (the RGI recording date), thereby potentially inducing spin-up effects in the first years of simulation. Since most RGI dates lie before 2010 (ca. 98 %), the effect on our calibration should be small.

On the other hand, we use the area at the RGI date in Equation 3.18, which leads to incongruities, since we use the 2010 to 2020 mass change and frontal ablation data.

3.5.2 Northern hemisphere and regional mass change

For most of the examined regions we find good agreement between our projections that do not include marine frontal processes and those previously generated using OGGM (published with Marzeion et al. (2020)); only for Svalbard our estimates are considerably lower. This is despite the utilisation of a glacier-by-glacier calibration in this work compared to an interpolation-based approach in the earlier work. Projections including marine frontal processes result in lower GMSLR estimates by 2100 in all regions except the Greenland periphery, as described in Section 3.4.3. The total northern hemisphere's GMSLR contribution's reduction of around 9 % could be considered rather small. Still, the projected mass changes for individual regions, and for the entirety of northern hemisphere marine-terminating glaciers, can be altered quite strongly by changes to the model described in the sections above.

One caveat here is that we are not able to account for increasing rates of frontal ablation due to increasing ocean temperatures in the current framework. Thus, frontal ablation rates might be underestimated for higher emission scenarios in our projections towards the end of the 21st century. Another process neglected in our simulations is the influence of subglacial discharge on frontal ablation (Slater et al., 2015). An increase in subglacial discharge by stronger surface melt over the course of the 21st century could enhance frontal ablation rates in relation to increasing atmospheric temperatures. As we do not include the influence of increases in thermal forcing and/or subglacial discharge on frontal ablation, the ratio of frontal ablation to total mass change decreases more strongly over time for higher emission scenarios. Explicitly including submarine melt, and thus oceanic forcing more comprehensively, might increase the dependence of frontal ablation projections on the climatic forcing. Such a potential increase in frontal ablation would be compensated by the fact that fewer glaciers will be marine-terminating in 2100 than in 2020, however. Kochtitzky and Copland (2022) have shown that several marine-terminating glaciers already retreated to land between 2000 and 2020.

A further limitation is that the dataset we use for calibrating the frontal ablation parameterization does not cover lake-terminating glaciers. Alaska, for example, contains quite large glaciers lake-terminating glaciers, and including them could thus further enhance the influence of frontal ablation on glacier mass change projections. The number of lake-terminating glaciers is likely to increase as glaciers retreat. Finally, we suppose that including the southern hemisphere would strongly enhance the impact of incorporating frontal ablation on large-scale glacier mass change projections. That is because glaciers of the Antarctic periphery store by far the most ice below sea level of all RGI regions (Farinotti et al., 2019).

3.5.3 Further sources of uncertainty

Glacier mass change and its interrelation with glacier dynamics is a complex issue. Examining marine-terminating glaciers adds a level of complexity, as additional processes and variables are involved compared to land-terminating glaciers. Hence, the numerical modeling of such glaciers requires additional parameters and adjustments, which are subject to uncertainties (Hourdin et al., 2017). In order to test the influence of certain parameters on the results presented in Section 3.4, we conducted additional experiments described in appendix 3.B.

External sources of uncertainties include the datasets we use as initial (RGI, DEMs) and atmospheric boundary conditions (CRU, GCMs), because they transmit their uncertainties to the model during calibration, ice thickness inversion, and dynamical projections. Parameterizations also add to the uncertainty, as shown exemplarily for the flow parameters in the appendix 3.B. Moreover, parameterizations always simplify and approximate physical processes that are not explicitly incorporated in the model formulation. Applying inappropriate parameterizations will thus introduce systematic errors to the model. For instance, a sliding parameterization that includes lubrication of the glacier bed by percolating surface melt, and therefore produces more sliding in lower parts of a glacier than in upper parts (with the same values of h, d, and α), might be more appropriate than the one we applied. Also, applying the same value for certain parameters to every glacier (i.e., global parameters) and keeping parameters constant throughout the simulations are simplifications that lead to further inaccuracies. Additional assumptions and simplifications in our modeling framework that we acknowledge are: i) negligence of floating tongues/ice shelves, lateral drag, and sediment dynamics/proglacial moraines, ii) the equilibrium assumption in the ice thickness inversion, iii) the usage of elevation-band flowlines, and iv) the omission of explicit submarine melt (i.e., oceanic thermal forcing as well as subglacial discharge) in the frontal ablation parameterization.

Ultimately, it is not our aim in this work to give as accurate projections as possible of future glacier mass changes, but to get a grasp of the influence of including frontal processes on these. In that regard, the above mentioned uncertainties do not challenge our main conclusions, but future efforts to project mass changes of marine-terminating glaciers should take them into account. For obtaining an increased accuracy, one could devise a calibration strategy that simultaneously constrains additional variables with observational estimates by, for instance, implementing a multi-objective optimization of both the flow parameters and the frontal ablation parameter. Variables that might be included in this are: ice thickness and velocity as well as (frontal) area changes. Such a procedure would likely improve the ability of the model to simulate glacier dynamics properly.

3.6 Conclusion

Since a large portion of the northern hemisphere's glacier mass is contained in marine-terminating glaciers, taking processes occurring at their fronts into account more rigorously is a step towards more robust glacier mass change projections. For the lowest and highest emission scenario, we project glacier GMSLR contributions by 2100 to be 74 ± 26 and 131 ± 44 mm SLE, respectively. We find that in projections accounting for marine frontal processes, the GMSLR contribution at the end of this century is reduced by around 9 %, and by up to roughly 13 mm SLE, compared to projections neglecting such processes. Though this might be a small impact regarding the whole northern hemisphere (excluding the Greenland Ice Sheet), the effect of this is an approximately 30 % difference when only regarding marine-terminating glaciers or individual regions. Such substantial impacts on regional results would have important consequences for potential changes in regional ocean circulation and ecology caused by increased freshwater input due to glacier mass loss. For the Greenland periphery we find a converse effect; up to roughly 2 % more total and 8 % more marine-terminating glacier mass is lost when including frontal processes in the modeling chain. Another interesting finding is that the difference in glacier mass change projections between the emission scenarios is smaller in the year 2100 when applying our marine-terminating glacier framework compared to projections neglecting marine frontal processes.

Because numerical modeling of glacier dynamics requires boundary conditions and parameterizations, calibration is a crucial step. Here, we calibrated the parameters responsible for the removal of ice mass from the glaciers: the sensitivity to atmospheric temperatures, and the frontal ablation parameter. In addition, we tested the variance in our results caused by other relevant parameters: the flow parameters, and the assumed fraction of mass changes in the terminus area below the water level. We find that varying the flow parameters, especially Glen's A, has a considerable effect on the projected amount of frontal ablation and total glacier mass change. The variance in results induced by this is smaller than that caused by differences in the atmospheric forcing data, namely the GCM ensemble. Still, for future studies that focus on most accurately projecting global glacier mass change, or on regions with much ice mass contained in marine-terminating glaciers, it might be considered to simultaneously calibrate the flow parameters and the frontal ablation parameter by constraining additional variables (i.e., velocity, thickness, area change) using observational estimates. Ultimately, repeating the exercise laid out in this work with calibration data for the southern hemisphere (excluding the Antarctic Ice Sheet), and lake-terminating glaciers, will probably reveal even more strongly that robustly modeling water-terminating glaciers has a significant effect on glacier mass projections in comparison to not doing so. One further crucial future step will be to simulate the effect of changing ocean temperatures and subglacial discharge on frontal ablation. Finally, glacier mass change reconstructions could benefit from accounting for frontal ablation and mass changes below sea level as well, especially when used to reconstruct sea level changes.

3.A Appendix A

Table 3.A.1: General Circulation Models (GCMs) used for projections and their availability for the emission scenarios considered in this work.

GCM	SSP1 2.6	SSP2 4.5	SSP3 7.0	SSP5 8.5	Source
CESM2-WACCM	x	x	x	x	Danabasoglu (2019b)
MPI-ESM1-2-HR	x	x	x	x	Schupfner et al. (2019)
GFDL-ESM4	x	x	x	x	John et al. (2018)
NorESM2-MM	x	x	x	x	Bentsen et al. (2019)
INM-CM4-8	x	x	x	x	Volodin et al. (2019a)
INM-CM5-0	x	x	x	x	Volodin et al. (2019b)
MRI-ESM2-0	x	x	x	x	Yukimoto et al. (2019)
CESM2	x	x	x	x	Danabasoglu (2019a)
EC-Earth3	x	x	x	x	EC-Earth Consortium (2019a)
EC-Earth3-Veg	x	x	x	x	EC-Earth Consortium (2019b)
CAMS-CSM1-0	x	x	x	x	Rong (2019)
BCC-CSM2-MR	x	x	x	x	Xin et al. (2019)
FGOALS-f3-L	x	x	x	x	Yu (2019)
TaiESM1	-	-	-	x	Lee and Liang (2020)
CMCC-CM2-SR5	-	x	-	x	Lovato and Peano (2020)

3.B Appendix B

3.B.1 Parameter sensitivity test setup

The two flow parameters (A and f_s in Equations 3.2, 3.11, and 3.13) play a significant role in our simulations, since they are changing the outcomes of the ice thickness inversion, and the behavior of ice dynamics. We conducted additional simulations to get a notion of these parameters' influence on the results. For those experiments we calibrated the frontal ablation parameter (k) with different values of the flow parameters and then reran the projections with one GCM and one emission scenario (BCC-CSM2-MR and SSP3 7.0). We additionally varied the assumed fraction of retreat volume below sea level (f_{bwl}) to get an impression of how strong the effect of this is. Table 3.B.1 shows the parameter space we investigated. The modeling chain was run once for every possible parameter combination; hence 27 times in total. Moreover, we conducted runs in which we halved the stress coupling length (see Section 3.2.2) applying the different values for the flow parameters given in Table 3.B.1 while keeping f_{bwl} at 0.75.

Table 3.B.1: Parameter values tested for the estimation of parameter sensitivity.

Parameter	low	default	high
f_s (m^2 s^{-1} Pa^{-3})	0	10^{-20}	5.7 x 10^{-20}
Glen's A (s^{-1} Pa^{-3})	1.2 x 10^{-25}	2.4 x 10^{-24}	2.4 x 10^{-23}
f_{bwl}	0.625	0.75	0.875

3.B.2 Parameter sensitivity results

Here we discuss the uncertainty in our results due to the influence of the flow parameters (Glen's A, and the sliding parameter f_s; see previous section, and Equation 3.13). Though such uncertainties apply to land-terminating glaciers to some degree as well, marine-terminating glaciers can be especially sensitive to ice thickness changes, which are a compound result of ice thickness inversion, ice dynamics, frontal ablation, and surface mass balance. This is because they can be prone to acceleration and rapid retreat when approaching flotation. Moreover, our frontal ablation parameterization is directly dependent on ice thickness, and the water depth estimated via the ice thickness inversion (see Equation 3.16). Also, with low values for these parameters, the ice thickness inversion will result in very thick glaciers and thus more ice that can potentially be removed and (if situated above the water level) add to GMSLR. Additionally, the flow parameters impact the simulation of ice dynamics and thus the geometric adjustment of glaciers to a certain perturbation in the forcing. In that sense, two dynamical feedbacks, with opposite signs, play a role: the elevation change of a glacier's terminus which is a negative feedback, and the change of a glaciers' surface elevation which is a positive feedback.

All the simulation results presented above were computed with certain parameter values (standard values named *default* in Table 3.B.1). As explained in Section 3.B.1, we therefore conducted additional experiments to get an impression of these parameters' influence. In

Fig. 3.B.1 it is visible that varying Glen's A has the largest impact on the results concerning the difference between taking frontal processes into account and not doing so (relating σ_A to σ_{tot}). Only the GCM ensemble's variance (σ_{GCM}^{ssp}) has an even stronger effect throughout the 21st century, though the decreasing variance in the high emission scenario during the second half of the displayed period is intriguing. Plausibly, varying the assumed fraction of mass changes in the terminus area below the water level has a linearly growing influence on the results ($\sigma_{f_{bwl}}$), while it is the overall weakest of the three investigated parameters. It can also be seen that there are positive covariances between the parameters, which is probably because varying the two flow parameters (A, f_s) has a somewhat similar effect. Regarding temporally accumulated frontal ablation, varying Glen's A has an even stronger relative effect, while varying f_{bwl} has nearly none (see Fig. 3.B.2). The large influence of A is mostly based on the fact that it has a strong influence on the initial ice thickness found by the inversion procedure (see Section 3.2.4) and this, in turn, strongly influences frontal ablation. Interestingly, the large variance in frontal ablation projections caused by varying A (σ_A) shown in Fig. 3.B.2 is not directly translated to the effect of including frontal processes in the projections (Fig. 3.B.1).

There are two effects of varying A attenuating each other regarding glacier mass loss over the course of the century. At first, more frontal ablation takes place with a lower A value due to the larger initial (frontal) ice thicknesses. The high frontal ablation overcompensates the reduced sensitivity to atmospheric temperatures, resulting in more glacier mass loss compared to projections not including marine frontal processes. Over the course of the century, as atmospheric temperatures increase, the effect of reduced sensitivities to these takes hold and the projections including frontal ablation result in less mass loss. As the ice thickness inversion produces less ice volume with a high A value, less ice will be available for further melt and frontal ablation towards the end of the century, which means that the difference in ice melt cannot grow more, while it does so in the simulations with a low A value (see Fig. 3.B.4). Such competing effects of varying A probably explain the peculiar shape of the standard deviation in Fig. 3.B.1.

The influence of changing the sliding parameter (f_s) on simulated frontal ablation is similar (see σ_{f_s} in Fig 3.B.2), although applying no sliding (i.e., $f_s = 0$) results in slightly less frontal ablation than applying the default value ($f_s = 10^{-20}$; see Fig. 3.B.5). That is despite including sliding results in thinner glaciers at the front and thus less mass to be removed by frontal ablation (see Equation 3.16). Though sliding also enhances dynamical thinning at the front, more mass is apparently removed from the front by the flotation criterion. Applying the high value for f_s results in the least frontal ablation though, probably because of the (frontal) ice thicknesses resulting from the inversion procedure being much smaller.

Concerning the uncertainty in total accumulated contribution to GMSLR by northern hemisphere glaciers, it is visible in Fig. 3.B.3 that varying Glen's A has again the strongest influence and produces a 1-σ standard deviation of close to 20 mm SLE. Varying the sliding parameter (f_s) results in a standard deviation of roughly 10 mm SLE, while varying f_{bwl} has an effect of less than 1 mm SLE. The non-linearity of the variance induced by the flow parameters can most likely be explained by their influence on the simulation of the dynamical/geometric feedbacks mentioned above in combination with the initial glacier volumes and frontal ablation. Figure 3.B.6 shows that simulations with lower values for the flow parameters generally result in higher GMSLR contribution estimates, which presumably is mostly due to the higher amounts of initial ice volume available for melt over the remainder of the century. Moreover, we find that the variance caused by the differences in the GCM ensemble (σ_{GCM}^{ssp}) is larger than that caused by varying any of the parameters considered here.

We additionally conducted runs in which we held f_{bwl} constant at 0.75, but halved the stress coupling length ($L_F = 4$ km in Equations 3.7 - 3.9) and applied the different parameter combinations for the flow parameters as in the experiments described above. The resulting accumulated frontal ablation estimates are 13 % higher in 2100 on average, which results in slightly higher average GMSLR contribution estimates (0.7 mm SLE) compared to results applying the higher value for L_F. The increase in frontal ablation produced by lowering the stress coupling length makes sense, since the additional force due to the hydrostatic pressure imbalance at the glacier front (see Equations 3.5 and 3.8) is distributed over a shorter distance. This causes a stronger thinning close to the front, which in turn causes more ice removal by the flotation criterion.

The analysis presented in this subsection demonstrates that further work on finding appropriate parameter values for individual glaciers is required in order to improve the accuracy of mass change projections for (marine-terminating) glaciers. We would like to emphasise that the default parameter set we used for computing our main results in Section 3.4 was not chosen for its suitability for all glaciers worldwide, but for its applicability to most glaciers without causing numerical errors in the dynamical model.

Figures 3.B.4 - 3.B.6 show that results obtained with the parameter set chosen for the simulations presented in the sections above are reasonably close to the parameter ensemble's mean and median though. In Figs. 3.B.1 - 3.B.3 the GCM ensemble's standard deviation with the default parameter set is given as well. This is the largest source of uncertainty in accumulated mass changes, though it differs between emission scenarios. The difference between GCMs is relatively small concerning accumulated frontal ablation in the whole northern hemisphere. This hints that the northern hemisphere's accumulated frontal ablation is somewhat independent of the atmospheric forcing in our simulations, although annual frontal ablation rates may differ between different GCMs.

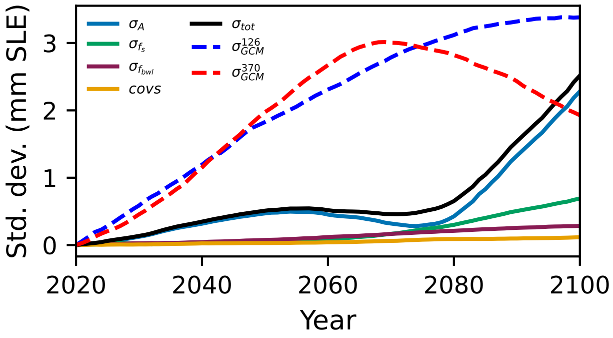

Figure 3.B.1: Northern hemisphere standard deviation (1-σ) of differences between projections accounting for marine frontal processes and those that do not, caused by varying different parameters. The yellow line displays covariances of the three tested parameters, and σ_{GCM}^{ssp} the variance of the GCM ensemble in the respective scenario with default parameter set. The subscripts in the legend refer to the respective parameter varied (see Table 3.B.1), and σ_{tot} to the ensemble of model runs' total variance.

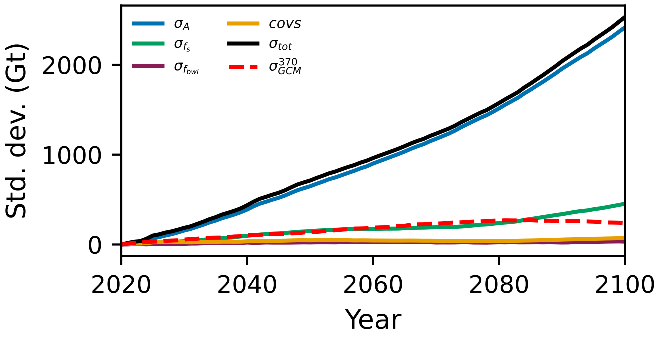

Figure 3.B.2: Same as Fig. 3.B.1, but for accumulated frontal ablation estimates. σ_{GCM}^{126} is excluded, due to its similarity with σ_{GCM}^{370} and thus better visibility.

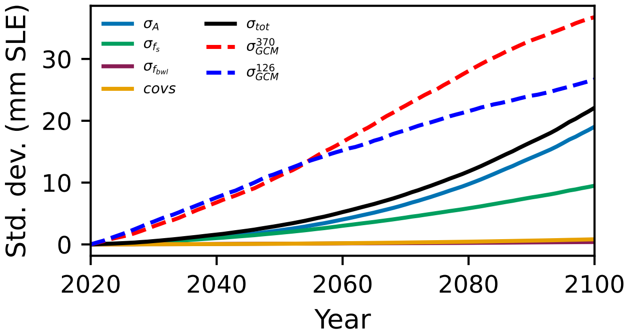

Figure 3.B.3: Same as Fig. 3.B.1, but for estimated accumulated GMSLR contribution.

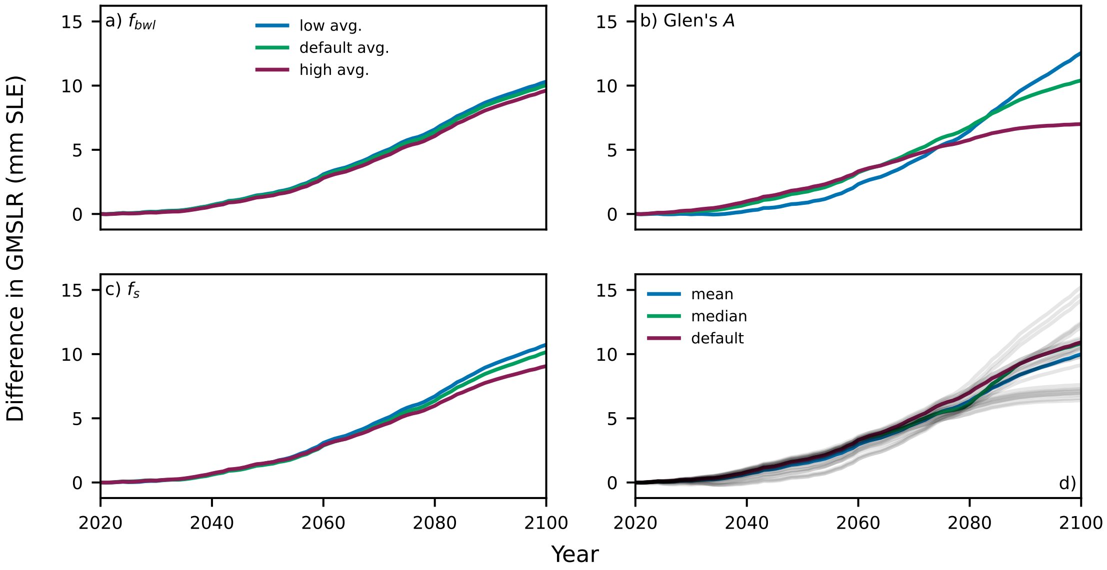

Figure 3.B.4: Estimated differences between projections accounting for frontal processes and those that do not, averaged over different parameter values. Panels a-c display averages over the 9 possible different parameter sets with the respective parameter value corresponding to the three different columns in Table 3.B.1. Panel d displays the results of all 27 parameter sets possible in Table 3.B.1 in grey shading with the mean/median as well as the result for the parameter set chosen for the computation of results in Section 3.4 (*default* in Tab 3.B.1) highlighted.

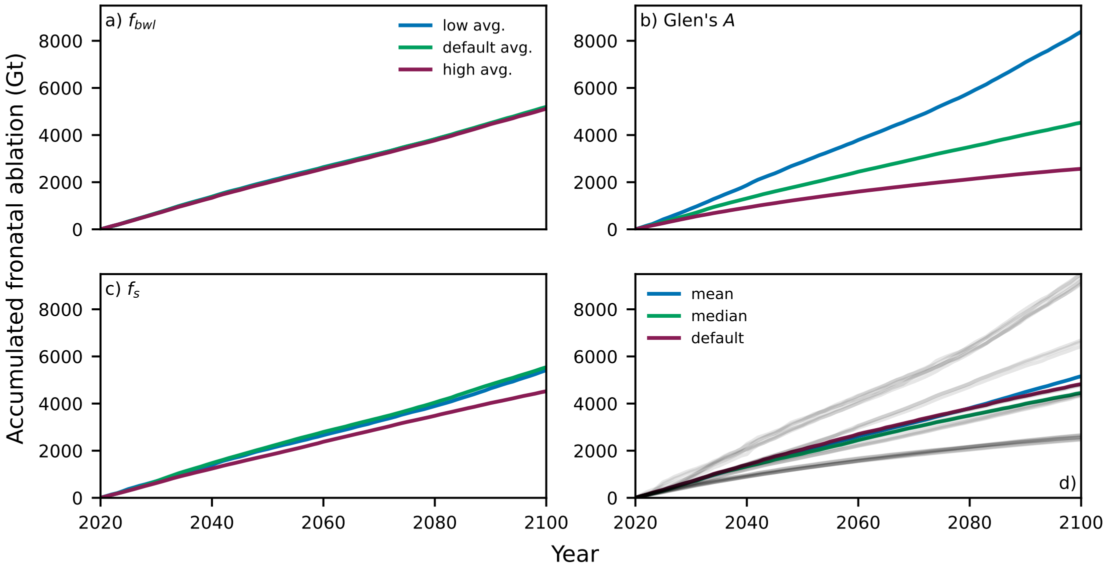

Figure 3.B.5: Same as Fig. 3.B.4, but for accumulated frontal ablation estimates.

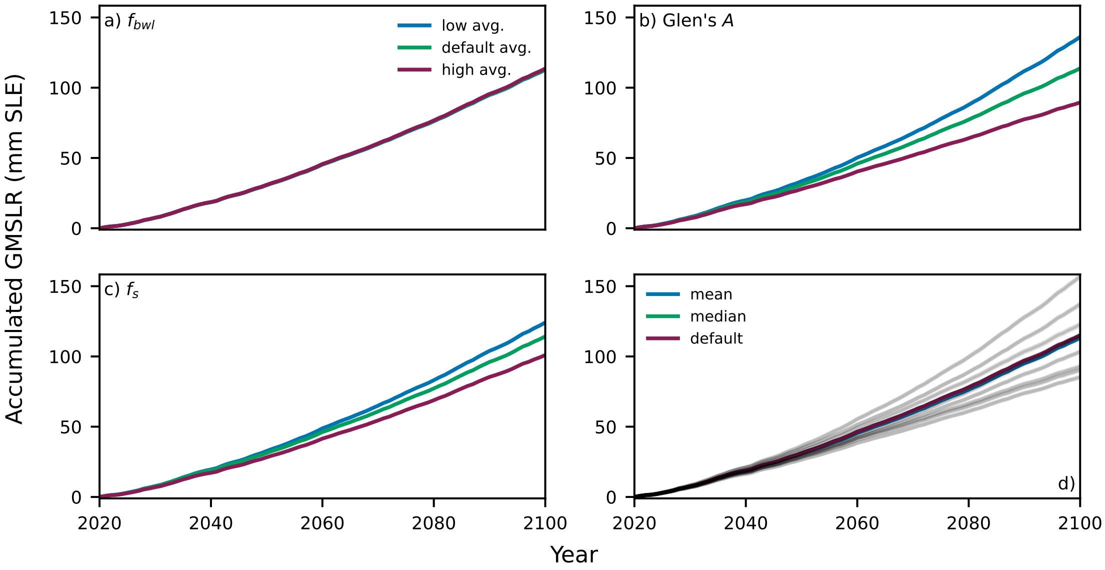

Figure 3.B.6: Same as Fig. 3.B.4, but for accumulated GMSLR contribution.

Data & code availability

The data of the projections including frontal ablation can be accessed at Zenodo (doi: 10.5281/zenodo.7550644). Further data inquiries can be made to the first author.
The model code repository used for this work is archived at Zenodo (doi: `10.5281/zenodo.7547966`) and its main part will be added to the OGGM core (`github.com/OGGM/oggm`) in the foreseeable future.

Author contributions

JHM designed the research together with FM, conceived and developed the changes to the model code, conducted the simulations and statistical evaluation, and wrote the manuscript. FM, LU, and BM contributed to the manuscript. WK and LC supplied and assisted with the data, and made contributions to the manuscript.

Chapter 4

Context

The previous chapter introduced frontal ablation to the dynamical core of the model OGGM. However, the simple parameterization merely scales total frontal ablation linearly to the water depth at the glacier front. As the submarine melt part of frontal ablation is mainly driven by ocean temperature (and salinity) and partly by subglacial discharge, an explicit formulation of submarine melt in the model is necessary to simulate marine-terminating glaciers' mass change more realistically. Especially for future projections, this might have a significant impact since subglacial discharge (due to enhanced surface melting), and ocean temperatures can be expected to increase due to anthropogenic climate change. Moreover, it is important to understand how the increased freshwater input from glacial melt changes the ocean's near-surface density and circulation. Changes in regional or even larger-scale ocean circulation can have significant consequences for the state of the climate system. There may be feedback mechanisms that increase oceanic heat transport to marine-terminating glacier fronts in response to an increase in freshwater forcing of the ocean. Since submarine melt and the impact of increased freshwater input from glaciers outside the ice sheets have not been studied yet, this chapter aims to produce a first estimate of both. To accomplish this, OGGM and NEMO are one-way coupled for a historical decade (2010 to 2019), and differences compared to uncoupled runs are investigated.

Freshwater input from glacier melt outside Greenland alters modeled northern high-latitude ocean circulation

Jan-Hendrik Malles[1,2], Ben Marzeion[1,2], and and Paul G. Myers[3]

[1]Institute of Geography, University of Bremen, Bremen, Germany
[2]MARUM - Center for Marine Environmental Sciences, University of Bremen, Bremen, Germany
[3]Department of Earth and Atmospheric Sciences, University of Alberta, Edmonton, Canada

Abstract

As anthropogenic climate change depletes Earth's ice reservoirs, large amounts of freshwater are released into the ocean. Since the ocean has a major influence on Earth's climate, understanding how the ocean changes in response to an increased freshwater input is crucial for understanding ongoing shifts in the climate system. Moreover, to comprehend the evolution of ice-ocean interactions, it is important to investigate if and how changes in the ocean might affect marine-terminating glaciers' stability. Though most attention in this context has been on freshwater input from Greenland, the other northern hemisphere glacierized regions are losing ice mass at a combined rate roughly half that of Greenland, and should not be neglected. In order to get a first estimate of how glacier mass loss around the Arctic affects the ocean and how potential changes in the ocean circulation might affect marine-terminating glaciers, we conduct one-way coupled experiments with an ocean general circulation model (NEMO-ANHA4) and a glacier evolution model (Open Global Glacier Model; OGGM) for the years 2010 to 2019. We find an increase in heat content of Baffin Bay and in the subpolar gyre's strength, which is consistent with previous results. Additionally, we find a decreased heat transport into the Barents Sea due to increased freshwater input from Svalbard and the Russian Arctic. The rerouting of Atlantic Water from the Barents Sea Opening through Fram Strait leads to an increased heat transport into the Arctic Ocean and a decrease of sea ice thickness in the Fram Strait area.

4.1 Introduction

The recent accumulation of heat in Earth's atmosphere and ocean due to anthropogenic climate change is diminishing the frozen water reservoirs on the planet, causing the release of large amounts of freshwater (Slater et al., 2021b). Melting of Earth's glaciers is impacting regional hydrology and increasing global mean sea-level (GMSL; Huss and Hock, 2018; Frederikse et al., 2020). Moreover, such an additional freshwater input to the ocean changes its surface density and thus has the potential to change the ocean circulation on scales ranging from individual fjords (Bartholomaus et al., 2016) to the Atlantic Meridional Overturning Circulation (AMOC; Hu et al., 2011; Frajka-Williams et al., 2016), which is an important component of the global climate system. While there have been numerous studies on changes in the AMOC's strength and a potential influence of recently increased freshwater influx and ocean warming, it is disputed whether the AMOC has already been forced out of its natural variability envelope (Jackson et al., 2022; Latif et al., 2022; Caesar et al., 2021; Fu et al., 2020; Böning et al., 2016). Concerning the regional impact of enhanced Greenland ice sheet (GrIS) freshwater runoff on ocean circulation, Castro de la Guardia et al. (2015) found significant changes in Baffin Bay in a numerical ocean circulation model. These changes entailed an increasing heat content in Baffin Bay with increasing (idealized) freshwater input along Greenland's west coast. This is a potential positive feedback, which could lead to larger heat transports towards marine-terminating glacier fronts. Anthropogenic climate change causes the ocean to take up vast amounts of heat (von Schuckmann et al., 2020). This increase in ocean temperature, in combination with potential changes in ocean circulation, increases submarine melt of marine-terminating glaciers, destabilizing their fronts and inducing further retreat and mass loss (Wood et al., 2021, 2018). Such interactions between changes in ice bodies and the ocean do not only bear importance for contemporary changes in the Earth system, but on time scales encompassing glacial cycles as well (Alvarez-Solas et al., 2013; Rainsley et al., 2018). This underscores the importance of knowledge about the coupled ice-ocean system for understanding past and ongoing changes of the Earth system, and for projecting future changes.

Although most attention in this context has been on the GrIS, as it is the largest ice reservoir in the northern hemisphere, there are also other places experiencing glacier mass loss and hence are releasing freshwater into the ocean. Around the high-latitude (North Atlantic and Arctic) ocean, such places are the Canadian Arctic Archipelago, Svalbard, Iceland, and the Russian Arctic. Since ice loss in these places combined is roughly half that of the GrIS (Hugonnet et al., 2021; Zemp et al., 2019; Slater et al., 2021b), it is worth investigating whether increased freshwater input at the coasts of aforementioned regions does affect the high-latitude ocean's circulation, as such changes might also impact marine ecosystems (Timmermans and Marshall, 2020; Hátún et al., 2009; Wassmann et al., 2011; Greene et al., 2008). Figure 4.1 charts the main features of the ocean surface currents in the Northern Atlantic and the gateways between the Atlantic and Arctic Ocean. Atlantic water masses are usually characterized as warmer and more saline compared to the Arctic water. Atlantic water is transported from the western boundary current to the north by a complex interplay of the mainly wind-driven subtropical and subpolar gyres and the density-driven Atlantic meridional overturning circulation (AMOC). The subpolar gyre is the circulating pattern around the Labrador Sea (LS) and the Irminger Sea (IS), which transports Atlantic water branching off to the west in the Irminger Sea to the Labrador Sea and into Baffin Bay (BB). The Labrador Sea also is a location of importance for the AMOC, as deep convection takes place there (Broecker, 1997). Warm Atlantic water mainly enters the Arctic ocean through Fram Strait (FS) as well as through the Barents Sea (BS), while Arctic Water mainly enters the Atlantic ocean through the Canadian Arctic Archipelago (CAA) and Fram Strait.

The amount of ice that is removed from glaciers (outside the GrIS) by submarine melt is essentially unknown. Submarine melt remains elusive, since it is intricate to measure directly and observations hence sparse. Attempts to quantify it therefore mostly rely on (high-resolution) ocean circulation models and employing a parameterization of ice-ocean heat transfer related to oceanic properties at the glacier front (Jenkins et al., 2001; Holland et al., 2008; Xu et al., 2013). As this is computationally costly and can only be applied to individual glaciers, a further step in trying to generalize such modeling results to different glaciers was to employ empirical power laws to describe the relation of submarine melt to oceanic properties as well as to subglacial discharge (Xu et al., 2013; Rignot et al., 2016; Wood et al., 2021). We make use of such a power law parameterization in our attempt to quantify submarine melt of marine-terminating glaciers outside the GrIS.

To tackle the issue of ice-ocean interactions outside the GrIS, we one-way couple the Nucleus for European Modelling of the Ocean (NEMO) model and the Open Global Glacier Model (OGGM) for the years 2010 - 2019. We run both models twice, in order to investigate potential coupling effects. In one NEMO experiment, we use glacial surface mass loss and frontal ablation derived from OGGM as additional liquid freshwater and iceberg input to NEMO, while we omit this additional freshwater forcing in the second NEMO run. Next, we use the two different NEMO runs' output variables as forcing of the submarine melt parameterization newly implemented in OGGM (see section 4.2.3). Finally, we explore the differences in results obtained from the two different NEMO and OGGM experiments and discuss future avenues for research on this topic.

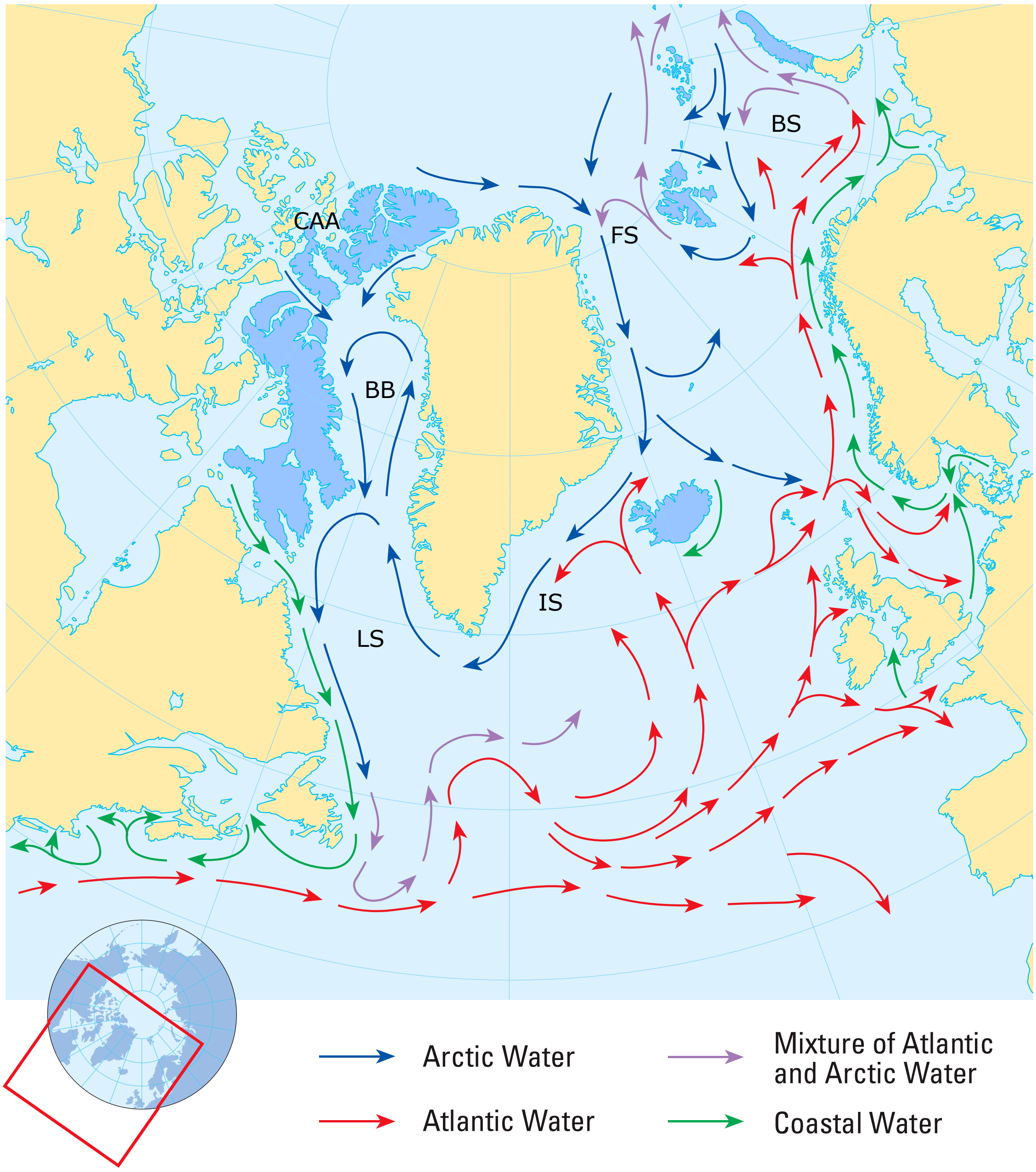

[!h]

Figure 4.1: Schematic of the main surface currents in the North Atlantic Ocean. Blue colored land areas indicate regions that contain glaciers outside of Greenland, see Figs. 4.11 and 4.A.1 for the actual glacier outlines. BB, BS, CAA, FS, IS, and LS indicate Baffin Bay, Barents Sea, Canadian Arctic Archipelago, Fram Strait, Irminger Sea, and Labrador Sea. Adapted from Arctic Monitoring and Assessment Programme (AMAP) (1998).

4.2 Data and methods

4.2.1 Ocean model

Our numerical experiments were conducted with NEMO v3.6 (Madec et al., 2016), which is coupled to a sea ice model (Louvain-la-Neuve Sea Ice Model 2; Bouillon et al., 2009). The configuration we use covers the Arctic and Northern Hemisphere Atlantic and has open boundaries at 20°S in the Atlantic Ocean as well as at the Bering Strait. The average horizontal resolution of the model is 1/4°, and it has 50 vertical levels (NEMO-ANHA4 configuration). For boundary and initial ocean conditions we use the Global Ocean ReanalYsis and Simulations data (GLORYS2v3; Masina et al., 2017) and for atmospheric forcing the Canadian Meteorological Center's reforecasts (CGRF; Smith et al., 2014). CGRF provides hourly fields of wind, air temperature and humidity, radiation fluxes, and total precipitation with a horizontal resolution of 33 km, which are linearly interpolated onto the NEMO-ANHA4 grid. The Lagrangian iceberg module implemented in NEMO is described by Marsh et al. (2015) and was further developed by Marson et al. (2018). The baseline continental runoff data (apart from Greenland) for our runs was obtained by linearly interpolating the data provided by Dai et al. (2009) on a 1 × 1° grid to the NEMO-ANHA4 grid. The Dai et al. (2009) data do not cover our model period from 2010 to 2019. We therefore applied the 1997 to 2007 monthly average baseline runoff. Freshwater input from Greenland is derived by remapping the data published by Bamber et al. (2018a) to the NEMO-ANHA4 grid. This data gives the total runoff, including from the ice sheet and peripheral glaciers, thus replacing the baseline runoff in this region. As this data set only ranges to the end of 2016, we use the 2010 to 2016 average for the three missing years. Runoff freshwater is added to the first vertical model level with a temperature corresponding to the surface temperature of the ocean grid cell. The addition of runoff entails enhanced vertical mixing of the grid cell's upper 30 m in our setup in, following Marson et al. (2021). Bamber et al. (2018a) give data for liquid runoff and solid ice discharge around Greenland. Here, we add half of the solid discharge estimates to the liquid freshwater input and the other half to the iceberg module, following the observation by Enderlin et al. (2016b) that roughly half of the icebergs' volume may melt before they exit fjords. The handling of additional freshwater from other glacierized regions is described in section 4.2.3.

4.2.2 Glacier model

The Open Global Glacier Model (OGGM) is a flowline model that can be used to model a large amount of individual glaciers at once (Maussion et al., 2019). Because observational data on glaciers, needed to constrain more complex representations of glaciological processes, are scarce, its computational cost is relatively low. We use the Randolph Glacier Inventory (RGI) version 6 (RGI Consortium, 2017; Pfeffer et al., 2014) to initialize the model for the ~15,000 glaciers surrounding the Arctic and North Atlantic (outside Greenland) that are included in our study. Topographical data is obtained from an appropriate digital elevation model (DEM), depending on the glacier's location. Here, we use single, binned elevation-band flowlines, constructed from the outlines and topographical data, using the approach described by Werder et al. (2020). Simulations of OGGM start in the year the glacier outlines contained in the RGI were recorded. The gridded atmospheric forcing data (monthly temperature and precipitation obtained from Climatic Research Unit Time-Series data set version 4.03 (CRU TS 4.03, Harris et al., 2020)) are interpolated to the glacier location. Temperatures are subsequently adjusted applying a linear lapse rate (6.50 °C/km) that is fixed globally. For precipitation, no lapse rate, but a global correction factor is applied (here, we use a value of 2.5), which is a common approach in large-scale glacier modeling (e.g., Giesen and Oerlemans, 2012b; Zekollari et al., 2022). The resulting temperature and precipitation values are used to compute the glaciers' surface mass balance by using a temperature-index melt model, which calculates surface melt rates from the near-surface atmospheric temperatures above a threshold temperature and neglects more intricate processes such as refreezing and the surface energy balance. The melt factor is calibrated using satellite-derived observations of glacier mass changes (Hugonnet et al., 2021). For information on details of OGGM, the reader is referred to Maussion et al. (2019).

Modeling marine-terminating glaciers requires some additional model features compared to land-terminating ones. That is because additional processes occur at their fronts which determine their dynamical behavior. The two main processes are an increasing basal/sliding velocity, moderated by the hydrostatic stress balance close to the front, and frontal ablation. Therefore, water-depth dependent sliding, hydrostatic stress coupling, and frontal ablation parameterizations were incorporated into OGGM's ice thickness inversion as well as ice dynamics schemes. To be able to calibrate the surface and frontal ablation parameterizations separately, the two mass budget parts have to be disentangled from observational data. For this purpose, the data of Kochtitzky et al. (2022) of frontal ablation is used in addition to the data of (Hugonnet et al., 2021). Frontal ablation is parameterized by using a linear scaling to the water depth:

$$Q_{fa} = k d_f h_f w_f \tag{4.1}$$

where $Q_f a$ is the frontal ablation flux (in m^3 a^{-1}), k the frontal ablation parameter (in a^{-1}), and d_f, h_f, and w_f the water depth, ice thickness, and ice width at the glacier front. In order to simulate submarine melt in OGGM, another parameterization is introduced, which will be described in section 4.2.3. More details of marine-terminating glacier modeling in OGGM are given in Malles et al. (2023).

4.2.3 One-way coupling of NEMO and OGGM

In order to estimate the effects of freshwater input to NEMO that is usually not accounted for, as well as the amount of mass removal from marine-terminating glaciers (outside the GrIS) by submarine melt, we adopt a simple one-way coupling scheme. This means we do not update the input to one model derived from the other one during the simulations. However, we implement the one-way coupling in both directions separately, so that we can roughly estimate the strength of any potential feedback. In the following, we describe how the respective inputs were derived and used for both models.

OGGM to NEMO

In one of our NEMO experiments, we use the OGGM output of glaciers' surface mass loss additional to half of the frontal ablation as additional liquid freshwater forcing, while the other half of the frontal ablation is added to the iceberg module, as is done for the Greenland solid ice discharge (this experiment hereafter is named *halfsolid*). We neglect the OGGM-freshwater and -iceberg fluxes in the other NEMO experiment (hereafter called *noOGGM*). The distribution of the resulting liquid freshwater forcing (excluding the baseline runoff described in the previous section) is displayed in Fig. 4.A.1. The liquid freshwater input (excluding the baseline runoff), averaged over 2010 to 2019, amounts to approximately 32 mSv ($\approx$ 1011 Gt a^{-1}) in the *halfsolid* run and of approximately 29 mSv ($\approx$ 903 Gt a^{-1}) in the *noOGGM* run. The calving input distribution is displayed in Fig. 4.A.2, which amounts to an average of approximately 9 mSv ($\approx$ 276 Gt a^{-1}) in the halfsolid run and to approximately 8 mSv ($\approx$ 248 Gt a^{-1}) in the *noOGGM* run. Note that the liquid freshwater and iceberg input around Greenland is derived from Bamber et al. (2018a) data, which contains total runoff and solid ice discharge, and is the same in both NEMO runs. This means that OGGM contributes roughly 4 mSv additional freshwater in the *halfsolid* run. The liquid freshwater from surface melt and the calving of individual glaciers deducted from OGGM output are put into the NEMO-ANHA4 grid cell with the lowest haversine distance to the respective glacier terminus location recorded in the RGI.

NEMO to OGGM

We use the outputs of the two NEMO experiments described above to calculate the thermal forcing of the ocean in the vicinity of marine-terminating glacier termini, which is then fed to the submarine melt parameterization of OGGM described below. Thermal forcing is defined as the distance of the potential temperature of a water mass to its freezing point. Here, we use the pressure- and salinity-dependent formulation of the freezing point given in Fofonoff and Millard Jr (1983).

Submarine melt parameterization in OGGM

While there has been previous work on incorporating frontal ablation into OGGM (Malles et al., 2023), it did not yet explicitly account for submarine melt. In this work we build on the previous work and add a parameterization of submarine melt rates (in m d^{-1}) following Rignot et al. (2016):

$$q_{sm} = (Ad\ q_{sg}^{\alpha} + B)\ T_f^{\beta} \tag{4.2}$$

where A is the subglacial discharge scaling parameter (in $d^{\alpha-1}$ $m^{-\alpha}$ $K^{-\beta}$), d the water depth at the glacier front (in m), q_{sg} the subglacial discharge normalized by submerged cross-section area at the glacier terminus (in m d^{-1}), α the subglacial discharge scaling exponent (dimensionless), B the ocean heat transfer scaling parameter (in m d^{-1} K$^{-\beta}$), T_f the oceanic thermal forcing in the vicinity of the glacier terminus (in K), and β the ocean heat transfer scaling exponent (dimensionless).

Equation 4.2 comprises two nested empirical power laws relating subglacial discharge and ocean potential temperature as well as salinity to submarine melt rates. The first power law (first term in the brackets) describes the increase in thermal erosion of marine-terminating glacier fronts due to subglacial discharge (q_{sg}). It is based on a statistical fit to modeling results that applied a parameterization, which was developed to represent heat and freshwater exchange across the ice-ocean interface in relation to ice temperature and ocean properties (Jenkins et al., 2001). This approach to computing freezing and melting at an ice-ocean interface, in combination with the injection of subglacial discharge, was used to model the circulation in front of a vertical ice cliff in a high resolution ocean-model and the resulting submarine melt (Xu et al., 2013). In essence, this power law expresses the increase in turbulence close to the glacier front in the presence of subglacial discharge, which increases the entrainment of warmer and saltier water from the ocean into the buoyant plume of freshwater. Suitable values for the exponent α were found to be below 1, since there is a saturation of the melt intensity caused by subglacial discharge. This is because the plume-ice contact area can no longer significantly increase at some point (Slater et al., 2016), while increasing subglacial discharge causes a freshening, and thus lower thermal forcing, of the water close to the glacier terminus. Values for the scaling parameter (A) are related to the vertical temperature gradient in front of the glacier and to the distribution and morphology of the subglacial discharge plumes along the glacier front. The second power law (BT_f^{β}) parameterizes the heat transport from the ocean to the ice and the resulting submarine melt in the absence of subglacial discharge. The scaling parameter B relates to the open ocean and fjord currents as well as to the ice temperature. The exponent β is related to the nonlinear relationship between submarine melt and thermal forcing (T_f) found by Xu et al. (2013) and Holland et al. (2008), which is based on the idea that submarine melt supplies buoyancy forcing to the plume convection at the glacier front, thereby increasing the entrainment of the open ocean's thermal forcing. Generally, the presence of icebergs in a fjord can change the fjords' water properties and thereby have an impact on submarine melt as well (Kajanto et al., 2023; Moon et al., 2018; Davison et al., 2020), but we neglect this here for simplicity.

To calculate total frontal ablation rates and to emulate calving due to the undercutting of glacier fronts by submarine melt, we adapt the parameterization of total frontal ablation rates previously applied in OGGM (see Eq. 4.1) to:

$$q_{fa} = max(kd, q_{sm}\frac{h}{d}) \tag{4.3}$$

where k (in a^{-1}) is the frontal ablation parameter, and h the ice thickness at the glacier front (in m). This allows for applying the values of the glacier-specific frontal ablation parameters that were calibrated by Malles et al. (2023), while constraining the parameters involved in the submarine melt parameterization as well, by ensuring that the total frontal ablation over the modeling period lies within the observationally estimated range given by Kochtitzky et al. (2022). As there are little to no observational estimates of submarine melt itself, it is not possible to constrain the four free parameters in Eq. 4.2 (A, α, B, β) for each glacier individually. Even if we had such estimates, we might be able to find different parameter combinations that complied with such observations. While this submarine melt parameterization has some physical foundations and was already applied in previously published works, it overparameterizes the model, because it introduces four additional parameters without additional observations to calibrate these. Therefore, we apply latin hypercube sampling to identify parameter sets that are consistent with observations of total frontal ablation over the same time period as the OGGM run (2010 to 2019). We sampled the following intervals 25 times:

- A: [3 x 10^{-5}, 1 x 10^{-3}]
- α: [0.25, 0.7]
- B: [1 x 10^{-3}, 0.75]
- β: [1.0, 2.0]

We run OGGM with each of the 25 sampled parameter sets for each marine-terminating glacier utilizing the halfsolid run output's thermal forcing. Afterwards, we only pick results from the parameter sets that yield total frontal ablation rates within the uncertainty bound of the observational estimates by Kochtitzky et al. (2022). To investigate a potential coupling effect, we apply the parameter sets selected for the halfsolid run to the thermal forcing derived from the noOGGM NEMO run output in a subsequent OGGM simulation. For six glaciers we do not find any valid parameter combination, but these glaciers together make up less than 1 % of the total marine-terminating glacier volume.

Thermal forcing values from the ocean model output are obtained by taking all NEMO-ANHA4 grid cells within a 50 km radius of the respective marine-terminating glacier's terminus into account. If there are less than three ocean model grid cells in the radius, we iteratively double the radius. This ensures that we do not only use the value from a single ocean model grid cell, since we do not know whether the closest one actually reflects water properties at the glacier front best. We then compute a depth-averaged value of the included cells' thermal forcing and apply a distance-weighted averaging to obtain the final value inserted in Equation 4.2. Here we use the full depth range of the grid cells, as NEMO-ANHA4 does not resolve individual fjords and it is unclear which depth range of the open ocean would be appropriate to include.

4.3 Results

4.3.1 Ocean model

In this section we will describe our findings regarding differences between the *halfsolid* and the *noOGGM* runs. Spatial plots display differences averaged over the last five years of the NEMO integrations (i.e., 2015 to 2019), assuming the initial upper ocean transient behavior has abated sufficiently during the first half of the simulations (Castro de la Guardia et al., 2015; Brunnabend et al., 2012), allowing us to explore the impact of the increased freshwater forcing in the halfsolid run.

Baffin Bay and Canadian Arctic Archipelago

Figure 4.2 shows the differences in temperature averaged over the upper 750 m between the *halfsolid* and *noOGGM* run. An average warming of around 0.05 K throughout the bay is visible. There are three main mechanisms that cause this: i) increased northward heat transport through Davis Strait, ii) less net volume transport from the Arctic through the Canadian Arctic Archipelago (i.e., Nares Strait, Lancaster Sound, and Jones Sound; hereafter named CAA), which leads to less lateral heat loss, and iii) stronger stratification leading to less vertical mixing and thus less heat transfer from the warmer subsurface water to the atmosphere. These mechanisms were identified and described previously by Castro de la Guardia et al. (2015) in a study that conducted idealized NEMO experiments to investigate the effects of increased freshwater input along Greenland's (west) coast on Baffin Bay. Although Castro de la Guardia et al. (2015) increased the freshwater input at the east coast of Baffin Bay in all but one of their experiments, we observe some similar effects on the ocean properties in the Baffin Bay area in our simulations, where the main addition of freshwater is at the west coast of Baffin Bay. We find an increase in sea surface height (SSH) gradient from the eastern and western shelves of Baffin Bay towards its center, even though the increase in the eastern part is roughly one order of magnitude smaller than the one found by Castro de la Guardia et al. (2015). This leads to a stronger cyclonic circulation in Baffin Bay (see Fig. 4.3), which in turn leads to enhanced vertical velocities, moving warmer subsurface waters from the West Greenland Current (WGC) to shallower depths. The lower increase in Baffin Bay temperatures we find compared to Castro de la Guardia et al. (2015) might be explained by smaller increases in sea surface height gradients and stratification, since our additional freshwater input to Baffin Bay is smaller by roughly a factor of 5 (50) compared to their experiment with the lowest (highest) additional freshwater forcing along Greenland's west coast.

We also find an increase in northward (positive) volume transport through Davis Strait throughout our simulation period in the *halfsolid* run compared to the *noOGGM* run, which is balanced by an increasing southward (negative) outflow, along the cyclonic pattern of the Baffin Bay Gyre (see Fig. 4.4). The increase in northward volume flow is not caused by an increase in northward freshwater flux, since the amount of freshwater added to the Greenland coast south of Davis Strait does not differ between our two setups. Moreover, the average increase in northward heat transport we find in the second half of our simulations is approx. 1.1 TW, which is roughly 5 % of the average total northward heat transport and roughly double the increase found by Castro de la Guardia et al. (2015). Northward volume transport through Davis Strait increases in the *halfsolid* run compared to the *noOGGM* run. This increase in volume flux roughly doubles from 0.025 to 0.05 Sv when comparing the first to the second half of our simulation period. The increase in northward heat inflow we find nearly quadruples from ~0.25 though (see Fig. 4.4). This increase of the heat to volume transport ratio is likely associated with the increase in the WGC's strength and thus larger transport of warm Atlantic water into Baffin Bay. The variability of the difference in heat transport through Davis Strait between our two NEMO setups also increases strongly in the second half of our simulation period, which is probably a spin-up effect. Interestingly, the increase in northward heat transport through Davis Strait we find is higher (1.1 vs 0.5 TW), but the average warming in Baffin Bay is smaller than the differences diagnosed by Castro de la Guardia et al. (2015) (~0.05 vs. ~0.3). This points to the significance of changes associated to an increasing SSH gradient and stratification of Baffin Bay, since they are much smaller in our experiments, as the difference in freshwater input to Baffin Bay between our two experiments is much smaller compared to even the smallest change in Castro de la Guardia et al. (2015).

Across the CAA we observe the following changes: an increase in temperatures in the Lancaster and Jones Sound regions due to the enhanced northward heat transport, and a decrease in salinity due to increased freshwater input (see Figs. 4.5 and 4.A.3). Particularly in areas close to Ellesmere Island's north coast we find a slight decrease in potential temperature though (~0.03 K), possibly due to increased freshwater input and the concomitant increase in vertical mixing near the surface in our setup. This can bring up warmer water to the surface, which is then subject to increased vertical heat loss.

Concerning volume fluxes through the CAA, the only statistically significant change we find, is a positive shift in volume flux (~0.02 Sv) through Lancaster Sound, which is ~3 % of the 0.6 Sv total southward (negative) flux (see Fig. 4.A.4) into Baffin Bay through this channel. Though there is a small (0.014 Sv $\approx$ 0.8 %) decrease in volume flux through the CAA into Baffin Bay, it is statistically not significant, which is in contrast to changes between 9 and 46 % in the experiments demonstrated by Castro de la Guardia et al. (2015). Volume flux through the CAA into Baffin Bay mainly is controlled by the SSH gradients across the straits connecting Baffin Bay to the Arctic Ocean (McGeehan and Maslowski, 2012; Hu and Myers, 2014), which means that these gradients did not change in a way that significantly alters the total volume flux between the Arctic and Baffin Bay comparing our two NEMO experiments.

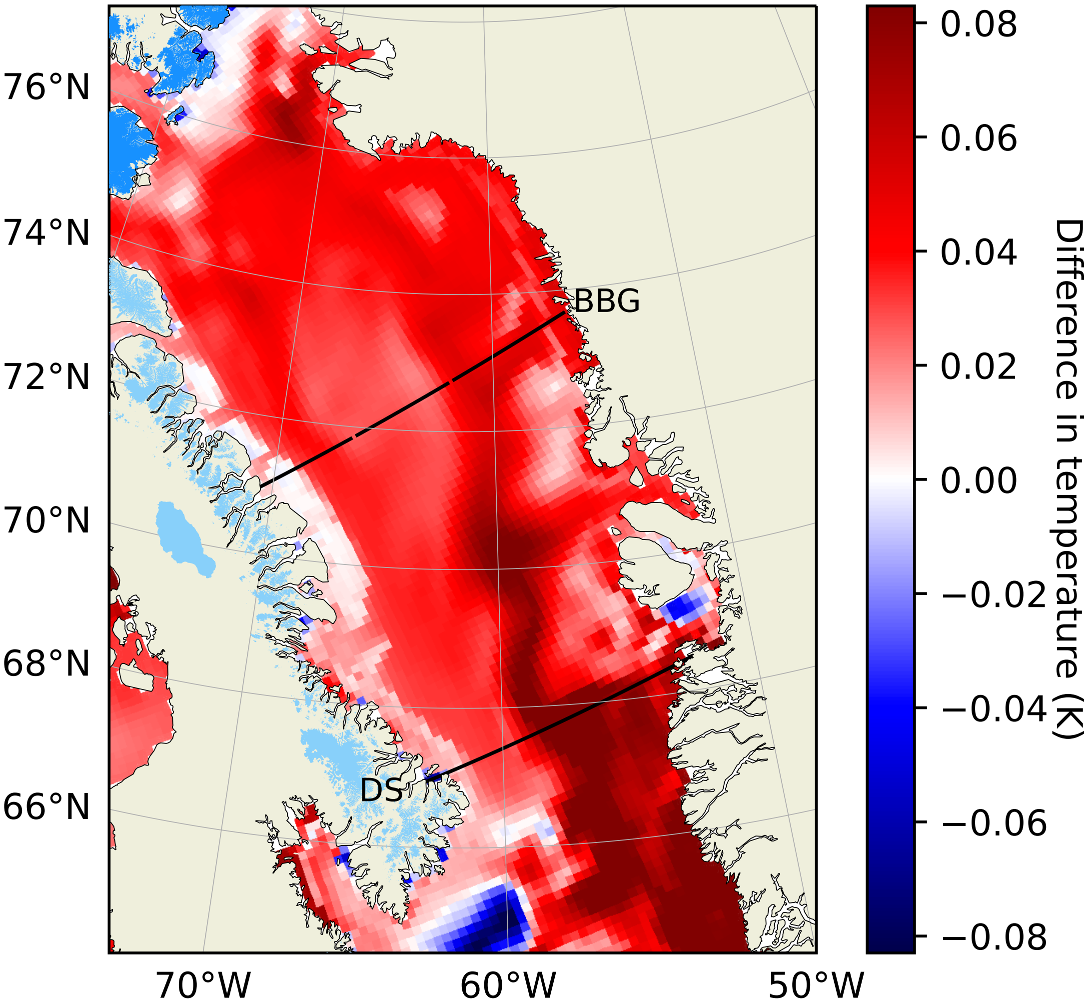

Figure 4.2: Difference in potential temperature averaged over up to 750 m water depth between the *halfsolid* and the *noOGGM* NEMO runs in Baffin Bay. BBG stands for the Baffin Bay Gyre section and DS for the Davis strait section. Colored land area indicates glacierized area as recorded in the RGI.

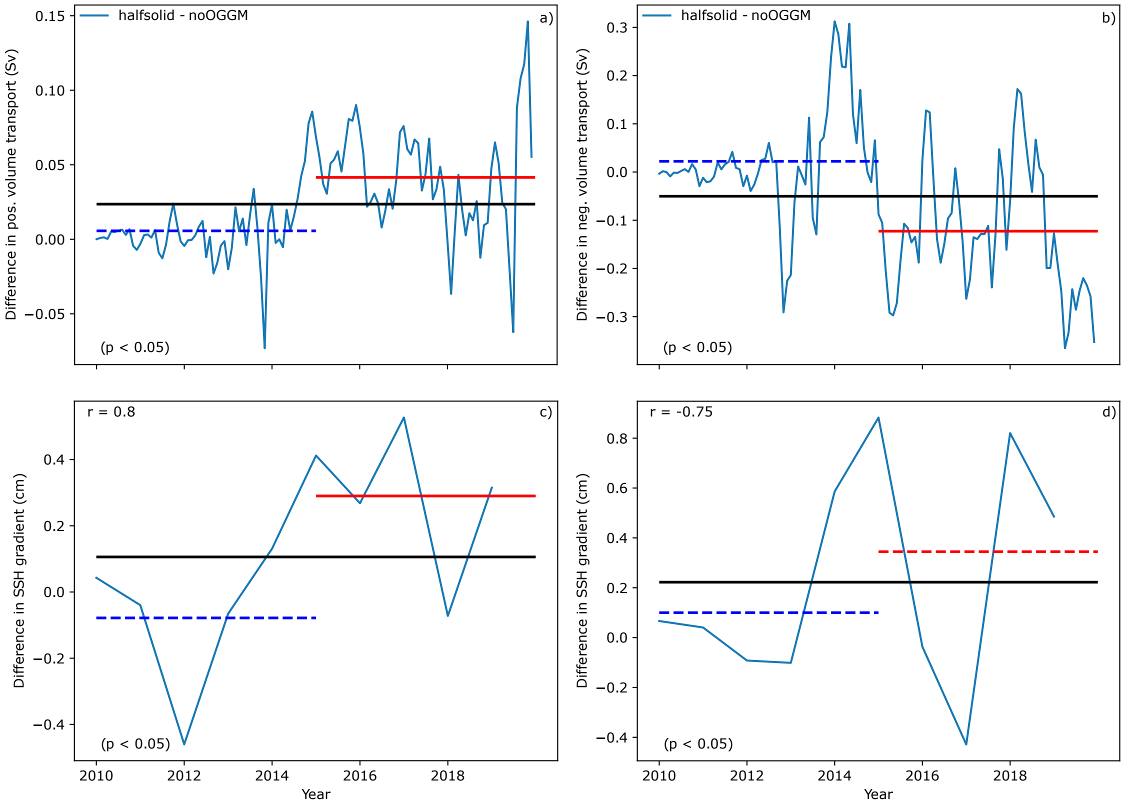

Figure 4.3: Differences in gyre strength and SSH gradients in Baffin Bay between the *halfsolid* and the *noOGGM* NEMO runs. a): northward (positive) volume transport through eastern part of the Baffin Bay Gyre (BBG) section in Fig. 4.2, b): southward (negative) volume transport through western part of the BBG section in Fig. 4.2, c): annual mean SSH gradient between point with the highest average SSH in the eastern part of the BBG section and the point with the lowest average SSH in the center part of the section, d): same as c), but for the point with the highest average SSH in western part of the BBG section. Differences in SSH gradients are displayed as annual means for better visibility. The lines in panels a) and b) show average differences over the first (blue) and last (red) five years, as well as over all years (black) of the model integrations. Values in the upper left corners of panels c) and d) are the correlation coefficients between annual mean north-/southward volume flux and SSH gradients from the east/west to the center of the Baffin Bay Gyre. Differences between the two NEMO runs that are statistically significant, according to paired Student's t-tests ($p < 0.05$), are drawn as solid lines and dashed otherwise. Values in the lower left corners show the p-values of paired Student's t-tests of differences between the differences of the first and last five modeled years.

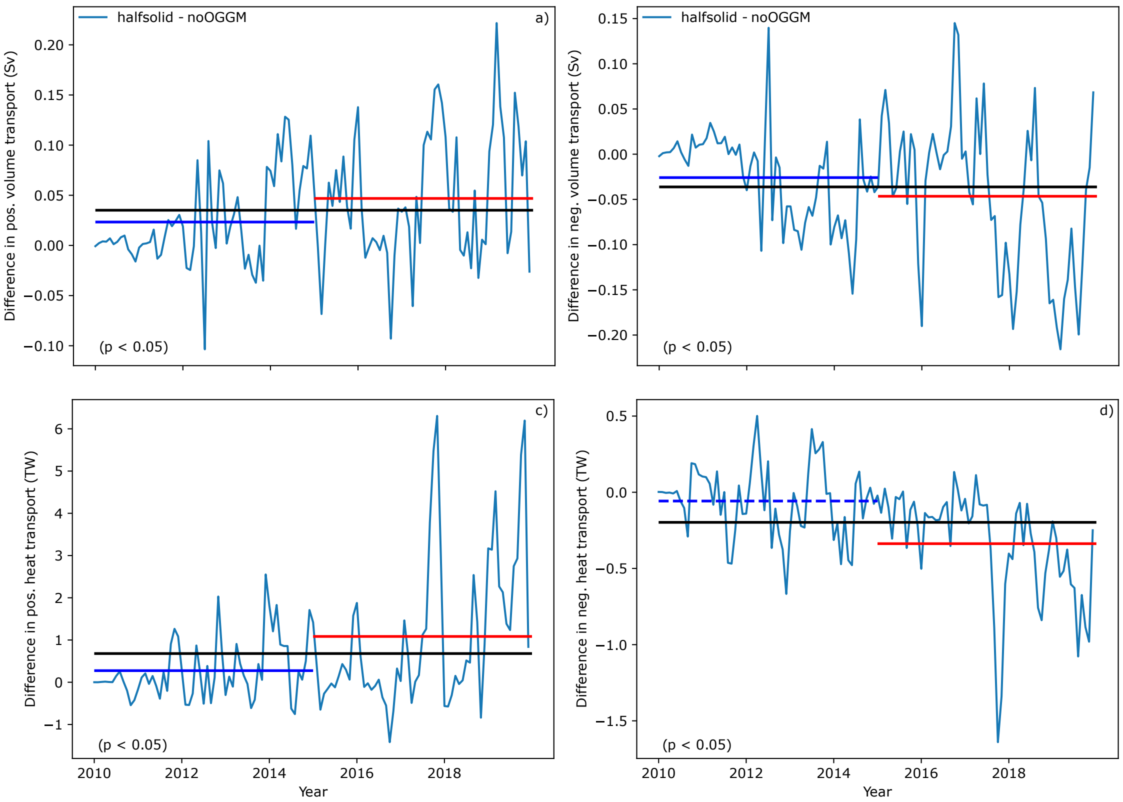

Figure 4.4: Differences in north- and southward volume and heat transport through Davis Strait between the *halfsolid* and the *noOGGM* NEMO runs. a): northward (positive) volume transport through Davis Strait (DS) section in Fig. 4.2, b): southward (negative) volume transport through DS, c): northward heat transport through DS, d): southward heat transport through DS. The lines show average differences over the first (blue) and last (red) five years as well, as over all years (black) of the model integrations. Differences between the two NEMO runs that are statistically significant, according to paired Student's t-tests ($p < 0.05$), are drawn as solid lines and dashed otherwise. Values in the lower left corners show the p-values of paired Student's t-tests of differences between the differences of the first and last five modeled years.

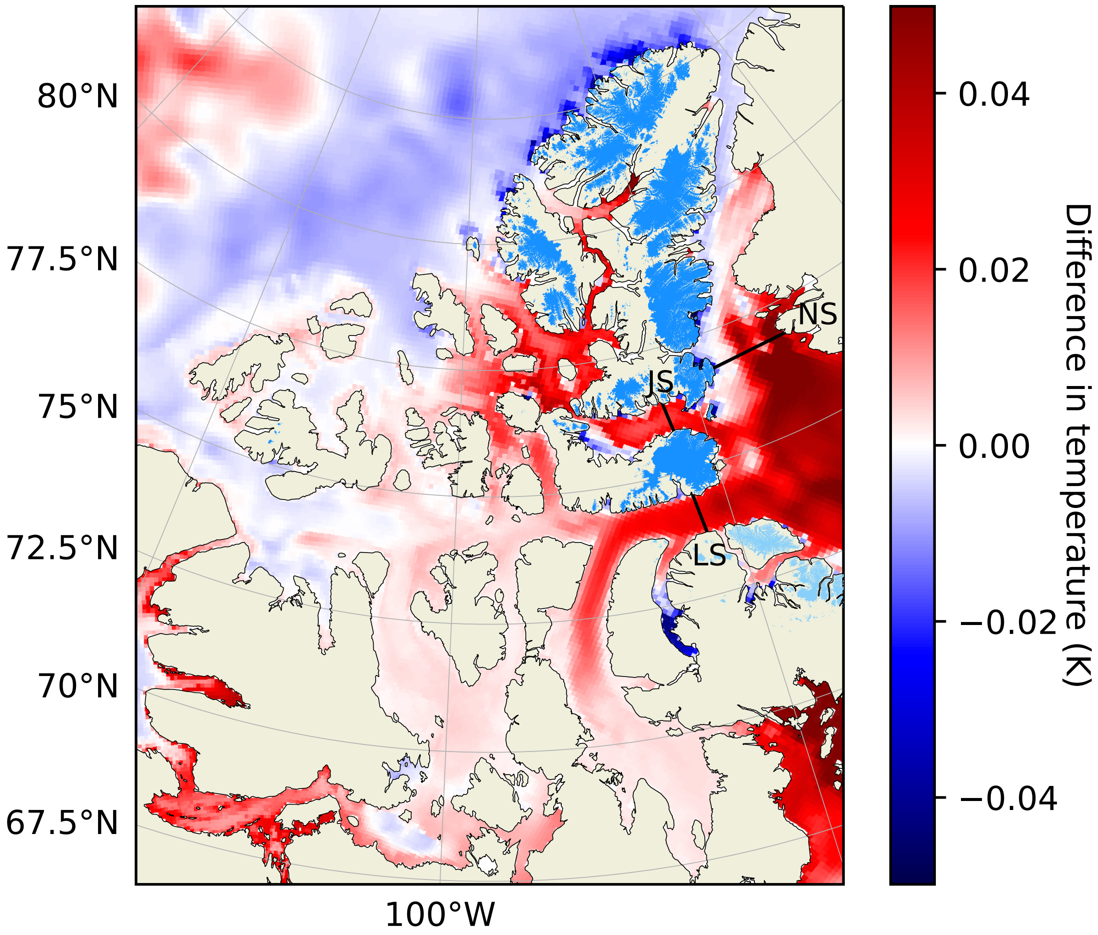

Figure 4.5: Difference in potential temperature averaged over up to 750 m water depth between the *halfsolid* and the *noOGGM* NEMO runs in the CAA region. NS stands for the Nares Strait, JS for the Jones Sound, and LS for the Lancasters sound section. Colored land area indicates glacierized area as recorded in the RGI.

AMOC and Subpolar Gyre

Although there are differences in mixed layer depth in the Labrador Sea region between our two NEMO runs (see Fig. 4.A.6), they are mostly not substantial, as the differences lie well within the model's as well as observed interannual variability (Kieke and Yashayaev, 2015). Moreover, we do not find a statistically significant difference in north-/southward or total volume flux across the 47°N latitude in the Atlantic, which indicates that there are no significant differences in AMOC strength between the *halfsolid* and *noOGGM* experiment.

Figure 4.6 shows differences in SSH as well as in density, temperatures, and salinity between our two NEMO runs. Regarding SSH, we find a decrease in the eastern and an increase in the western part. The reverse is true for differences in density, which are primarily driven by colder temperatures, since salinity decreases, but density increases in the eastern subpolar gyre area. The decrease in SSH and increase in density of the upper upper 750 m in the eastern subpolar gyre indicate an increase in its strength (Hakkinen and Rhines, 2004; Chafik et al., 2022). Moreover, the pattern of increased salinity around the northern subpolar gyre (see Fig. 4.6 c)) resembles the pattern found by Born et al. (2016) comparing a strong to a weak mode of the gyre.

Hence, a relation between the strength of deep convection (mixed layer depth) in the Labrador Sea and the strength of the subpolar gyre might be reflected in our results. The proposed relation is as follows: due to decreased density, in our case caused by increased freshwater input, deep convection decreases and SSH increases in the Labrador Sea. This leads to more of the water that is cooled by surface heat loss in the Labrador Sea to leave that area and be accumulated in the center of the subpolar gyre (see Fig. 4.6 panel d)). In turn, an increased density and decreased SSH in the eastern subpolar gyre lead to an increase in the gyre's strength, moving more of the Atlantic water around it. Sun et al. (2021) proposed oscillating feedbacks of the subpolar gyre's strength and the deep convection in the Labrador Sea, asserting that an increased gyre strength leads to an increased density transport into the Labrador Sea, increasing the deep convection. This would decrease SSH in the Labrador Sea and the export of cooled water to the gyre's interior, thereby decreasing it's strength. In panel b) of Fig. 4.6 and in Fig. 4.A.6, some areas of the northeastern Labrador Sea indeed show a slightly higher density and mixed layer depth, hinting at this feedback potentially being in effect. While, as stated above, the changes in mixed layer depth we found are small, the coherence of our findings with mechanisms linking Labrador Sea deep convection and the subpolar gyre's strength presented in previous publications is intriguing. Further research might be conducted investigating whether the positive feedback of the oscillation mechanism proposed by Sun et al. (2021) can offset increased freshwater input over a longer time span.

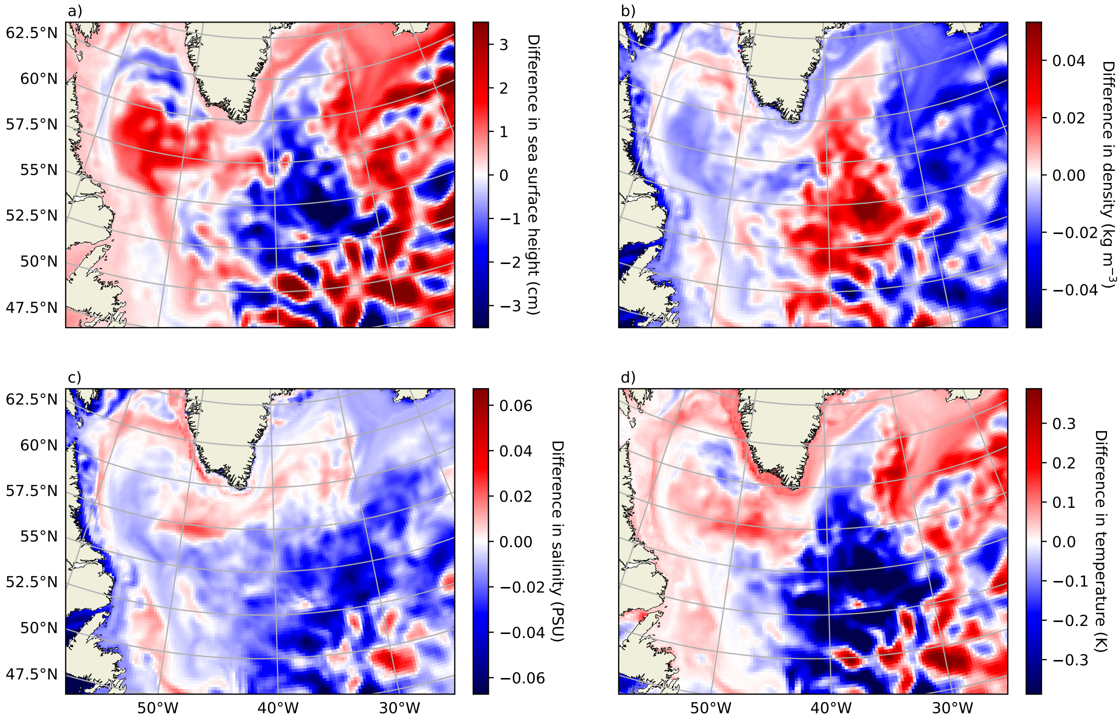

Figure 4.6: Difference in a) SSH, b) density, c) salinity, and d) potential temperature averaged over up to 750 m water depth between the *halfsolid* and the *noOGGM* NEMO runs in the supolar gyre region.

Barents and Nordic Seas

We show the SSH difference between the *halfsolid* and the *noOGGM* runs in Fig. 4.7. The increased freshwater input from Svalbard and the Russian Arctic in the *halfsolid* run (see Fig. 4.A.1) increases the SSH in the northern Barents Sea. This leads to an increased anticyclonic circulation around that area, leading, in turn, to a lower volume flux through the Barents Sea Opening. This implies a lower (positive) flux of Atlantic water into the Barents Sea, decreasing temperatures in most parts (see Fig. 4.8 and Fig. 4.9 panel a)). The volume flux out of the Barents Sea increases, leading to a net volume flux decrease of 0.11 Sv (∼4 %). However, the flux of freshwater (using a reference salinity of 34.8 PSU) out of Barents Sea into the North Atlantic decreases by 8 % (Fig. 4.9 panel c)), meaning that the additional freshwater input from Svalbard and the Russian Arctic remains in the Barents Sea and Arctic ocean. This also shows in the decreased salinity values in the western Barents Sea and in the Kara Sea (see Fig. 4.A.5)

The Atlantic water not entering the Barents Sea is routed towards the Fram Strait instead, leading to an increased northward (positive) volume flux (see Fig. 4.9 panel b)). Some of this warm water subsequently enters the Barents and Kara Seas from the north (see Fig. 4.8), while the remainder follows roughly the eastern Arctic shelf break (see next section). This increased positive volume flux through Fram Strait begins after roughly half of the NEMO integration time, presumably due to the buildup of meltwater in the spin-up period. This increase in volume flux into the Arctic ocean through Fram Strait is accompanied by an increased outflux, yielding a net increase in northward (positive) volume flux through Fram Strait of ∼0.24 SV (≈ 9 %). The southward (negative) flux of freshwater through Fram Strait is insignificantly small, indicating that the enhanced southward flux is due to enhanced recirculation of Atlantic water. Since not all of the increased volume flux into the Arctic through Fram Strait can be explained by the net positive (eastward) volume flux difference we find for the Barents Sea, we also analyzed the volume fluxes through the Denmark Strait, finding a decrease in southward (negative) as well as an increase in northward (positive) transport. The net increase of ∼0.1 Sv (≈ 3 %) through Denmark Strait almost closes the gap between the net decrease of Atlantic water volume flux into the Barents Sea and the net increase of the same into the Arctic ocean through Fram Strait. This change in volume fluxes through Denmark Strait could be linked to the changes in SSH in the areas of the Norwegian and Greenland Seas as well as around Iceland (see Figs. 4.7 and 4.6 a)), indicating an increased strength of the gyres present in these areas (Raj et al., 2019; Chatterjee et al., 2018).

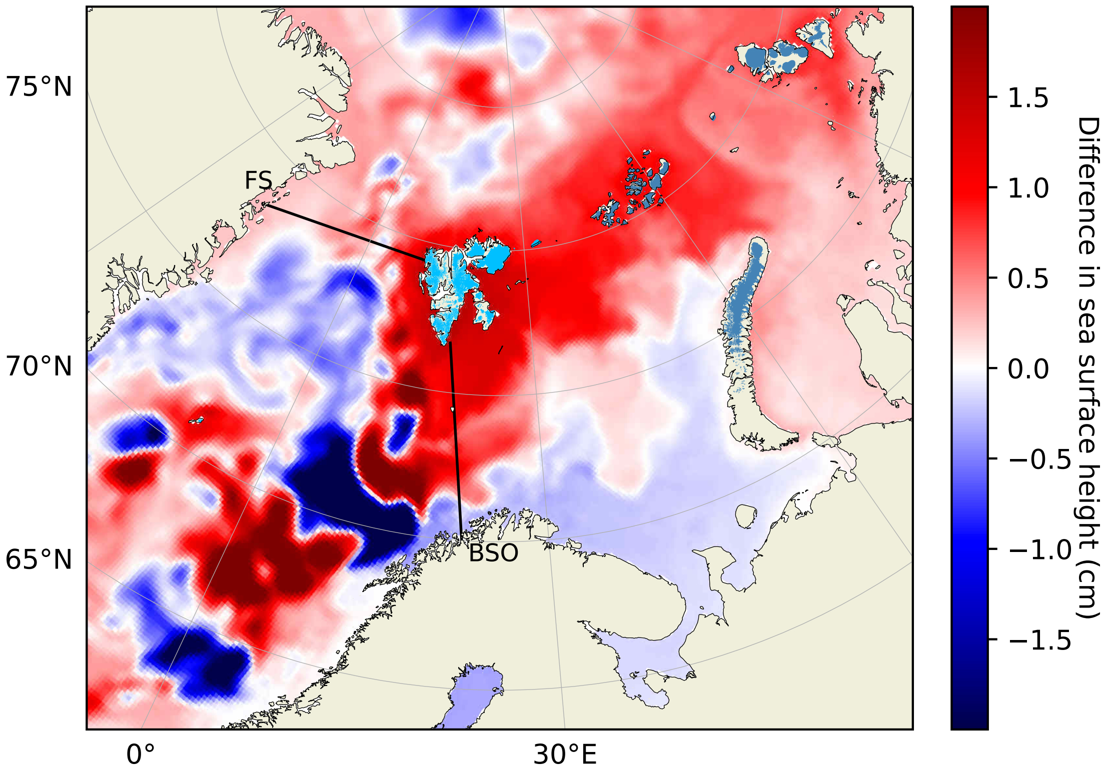

Figure 4.7: Difference in sea surface height between the *halfsolid* and the *noOGGM* NEMO runs in the Barents and Nordic Seas area. FS stands for Fram Strait and BSO for Barents Sea Opening sections. Colored land area indicates glacierized area as recorded in the RGI.

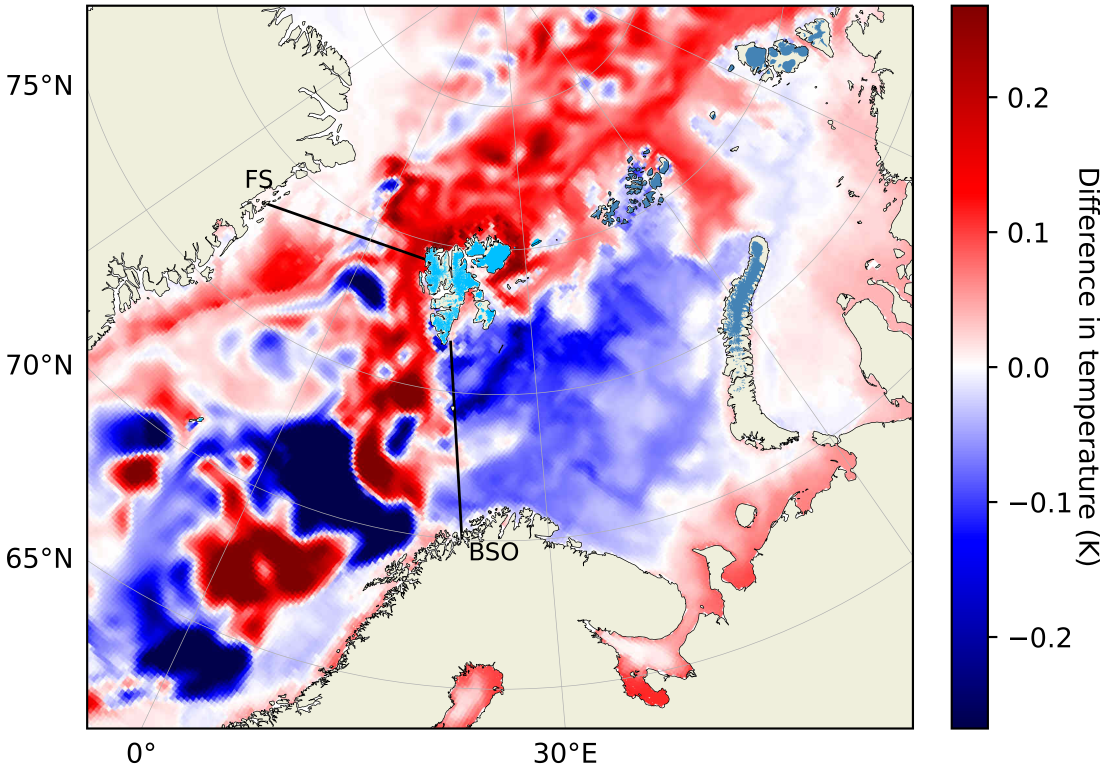

Figure 4.8: Difference in potential temperature averaged over up to 750 m water depth between the *halfsolid* and the *noOGGM* NEMO runs in the Barents and Nordic Seas area. FS stands for Fram Strait and BSO for Barents Sea Opening. Colored land area indicates glacierized area as recorded in the RGI.

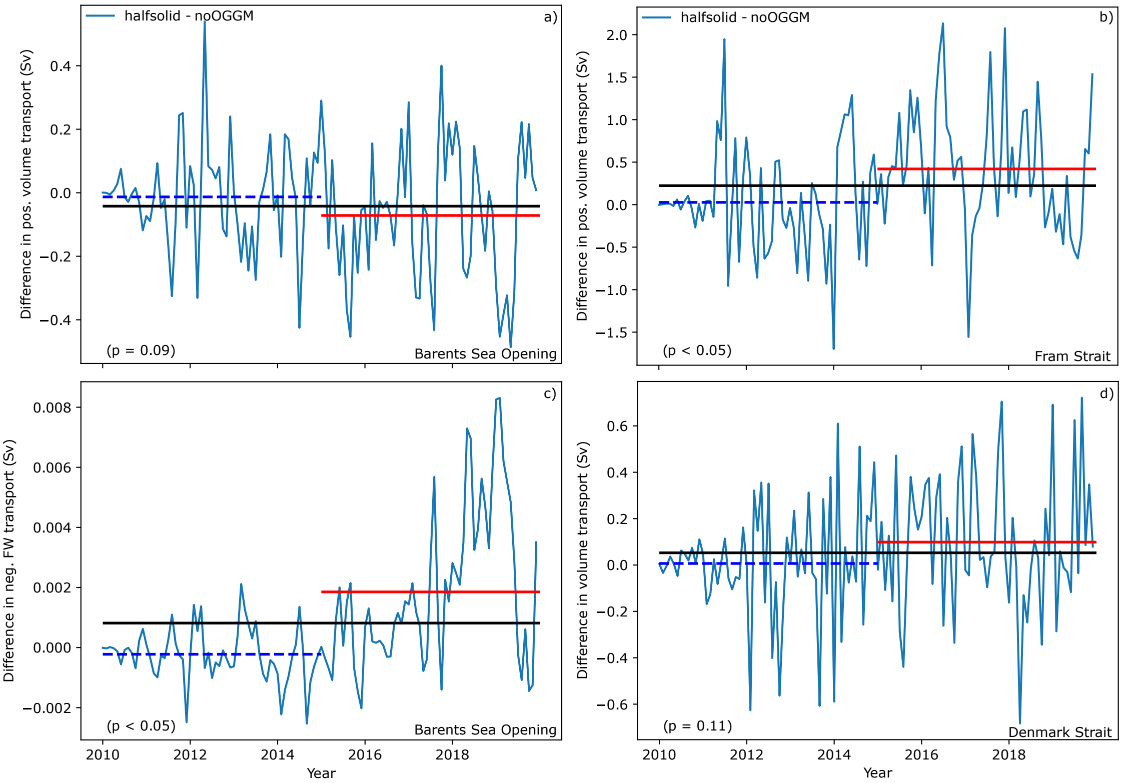

Figure 4.9: Difference in positive transport through Fram Strait (FS) and the Barents Sea Opening (BSO) between the *halfsolid* and the *noOGGM* NEMO runs. Positive transport through FS means northward, while positive transport through BSO means eastward. The horizontal lines show average differences over the first (blue) and last (red) five years, as well as over all years (black) of the model integrations. Differences between the two NEMO runs that are statistically significant, according to paired Student's t-tests ($p < 0.05$), are drawn as solid lines and dashed otherwise. Values in the lower left corners show the p-values of paired Student's t-tests of differences between the differences of the first and last five modeled years.

Arctic Ocean and Sea Ice

We find a band of warmer water in the *halfsolid* run in the eastern part of the Arctic Ocean that follows the shelf break (Arctic Circumpolar Current; see Fig. 4.10)) and is caused by the increased import of Atlantic Water through Fram Strait, which was discussed in the previous section. Inspecting differences in salinity, a patch of relatively strongly increased salinity north of the New Siberian Islands is visible (see Fig. 4.A.8). In addition, we find an area of decreased SSH around the Mendeleev Ridge, which might point to changes in circulation at the junction of the Beaufort Gyre and the Transpolar Drift (see Fig. 4.A.7). The changes in salinity as well as in SSH can be explained by the the enhanced Arctic Circumpolar Current, as it might decrease the export of fresher water from the shelf to the interior of the Arctic ocean, leading to the saltier water from the Atlantic to be accumulated on the East Siberian Shelf and around the Mendeleev Ridge. This is consistent with Figs. 4.A.8 and 4.A.7 indicating that more freshwater stays on the eastern Arctic shelfs, as we see decreased salinity and increased SSH there.

The largest decreases in sea ice thickness between the two NEMO simulation can be found in the western Greenland Sea, north of Svalbard, and in the CAA (Fig. 4.11). The decrease in sea ice thickness in the former two areas is caused by the changes in the pathway of Atlantic Water in the Nordic Seas. Enhanced transport through Fram Strait and enhanced recirculation towards Greenland's east coast increase the advection of heat in these regions (see Fig. 4.8). In the CAA region, we find a similarly strong decrease in sea ice thickness. The lower increase in upper layer temperature in the CAA compared to the Fram Strait and eastern Greenland areas, suggests that other factors than increased ocean heat content play a role there. The decrease in ice thickness in the CAA is likely also driven by less sea ice advection, since the increase in SSH across the region (see Figs. 4.A.9 and 4.A.7) leads to a divergent flow out of the area. As expected from the higher temperatures in Baffin Bay in the *halfsolid* run, the sea ice is slightly thinner in this area as well. The only area where we find a slightly increased sea ice thickness is between the Barents and Kara Sea, which is most probably related to the decreased heat transport into Barents Sea due to the rerouting of Atlantic Water described above. That there is a net sea ice thickness decrease in the northern hemisphere when comparing our two NEMO experiments is intriguing, since we only add freshwater to the ocean, which should not increase its heat content. This points to structural changes in ocean heat distribution due to the increased freshwater input in the *halfsolid* experiment.

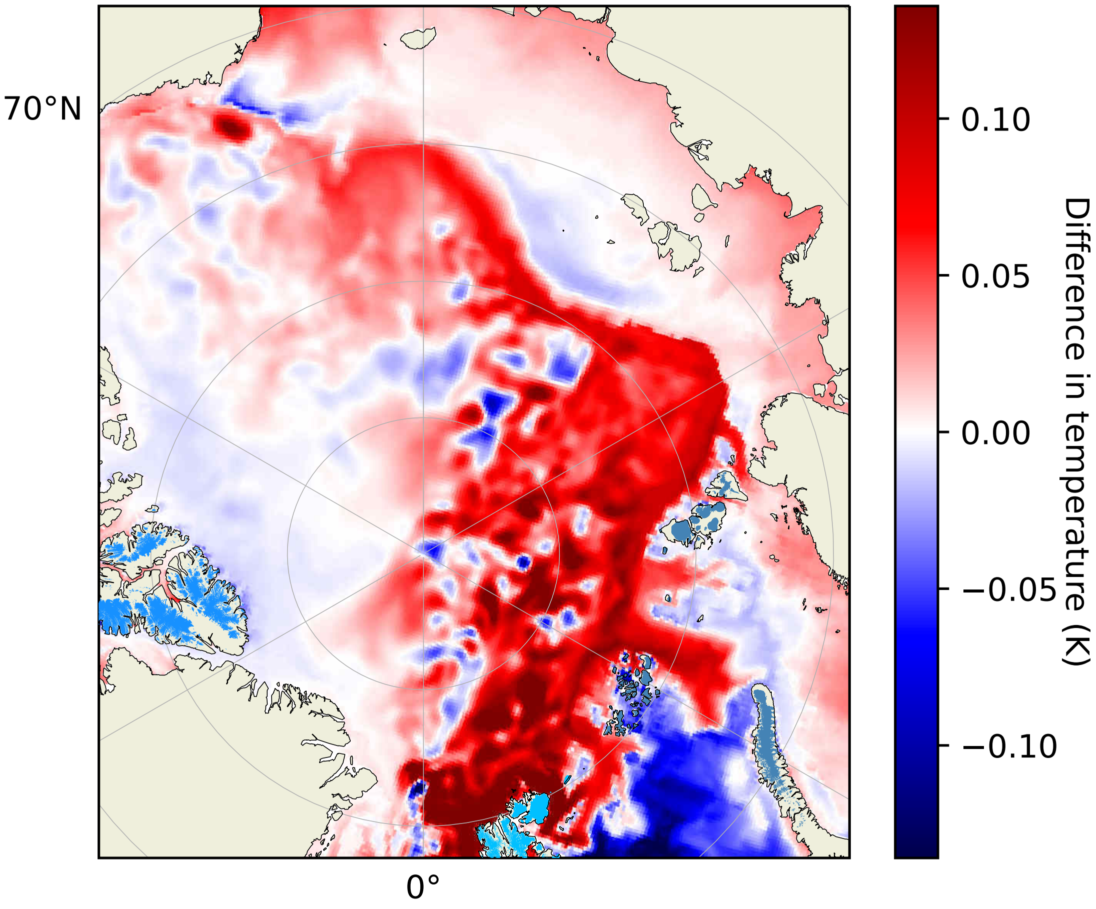

Figure 4.10: Difference in potential temperature averaged over up to 750 m water depth between the *halfsolid* and the *noOGGM* NEMO runs in the Arctic. Colored land area indicates glacierized area as recorded in the RGI.

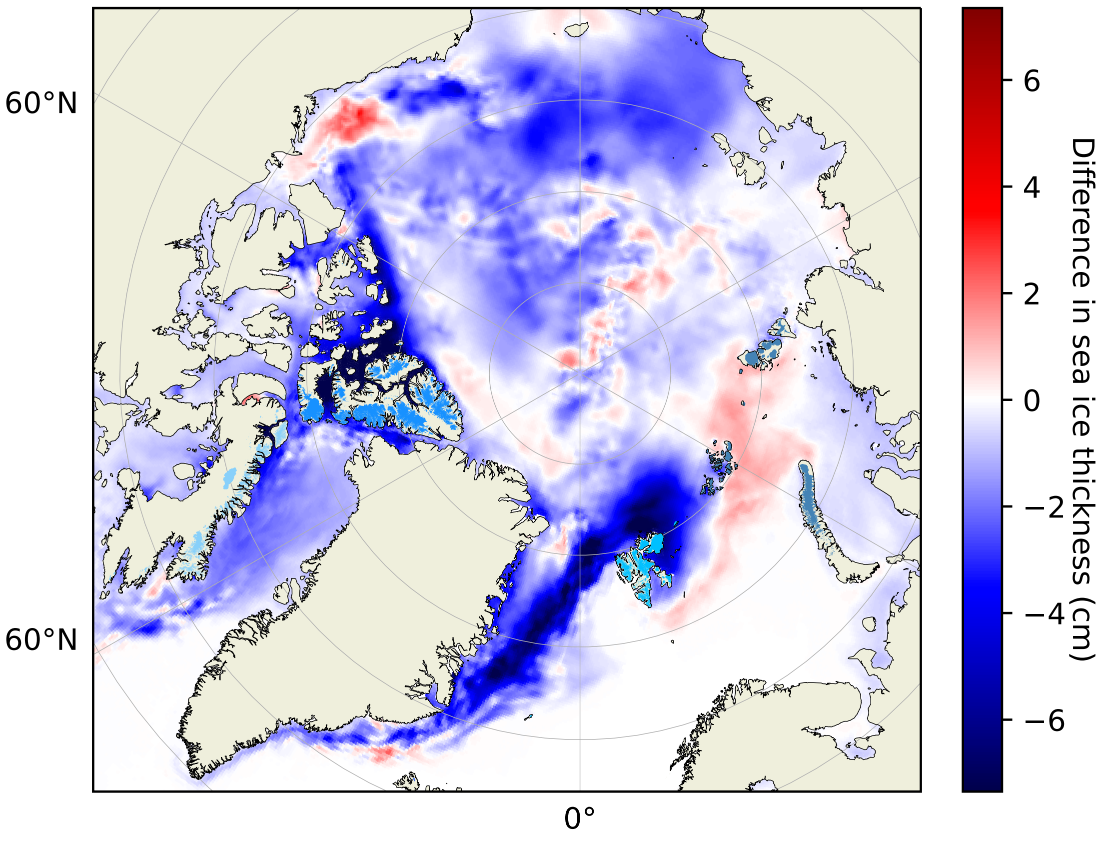

Figure 4.11: Difference in sea ice thickness between the *halfsolid* and the *noOGGM* NEMO runs. Colored land area indicates glacierized area as recorded in the RGI.

4.3.2 Glacier model

Figure 4.12 and Table 4.1 show the results of our OGGM runs with the submarine melt parameterization described above. Submarine melt accounts for between 10 and 27 % of total frontal ablation according to the method we applied, exhibiting a relatively large interquartile range of the results with different valid parameter sets from the latin hypercube sampling. We find the lowest median submarine melt fraction in Arctic Canada North (12 [10, 30] %) and the highest in Arctic Canada South (35 [18, 44] %). Note that we exclude Flade Isblink from our results for the Greenland periphery here, as its RGI outlines are erroneous and it maintains an ice shelf (Möller et al., 2022), making the dynamical modeling of it problematic in our framework. Tables 4.1 and 4.2 provide an indication of the prevalent frontal ablation mechanisms in the different regions. That we estimate the largest fraction of frontal ablation caused by submarine melt for the region Arctic Canada South, but the highest thermal forcing for Svalbard, indicates that in the latter region frontal mass loss is more dynamically driven. That is because in OGGM, volume below flotation at the front is removed and added to the calving output variable (i.e., no ice shelves can form). Therefore, if much ice is removed by the flotation criterion, less can be removed by submarine melt when total frontal ablation rates are constrained with observational estimates.

Table 4.1 shows that there is no large difference in the submarine melt estimates when applying the thermal forcing derived from the *noOGGM* runs. This suggests that there are only small coupling effects on glacier mass change over the decadal timescale we investigated here. Tab. 4.2 shows that the differences in thermal forcing in the vicinity of marine-terminating glaciers are small on average over the last five years of the NEMO integration. We find the largest increase in Svalbard, caused by the rerouting of warm and saline Atlantic Water from the southern Barents Sea opening to the Fram Strait, where some of it enters the Barents Sea from the north close to Svalbard (see Fig. 4.8). This is also the region where we find the strongest increase in submarine melt using the *halfsolid* NEMO run output compared to the *noOGGM* output (see Tab. 4.1). In contrast, thermal forcing is slightly decreased in the *halfsolid* run in Arctic Canada North and the Russian Arctic. In the latter case this is due to less heat transport from the Atlantic into Barents Sea. Tables. 4.1 and 4.2 furthermore indicates a perceptible influence of the dependence on water depth of Eq. 4.2. For example, in Arctic Canada South we find less of an increase in submarine melt at the third than at the first quartile comparing the *halfsolid* to the *noOGGM* NEMO run. This is probably because with stronger submarine melt, we simulate stronger retreat of marine-terminating glacier fronts due to undercutting, which, depending on the submerged bed topography, can decrease the water depth. This leads to a decreased sensitivity to subglacial discharge in Eq. 4.2, while the amount of subglacial discharge is the same in both OGGM simulations. The Greenland periphery is the only region for which we find a smaller absolute percentage change in submarine melt rates than in thermal forcing (see Tabs. 4.1 and 4.2), likely indicating that in this region subglacial discharge has a stronger influence on submarine melt in our model than in the other regions.

Table 4.3 displays the median and interquartile range of valid parameter sets we found in the different regions as well as the median and interquartile range of the number of valid parameter sets found per glacier. It shows that there are differences between the regions for the parameters B, β, and to a minor extent A, which are related to the efficiency of heat transfer from the open ocean into the glacier front and the increase of this heat transfer due to subglacial meltwater discharge. Greenland periphery and Arctic Canada South exhibit the largest median (and third quartile) values for A and B. Moreover, we generally found more valid parameter sets for the glaciers in the Greenland periphery and Arctic Canada South. Those findings point to regional differences in the valid parameter ranges and it appears to be the case that the parameter range could be adjusted for the individual regions/glaciers. While our aim in this work was to produce a first estimate of submarine melt of glaciers outside the GrIS, finding more accurate parameter values for the parameterization warrants further investigations in the future.

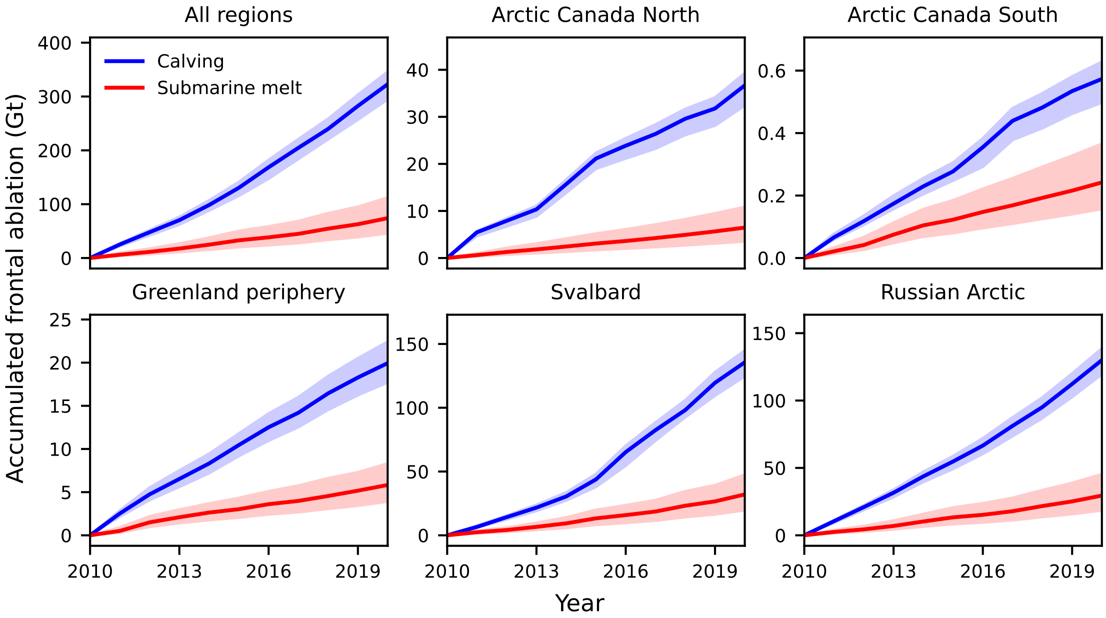

Figure 4.12: Estimated amounts of the two frontal ablation components submarine melt and calving. Solid lines represent the median and shadings the interquartile range of the valid parameter sets. Note the different scales for the different regions.

Table 4.1: Estimates of submarine melt rates (median [interquatile range]) between 2015 and 2019 of marine-terminating glaciers in the NEMO-ANHA4 domain. Q_{sm} are submarine melt rates, Q_{fa} the total frontal ablation rates, and ΔQsm the difference in submarine melt rates between the *halfsolid* and the *noOGGM* NEMO runs over the period. n is the number of marine-terminating glaciers in the region.

Region	Q_{sm} (Gt a^{-1})	Q_{sm} / Q_{fa} (%)	ΔQsm (%)	n
03 Arctic Canada North	0.7 [0.4, 1.1]	12 [10, 30]	-2.9 [-2.9, -3.9]	225
04 Arctic Canada South	0.03 [0.02, 0.04]	35 [18, 44]	0.7 [1.1, 0.5]	86
05 Greenland periphery	0.5 [0.3, 0.8]	22 [11, 34]	0.9 [1.2, 1.7]	491
07 Svalbard	3.7 [2.3, 5.5]	19 [10, 27]	6.7 [5.9, 7.0]	163
09 Russian Arctic	3.2 [2.0, 4.9]	16 [11, 27]	-2.7 [-2.6, -2.5]	359
All regions	8.1 [4.9, 12.5]	17 [10, 27]	1.5 [1.3, 1.4]	1325

Table 4.2: Average of ocean variables in the vicinity of marine-terminating glacier fronts over 2015 to 2019, weighted by submerged frontal cross-section area. T_f is thermal forcing, T potential temperature, S salinity, and d_o the distance-averaged ocean depth of grid cells taken into account for the calculation. The percent difference between the *halfsolid* and the *noOGGM* NEMO runs is given in the brackets.

Region	T_f (K)	T (°C)	S (PSU)	d_o (m)
03 Arctic Canada North	0.67 (-1.4)	-1.21 (-0.6)	33.0 (-0.1)	236.4
04 Arctic Canada South	0.87 (0.4)	-0.99 (0.6)	32.3 (-0.1)	172.8
05 Greenland periphery	1.61 (1.9)	-0.21 (12.7)	32.7 (-0.0)	145.6
07 Svalbard	2.02 (3.5)	0.13 (128)	34.2 (-0.2)	124.6
09 Russian Arctic	1.19 (-1.7)	-0.74 (-2.6)	34.4 (-0.1)	157.2

Table 4.3: Ranges (median [interquatile range]) of parameter values in Eq. 4.2 complying with total frontal ablation estimates from satellite-derived observations (Kochtitzky et al., 2022). n is the median number of valid parameter sets found for individual glaciers in the regions.

Region	A x 10^{-4}	α	B x 10^{-2}	β	n
03 Arctic Canada N.	1.5 [0.6, 3.6]	0.48 [0.37, 0.58]	1.5 [0.4, 5.6]	1.53 [1.21, 1.73]	20 [16, 24]
04 Arctic Canada S.	1.8 [0.6, 3.9]	0.48 [0.37, 0.58]	2.1 [0.4, 11.0]	1.51 [1.22, 1.73]	25 [19, 25]
05 Greenland peri.	1.8 [0.6, 3.9]	0.48 [0.37, 0.58]	2.1 [0.4, 11.0]	1.51 [1.26, 1.73]	25 [15, 25]
07 Svalbard	1.2 [0.6, 2.4]	0.47 [0.34, 0.57]	0.8 [0.2, 2.1]	1.41 [1.20, 1.66]	10 [4, 13]
09 Russian Arctic	1.5 [0.6, 3.6]	0.48 [0.37, 0.58]	0.8 [0.4, 3.3]	1.46 [1.21, 1.71]	16 [14, 19]

4.4 Discussion

Although our rather simple approach is sufficient to produce first estimates of the coupling effects between OGGM and NEMO on a decadal timescale, we now lay out some aspects that could be improved in future works on the subject of northern hemisphere ice-ocean interactions outside the GrIS. Concerning the aspect of using OGGM output as an input for NEMO, it is arguable whether putting the meltwater runoff and calving estimates derived from OGGM simply into the NEMO grid cell nearest to the glacier terminus is a sound approach. Particularly in regions with complex topography and/or fjord systems, as for example the CAA, more sophisticated routing approaches might be advisable. Also, whether the *halfsolid* assumption is valid for regions outside Greenland needs to be investigated, since it is not clear how much of the iceberg mass actually melts within the fjords before the icebergs reach the open ocean/NEMO grid cell. When differentiating between solid and liquid discharge, the amount of submarine melt should be taken into account as well. Moreover, there might be other hydrological changes in glacierized areas, as, for example, more liquid and less solid precipitation, which might change the runoff from such regions systematically and should thus be included in the (baseline) freshwater forcing in future studies. Additionally, the baseline runoff and the Bamber et al. (2018a) data not covering the whole modeling period, might induce some uncertainty in our results, since the impact of the additional freshwater we examined could be altered. If, for instance, the ratio of the additional freshwater in the *halfsolid* run to the baseline plus Greenland runoff was larger (smaller), the impact would presumably be larger (smaller) as well. Ultimately, we did not aim to produce as accurate hindcasts as possible, but to obtain first estimates of the coupling effects between OGGM and NEMO, for which we consider a somewhat idealized setup appropriate.

We implicitly assume that the amount of submarine melt of glaciers outside the GrIS is so small that the amount of heat drained from the ocean necessary to produce this melt is negligibly small for the ocean heat budget. A rough estimate yields that approx. 2.9×10^{18} J a^{-1} would be needed for our median estimate of 8.1 Gt a^{-1} submarine melt. This is three orders of magnitude smaller than the estimated annual ocean heat uptake due to anthropogenic climate change (Cheng et al., 2022), indicating that the impact of submarine melt from glaciers outside the ice sheets is small on the global scale of the ocean heat budget, though it might be relevant on a local scale. Similarly, it would be interesting to see what the effect of adjusting the freshwater input's temperature to values different from the ocean surface temperatures are. Especially glacial meltwater might actually be colder, and thus such an adjustment might have an influence on the model results. Moreover, it might be the case that the increased surface layer mixing in all NEMO grid cells where we add liquid freshwater to the ocean is inaccurate. That is because in reality, the glacial meltwater is injected into the fjords, which is some distance apart from the open ocean, and the meltwater might be stored in the fjords for some time before being released to the ocean (Straneo and Cenedese, 2015; Sanchez et al., 2023). Thus, increased surface mixing might not actually occur at the open ocean locations where it is added to the NEMO-ANHA4 grid in our simulations.

Other aspects that could be improved regarding the modeling approach is the resolution of the ocean model, because the NEMO-ANHA4 setup is probably too coarse to yield a good representation of ocean eddies, which is of importance for processes in, e.g., the Labrador Sea (Pennelly and Myers, 2022). Furthermore, employing a fully coupled ocean-atmosphere model could provide insights into how ocean-atmosphere interactions might modulate the findings described in this work. Applying (passive) tracers in future studies could furthermore reveal where the melt from the OGGM glaciers moves in the ocean. Combining such potential improvements with a longer integration time of NEMO would consolidate knowledge about the influence of glaciers outside the GrIS on the ocean circulation and make sure potential spin-up effects have fully abated.

Concerning the sea ice thickness differences between our *halfsolid* and *noOGGM* NEMO experiments, it is intriguing that Labe et al. (2018) find a comparatively strong negative trend of sea ice thickness between 1979 to 2015 in some similar areas. These areas are the (north)western Queen Elizabeth Island in the CAA, and north of Svalbard. This might hint at the fact that increased freshwater input from glaciers outside Greenland is a relevant process for sea ice thickness changes.

On the side of OGGM, it became apparent from Table 4.3 that the parameter ranges sampled with the latin hypercube approach should be adjusted for individual regions. Xu et al. (2013) also suggest that the parameter values might actually differ between (high and low) subglacial discharge regimes. Moreover, the parameters in Eq. 4.2 probably depend on processes like subglacial hydrology and frontal plume formation, fjord circulation and subglacial discharge's effect on it, and on fjord-ocean water interchange as well as on the fjord geometry. As we find the largest regional differences in the parameters that control the efficiency of heat transfer from the open ocean into the glacier front in the absence of subglacial discharge (B and β), the differences in parameter values might be best explained by differences in fjord properties and fjord-ocean exchange. Since resolving individual fjords in an ocean circulation model would necessitate a very fine spatial resolution, it is too computationally expensive to run such a setup for all the relevant fjords and longer time periods. This points to the fact the fjord water properties in relation to open ocean water properties and subglacial discharge need to be better understood and incorporated in models in order to better constrain the involved parameters. Another aspect that could be further investigated concerning the submarine melt parameterization is which part of the ocean in the marine-terminating glaciers' vicinity should be used to source the thermal forcing from before inserting it in Eq. 4.2. Refining the distance from the glacier termini as well as the ocean depth range that should be taken into account could help to better constrain submarine melt estimates. Furthermore, dynamically modeling marine-terminating glaciers requires additional parameters compared to land-terminating glaciers that need to be constrained and might be interrelated. For instance, the frontal ablation parameter (k) depends on the choice of values for the parameters involved in the modeling of ice dynamics, since these parameters control the initial geometry given by the ice thickness inversion as well as the dynamical mechanisms of frontal ablation (Malles et al., 2023). This means that when aiming at most accurately simulating (frontal) ice dynamics, such parameters need to be better constrained, although this was not the aim in this work.

An obvious next step is the continuation of the simulations into future projections, since glacier mass loss is projected to increase in the future and hence the impact of increased freshwater input can be expected to grow. For this, a coupling scheme that updates the forcings between the models, for example in the form of a decadal step-coupling, would have to be developed. Regarding projections of future glacier mass loss, it would be interesting to investigate how future changes of ocean properties (different from the effects caused by the meltwater) will influence projected frontal ablation rates. For example, increased thermal forcing in combination with increased subglacial discharge would increase submarine melt rates, which might lead to stronger undercutting and thus accelerated retreat (Wood et al., 2021, 2018). On the other hand, the number of marine-terminating glaciers is already decreasing and projected to continue decreasing in the future (Kochtitzky et al., 2022; Malles et al., 2023), which might attenuate the potential increase in submarine melt.

4.5 Conclusion

We have presented the first investigation of ice-ocean interactions in the northern hemisphere outside the GrIS, applying one-way coupling of an ocean general circulation model (NEMO-ANHA4) and a glacier evolution model (OGGM) for the years 2010 to 2019. On the ocean side, we found that the NEMO simulation forced with freshwater input derived from glacier mass loss estimates given by OGGM showed considerable differences to the experiment solely forced with freshwater input from the GrIS. Consistent with what has been found in a previous study on the influence of increased freshwater input from the western GrIS on Baffin Bay, we found an increased ocean heat content in this region. We also found changes in the Nordic Seas that were brought about by the increased freshwater input around Svalbard and the Russian Arctic and lead to a decreased transport of Atlantic Water into the Barents Sea, causing this water to be rerouted through Fram Strait into the Arctic. Furthermore, we find sea surface height changes in the Baffin Bay, the CAA, the Nordic Seas, the central subpolar gyre and even in the Arctic Ocean that indicate changes in gyre circulations across the northern hemisphere. Concerning the AMOC, our results do not suggest a significant change and the decrease in mixed layer depth over the Labrador Sea region in the OGGM-forced NEMO simulation falls within the range of interannual and model variability. Still, the finding that the subpolar gyre's strength is increased in combination with the slightly decreased mixed layer depth in the Labrador Sea points to changes of the joint dynamical system in response to increased freshwater forcing that are consistent with previous investigations. Regarding the Arctic Ocean, an intrusion of rerouted warm Atlantic water through Fram Strait leads to a band of warmer water along the eastern shelf break. This rerouting of Atlantic water also goes along with a decrease in sea ice thickness in the Fram Strait region and north of Svalbard. We also find a comparatively strong decrease in sea ice thickness in the Canadian Arctic

Archipelago. In total, sea ice thickness is decreased in the northern hemisphere when including freshwater forcing from glacial melt outside the GrIS.

Concerning the influence of the oceanic forcing on glacier mass loss, we find that for marine-terminating glaciers in the domain of the NEMO-ANHA4 configuration, submarine melt accounts for a median 17 % ($\sim$8.1 Gt a^{-1}) of frontal ablation throughout the spun-up simulation period (2015 to 2019), with an interquartile range of 10 to 27 % ($\sim$4.9 to 12.5 Gt a^{-1}). The increase in submarine melt when applying the thermal forcing from the NEMO experiment that includes freshwater input from the OGGM glaciers, compared to the experiment that does not include it, is very small (1.5 [1.3, 1.4] %). The only region where we find a notable increase of submarine melt is Svalbard. This is caused by the rerouting of warm Atlantic Water through Fram Strait, which thereby reaches Svalbard from the north. On the other hand, we find a slight decrease in Arctic Canada North and the Russian Arctic. Our results suggest that the parameter ranges applied in the latin hypercube sampling of the estimated parameter space should be adjusted for the individual regions, as we find less viable parameter sets for individual glaciers in some regions than in others, when applying the same ranges for all regions.

Future studies investigating northern hemisphere ice-ocean interactions could improve several aspects of this work. Using a higher resolution ocean model configuration and analyzing passive tracer movements could yield stronger insights into the impact of increased freshwater input from glacier mass loss outside the GrIS on ocean circulation. Additionally, advancing the simulations into future projections would be crucial in gaining a better understanding of potential future changes in the ocean as well as in glacier mass changes due to ice-ocean interactions. This would necessitate an actual two-way coupling of the models, for example in the way of a decadal step-coupling. Another approach could be to conduct decadal snapshot simulations similar to what was presented in this work, but for a future period in which the melt signal from northern hemisphere glaciers outside Greenland will be larger. Applying a more thorough approach of injecting the glacial meltwater into the ocean in terms of the routing from the glacier termini, the temperature and depth at which it is injected, and the way it changes mixing in the ocean model might help to improve the accuracy of coupled simulations.

4.A Appendix

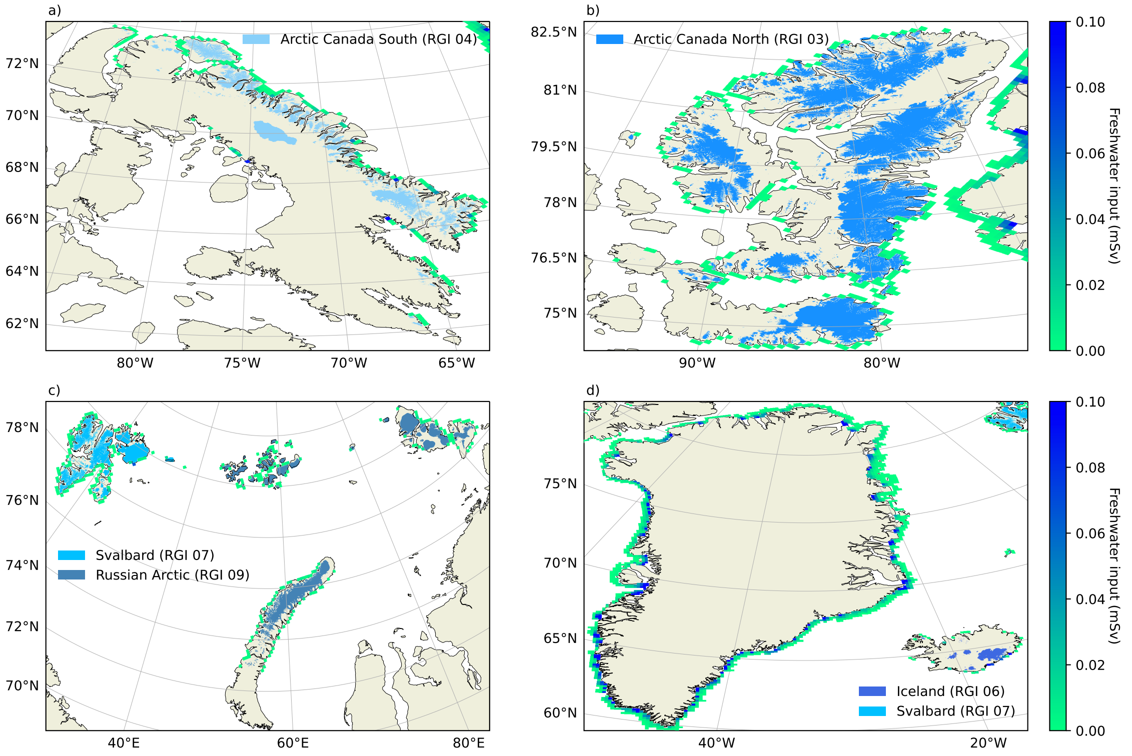

Figure 4.A.1: Distribution of liquid freshwater input in the *halfsolid* NEMO run setup (2010 to 2019 average), apart from the baseline continental runoff derived from Dai et al. (2009). In the *noOGGM* run setup only the runoff around Greenland, displayed in panel d) and derived from Bamber et al. (2018a), is an additional input to the ocean. Colored land areas indicate the named glacierized regions as recorded in the RGI.

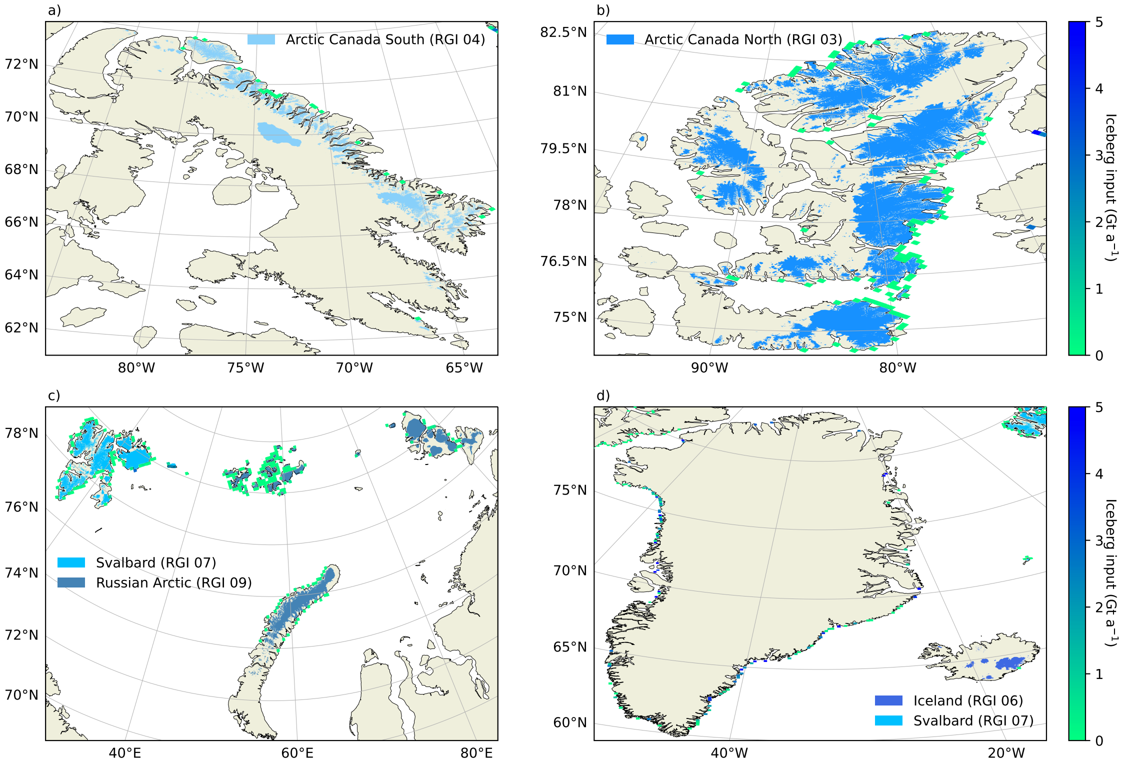

Figure 4.A.2: Iceberg input distribution in the *halfsolid* NEMO run setup (2010 to 2019 average). In the *noOGGM* run setup only the icebergs around Greenland, displayed in panel d) and derived from Bamber et al. (2018a), are added to the ocean. Colored land areas indicate the named glacierized regions as recorded in the RGI.

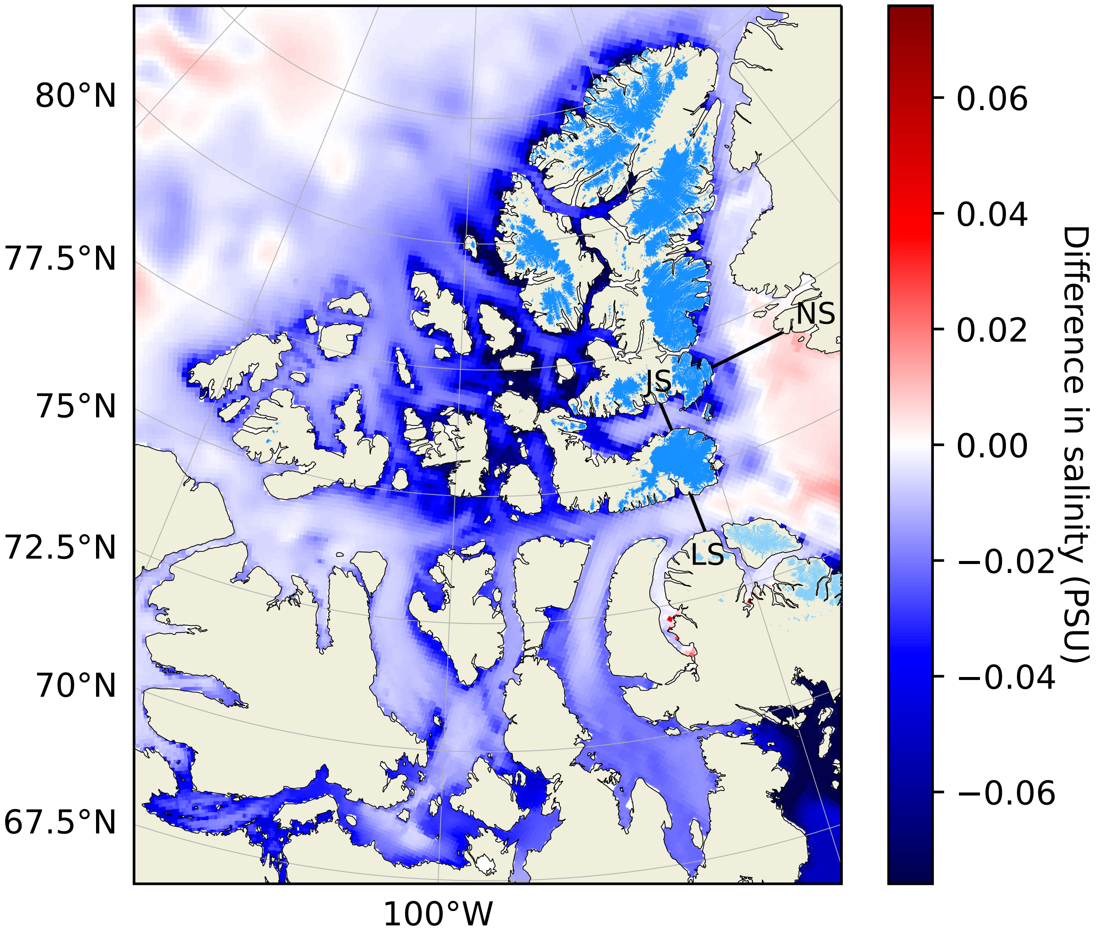

Figure 4.A.3: Difference in salinity averaged over up to 750 m water depth between the *halfsolid* and the *noOGGM* NEMO runs in the CAA region. Colored land area indicates glacierized area as recorded in the RGI.

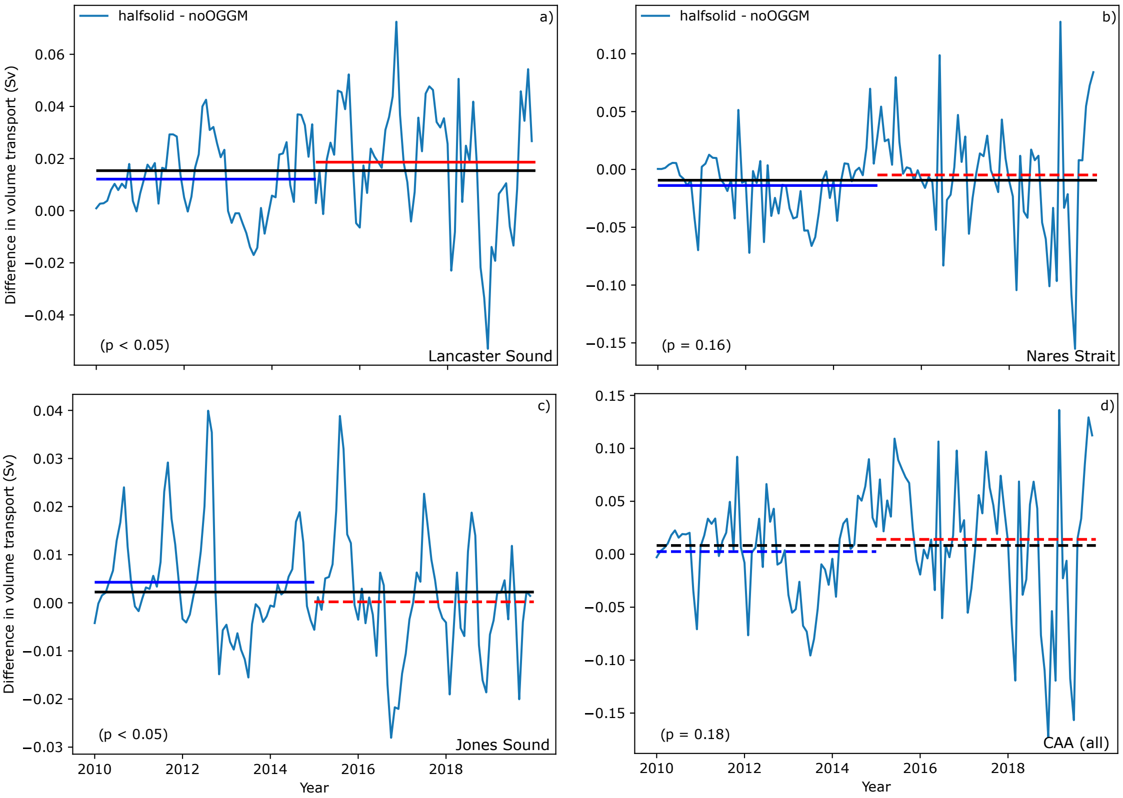

Figure 4.A.4: Differences in volume transport through the three main ocean pathways connecting the CAA and Baffin Bay, and the volume transport through all three. Note that volume flux northward through the CAA is defined as positive. The horizontal lines show average differences over the first (blue) and last (red) five years, as well as over all years (black) of the model integrations. Differences between the two NEMO runs that are statistically significant, according to paired Student's t-tests ($p < 0.05$), are drawn as solid lines and dashed otherwise. Values in the lower left corners show the p-values of paired Student's t-tests of differences between the differences of the first and last five modeled years.

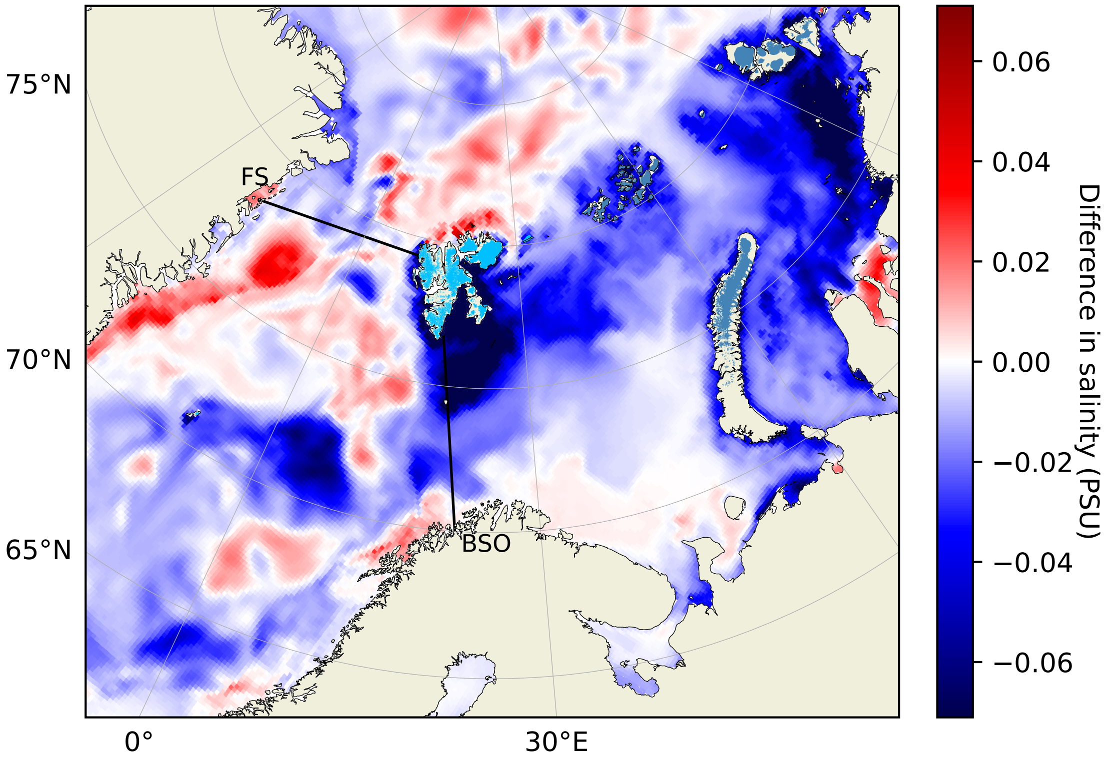

Figure 4.A.5: Difference in salinity averaged over up to 750 m water depth between the *halfsolid* and the *noOGGM* NEMO runs in the Barents and Nordic Seas area. Colored land area indicates glacierized area as recorded in the RGI.

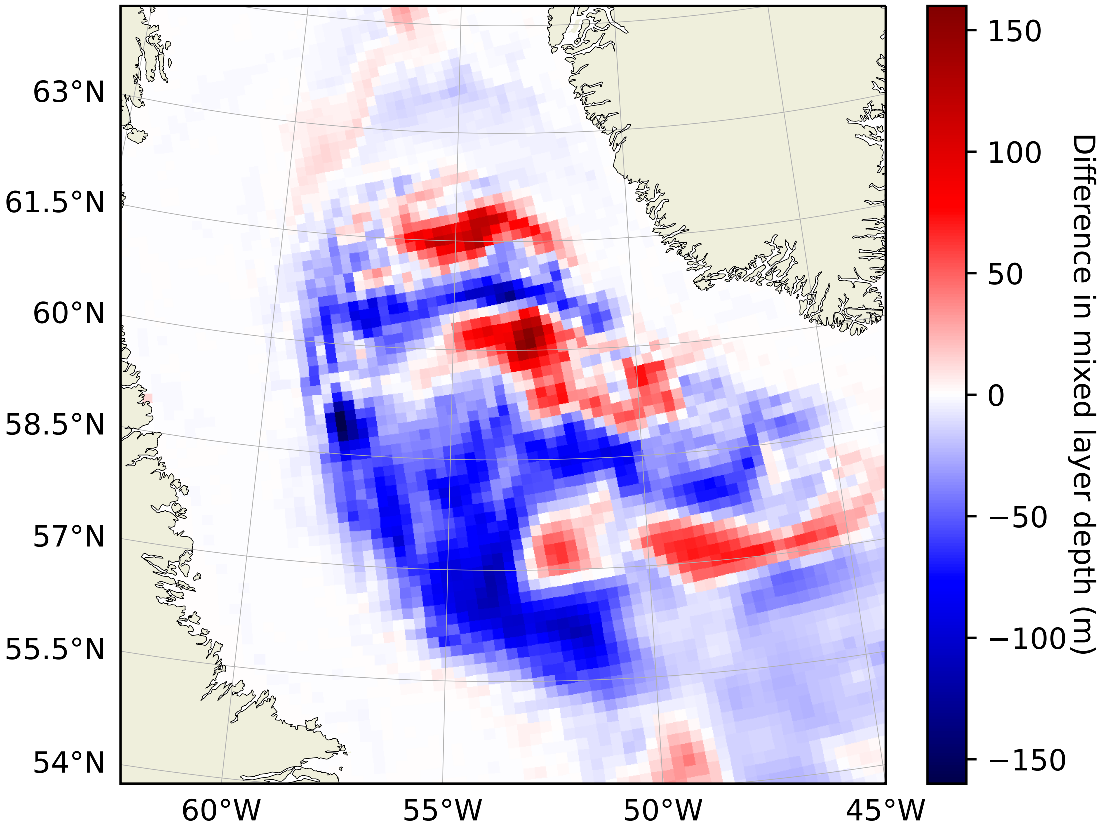

Figure 4.A.6: Difference in mixed layer depth between the *halfsolid* and the *noOGGM* NEMO runs in the Labrador Sea.

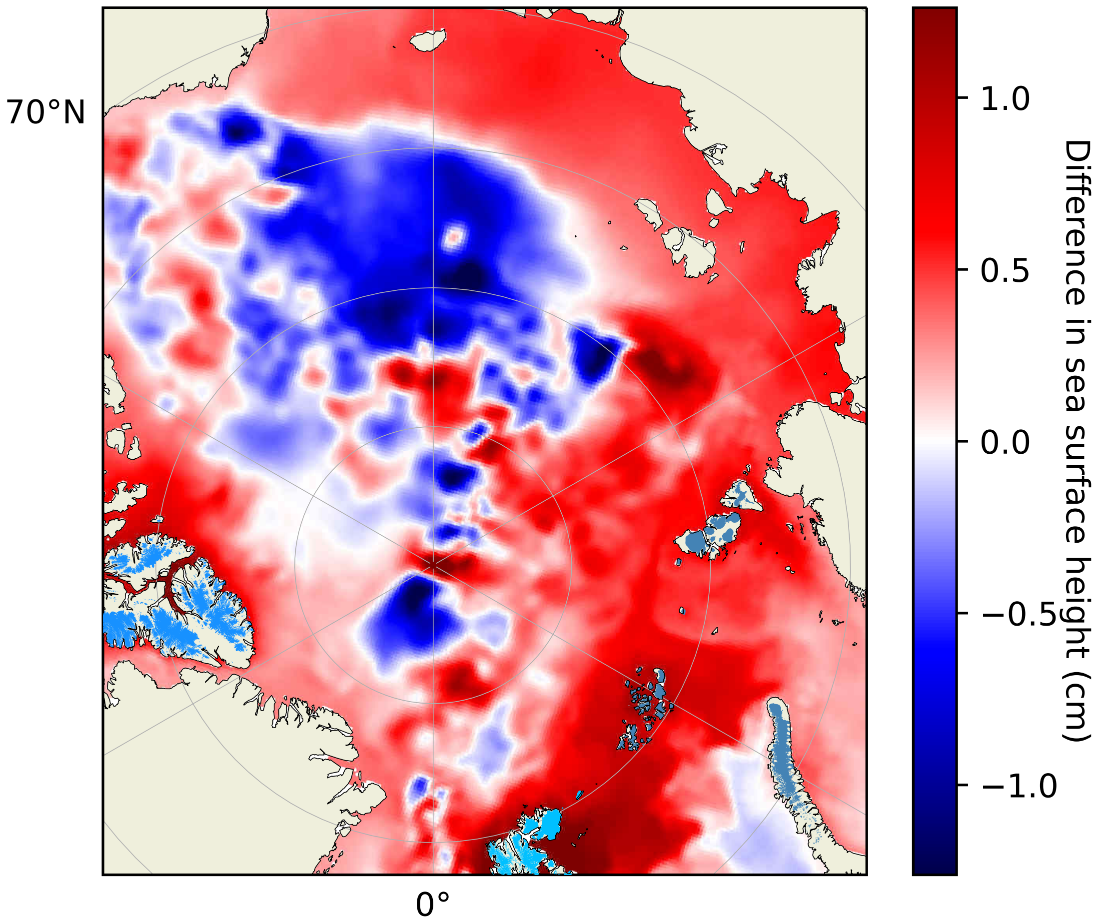

Figure 4.A.7: Difference in sea surface height between the *halfsolid* and the *noOGGM* NEMO runs in the Arctic. Colored land area indicates glacierized area as recorded in the RGI.

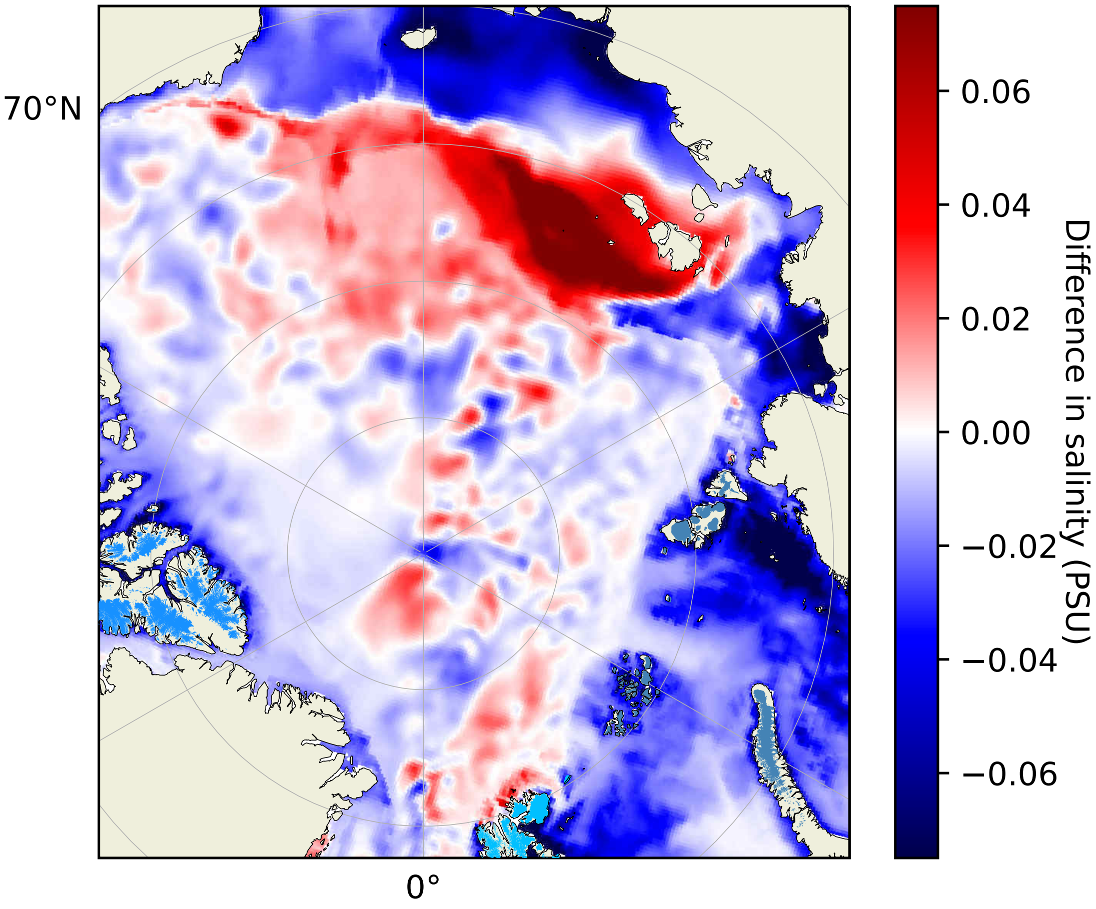

Figure 4.A.8: Difference in salinity averaged over up to 750 m water depth between the *halfsolid* and the *noOGGM* NEMO runs in the Arctic. Colored land area indicates glacierized area as recorded in the RGI.

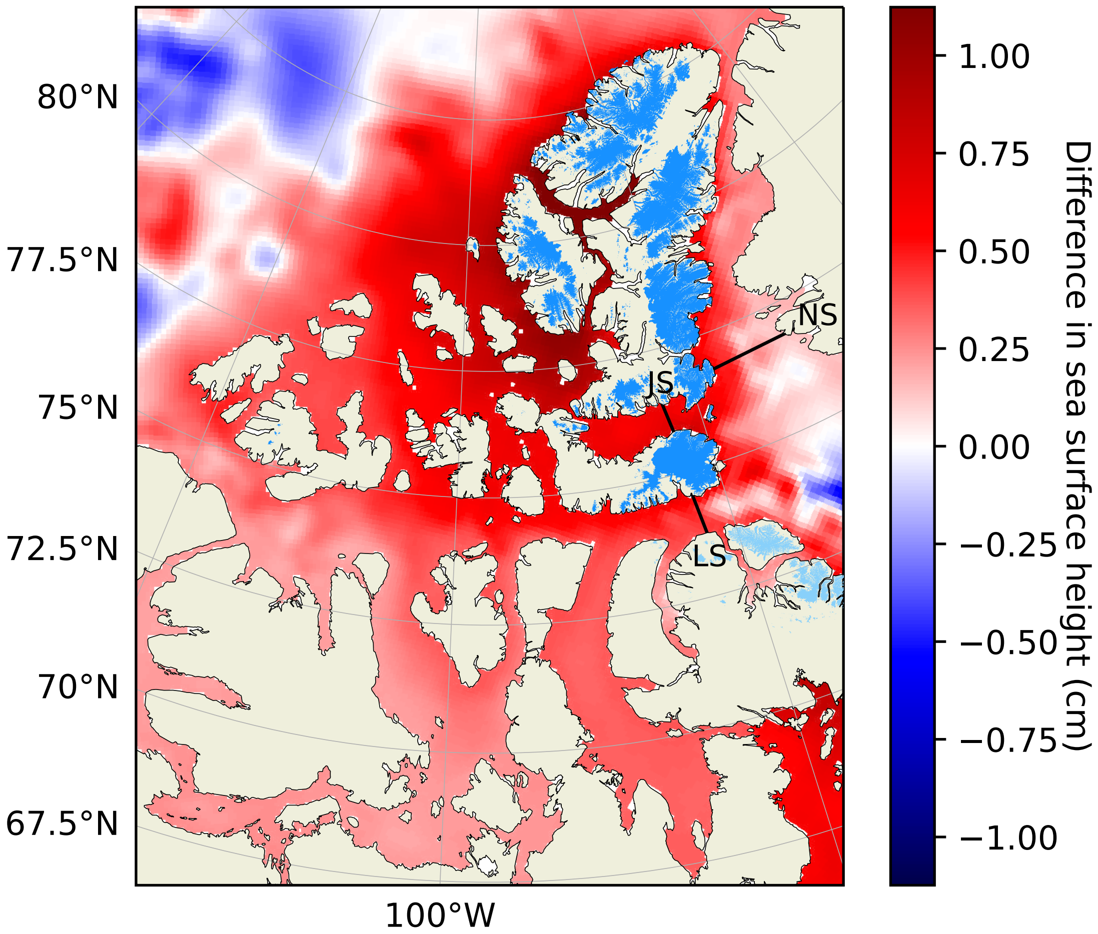

Figure 4.A.9: Difference in sea surface height between the *halfsolid* and the *noOGGM* NEMO runs in the CAA region. Colored land area indicates glacierized area as recorded in the RGI.

Data & code availability

Model results and code will be made available with the revised publication of this manuscript.

Author contributions

All three authors designed the study. JHM conceived and developed the changes to the glacier model code, prepared the data, conducted the numerical simulations and statistical evaluation, and wrote the manuscript. BM and PGM contributed to the manuscript.

Chapter 5: Discussion and Outlook

In this chapter, the attainment of the objectives stated in Section 1.7 will be discussed, and outlooks on how to address potential shortcomings will be given:

1. Quantify the uncertainty in numerical global glacier mass change reconstructions for the 20th century.

As shown in Chapter 2, most of the uncertainty in 20th-century global glacier mass change reconstruction is caused by differences in the atmospheric data sets from different reanalysis models. In comparison, the estimated glacier model uncertainty appears to be small, which is mainly due to the assumption of uncorrelated model error estimates for all individual glaciers. Such an assumption is probably not tenable, as inaccuracies in the atmospheric forcing might be translated into errors in the surface mass balance of nearby glaciers in a similar way. One way for this to occur is that regional errors in the forcing data affect several nearby glaciers. Another way could be due to the simple temperature index model approach for the mass balance parameterization; not explicitly accounting for the energy balance might lead to similar inaccuracies for glaciers with similar characteristics and locations. Another issue is the usage of only in-situ mass balance observations. While that allowed for applying a multi-objective optimization procedure that considers a temporal mean and interannual variability, in-situ data is spatially biased, and it is thus arguable whether it is sufficient to validate against this data. Moreover, only the global sample of glaciers for which in-situ mass balance observations are available was considered in the validation, hence neglecting potential inaccuracies on the regional scale. In addition to the potential flaws in the statistical evaluation, there are shortcomings in the model applied to achieve the stated objective. Using the area-volume scaling law without calibrating the scale factor is one example that might lead to systematic errors in the glaciers' geometric response to the mass balance forcing, although it was tried to include the uncertainty caused by this in the model error calculation. Moreover, the used model does not explicitly account for changes in ice thickness, thus not considering the positive surface-elevation mass balance feedback, which might lead to systematic errors. Finally, not accounting for frontal ablation and volume below sea level in the model probably leads to overestimating glaciers' past global mean sea level rise contributions, especially assuming more glaciers were marine-terminating in the early 20th century than today.

Though the shortcomings in ice dynamics and frontal ablation, as well as accounting for volume below sea level, could be remedied by using a model that actually resolves these processes, this would come with its own challenges of calibrating the involved parameters and initializing the model. However, using, for instance, OGGM for this task would be computationally more expensive. Initializing glaciers on a global scale remains a challenge, partly because some of today's land-terminating glaciers were marine-terminating in the past, and bathymetry in front of glaciers close to the ocean is usually not included in numerical models used to simulate glacier evolution outside the ice sheets. Concerning the issues of the surface mass balance calibration above, a potential remedy could be utilizing satellite-derived data for individual glaciers of, e.g., Hugonnet et al. (2021), although this disallows for calibrating the interannual variability of the surface mass balance. This is because the annual values these authors give are highly uncertain; hence, at least pentadal or even decadal averages should be used. When calibrating the melt factor in the temperature index model based on decadal-average geodetic and atmospheric data without considering variability, the validity of different parameter sets might not be distinguishable though (*equifinality*). One relatively simple way to still use the multi-year averages of geodetic data in the framework presented in Chapter 2 would be to merely replace the in-situ data's average with the geodetic data's averages in the bias calculation. Ultimately, a calibration method considering all available information on the surface mass balance needs to be devised to attain more accurate glacier mass change reconstructions.

2. Incorporate more accurate descriptions of marine-terminating glaciers in a numerical glacier evolution model and characterize the resulting changes in future glacier mass change projections.

There are two main issues with this objective: i) The simple parameterization of frontal ablation applied in Chapter 3 likely does not capture the complex nature of frontal ablation processes and is not related to changes in subglacial discharge and ocean temperature, and ii) thorough numerical modeling of marine-terminating glaciers' dynamics involves additional parameters that are hard to constrain (e.g., sliding parameter, stress-coupling length, or precipitation correction factor) since the processes they are used to parameterize are intricate to observe. The following two paragraphs will discuss these two issues in more detail.

Frontal ablation results from submarine melt and mechanical iceberg calving, which are also interrelated because submarine melt can cause undercutting that can lead to calving events. Parameterizing frontal ablation merely by linear scaling to the water depth does arguably not capture all frontal ablation processes since mechanical processes that lead to calving events might actually have an inverse relation to water depth. That is because a lower water depth at the front increases the hydrostatic stress imbalance. Thus, higher stress in the glacier front might increase ice fracturing and failure, potentially limiting the possible height above buoyancy (Bassis and Walker, 2011). On the other hand, undercutting by submarine melt might be, in part, related to water depth, based on the assumption that deeper fjord water might contain more heat-providing ocean water. Also, a higher water depth, with the same frontal thickness, will result in a higher velocity at the front, which can increase velocity gradients upstream and thus result in fracturing that leads to calving (Benn et al., 2007b). Hence, combining the water-depth parameterization with stress-related mechanisms as, for instance, in Schlemm and Levermann (2019), would address issue (i) above and make the description of calving in the model more physically sound. The issue of explicitly including submarine melt in the frontal ablation parameterization was addressed in Chapter 4. The appropriateness of the ice velocity formulation described in Chapter 3 might also be debatable because it double counts the basal shear (or driving) stress since the parameterization of both sliding and deformation velocity use the same value. Applying a parameterization similar to Eqs. 14 -

15 in Benn et al. (2007a) could be looked into to avoid this issue. Moreover, not including sediment dynamics in the model might reduce the model's ability to model the evolution of marine-terminating glaciers realistically. Especially on longer timescales and under less retreat-augmenting conditions (intense surface melt due to anthropogenic greenhouse gas emissions), sediment dynamics might play an important role (*tidewater glacier cycle*).

Generally, the fidelity of the modeled glacier mass change projections could be enhanced by constraining the involved parameters using all available information from observational data in the calibration procedure. Constraining ice velocity, ice thickness, frontal mass budget (i.e., retreat and advance), and total frontal ablation concurrently for individual glaciers should lead to more realistic simulations of marine frontal processes (Enderlin et al., 2013a). Since sliding is an essential process of marine-terminating glaciers' dynamics, but hard to observe, the issue of separating sliding and deformation velocity remains. Similarly, inferring the stress-coupling length for individual glaciers is laborious.

3. Generate a first estimate of northern hemisphere ice-ocean interactions outside the Greenland Ice Sheet by coupling a glacier evolution to an ocean circulation model.
   (a) Produce a first estimate of marine-terminating glaciers' submarine melt outside the ice sheets.
   (b) Explore the impact of increased freshwater input due to glacier melt on an ocean circulation model.

These objective(s) were mostly accomplished, although there are some issues that, if addressed, could strengthen the insights on ice-ocean interactions outside the ice sheets. Most of these issues were already pointed out in the discussion of Chapter 4, but here a brief recapitulation shall be given for completeness. The main problem with the work in Chapter 4 is probably the relatively short simulation period of ten years. That is because it cannot be ruled out that the ocean model is not fully spun up after one decade, and feedbacks in the coupled system might not fully unfold on this timescale. For a more extended integration of coupled glacier-ocean experiments, it would be sensible to actually two-way couple the models. Otherwise, potential feedbacks in the coupled system could not be simulated. A straightforward approach would be a decadal step-coupling scheme, assuming no significant feedbacks are acting on smaller timescales. In such a scheme, the way glacial meltwater is inserted into the ocean should also be improved concerning input location, temperature, and entailed surface mixing. In theory, energy conservation should also be considered when simulating submarine melt, as heat energy is drained from the ocean in the process. However, the required amount of heat is small when only considering marine-terminating glaciers outside the ice sheets, especially since the ocean takes up vast amounts of heat every year due to anthropogenic climate change that are roughly three orders of magnitude larger. Respecting the fact that heat is drained from the ocean when submarine melt occurs could nevertheless influence ocean properties close to marine-terminating termini.

Furthermore, the ocean model resolution should be finer to more accurately simulate processes in, for instance, the Labrador Sea, where eddies play an important role in ocean circulation. However, this would increase the computational cost of a coupled experiment, and thus longer model runs might be less practicable with such a setup. Hence, for investigating the glacier mass loss' impact on ocean circulation in the future, when glaciers are expected to lose even more mass than today, conducting decadal snapshot simulations might be an approach to circumvent more extended model integrations. The more substantial freshwater input from glacier melt in setups for modeling future periods might also make the signal of this perturbation more perceptible in the ocean model results. On the other hand, the continuing ocean warming might cause stronger submarine melt at glacier fronts that will not have retreated to land. Future studies trying to quantify the impact of increased freshwater input due to glacier melt outside the ice sheets should also use more accurate data products for the runoff apart from glacier mass loss to yield a more accurate signal of the process of interest in the results. That is because if the ratios of additional and control runoff are inaccurate, the impact of the additional runoff will likely be distorted.

Regarding potential improvements in modeling the glacier side of ice-ocean interactions, the most prominent would be constraining the parameters added to the model by the submarine melt parameterization. Since this process is hard to observe, data for this is very limited. This leaves the model overparameterized, although Chapter 4 indicated that the range of valid parameters might be different for the individual glacier inventory regions, and finding the suitable ranges for the individual regions might be a first step in more accurately modeling submarine melt. Including representations of subglacial hydrology as well as of fjord properties and fjord-ocean interactions in the (coupled) models could help in this regard. Finally, future work might look into the effect of increasing ocean temperatures in the future on glacier mass changes, which could be done applying the framework presented in Chapter 4.

While some of the problematic aspects of this work were discussed above, a summary of the main sources of errors in this work are given in the following for a more concise overview:

- **External data sets**:
  - *Initial conditions*: Erroneous DEMs can influence the ice thickness inversion and the (frontal) dynamics due to wrong estimations of the freeboard (and thereby water level) or the elevation profile. Outlines from the RGI can give, for example, erroneous front widths, influencing the ice thickness inversion, ice dynamics, and frontal ablation parameterization.

  - *Calibration data*: Inaccuracies or (systematic) errors in the calibration data will inevitably introduce (systematic) errors to the simulations. As these are performed on large spatial scales, random errors in the calibration data on individual glaciers may cancel each other out to some degree. However, it is unclear to what degree exactly.

  - *Amtospheric forcing*: There is a large spread of the results due to differences in reconstructed and projected atmospheric forcing. This is the largest source of uncertainty, concerning the influence of including frontal processes and glacier mass change estimates in general, of the sources that were quantified in this work.

- **Model approximations, parameterizations, and simplifications**:
  - *Flow parameters*: As presented in Chapter 3, the choice of flow parameters can significantly influence the results since they change the ice thickness inversion and ice dynamics. Not considering lateral drag in the computations could influence (frontal) dynamics and thereby on the results (Adhikari and Marshall, 2012; Frank et al., 2022). The influence of including lateral drag is mainly related to glaciers' width-to-thickness ratios, though the implications for large-scale glacier dynamics are not clear and out of the scope of this work. Also, the factors in the geometric scaling laws applied in Chapter 2 were held constant for all glaciers, which might not be appropriate.

  - *Constancy of parameters*: In this work, it was assumed that all parameters stay constant through time. Parameterizations are used to approximate physical processes of the natural world that are not explicitly incorporated in the model formulation. They can thus only represent these processes in the way they occurred during the period chosen for calibration. However, these physical processes may vary over time, and parameters, such as the glacier sensitivity to atmospheric temperatures (melt factor) or the frontal ablation parameter, should thus probably not be constant. Temporal changes in appropriate values for the melt factor might be due to climatic or surface albedo changes (e.g., due to changing debris cover). That is because the melt factor depends, apart from topographical features such as aspect, shading, and slope, on the individual energy balance components' relative contributions to the total heat budget. Hence, if the relative energy balance contributions or the surface albedo systematically change, the calibrated melt factor might become inappropriate. Another example would be Glen's A, since it is a function of ice temperature, and one could suspect that it changes as a function of atmospheric (or basal) temperatures.

  - *Global parameters*: The same values for several parameters were applied to all modeled glaciers. Examples are the precipitation factor (a or f_p in Eqs. 2.3, 3.1, and 3.18), or, specifically for marine-terminating glaciers, the 'stress coupling length' (L_F in Section 3.2.2). In reality, values for these parameters probably vary from glacier to glacier, but are hard to constrain on such small spatial scales due to a lack of observations.

- *Flotation criterion/neglecting floating tongues and ice shelves*: Although most marine-terminating glaciers that are not connected to the Greenland Ice Sheet do not possess a floating tongue or ice shelf anymore, it is acknowledged that this assumption might be inaccurate for some glaciers. Though the affected ones, besides the Flade Isblink ice cap, which was excluded in the last two main chapters, do not represent a significant fraction of the total ice volume in the northern hemisphere. Not being able to model this type of glacier fronts in the current framework might be more problematic when dealing with climatic boundary conditions that favor the occurrence of floating tongues/ice shelves.

- *Sliding parameterization*: Since ice velocities at the termini of marine-terminating glaciers can be caused primarily by sliding, it is crucial to represent it in a realistic manner. The sliding law adopted in the last two main chapters might not be the most appropriate. Investigating this issue further could be beneficial to better represent marine-terminating glaciers in large-scale numerical models.

- *Ice thickness inversion/spin-up*: As described above, the ice thickness inversion method applied in the last two main chapters of this work likely results in too much ice volume at the beginning of the simulations (the RGI recording date), thereby probably inducing spin-up effects in the first years of simulation. As most RGI dates lie before 2010, the effect on the calibration should be relatively small.

- *Calibration strategies*: This work applied two different approaches to calibrating the surface mass balance model. In Chapter 2, the surface mass balance was calibrated by a multi-objective optimization procedure, aiming to reproduce measured in-situ time series not only in terms of the mean but also in terms of the interannual variability. In contrast, the method applied in Chapter 3 is much simpler: solely inferring the melt factor (μ) from satellite observations and reanalysis data over ten years without taking interannual variability into account. A thorough calibration should take both mean and variance into account, however. Otherwise, different parameter sets resulting in the same average mass balance over the calibration period cannot be distinguished in how well they can represent the real-world surface mass balance (variability).

- *Unconscious model errors/bugs*: As with all scientific experiments, the setup of numerical models is prone to human error. This means that besides the consciously chosen model approximations and parameterizations, results could be distorted by errors unconsciously introduced to the numerical model's computer program code.

Chapter 6: Conclusion

The melting of Earth's ice is a huge challenge for humanity, as it threatens the livelihood of many due to increasing sea levels and changing hydrology in areas with large populations. Therefore, understanding glacier mass changes and how to numerically model them for time periods outside observed temporal and spatial domains is crucial for quantifying the implications of this imminent threat. This work provides a small piece to the mosaic of the picture that science can paint of reality. This picture can be used to tell the story of massive human-induced changes on their home planet. Here, a brief synthesis of this work shall be given in order to provide a concise overview:

- Uncertainty in large-scale glacier mass change reconstructions increases when moving outside the temporal and spatial domain of available in-situ atmospheric and glacier (surface) mass balance data. Moreover, the two data types' spatial domains tend to coincide. Uncertainty due to the differences in data products that provide global coverage of historical atmospheric data by means of in-situ data assimilation (reanalysis) seems to dominate the uncertainty in large-scale glacier mass change reconstructions for the 20th century. However, this statistical inference might partly be based on an underestimation of the numerical model's error.

- Taking marine frontal processes into account in a large-scale glacier evolution model systematically changes the projected global mean sea level rise contributions of glaciers outside the ice sheets. It furthermore facilitates the differentiation of the mass balance into surface and frontal processes, which makes it possible to use surface melt and iceberg calving as separate inputs to an ocean circulation model. However, significant uncertainties remain due to the lack of knowledge about appropriate values for some of the involved parameters and the spread between different climate model projections.

- A simple one-way coupling of a glacier evolution model and an ocean general circulation model revealed statistically significant changes in the simulated ocean circulation. It indicated potential (regional) feedbacks between the two Earth system components. Although the coupling appears to mostly affect the ocean side, a more sophisticated and longer-run coupling of the models might help better quantify the coupling processes. While a first estimate of submarine melt of glacier outside the ice sheets was given, it remains an elusive process, as observations of it are lacking and the parameters involved in numerical modeling thus hard to constrain.

Overall, this work illustrates that moving numerical Earth system models toward reality is laborious and dependent on our understanding of reality. Our knowledge about reality is usually defined by the collected observational data, as this is the main data source for verifying results from theoretical models that are conceived to describe reality, but not based on first principles. Hence, the emergence of new observational data should allow for more robust approximations of processes in numerical models, although one has to be aware of the different observational data sets' inaccuracies and their implications for applying them in the process of tuning numerical models. Therefore, when integrating numerical models for temporal or spatial domains that are not well-observed, it is mandatory to survey the uncertainties in the results. Nevertheless, one should be aware that acknowledging uncertainties does not diminish such results' (societal) importance.

Bibliography

Adhikari, S. and Marshall, S. J., 2012: *Parameterization of lateral drag in flowline models of glacier dynamics*, Journal of Glaciology, 58, 1119–1132, doi: 10.3189/2012JoG12J018.

Alvarez-Solas, J., Robinson, A., Montoya, M., and Ritz, C., 2013: *Iceberg discharges of the last glacial period driven by oceanic circulation changes*, Proceedings of the National Academy of Sciences, 110, 16 350–16 354, doi: 10.1073/pnas.1306622110.

Arctic Monitoring and Assessment Programme (AMAP), 1998: *AMAP assessment report: Arctic pollution issues*, Arctic Monitoring and Assessment Programme (AMAP), Oslo, Norway.

Bahr, D. B., 1997: *Global distributions of glacier properties: A stochastic scaling paradigm*, Water Resources Research, 33, 1669–1679, doi: 10.1029/97WR00824.

Bahr, D. B., Meier, M. F., and Peckham, S. D., 1997: *The physical basis of glacier volume-area scaling*, Journal of Geophysical Research: Solid Earth, 102, 20 355–20 362, doi: 10.1029/97JB01696.

Bahr, D. B., Pfeffer, W. T., and Kaser, G., 2015: *A review of volume-area scaling of glaciers*, Reviews of Geophysics, 53, 95–140, doi: 10.1002/2014RG000470.

Bamber, J. L., Tedstone, A. J., King, M. D., Howat, I. M., Enderlin, E. M., van den Broeke, M. R., and Noel, B., 2018a: *Land Ice Freshwater Budget of the Arctic and North Atlantic Oceans: 1. Data, Methods, and Results*, Journal of Geophysical Research: Oceans, 123, 1827–1837, doi: 10.1002/2017JC013605.

Bamber, J. L., Westaway, R. M., Marzeion, B., and Wouters, B., 2018b: *The land ice contribution to sea level during the satellite era*, Environmental Research Letters, 13, 063 008, doi: 10.1088/1748-9326/aac2f0.

Bartholomaus, T. C., Stearns, L. A., Sutherland, D. A., Shroyer, E. L., Nash, J. D., Walker, R. T., Catania, G., Felikson, D., Carroll, D., Fried, M. J., and et al., 2016: *Contrasts in the response of adjacent fjords and glaciers to ice-sheet surface melt in West Greenland*, Annals of Glaciology, 57, 25–38, doi: 10.1017/aog.2016.19.

Bassis, J. N. and Walker, C. C., 2011: *Upper and lower limits on the stability of calving glaciers from the yield strength envelope of Ice*, Proceedings of the Royal Society A: Mathematical, Physical and Engineering Sciences, 468, 913–931, doi: 10.1098/rspa.2011.0422.

Benn, D. I., Hulton, N. R., and Mottram, R. H., 2007a: *'Calving laws','sliding laws' and the stability of tidewater glaciers*, Annals of glaciology, 46, 123–130, doi: 10.3189/172756407782871161.

Benn, D. I., Warren, C. R., and Mottram, R. H., 2007b: *Calving processes and the dynamics of calving glaciers*, Earth-Science Reviews, 82, 143–179, doi: 10.1016/j.earscirev.2007.02.002.

Bentsen, M., Olivié, D. J. L., Seland, Ø., Toniazzo, T., Gjermundsen, A., Graff, L. S., Debernard, J. B., Gupta, A. K., He, Y., Kirkevåg, A., Schwinger, J., Tjiputra, J., Aas, K. S., Bethke, I., Fan, Y., Griesfeller, J., Grini, A., Guo, C., Ilicak, M., Karset, I. H. H., Landgren, O. A., Liakka, J., Moseid, K. O., Nummelin, A., Spensberger, C., Tang, H., Zhang, Z., Heinze, C., Iversen, T., and Schulz, M., 2019: *NCC NorESM2-MM model output prepared for CMIP6 ScenarioMIP*, Earth System Grid Federation, doi: 10.22033/ESGF/CMIP6.608.

Bigg, G. R., Jickells, T. D., Liss, P. S., and Osborn, T. J., 2003: *The role of the oceans in climate*, International Journal of Climatology, 23, 1127–1159, doi: 10.1002/joc.926.

Böning, C. W., Behrens, E., Biastoch, A., Getzlaff, K., and Bamber, J. L., 2016: *Emerging impact of Greenland meltwater on deepwater formation in the North Atlantic Ocean*, Nature Geoscience, 9, 523–527, doi: 10.1038/ngeo2740.

Born, A., Stocker, T. F., and Sandø, A. B., 2016: *Transport of salt and freshwater in the Atlantic Subpolar Gyre*, Ocean Dynamics, 66, 1051–1064, doi: 10.1007/s10236-016-0970-y.

Bouillon, S., Ángel Morales Maqueda, M., Legat, V., and Fichefet, T., 2009: *An elastic–viscous–plastic sea ice model formulated on Arakawa B and C grids*, Ocean Modelling, 27, 174–184, doi: 10.1016/j.ocemod.2009.01.004.

Brinkerhoff, D., Truffer, M., and Aschwanden, A., 2017: *Sediment transport drives tidewater glacier periodicity*, Nature Communications, 8, 90, doi: 10.1038/s41467-017-00095-5.

Broecker, W. S., 1997: *Thermohaline Circulation, the Achilles Heel of Our Climate System: Will Man-Made CO¡sub¿2¡/sub¿ Upset the Current Balance?*, Science, 278, 1582–1588, doi: 10.1126/science.278.5343.1582.

Brunnabend, S.-E., Schröter, J., Timmermann, R., Rietbroek, R., and Kusche, J., 2012: *Modeled steric and mass-driven sea level change caused by Greenland Ice Sheet melting*, Journal of Geodynamics, 59-60, 219–225, doi: 10.1016/j.jog.2011.06.001, mass Transport and Mass Distribution in the System Earth.

Caesar, L., McCarthy, G. D., Thornalley, D. J. R., Cahill, N., and Rahmstorf, S., 2021: *Current Atlantic Meridional Overturning Circulation weakest in last millennium*, Nature Geoscience, 14, 118–120, doi: 10.1038/s41561-021-00699-z.

Castro de la Guardia, L., Hu, X., and Myers, P. G., 2015: *Potential positive feedback between Greenland Ice Sheet melt and Baffin Bay heat content on the west Greenland shelf*, Geophysical Research Letters, 42, 4922–4930, doi: 10.1002/2015GL064626.

Chafik, L., Holliday, N. P., Bacon, S., and Rossby, T., 2022: *Irminger Sea Is the Center of Action for Subpolar AMOC Variability*, Geophysical Research Letters, 49, e2022GL099 133, doi: 10.1029/2022GL099133, e2022GL099133 2022GL099133.

Chatterjee, S., Raj, R. P., Bertino, L., Skagseth, O., Ravichandran, M., and Johannessen, O. M., 2018: *Role of Greenland Sea Gyre Circulation on Atlantic Water Temperature Variability in the Fram Strait*, Geophysical Research Letters, 45, 8399–8406, doi: 10.1029/2018GL079174.

Cheng, L., Foster, G., Hausfather, Z., Trenberth, K. E., and Abraham, J., 2022: *Improved Quantification of the Rate of Ocean Warming*, Journal of Climate, 35, 4827 – 4840, doi: 10.1175/JCLI-D-21-0895.1.

Ciracì, E., Velicogna, I., and Swenson, S., 2020: *Continuity of the Mass Loss of the World's Glaciers and Ice Caps From the GRACE and GRACE Follow-On Missions*, Geophysical Research Letters, 47, doi: 10.1029/2019GL086926.

Cogley, J. G., 2009: *Geodetic and direct mass-balance measurements: comparison and joint analysis*, Annals of Glaciology, 50, 96–100, doi: 10.3189/172756409787769744.

Cogley, J. G., Arendt, A., Bauder, A., Braithwaite, R., Hock, R., Jansson, P., Kaser, G., Moller, M., Nicholson, L., Rasmussen, L., et al., 2011: *Glossary of glacier mass balance and related terms*, IHP-VII Technical Documents in Hydrology No. 86, IACS Contribution No. 2, 86, 124.

Cook, A. J., Copland, L., Noël, B. P., Stokes, C. R., Bentley, M. J., Sharp, M. J., Bingham, R. G., and van den Broeke, M. R., 2019: *Atmospheric forcing of rapid marine-terminating glacier retreat in the Canadian Arctic Archipelago*, Science Advances, 5, eaau8507, doi: 10.1126/sciadv.aau8507.

Copland, L. and Mueller, D., 2017: *Arctic ice shelves and ice islands*, Springer Dordrecht, doi: 10.1007/978-94-024-1101-0.

Cruz, R., Harasawa, H., Lal, M., Wu, S., Anokhin, Y., Punsalmaa, B., Honda, Y., Jafari, M., Li, C., and Huu Ninh, N., 2007: *Asia. Climate Change 2007: Impacts, Adaptation and Vulnerability. Contribution of Working Group II to the Fourth Assessment Report of the Intergovernmental Panel of Climate Change*, Journal of Environment Quality, doi: 10.2134/jeq2008.0015br.

Cuffey, K. M. and Paterson, W. S. B., 2010: *The Physics of Glaciers*, Elsevier Academic Press.

Cushman-Roisin, B. and Beckers, J.-M., 2011: *Introduction to geophysical fluid dynamics: physical and numerical aspects*, Elsevier Academic Press.

Dai, A., Qian, T., Trenberth, K. E., and Milliman, J. D., 2009: *Changes in continental freshwater discharge from 1948 to 2004*, Journal of climate, 22, 2773–2792, doi: 10.1175/2008JCLI2592.1.

Danabasoglu, G., 2019a: *NCAR CESM2 model output prepared for CMIP6 ScenarioMIP*, Earth System Grid Federation, doi: 10.22033/ESGF/CMIP6.2201.

Danabasoglu, G., 2019b: *NCAR CESM2-WACCM model output prepared for CMIP6 ScenarioMIP*, Earth System Grid Federation, doi: 10.22033/ESGF/CMIP6.10026.

Davison, B. J., Cowton, T. R., Cottier, F. R., and Sole, A. J., 2020: *Iceberg melting substantially modifies oceanic heat flux towards a major Greenlandic tidewater glacier*, Nature Communications, 11, 5983, doi: 10.1038/s41467-020-19805-7.

De Andrés, E., Otero, J., Navarro, F., Prominska, A., Lapazaran, J., and Walczowski, W., 2018: *A two-dimensional glacier–fjord coupled model applied to estimate submarine melt rates and front position changes of Hansbreen, Svalbard*, Journal of Glaciology, 64, 745–758, doi: 10.1017/jog.2018.61.

Dee, D. P., Uppala, S. M., Simmons, A. J., Berrisford, P., Poli, P., Kobayashi, S., Andrae, U., Balmaseda, M. A., Balsamo, G., Bauer, P., Bechtold, P., Beljaars, A. C. M., van de Berg, L., Bidlot, J., Bormann, N., Delsol, C., Dragani, R., Fuentes, M., Geer, A. J., Haimberger, L., Healy, S. B., Hersbach, H., Hólm, E. V., Isaksen, L., Kållberg, P., Köhler, M., Matricardi, M., McNally, A. P., Monge-Sanz, B. M., Morcrette, J.-J., Park, B.-K., Peubey, C., de Rosnay, P., Tavolato, C., Thépaut, J.-N., and Vitart, F., 2011: *The ERA-Interim reanalysis: configuration and performance of the data assimilation system*, Quarterly Journal of the Royal Meteorological Society, 137, 553–597, doi: 10.1002/qj.828.

EC-Earth Consortium, 2019a: *EC-Earth-Consortium EC-Earth3 model output prepared for CMIP6 ScenarioMIP*, Earth System Grid Federation, doi: 10.22033/ESGF/CMIP6.251.

EC-Earth Consortium, 2019b: *EC-Earth-Consortium EC-Earth3-Veg model output prepared for CMIP6 ScenarioMIP*, Earth System Grid Federation, doi: 10.22033/ESGF/CMIP6.727.

Eis, J., Maussion, F., and Marzeion, B., 2019: *Initialization of a global glacier model based on present-day glacier geometry and past climate information: an ensemble approach*, The Cryosphere, 13, 3317–3335, doi: 10.5194/tc-13-3317-2019.

Eis, J., Van der Laan, L., Maussion, F., and Marzeion, B., 2021: *Reconstruction of past glacier changes with an ice-flow glacier model: proof of concept and validation*, Frontiers in Earth Science, 9, 77, doi: 10.3389/feart.2021.595755.

Enderlin, E. M., Howat, I. M., and Vieli, A., 2013a: *The sensitivity of flowline models of tidewater glaciers to parameter uncertainty*, The Cryosphere, 7, 1579–1590.

Enderlin, E. M., Howat, I. M., and Vieli, A., 2013b: *High sensitivity of tidewater outlet glacier dynamics to shape*, The Cryosphere, 7, 1007–1015, doi: 10.5194/tc-7-1007-2013.

Enderlin, E. M., Hamilton, G. S., O'Neel, S., Bartholomaus, T. C., Morlighem, M., and Holt, J. W., 2016a: *An empirical approach for estimating stress-coupling lengths for marine-terminating glaciers*, Frontiers in Earth Science, 4, 104, doi: 10.3389/feart.2016.00104.

Enderlin, E. M., Hamilton, G. S., Straneo, F., and Sutherland, D. A., 2016b: *Iceberg meltwater fluxes dominate the freshwater budget in Greenland's iceberg-congested glacial fjords*, Geophysical Research Letters, 43, 11,287–11,294, doi: 10.1002/2016GL070718.

Eyring, V., Bony, S., Meehl, G. A., Senior, C. A., Stevens, B., Stouffer, R. J., and Taylor, K. E., 2016: *Overview of the Coupled Model Intercomparison Project Phase 6 (CMIP6) experimental design and organization*, Geoscientific Model Development, 9, 1937–1958, doi: 10.5194/gmd-9-1937-2016.

Farinotti, D., Huss, M., Bauder, A., Funk, M., and Truffer, M., 2009: *A method to estimate the ice volume and ice-thickness distribution of alpine glaciers*, Journal of Glaciology, 55, 422–430, doi: 10.3189/002214309788816759.

Farinotti, D., Huss, M., Fürst, J. J., Landmann, J., Machguth, H., Maussion, F., and Pandit, A., 2019: *A consensus estimate for the ice thickness distribution of all glaciers on Earth*, Nature Geoscience, 12, 168–173, doi: 10.1038/s41561-019-0300-3.

Fofonoff, N. and Millard Jr, R., 1983: *Algorithms for the computation of fundamental properties of seawater*, UNESCO Technical Papers in Marine Sciences, 44, doi: 10.25607/OBP-1450.

Frajka-Williams, E., Bamber, J. L., and Våge, K., 2016: *Greenland Melt and the Atlantic Meridional Overturning Circulation*, Oceanography, 29, 22–33, doi: 10.5670/oceanog.2016.96.

Frank, T., Åkesson, H., de Fleurian, B., Morlighem, M., and Nisancioglu, K. H., 2022: *Geometric controls of tidewater glacier dynamics*, The Cryosphere, 16, 581–601, doi: 10.5194/tc-16-581-2022.

Frederikse, T., Landerer, F., Caron, L., Adhikari, S., Parkes, D., Humphrey, V. W., Dangendorf, S., Hogarth, P., Zanna, L., Cheng, L., and Wu, Y.-H., 2020: *The causes of sea-level rise since 1900*, Nature, 584, 393–397, doi: 10.1038/s41586-020-2591-3.

Fu, Y., Li, F., Karstensen, J., and Wang, C., 2020: *A stable Atlantic Meridional Overturning Circulation in a changing North Atlantic Ocean since the 1990s*, Science Advances, 6, eabc7836, doi: 10.1126/sciadv.abc7836.

Gardner, A. S., Moholdt, G., Cogley, J. G., Wouters, B., Arendt, A. A., Wahr, J., Berthier, E., Hock, R., Pfeffer, W. T., Kaser, G., Ligtenberg, S. R. M., Bolch, T., Sharp, M. J., Hagen, J. O., van den Broeke, M. R., and Paul, F., 2013: *A Reconciled Estimate of Glacier Contributions to Sea Level Rise: 2003 to 2009*, Science, 340, 852–857, doi: 10.1126/science.1234532.

Gelaro, R., McCarty, W., Suárez, M. J., Todling, R., Molod, A., Takacs, L., Randles, C. A., Darmenov, A., Bosilovich, M. G., Reichle, R., Wargan, K., Coy, L., Cullather, R., Draper, C., Akella, S., Buchard, V., Conaty, A., da Silva, A. M., Gu, W., Kim, G.-K., Koster, R., Lucchesi, R., Merkova, D., Nielsen, J. E., Partyka, G., Pawson, S., Putman, W., Rienecker, M., Schubert, S. D., Sienkiewicz, M., and Zhao, B., 2017: *The Modern-Era Retrospective Analysis for Research and Applications, Version 2 (MERRA-2)*, Journal of Climate, 30, 5419–5454, doi: 10.1175/JCLI-D-16-0758.1.

Giesen, R. and Oerlemans, J., 2012a: *Global application of a surface mass balance model using gridded climate data*, The Cryosphere Discuss, 6, 1445–1490, doi: 10.5194/tcd-6-1445-2012.

Giesen, R. H. and Oerlemans, J., 2012b: *Calibration of a surface mass balance model for global-scale applications*, The Cryosphere, 6, 1463–1481, doi: 10.5194/tc-6-1463-2012.

Giesen, R. H. and Oerlemans, J., 2013: *Climate-model induced differences in the 21st century global and regional glacier contributions to sea-level rise*, Climate Dynamics, 41, 3283–3300, doi: 10.1007/s00382-013-1743-7.

Gleckler, P. J., Taylor, K. E., and Doutriaux, C., 2008: *Performance metrics for climate models*, Journal of Geophysical Research: Atmospheres, 113, doi: 10.1029/2007JD008972.

Glen, J. W., 1955: *The creep of polycrystalline ice*, Proceedings of the Royal Society of London. Series A. Mathematical and Physical Sciences, 228, 519–538, doi: 10.1098/rspa.1955.0066.

Goelzer, H., Nowicki, S., Payne, A., Larour, E., Seroussi, H., Lipscomb, W. H., Gregory, J., Abe-Ouchi, A., Shepherd, A., Simon, E., Agosta, C., Alexander, P., Aschwanden, A., Barthel, A., Calov, R., Chambers, C., Choi, Y., Cuzzone, J., Dumas, C., Edwards, T., Felikson, D., Fettweis, X., Golledge, N. R., Greve, R., Humbert, A., Huybrechts, P., Le clec'h, S., Lee, V., Leguy, G., Little, C., Lowry, D. P., Morlighem, M., Nias, I., Quiquet, A., Rückamp, M., Schlegel, N.-J., Slater, D. A., Smith, R. S., Straneo, F., Tarasov, L., van de Wal, R., and van den Broeke, M., 2020: *The future sea-level contribution of the Greenland ice sheet: a multi-model ensemble study of ISMIP6*, The Cryosphere, 14, 3071–3096, doi: 10.5194/tc-14-3071-2020.

Goosse, H., Barriat, P.-Y., Dalaiden, Q., Klein, F., Marzeion, B., Maussion, F., Pelucchi, P., and Vlug, A., 2018: *Testing the consistency between changes in simulated climate and Alpine glacier length over the past millennium*, Climate of the Past, 14, 1119–1133, doi: 10.5194/cp-14-1119-2018.

Greene, C. H., Pershing, A. J., Cronin, T. M., and Ceci, N., 2008: *Arctic climate change and its impacts on the ecology of the North Atlantic*, Ecology, 89, S24–S38, doi: 10.1890/07-0550.1.

Greve, R. and Blatter, H., 2009: *Dynamics of ice sheets and glaciers*, Springer-Verlag, Berlin Heidelberg, doi: 10.1007/978-3-642-03415-2.

Gulev, S.K., Thorne, P., Ahn, J., Dentener, F., Domingues, C., Gerland, S., Gong, D., Kaufman, D., Nnamchi, H., Quaas, J., Rivera, J., Sathyendranath, S., Smith, S., Trewin, B., von Schuckmann, K., and Vose, R., 2021: *Contribution of Working Group I to the Sixth Assessment Report of the Intergovernmental Panel on Climate Change*, Changing State of the Climate System. In Climate Change 2021: The Physical Science Basis., p. 287–422, doi: 10.1017/9781009157896.004.

Hakkinen, S. and Rhines, P. B., 2004: *Decline of subpolar North Atlantic circulation during the 1990s*, Science, 304, 555–559, doi: 10.1126/science.1094917.

Harris, I. and Jones, P., 2020: *CRU TS4.03: Climatic Research Unit (CRU) Time-Series (TS) version 4.03 of high-resolution gridded data of month-by-month variation in climate (Jan. 1901- Dec. 2018)*, Centre for Environmental Data Analysis, doi: 10.5285/10d3e3640f004c578403419aac167d82.

Harris, I., Jones, P., Osborn, T., and Lister, D., 2014: *Updated high-resolution grids of monthly climatic observations – the CRU TS3.10 Dataset*, International Journal of Climatology, 34, 623–642, doi: 10.1002/joc.3711.

Harris, I., Osborn, T. J., Jones, P., and Lister, D., 2020: *Version 4 of the CRU TS monthly high-resolution gridded multivariate climate dataset*, Scientific data, 7, 1–18, doi: 10.1038/s41597-020-0453-3.

Harrison, W. D., Elsberg, D. H., Echelmeyer, K. A., and Krimmel, R. M., 2001: *On the characterization of glacier response by a single time-scale*, Journal of Glaciology, 47, 659–664, doi: 10.3189/172756501781831837.

Hersbach, H., Bell, B., Berrisford, P., Hirahara, S., Horányi, A., Muñoz-Sabater, J., Nicolas, J., Peubey, C., Radu, R., Schepers, D., Simmons, A., Soci, C., Abdalla, S., Abellan, X., Balsamo, G., Bechtold, P., Biavati, G., Bidlot, J., Bonavita, M., De Chiara, G., Dahlgren, P., Dee, D., Diamantakis, M., Dragani, R., Flemming, J., Forbes, R., Fuentes, M., Geer, A., Haimberger, L., Healy, S., Hogan, R. J., Hólm, E., Janisková, M., Keeley, S., Laloyaux, P., Lopez, P., Lupu, C., Radnoti, G., de Rosnay, P., Rozum, I., Vamborg, F., Villaume, S., and Thépaut, J.-N., 2020: *The ERA5 global reanalysis*, Quarterly Journal of the Royal Meteorological Society, 146, 1999–2049, doi: 10.1002/qj.3803.

Hirabayashi, Y., Zang, Y., Watanabe, S., Koirala, S., and Kanae, S., 2013: *Projection of glacier mass changes under a high-emission climate scenario using the global glacier model HYOGA2*, Hydrological Research Letters, 7, 6–11, doi: 10.3178/hrl.7.6.

Hock, R., Rasul, G., Adler, C., Cáceres, B., Gruber, S., Hirabayashi, Y., Jackson, M., Kääb, A., Kang, S., Kutuzov, S., Milner, A., Molau, U., Morin, S., Orlove, B., and Steltzer, H., 2019a: *High Mountain Areas*, IPCC Special Report on the Ocean and Cryosphere in a Changing Climate, pp. 131–202, doi: 10.1017/9781009157964.004.

Hock, R., 2003: *Temperature index melt modelling in mountain areas*, Journal of Hydrology, 282, 104–115, doi: 10.1016/S0022-1694(03)00257-9, mountain Hydrology and Water Resources.

Hock, R., Bliss, A., Marzeion, B., Giesen, R. H., Hirabayashi, Y., Huss, M., Radić, V., and Slangen, A. B., 2019b: *GlacierMIP–A model intercomparison of global-scale glacier mass-balance models and projections*, Journal of Glaciology, 65, 453–467, doi: 10.1017/jog.2019.22.

Holland, P. R., Jenkins, A., and Holland, D. M., 2008: *The Response of Ice Shelf Basal Melting to Variations in Ocean Temperature*, Journal of Climate, 21, 2558 – 2572, doi: 10.1175/2007JCLI1909.1.

Hourdin, F., Mauritsen, T., Gettelman, A., Golaz, J.-C., Balaji, V., Duan, Q., Folini, D., Ji, D., Klocke, D., Qian, Y., et al., 2017: *The art and science of climate model tuning*, Bulletin of the American Meteorological Society, 98, 589–602, doi: 10.1175/BAMS-D-15-00135.1.

Howat, I. M., Joughin, I., Tulaczyk, S., and Gogineni, S., 2005: *Rapid retreat and acceleration of Helheim Glacier, east Greenland*, Geophysical Research Letters, 32, doi: 10.1029/2005GL024737.

Hu, A., Meehl, G. A., Han, W., and Yin, J., 2011: *Effect of the potential melting of the Greenland Ice Sheet on the Meridional Overturning Circulation and global climate in the future*, Deep Sea Research Part II: Topical Studies in Oceanography, 58, 1914–1926, doi: 10.1016/j.dsr2.2010.10.069, climate and the Atlantic Meridional Overturning Circulation.

Hu, X. and Myers, P. G., 2014: *Changes to the Canadian Arctic Archipelago Sea Ice and Freshwater Fluxes in the Twenty-First Century under the Intergovernmental Panel on Climate Change A1B Climate Scenario*, Atmosphere-Ocean, 52, 331–350, doi: 10.1080/07055900.2014.942592.

Hugonnet, R., McNabb, R., Berthier, E., Menounos, B., Nuth, C., Girod, L., Farinotti, D., Huss, M., Dussaillant, I., Brun, F., et al., 2021: *Accelerated global glacier mass loss in the early twenty-first century*, Nature, 592, 726–731, doi: 10.1038/s41586-021-03436-z.

Huss, M. and Farinotti, D., 2012: *Distributed ice thickness and volume of all glaciers around the globe*, Journal of Geophysical Research: Earth Surface, 117, doi: 10.1029/2012JF002523.

Huss, M. and Hock, R., 2015: *A new model for global glacier change and sea-level rise*, Frontiers in Earth Science, 3, 54, doi: 10.3389/feart.2015.00054.

Huss, M. and Hock, R., 2018: *Global-scale hydrological response to future glacier mass loss*, Nature Climate Change, 8, 135–140, doi: 10.1038/s41558-017-0049-x.

Huss, M., Hock, R., Bauder, A., and Funk, M., 2012: *Conventional versus reference-surface mass balance*, Journal of Glaciology, 58, 278–286, doi: 10.3189/2012JoG11J216.

Hátún, H., Payne, M., Beaugrand, G., Reid, P., Sandø, A., Drange, H., Hansen, B., Jacobsen, J., and Bloch, D., 2009: *Large bio-geographical shifts in the north-eastern*

Atlantic Ocean: From the subpolar gyre, via plankton, to blue whiting and pilot whales, Progress in Oceanography, 80, 149–162, doi: 10.1016/j.pocean.2009.03.001.

Jackson, L. C., Biastoch, A., Buckley, M. W., Desbruyères, D. G., Frajka-Williams, E., Moat, B., and Robson, J., 2022: *The evolution of the North Atlantic Meridional Overturning Circulation since 1980*, Nature Reviews Earth & Environment, 3, 241–254, doi: 10.1038/s43017-022-00263-2.

Jacob, T., Wahr, J., Pfeffer, W. T., and Swenson, S., 2012: *Recent contributions of glaciers and ice caps to sea level rise*, Nature, 482, 514–518, doi: 10.1038/nature10847.

Jenkins, A., Hellmer, H. H., and Holland, D. M., 2001: *The Role of Meltwater Advection in the Formulation of Conservative Boundary Conditions at an Ice–Ocean Interface*, Journal of Physical Oceanography, 31, 285 – 296, doi: 10.1175/1520-0485(2001)031⟨0285:TROMAI⟩2.0.CO;2.

John, J. G., Blanton, C., McHugh, C., Radhakrishnan, A., Rand, K., Vahlenkamp, H., Wilson, C., Zadeh, N. T., Dunne, J. P., Dussin, R., Horowitz, L. W., Krasting, J. P., Lin, P., Malyshev, S., Naik, V., Ploshay, J., Shevliakova, E., Silvers, L., Stock, C., Winton, M., and Zeng, Y., 2018: *NOAA-GFDL GFDL-ESM4 model output prepared for CMIP6 ScenarioMIP*, Earth System Grid Federation, doi: 10.22033/ESGF/CMIP6.1414.

Jouvet, G., Cordonnier, G., Kim, B., Lüthi, M., Vieli, A., and Aschwanden, A., 2022: *Deep learning speeds up ice flow modelling by several orders of magnitude*, Journal of Glaciology, 68, 651–664, doi: 10.1017/jog.2021.120.

Kajanto, K., Straneo, F., and Nisancioglu, K., 2023: *Impact of icebergs on the seasonal submarine melt of Sermeq Kujalleq*, The Cryosphere, 17, 371–390, doi: 10.5194/tc-17-371-2023.

Kaser, G., Großhauser, M., and Marzeion, B., 2010: *Contribution potential of glaciers to water availability in different climate regimes*, Proceedings of the National Academy of Sciences, 107, 20 223–20 227, doi: 10.1073/pnas.1008162107.

Kieke, D. and Yashayaev, I., 2015: *Studies of Labrador Sea Water formation and variability in the subpolar North Atlantic in the light of international partnership and collaboration*, Progress in Oceanography, 132, 220–232, doi: 10.1016/j.pocean.2014.12.010, oceanography of the Arctic and North Atlantic Basins.

Kienholz, C., Rich, J. L., Arendt, A. A., and Hock, R., 2014: *A new method for deriving glacier centerlines applied to glaciers in Alaska and northwest Canada*, The Cryosphere, 8, 503–519, doi: 10.5194/tc-8-503-2014, .

Kobayashi, S., Ota, Y. Harada, Y., Ebita, A., Moriya, M., Onoda, H., Onogi, K., Kamahori, H., Kobayashi, C., Endo, H., Miyaoka, K., and Takahashi, K., 2015: *The JRA-55 Reanalysis: General Specifications and Basic Characteristics*, Journal of the Meteorological Society of Japan. Ser. II, 93, 5–48, doi: 10.2151/jmsj.2015-001.

Kochtitzky, W. and Copland, L., 2022: *Retreat of Northern Hemisphere Marine-Terminating Glaciers, 2000–2020*, Geophysical Research Letters, 49, e2021GL096 501, doi: 10.1029/2021GL096501.

Kochtitzky, W., Copland, L., Van Wychen, W., Hugonnet, R., Hock, R., Dowdeswell, J. A., Benham, T., Strozzi, T., Glazovsky, A., Lavrentiev, I., Rounce, D. R., Millan, R., Cook, A., Dalton, A., Jiskoot, H., Cooley, J., Jania, J., and Navarro, F., 2022: *The unquantified mass loss of Northern Hemisphere marine-terminating glaciers from 2000–2020*, Nature Communications, 13, 5835, doi: 10.1038/s41467-022-33231-x.

Labe, Z., Magnusdottir, G., and Stern, H., 2018: *Variability of Arctic Sea Ice Thickness Using PIOMAS and the CESM Large Ensemble*, Journal of Climate, 31, 3233 – 3247, doi: 10.1175/JCLI-D-17-0436.1.

Laloyaux, P., de Boisseson, E., Balmaseda, M., Bidlot, J.-R., Broennimann, S., Buizza, R., Dalhgren, P., Dee, D., Haimberger, L., Hersbach, H., Kosaka, Y., Martin, M., Poli, P., Rayner, N., Rustemeier, E., and Schepers, D., 2018: *CERA-20C: A Coupled Reanalysis of the Twentieth Century*, Journal of Advances in Modeling Earth Systems, 10, 1172–1195, doi: 10.1029/2018MS001273.

Latif, M., Sun, J., Visbeck, M., and Hadi Bordbar, M., 2022: *Natural variability has dominated Atlantic Meridional Overturning Circulation since 1900*, Nature Climate Change, 12, 455–460, doi: 10.1038/s41558-022-01342-4.

Le Sommer, J., Chassignet, E. P., and Wallcraft, A. J., 2018: *Ocean circulation modeling for operational oceanography: Current status and future challenges*, New Frontiers in Operational Oceanography, pp. 289–308, doi: 10.17125/gov2018.ch12.

Leclercq, P. W., Oerlemans, J., and Cogley, J. G., 2011: *Estimating the Glacier Contribution to Sea-Level Rise for the Period 1800–2005*, Surveys in Geophysics, 32, 19, doi: 10.1007/s10712-011-9121-7.

Lee, W.-L. and Liang, H.-C., 2020: *AS-RCEC TaiESM1.0 model output prepared for CMIP6 ScenarioMIP*, Earth System Grid Federation, doi: 10.22033/ESGF/CMIP6.9688.

Lovato, T. and Peano, D., 2020: *CMCC CMCC-CM2-SR5 model output prepared for CMIP6 ScenarioMIPP*, Earth System Grid Federation, doi: 10.22033/ESGF/CMIP6.1365.

Madec, G., Bourdallé-Badie, R., Bouttier, P.-A., Bricaud, C., Bruciaferri, D., Calvert, D., Chanut, J., Clementi, E., Coward, A., Delrosso, D., et al., 2016: *NEMO ocean engine, version 3.6 stable*, Technical Report, Note du Pôle de modélisation de l'Institut Pierre-Simon Laplace 27, ISSN 1288-1619.

Malles, J.-H., Maussion, F., Ultee, L., Kochtitzky, W., Copland, L., and Marzeion, B., 2023: *Exploring the impact of a frontal ablation parameterization on projected 21st-century mass change for Northern Hemisphere glaciers*, Journal of Glaciology, p. 1–16, doi: 10.1017/jog.2023.19.

Manabe, S. and Stouffer, R. J., 1988: *Two Stable Equilibria of a Coupled Ocean-Atmosphere Model*, Journal of Climate, 1, 841 – 866, doi: 10.1175/1520-0442(1988) 001⟨0841:TSEOAC⟩2.0.CO;2.

Mankin, J. S. and Diffenbaugh, N. S., 2015: *Influence of temperature and precipitation variability on near-term snow trends*, Climate Dynamics, 45, 1099–1116, doi: 10.1007/ s00382-014-2357-4.

Marler, R. and Arora, J., 2004: *Survey of multi-objective optimization methods for engineering*, Structural and Multidisciplinary Optimization, 26, 369–395, doi: 10.1007/ s00158-003-0368-6.

Marsh, R., Ivchenko, V. O., Skliris, N., Alderson, S., Bigg, G. R., Madec, G., Blaker, A. T., Aksenov, Y., Sinha, B., Coward, A. C., Le Sommer, J., Merino, N., and Zalesny, V. B., 2015: *NEMO–ICB (v1.0): interactive icebergs in the NEMO ocean model globally configured at eddy-permitting resolution*, Geoscientific Model Development, 8, 1547–1562, doi: 10.5194/gmd-8-1547-2015.

Marson, J. M., Myers, P. G., Hu, X., and Le Sommer, J., 2018: *Using Vertically Integrated Ocean Fields to Characterize Greenland Icebergs' Distribution and Lifetime*, Geophysical Research Letters, 45, 4208–4217, doi: 10.1029/2018GL077676.

Marson, J. M., Gillard, L. C., and Myers, P. G., 2021: *Distinct Ocean Responses to Greenland's Liquid Runoff and Iceberg Melt*, Journal of Geophysical Research: Oceans, 126, e2021JC017 542, doi: 10.1029/2021JC017542, e2021JC017542 2021JC017542.

Marzeion, B., Jarosch, A. H., and Hofer, M., 2012: *Past and future sea-level change from the surface mass balance of glaciers*, The Cryosphere, 6, 1295–1322, doi: 10.5194/ tc-6-1295-2012.

Marzeion, B., Leclercq, P. W., Cogley, J. G., and Jarosch, A. H., 2015: *Brief Communication: Global reconstructions of glacier mass change during the 20th century are consistent*, The Cryosphere, 9, 2399–2404, doi: 10.5194/tc-9-2399-2015.

Marzeion, B., Champollion, N., Haeberli, W., Langley, K., Leclercq, P., and Paul, F., 2017: *Observation-Based Estimates of Global Glacier Mass Change and Its Contribution to Sea-Level Change*, Surveys in Geophysics, 38, 105–130, doi: 10.1007/s10712-016-9394-y.

Marzeion, B., Hock, R., Anderson, B., Bliss, A., Champollion, N., Fujita, K., Huss, M., Immerzeel, W. W., Kraaijenbrink, P., Malles, J.-H., et al., 2020: *Partitioning the uncertainty of ensemble projections of global glacier mass change*, Earth's Future, 8, e2019EF001 470, doi: doi.org/10.1029/2019EF001470.

Masina, S., Storto, A., Ferry, N., Valdivieso, M., Haines, K., Balmaseda, M., Zuo, H., Drevillon, M., and Parent, L., 2017: *An ensemble of eddy-permitting global ocean reanalyses from the MyOcean project*, Climate Dynamics, 49, 813–841, doi: 10.1007/s00382-015-2728-5.

Maussion, F., Butenko, A., Champollion, N., Dusch, M., Eis, J., Fourteau, K., Gregor, P., Jarosch, A. H., Landmann, J., Oesterle, F., et al., 2019: *The open global glacier model (OGGM) v1. 1*, Geoscientific Model Development, 12, 909–931, doi: 10.5194/gmd-12-909-2019.

McFadden, E. M., Howat, I. M., Joughin, I., Smith, B. E., and Ahn, Y., 2011: *Changes in the dynamics of marine terminating outlet glaciers in west Greenland (2000–2009)*, Journal of Geophysical Research: Earth Surface, 116, doi: 10.1029/2010JF001757.

McGeehan, T. and Maslowski, W., 2012: *Evaluation and control mechanisms of volume and freshwater export through the Canadian Arctic Archipelago in a high-resolution pan-Arctic ice-ocean model*, Journal of Geophysical Research: Oceans, 117, doi: 10.1029/2011JC007261.

McKay, D. I. A., Staal, A., Abrams, J. F., Winkelmann, R., Sakschewski, B., Loriani, S., Fetzer, I., Cornell, S. E., Rockström, J., and Lenton, T. M., 2022: *Exceeding 1.5 °C global warming could trigger multiple climate tipping points*, Science, 377, eabn7950, doi: 10.1126/science.abn7950.

Meier, M. F. and Post, A., 1987: *Fast tidewater glaciers*, Journal of Geophysical Research: Solid Earth, 92, 9051–9058, doi: 10.1029/JB092iB09p09051.

Meire, L., Mortensen, J., Meire, P., Juul-Pedersen, T., Sejr, M. K., Rysgaard, S., Nygaard, R., Huybrechts, P., and Meysman, F. J. R., 2017: *Marine-terminating glaciers sustain high productivity in Greenland fjords*, Global Change Biology, 23, 5344–5357, doi: 10.1111/gcb.13801.

Millan, R., Mouginot, J., Rabatel, A., and Morlighem, M., 2022: *Ice velocity and thickness of the world's glaciers*, Nature Geoscience, 15, 124–129, doi: 10.1038/s41561-021-00885-z.

Moon, T., Sutherland, D. A., Carroll, D., Felikson, D., Kehrl, L., and Straneo, F., 2018: *Subsurface iceberg melt key to Greenland fjord freshwater budget*, Nature Geoscience, 11, 49–54, doi: 10.1038/s41561-017-0018-z.

Möller, M., Friedl, P., Palmer, S. J., and Marzeion, B., 2022: *Grounding Line Retreat and Ice Discharge Variability at Two Surging, Ice Shelf-Forming Basins of Flade Isblink Ice Cap, Northern Greenland*, Journal of Geophysical Research: Earth Surface, 127, e2021JF006 302, doi: 10.1029/2021JF006302, e2021JF006302 2021JF006302.

New, M., Hulme, M., and Jones, P., 1999: *Representing Twentieth-Century Space–Time Climate Variability. Part I: Development of a 1961–90 Mean Monthly Terrestrial Climatology*, Journal of Climate, 12, 829–856, doi: 10.1175/1520-0442(1999)012⟨0829:RTCSTC⟩2.0.CO;2.

New, M., Lister, D., Hulme, M., and Ian Makin, I., 2002: *A high-resolution data set of surface climate over global land areas*, Climate Research, 21, 1–25, doi: 10.3354/cr021001.

Nick, F. M., Vieli, A., Howat, I. M., and Joughin, I., 2009: *Large-scale changes in Greenland outlet glacier dynamics triggered at the terminus*, Nature Geoscience, 2, 110–114, doi: 10.1038/ngeo394.

Nye, J. F., 1963: *On the Theory of the Advance and Retreat of Glaciers*, Geophysical Journal International, 7, 431–456, doi: 10.1111/j.1365-246X.1963.tb07087.x.

Oerlemans, J., 1997: *A flowline model for Nigardsbreen, Norway: projection of future glacier length based on dynamic calibration with the historic record*, Annals of Glaciology, 24, 382–389, doi: 10.3189/S0260305500012489.

Oerlemans, J. and Nick, F., 2006: *Modelling the advance–retreat cycle of a tidewater glacier with simple sediment dynamics*, Global and Planetary Change, 50, 148–160, doi: 10.1016/j.gloplacha.2005.12.002.

Oerlemans, J. and Nick, F. M., 2005: *A minimal model of a tidewater glacier*, Annals of Glaciology, 42, 1–6, doi: 10.3189/172756405781813023.

Ohmura, A., 2001: *Physical Basis for the Temperature-Based Melt-Index Method*, Journal of Applied Meteorology, 40, 753 – 761, doi: 10.1175/1520-0450(2001)040⟨0753: PBFTTB⟩2.0.CO;2.

Ohmura, A., 2006: *Changes in mountain glaciers and ice caps during the 20th century*, Annals of Glaciology, 43, 361–368, doi: 10.3189/172756406781812212.

Ohmura, A., Bauder, A., Müller, H., and Kappenberger, G., 2007: *Long-term change of mass balance and the role of radiation*, Annals of Glaciology, 46, 367–374, doi: 10.3189/172756407782871297.

Oppenheimer, M., Glavovic, B., Hinkel, J., van de Wal, R., Magnan, A., Abd-Elgawad, A., Cai, R., Cifuentes-Jara, M., DeConto, R., Ghosh, T., Hay, J., Isla, F., Marzeion, B., Meyssignac, B., and Sebesvari, Z., 2019: *Sea Level Rise and Implications for Low-Lying Islands, Coasts and Communities*, IPCC Special Report on the Ocean and Cryosphere in a Changing Climate, pp. 131–202, doi: 10.1017/9781009157964.006.

Parkes, D. and Goosse, H., 2020: *Modelling regional glacier length changes over the last millennium using the Open Global Glacier Model*, The Cryosphere, 14, 3135–3153, doi: 10.5194/tc-14-3135-2020.

Parkes, D. and Marzeion, B., 2018: *Twentieth-century contribution to sea-level rise from uncharted glaciers*, Nature, 563, 551–554, doi: 10.1038/s41586-018-0687-9.

Paul, F., Barrand, N., Baumann, S., Berthier, E., Bolch, T., Casey, K., Frey, H., Joshi, S., Konovalov, V., Le Bris, R., and et al., 2013: *On the accuracy of glacier outlines derived from remote-sensing data*, Annals of Glaciology, 54, 171–182, doi: 10.3189/2013AoG63A296.

Pennelly, C. and Myers, P. G., 2022: *Tracking Irminger Rings' properties using a submesoscale ocean model*, Progress in Oceanography, 201, 102 735, doi: 10.1016/j.pocean.2021.102735.

Pfeffer, W. T., Arendt, A. A., Bliss, A., Bolch, T., Cogley, J. G., Gardner, A. S., Hagen, J.-O., Hock, R., Kaser, G., Kienholz, C., and et al., 2014: *The Randolph Glacier Inventory: a globally complete inventory of glaciers*, Journal of Glaciology, 60, 537–552, doi: 10.3189/2014JoG13J176.

Poli, P., Hersbach, H., Dee, D. P., Berrisford, P., Simmons, A. J., Vitart, F., Laloyaux, P., Tan, D. G. H., Peubey, C., Thépaut, J.-N., Trémolet, Y., Hólm, E. V., Bonavita, M., Isaksen, L., and Fisher, M., 2016: *ERA-20C: An Atmospheric Reanalysis of the Twentieth Century*, Journal of Climate, 29, 4083–4097, doi: 10.1175/JCLI-D-15-0556.1.

Rabatel, A., Sanchez, O., Vincent, C., and Six, D., 2018: *Estimation of Glacier Thickness From Surface Mass Balance and Ice Flow Velocities: A Case Study on Argentière Glacier, France*, Frontiers in Earth Science, 6, doi: 10.3389/feart.2018.00112.

Radić, V. and Hock, R., 2011: *Regionally differentiated contribution of mountain glaciers and ice caps to future sea-level rise*, Nature Geoscience, 4, 91–94, doi: 10.1038/ngeo1052.

Radić, V., Bliss, A., Beedlow, A. C., Hock, R., Miles, E., and Cogley, J. G., 2014: *Regional and global projections of twenty-first century glacier mass changes in response to climate scenarios from global climate models*, Climate Dynamics, 42, 37–58, doi: 10.1007/s00382-013-1719-7.

Rainsley, E., Menviel, L., Fogwill, C. J., Turney, C. S. M., Hughes, A. L. C., and Rood, D. H., 2018: *Greenland ice mass loss during the Younger Dryas driven by Atlantic Meridional Overturning Circulation feedbacks*, Scientific Reports, 8, 11 307, doi: 10.1038/s41598-018-29226-8.

Raj, R. P., Chatterjee, S., Bertino, L., Turiel, A., and Portabella, M., 2019: *The Arctic Front and its variability in the Norwegian Sea*, Ocean Science, 15, 1729–1744, doi: 10.5194/os-15-1729-2019.

Recinos, B., Maussion, F., Rothenpieler, T., and Marzeion, B., 2019: *Impact of frontal ablation on the ice thickness estimation of marine-terminating glaciers in Alaska*, The Cryosphere, 13, 2657–2672, doi: 10.5194/tc-13-2657-2019.

Recinos, B., Maussion, F., Noël, B., Möller, M., and Marzeion, B., 2021: *Calibration of a frontal ablation parameterisation applied to Greenland's peripheral calving glaciers*, Journal of Glaciology, 67, 1177–1189, doi: 10.1017/jog.2021.63.

RGI, 2017: *Randolph Glacier Inventory (RGI) - A Dataset of Global Glacier Outlines: Version 6.0*, Technical Report, Global Land Ice Measurements from Space, Boulder, Colorado, USA, doi: 10.7265/N5-RGI-60.

RGI Consortium, 2017: *Randolph Glacier Inventory (RGI) - A Dataset of Global Glacier Outlines: Version 6.0*, doi: 10.7265/N5-RGI-60.

Rignot, E., Xu, Y., Menemenlis, D., Mouginot, J., Scheuchl, B., Li, X., Morlighem, M., Seroussi, H., den Broeke, M. v., Fenty, I., et al., 2016: *Modeling of ocean-induced ice melt* *rates of five west Greenland glaciers over the past two decades*, Geophysical Research Letters, 43, 6374–6382, doi: 10.1002/2016GL068784.

Robel, A. A., 2017: *Thinning sea ice weakens buttressing force of iceberg mélange and promotes calving*, Nature Communications, 8, 1–7, doi: 10.1038/ncomms14596.

Roe, G. H., Christian, J. E., and Marzeion, B., 2021: *On the attribution of industrial-era glacier mass loss to anthropogenic climate change*, The Cryosphere, 15, 1889–1905, doi: 10.5194/tc-15-1889-2021.

Rong, X., 2019: *CAMS CAMS-CSM1.0 model output prepared for CMIP6 ScenarioMIP*, Earth System Grid Federation, doi: 10.22033/ESGF/CMIP6.11004.

Rothman, D. H., 2017: *Thresholds of catastrophe in the Earth system*, Science Advances, 3, e1700 906, doi: 10.1126/sciadv.1700906.

Rothman, D. H., 2019: *Characteristic disruptions of an excitable carbon cycle*, Proceedings of the National Academy of Sciences, 116, 14 813–14 822, doi: 10.1073/pnas.1905164116.

Rye, C. J., Willis, I. C., Arnold, N. S., and Kohler, J., 2012: *On the need for automated multiobjective optimization and uncertainty estimation of glacier mass balance models*, Journal of Geophysical Research: Earth Surface, 117, doi: 10.1029/2011JF002184.

Saha, S., Moorthi, S., Pan, H.-L., Wu, X., Wang, J., Nadiga, S., Tripp, P., Kistler, R., Woollen, J., Behringer, D., Liu, H., Stokes, D., Grumbine, R., Gayno, G., Wang, J., Hou, Y.-T., Chuang, H.-y., Juang, H.-M. H., Sela, J., Iredell, M., Treadon, R., Kleist, D., Van Delst, P., Keyser, D., Derber, J., Ek, M., Meng, J., Wei, H., Yang, R., Lord, S., van den Dool, H., Kumar, A., Wang, W., Long, C., Chelliah, M., Xue, Y., Huang, B., Schemm, J.-K., Ebisuzaki, W., Lin, R., Xie, P., Chen, M., Zhou, S., Higgins, W., Zou, C.-Z., Liu, Q., Chen, Y., Han, Y., Cucurull, L., Reynolds, R. W., Rutledge, G., and Goldberg, M., 2010: *The NCEP Climate Forecast System Reanalysis*, Bulletin of the American Meteorological Society, 91, 1015–1058, doi: 10.1175/2010BAMS3001.1.

Sanchez, R., Slater, D., and Straneo, F., 2023: *Delayed Freshwater Export from a Greenland tidewater glacial fjord*, Journal of Physical Oceanography, doi: 10.1175/JPO-D-22-0137.1.

Schlemm, T. and Levermann, A., 2019: *A simple stress-based cliff-calving law*, The Cryosphere, 13, 2475–2488, doi: 10.5194/tc-13-2475-2019.

Schoof, C., 2007: *Ice sheet grounding line dynamics: Steady states, stability, and hysteresis*, Journal of Geophysical Research: Earth Surface, 112, doi: 10.1029/2006JF000664.

Schupfner, M., Wieners, K.-H., Wachsmann, F., Steger, C., Bittner, M., Jungclaus, J., Früh, B., Pankatz, K., Giorgetta, M., Reick, C., Legutke, S., Esch, M., Gayler, V., Haak, H., de Vrese, P., Raddatz, T., Mauritsen, T., von Storch, J.-S., Behrens, J., Brovkin, V., Claussen, M., Crueger, T., Fast, I., Fiedler, S., Hagemann, S., Hohenegger, C., Jahns, T., Kloster, S., Kinne, S., Lasslop, G., Kornblueh, L., Marotzke, J., Matei, D., Meraner, K., Mikolajewicz, U., Modali, K., Müller, W., Nabel, J., Notz, D., Peters-von Gehlen, K., Pincus, R., Pohlmann, H., Pongratz, J., Rast, S., Schmidt, H., Schnur, R., Schulzweida, U., Six, K., Stevens, B., Voigt, A., and Roeckner, E., 2019: *DKRZ MPI-ESM1.2-HR model output prepared for CMIP6 ScenarioMIP*, Earth System Grid Federation, doi: 10.22033/ESGF/CMIP6.2450.

Shannon, S., Smith, R., Wiltshire, A., Payne, T., Huss, M., Betts, R., Caesar, J., Koutroulis, A., Jones, D., and Harrisson, S., 2019: *Global glacier volume projections under high end climate change scenarios*, The Cryosphere, 1, 325–350, doi: 10.5194/tc-13-325-2019.

Shugar, D. H., Burr, A., Haritashya, U. K., Kargel, J. S., C, S. W., Kennedy, M. C., Bevington, A. R., Betts, R. A., Harrison, S., and Strattman, K., 2020: *Rapid worldwide growth of glacial lakes since 1990*, Nature Climate Change, pp. 1–7, doi: 10.1038/s41558-020-0855-4.

Slangen, A. B. A., Meyssignac, B., Agosta, C., Champollion, N., Church, J. A., Fettweis, X., Ligtenberg, S. R. M., Marzeion, B., Melet, A., Palmer, M. D., Richter, K., Roberts, C. D., and Spada, G., 2017: *Evaluating Model Simulations of Twentieth-Century Sea Level Rise. Part I: Global Mean Sea Level Change*, Journal of Climate, 30, 8539–8563, doi: 10.1175/JCLI-D-17-0110.1.

Slater, D. A., Nienow, P. W., Cowton, T. R., Goldberg, D. N., and Sole, A. J., 2015: *Effect of near-terminus subglacial hydrology on tidewater glacier submarine melt rates*, Geophysical Research Letters, 42, 2861–2868, doi: 10.1002/2014GL062494.

Slater, D. A., Goldberg, D. N., Nienow, P. W., and Cowton, T. R., 2016: *Scalings for Submarine Melting at Tidewater Glaciers from Buoyant Plume Theory*, Journal of Physical Oceanography, 46, 1839 – 1855, doi: 10.1175/JPO-D-15-0132.1.

Slater, D. A., Benn, D. I., Cowton, T. R., Bassis, J. N., and Todd, J. A., 2021a: *Calving Multiplier Effect Controlled by Melt Undercut Geometry*, Journal of Geophysical Research: Earth Surface, 126, e2021JF006 191, doi: 10.1029/2021JF006191, e2021JF006191 2021JF006191.

Slater, T., Lawrence, I. R., Otosaka, I. N., Shepherd, A., Gourmelen, N., Jakob, L., Tepes, P., Gilbert, L., and Nienow, P., 2021b: *Review article: Earth's ice imbalance*, The Cryosphere, 15, 233–246, doi: 10.5194/tc-15-233-2021.

Slivinski, L. C., Compo, G. P., Whitaker, J. S., Sardeshmukh, P. D., Giese, B. S., McColl, C., Allan, R., Yin, X., Vose, R., Titchner, H., Kennedy, J., Spencer, L. J., Ashcroft, L., Brönnimann, S., Brunet, M., Camuffo, D., Cornes, R., Cram, T. A., Crouthamel, R., Domínguez-Castro, F., Freeman, J. E., Gergis, J., Hawkins, E., Jones, P. D., Jourdain, S., Kaplan, A., Kubota, H., Blancq, F. L., Lee, T.-C., Lorrey, A., Luterbacher, J., Maugeri, M., Mock, C. J., Moore, G. K., Przybylak, R., Pudmenzky, C., Reason, C., Slonosky, V. C., Smith, C. A., Tinz, B., Trewin, B., Valente, M. A., Wang, X. L., Wilkinson, C., Wood, K., and Wyszyński, P., 2019: *Towards a more reliable historical* *reanalysis: Improvements for version 3 of the Twentieth Century Reanalysis system*, Quarterly Journal of the Royal Meteorological Society, 145, 2876–2908, doi: 10.1002/qj.3598.

Small, C. and Nicholls, R. J., 2003: *A Global Analysis of Human Settlement in Coastal Zones*, Journal of Coastal Research, 19, 584–599.

Smith, G. C., Roy, F., Mann, P., Dupont, F., Brasnett, B., Lemieux, J.-F., Laroche, S., and Bélair, S., 2014: *A new atmospheric dataset for forcing ice–ocean models: Evaluation of reforecasts using the Canadian global deterministic prediction system*, Quarterly Journal of the Royal Meteorological Society, 140, 881–894, doi: 10.1002/qj.2194.

Stearns, L. and Van der Veen, C., 2018: *Friction at the bed does not control fast glacier flow*, Science, 361, 273–277, doi: 10.1126/science.aat2217.

Steffen, W., Rockström, J., Richardson, K., Lenton, T. M., Folke, C., Liverman, D., Summerhayes, C. P., Barnosky, A. D., Cornell, S. E., Crucifix, M., Donges, J. F., Fetzer, I., Lade, S. J., Scheffer, M., Winkelmann, R., and Schellnhuber, H. J., 2018: *Trajectories of the Earth System in the Anthropocene*, Proceedings of the National Academy of Sciences, 115, 8252–8259, doi: 10.1073/pnas.1810141115.

Stommel, H., 1958: *The abyssal circulation*, Deep Sea Research (1953), 5, 80–82, doi: 10.1016/S0146-6291(58)80014-4.

Straneo, F. and Cenedese, C., 2015: *The Dynamics of Greenland's Glacial Fjords and Their Role in Climate*, Annual Review of Marine Science, 7, 89–112, doi: 10.1146/annurev-marine-010213-135133, pMID: 25149564.

Straneo, F., Heimbach, P., Sergienko, O., Hamilton, G., Catania, G., Griffies, S., Hallberg, R., Jenkins, A., Joughin, I., Motyka, R., et al., 2013: *Challenges to understanding the dynamic response of Greenland's marine terminating glaciers to oceanic and atmospheric forcing*, Bulletin of the American Meteorological Society, 94, 1131–1144, doi: 10.1175/BAMS-D-12-00100.1.

Sun, J., Latif, M., and Park, W., 2021: *Subpolar Gyre–AMOC–Atmosphere Interactions on Multidecadal Timescales in a Version of the Kiel Climate Model*, Journal of Climate, 34, 6583 – 6602, doi: 10.1175/JCLI-D-20-0725.1.

Tamang, S. K., Ebtehaj, A. M., Prein, A. F., and Heymsfield, A. J., 2020: *Linking Global Changes of Snowfall and Wet-Bulb Temperature*, Journal of Climate, 33, 39 – 59, doi: 10.1175/JCLI-D-19-0254.1.

Taylor, K. E., 2001: *Summarizing multiple aspects of model performance in a single diagram*, Journal of Geophysical Research: Atmospheres, 106, 7183–7192, doi: 10.1029/2000JD900719.

Timmermans, M.-L. and Marshall, J., 2020: *Understanding Arctic Ocean Circulation: A Review of Ocean Dynamics in a Changing Climate*, Journal of Geophysical Research: Oceans, 125, e2018JC014 378, doi: 10.1029/2018JC014378, e2018JC014378 10.1029/2018JC014378.

Vallis, G. K., 2012: *Climate and the Oceans*, Princeton University Press.

Van de Wal, R. S. W. and Wild, M., 2001: *Modelling the response of glaciers to climate change by applying volume-area scaling in combination with a high resolution GCM*, Climate Dynamics, 18, 359–366, doi: 10.1007/s003820100184.

Vieli, A. and Payne, A. J., 2005: *Assessing the ability of numerical ice sheet models to simulate grounding line migration*, Journal of Geophysical Research: Earth Surface, 110, doi: 10.1029/2004JF000202.

Volodin, E., Mortikov, E., Gritsun, A., Lykossov, V., Galin, V., Diansky, N., Gusev, A., Kostrykin, S., Iakovlev, N., Shestakova, A., and Emelina, S., 2019a: *INM INM-CM4-8 model output prepared for CMIP6 ScenarioMIP*, Earth System Grid Federation, doi: 10.22033/ESGF/CMIP6.12321.

Volodin, E., Mortikov, E., Gritsun, A., Lykossov, V., Galin, V., Diansky, N., Gusev, A., Kostrykin, S., Iakovlev, N., Shestakova, A., and Emelina, S., 2019b: *INM INM-CM5-0 model output prepared for CMIP6 ScenarioMIP*, Earth System Grid Federation, doi: 10.22033/ESGF/CMIP6.12322.

von Schuckmann, K., Cheng, L., Palmer, M. D., Hansen, J., Tassone, C., Aich, V., Adusumilli, S., Beltrami, H., Boyer, T., Cuesta-Valero, F. J., Desbruyères, D., Domingues, C., García-García, A., Gentine, P., Gilson, J., Gorfer, M., Haimberger, L., Ishii, M., Johnson, G. C., Killick, R., King, B. A., Kirchengast, G., Kolodziejczyk, N., Lyman, J., Marzeion, B., Mayer, M., Monier, M., Monselesan, D. P., Purkey, S., Roemmich, D., Schweiger, A., Seneviratne, S. I., Shepherd, A., Slater, D. A., Steiner, A. K., Straneo, F., Timmermans, M.-L., and Wijffels, S. E., 2020: *Heat stored in the Earth system: where does the energy go?*, Earth System Science Data, 12, 2013–2041, doi: 10.5194/essd-12-2013-2020.

Wassmann, P., Duarte, C. M., Agusti, S., and Sejr, M. K., 2011: *Footprints of climate change in the Arctic marine ecosystem*, Global Change Biology, 17, 1235–1249, doi: 10.1111/j.1365-2486.2010.02311.x.

Welty, E., Zemp, M., Navarro, F., Huss, M., Fürst, J. J., Gärtner-Roer, I., Landmann, J., Machguth, H., Naegeli, K., Andreassen, L. M., Farinotti, D., Li, H., and Contributors, G., 2020: *Worldwide version-controlled database of glacier thickness observations*, Earth System Science Data, 12, 3039–3055, doi: 10.5194/essd-12-3039-2020.

Werder, M. A., Huss, M., Paul, F., Dehecq, A., and Farinotti, D., 2020: *A Bayesian ice thickness estimation model for large-scale applications*, Journal of Glaciology, 66, 137–152, doi: 10.1017/jog.2019.93.

WGMS, 2015: *Global Glacier Change Bulletin No. 1 (2012-2013)*, Zemp, M., Gärtner-Roer, I., Nussbaumer, S.U., Hüsler, F., Machguth, H., Mölg, N., Paul F., and Hoelzle, M. (eds.), ICSU(WDS)/IUGG(IACS)/UNEP/UNESCO/WMO, World Glacier Monitoring Service, Zurich, Switzerland, p. 230, doi: doi:10.5904/wgms-fog-2015-11.

WGMS, 2018: *Fluctuations of Glaciers Database*, World Glacier Monitoring Service, Zurich, Switzerland, doi: 10.5904/wgms-fog-2018-11.

WGMS, 2020: *Global Glacier Change Bulletin No. 3 (2016-2017)*, Zemp, M., Gärtner-Roer, I., Nussbaumer, S. U., Bannwart, J., Rastner, P., Paul, F., and Hoelzle, M. (eds.), ISC(WDS)/IUGG(IACS)/UNEP/UNESCO/WMO, World Glacier Monitoring Service, Zurich, Switzerland, doi: 10.5904/wgms-fog-2020-08.

White, A. and Copland, L., 2019: *Loss of floating glacier tongues from the Yelverton Bay region, Ellesmere Island, Canada*, Journal of Glaciology, 65, 376–394, doi: 10.1017/jog.2019.15.

Wijngaard, R. R., Biemans, H., Lutz, H., Shrestha, A. B., Wester, P., and Immerzeel, W., 2018: *Climate change vs. socio-economic development:understanding the future South Asian water gap*, Hydrology and Earth System Sciences, 22, 6297–6321, doi: 10.5194/hess-22-6297-2018.

Wild, M., 2012: *Enlightening Global Dimming and Brightening*, Bulletin of the American Meteorological Society, 93, 27–37, doi: 10.1175/BAMS-D-11-00074.1.

Wood, M., Rignot, E., Fenty, I., Menemenlis, D., Millan, R., Morlighem, M., Mouginot, J., and Seroussi, H., 2018: *Ocean-Induced Melt Triggers Glacier Retreat in Northwest Greenland*, Geophysical Research Letters, 45, 8334–8342, doi: 10.1029/2018GL078024.

Wood, M., Rignot, E., Fenty, I., An, L., Bjørk, A., van den Broeke, M., Cai, C., Kane, E., Menemenlis, D., Millan, R., Morlighem, M., Mouginot, J., Noël, B., Scheuchl, B., Velicogna, I., Willis, J. K., and Zhang, H., 2021: *Ocean forcing drives glacier retreat in Greenland*, Science Advances, 7, eaba7282, doi: 10.1126/sciadv.aba7282.

Wouters, B., Gardner, A. S., and Moholdt, G., 2019: *Global Glacier Mass Loss During the GRACE Satellite Mission (2002-2016)*, Frontiers in Earth Science, 7, 96, doi: 10.3389/feart.2019.00096.

Xin, X., Wu, T., Shi, X., Zhang, F., Li, J., Chu, M., Liu, Q., Yan, J., Ma, Q., and Wei, M., 2019: *BCC BCC-CSM2MR model output prepared for CMIP6 ScenarioMIP*, Earth System Grid Federation, doi: 10.22033/ESGF/CMIP6.1732.

Xu, Y., Rignot, E., Fenty, I., Menemenlis, D., and Flexas, M. M., 2013: *Subaqueous melting of Store Glacier, west Greenland from three-dimensional, high-resolution numerical modeling and ocean observations*, Geophysical Research Letters, 40, 4648–4653, doi: 10.1002/grl.50825.

Yu, Y., 2019: *CAS FGOALS-f3-L model output prepared for CMIP6 ScenarioMIP*, Earth System Grid Federation, doi: 10.22033/ESGF/CMIP6.2046.

Yukimoto, S., Koshiro, T., Kawai, H., Oshima, N., Yoshida, K., Urakawa, S., Tsujino, H., Deushi, M., Tanaka, T., Hosaka, M., Yoshimura, H., Shindo, E., Mizuta, R., Ishii, M., Obata, A., and Adachi, Y., 2019: *MRI MRI-ESM2.0 model output prepared for CMIP6 ScenarioMIP*, Earth System Grid Federation, doi: 10.22033/ESGF/CMIP6.638.

Zekollari, H., Huss, M., Farinotti, D., and Lhermitte, S., 2022: *Ice-Dynamical Glacier Evolution Modeling—A Review*, Reviews of Geophysics, 60, e2021RG000 754, doi: doi.org/10.1029/2021RG000754, e2021RG000754 2021RG000754.

Zemp, M., Huss, M., Thibert, E., Eckert, N., McNabb, R., Huber, J., Barandun, M., Machguth, H., Nussbaumer, S. U., Gärtner-Roer, I., Thomson, L., Paul, F., Maussion, F., Kutuzov, S., and Cogley, J. G., 2019: *Global glacier mass changes and their contributions to sea-level rise from 1961 to 2016*, Nature, 568, 382–386, doi: 10.1038/s41586-019-1071-0.

Zemp, M., Nussbaumer, S., Gärtner-Roer, I., Bannwart, J., Paul, F., and Hoelzle, M., 2021: *Global Glacier Change Bulletin No. 4 (2018–2019)*, p. 278, doi: 10.5904/wgms-fog-2021-05.

Zoet, L. K. and Iverson, N. R., 2020: *A slip law for glaciers on deformable beds*, Science, 368, 76–78, doi: 10.1126/science.aaz1183.

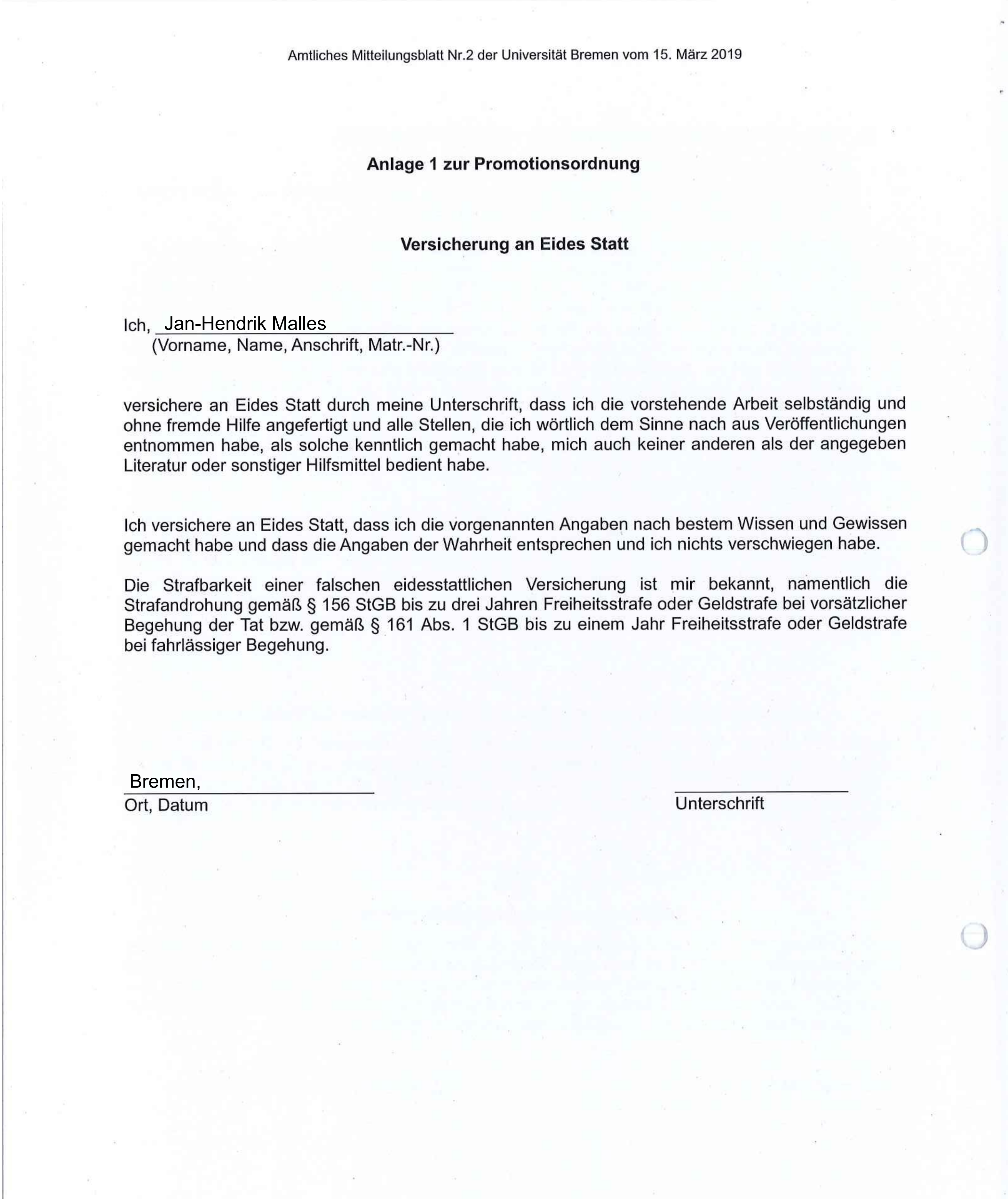

Anlage 1 zur Promotionsordnung

Versicherung an Eides Statt

Ich, Jan-Hendrik Malles
(Vorname, Name, Anschrift, Matr.-Nr.)

versichere an Eides Statt durch meine Unterschrift, dass ich die vorstehende Arbeit selbständig und ohne fremde Hilfe angefertigt und alle Stellen, die ich wörtlich dem Sinne nach aus Veröffentlichungen entnommen habe, als solche kenntlich gemacht habe, mich auch keiner anderen als der angegeben Literatur oder sonstiger Hilfsmittel bedient habe.

Ich versichere an Eides Statt, dass ich die vorgenannten Angaben nach bestem Wissen und Gewissen gemacht habe und dass die Angaben der Wahrheit entsprechen und ich nichts verschwiegen habe.

Die Strafbarkeit einer falschen eidesstattlichen Versicherung ist mir bekannt, namentlich die Strafandrohung gemäß § 156 StGB bis zu drei Jahren Freiheitsstrafe oder Geldstrafe bei vorsätzlicher Begehung der Tat bzw. gemäß § 161 Abs. 1 StGB bis zu einem Jahr Freiheitsstrafe oder Geldstrafe bei fahrlässiger Begehung.

Bremen,
Ort, Datum

Unterschrift